INVESTIGATION OF HIGH SPECTRAL RESOLUTION SIGNATURES AND RADIATIVE FORCING OF TROPOSPHERIC AEROSOL IN THE THERMAL INFRARED

A Dissertation
Presented to
The Academic Faculty

By

Gregory J. Boer

In Partial Fulfillment
Of the Requirements for the Degree
Doctor of Philosophy in
School of Earth and Atmospheric Sciences

Georgia Institute of Technology
May 2010

Approved by:

Dr. Irina Sokolik, Advisor
School of Earth and Atmospheric Sciences
Georgia Institute of Technology

Dr. Carol Paty
School of Earth and Atmospheric Sciences
Georgia Institute of Technology

Dr. Judith Curry
School of Earth and Atmospheric Sciences
Georgia Institute of Technology

Dr. Olga Kalashnikova
Jet Propulsion Laboratory
NASA

Dr. Josef Dufek
School of Earth and Atmospheric Sciences
Georgia Institute of Technology

Date Approved: December 3, 2009

To Pat and Cokie

ACKNOWLEDGEMENTS

I wish to thank my advisor, Dr. Irina Sokolik, for her guidance and support in mentoring me throughout my years as a student both at the University of Colorado and Georgia Tech. I would especially like to thank Gail Anderson of the Air Force Research Laboratory for providing the Alpha version of MODTRAN used in the development of this research, and for numerous discussions on the functionality and capabilities of MODTRAN. I would also like to thank Dr. Snell of AER for providing IDL code to apply AIRS spectral response functions to the output of MODTRAN. I am very grateful for the support received as a research fellow at the Center for Strategic Intelligence Research at the National Defense Intelligence College. I would like to thank my family for their encouragement in completing this dissertation, and finally I would like to thank Pat for her patience with the time and effort this dissertation took.

TABLE OF CONTENTS

LIST OF TABLES

LIST OF FIGURES

LIST OF SYMBOLS AND ABBREVIATIONS

α_i	Ellipsoid polarizability along semiaxis
β	$(\varepsilon\text{-}1)^{-1}$
β'	Real part of β
β''	Imaginary part of β
β_e	Extinction Coefficient
β_s	Scattering Coefficient
β_a	Absorption Coefficient
ε	Complex dielectric constant (m^2)
Φ	Radiant flux (W)
$\gamma(\theta)$	Volume scattering function ($m^{-1}sr^{-1}$)
λ	Wavelength
ν	Wavenumber (cm^{-1})
ν_u	Upper frequency limit of attenuated total reflectance data
ρ	Density
ϖ	Single scattering albedo
θ	Angle
θ	Phase of complex reflectivity
θ_{ν_u}	Phase correction term for ATR Kramers-Kronig transformation
σ_g	Geometric standard deviation
ω	Solid angle

a, b, c	Ellipsoid semiaxes
C_{sca}	Scattering Coefficient
C_{abs}	Absorption Coefficient
C_p	Specific heat at constant pressure
E	Irradiance (Wm^{-2})
f_i	Volume mixing fraction
ΔF	Radiative forcing
F	Net flux
F_ν	Spectral net flux
$F^{\uparrow}$	Upward flux
$F^{\downarrow}$	Downward flux
$g, \langle \cos\theta \rangle$	Asymmetry parameter
I	Radiative Intensity (wsr^{-1})
k	Imaginary part of the complex index of refraction
$\tilde{k}$	Wavenumber ($2\pi/\lambda$)
L	Geometric shape factor
m	Complex index of refraction
M_i	Molecular weight of component i
n	Real part of the complex index of refraction
n_∞	High frequency value of n
n_{el}	Electronic transition component of n
$n(r)$	Number size distribution (m^{-4})
N_0	Total particle concentration (cm^{-3})

P	Cauchy principal value
$P(\theta)$	Scattering phase function
R	Molar refraction
R_i	Partial molar refraction of component i
r_s	Magnitude of complex reflectivity, s-polarized
r	Particle radius
r_g	Median radius
S_{11}	Element 1,1 of Stokes scattering matrix
T	Temperature
V_m	Molar volume
v	Volume
w_i	Mass fraction of component i
z	Height

AERI	Atmospheric Emitted Radiance Interferometer
AFGL	Air Force Geophysics Laboratory
AFRL	Air Force Research Laboratory
AIRS	Atmospheric Infrared Sounder
AMMA	African Monsoon Multidisciplinary Analysis
AN	Ammonium Nitrate
AOD	Aerosol Optical Depth
ARIES	Airborne Research Interferometer Evaluation System
ARM	Atmospheric Radiation Measurement
AS	Ammonium Sulfate

ASPEN	Atmospheric Sounding Processing Environment
ATR	Attenuated Total Reflectance
B	Bruggeman
BC	Black Carbon
BOA	Bottom of the Atmosphere
BT	Brightness Temperature
BTD	Brightness Temperature Difference
CALIPSO	Cloud-Aerosol Lidar and Infrared Pathfinder Satellite Observation
CALIOP	Cloud-Aerosol Lidar with Orthogonal Polarization
CDE	Continuous Distribution of Ellipsoids
CFC	chlorofluorocarbons
CKD	Clough-Kneizys-Davies
DDA	Discrete Dipole Approximation
DISORT	Discrete Ordinate Radiative Transfer
DODO	Dust Outflow and Deposition to Ocean
EMA	Effective Medium Approximation
FASCODE	Fast Atmospheric Signature CODE
FIR	Far Infrared
FTIR	Fourier Transform Infrared
GCM	General Circulation Model
IAPWS	International Association for the Properties of Water and Steam
IASI	Infrared Atmospheric Sounding Interferometer
IMG	Interferometric Monitor for Greenhouse Gases
IR	Infrared
K-K	Kramers-Kronig

LAARI	Library of Atmospheric Aerosol Refractive Indices
L-L	Lorentz-Lorenz
L1B	Level 1B
MITR	mineral-transported
maxne	maximum normalized error
MEM	Mineralogy-based External Mixture
M-G	Maxwell-Garnett
MIPAS	Michelson Interferometer for Passive Atmospheric Sounding
mne	mean normalized error
MODIS	Moderate Resolution Imaging Spectroradiometer
MODTRAN	MODerate resolution atmospheric TRANsmission
MOD5v3r5	MODTRAN5 Version 3 Release 5
NA	Nitric Acid
NCAR	National Center for Atmospheric Research
NIR	Near Infrared
NWP	Numerical Weather Prediction
OPAC	Optical Properties of Aerosols and Clouds
PCHIP	piecewise cubic Hermite interpolating polynomial
RMS	Root Mean Square
SA	Sulfuric Acid
SAMUM	Saharan Mineral Dust Experiment
SAP	Spectral Aerosol Profile
SHADE	Saharan Dust Experiment
SST	Sea Surface Temperature
SWIR	Shortwave Infrared

TIR	Thermal Infrared
TOA	Top of the Atmosphere
VADC	volume-average dielectric constant
VARI	volume-average refractive index
VIS	Visible
VRI	Volz Saharan dust refractive index
WARI	weighted-average refractive index

SUMMARY

Tropospheric aerosol is well known to affect the transport of radiant energy through the atmosphere, thereby impacting the radiative balance and climate of the Earth along with remote sensing of geophysical properties. Significant research and optical modeling has been conducted for aerosol in the solar regime, but little work has been done to date in the thermal infrared, especially at high spectral resolution.

In this dissertation we begin to address these issues in a number of ways. First, we have developed a high spectral resolution library of atmospheric aerosol optical constants to support advanced modeling of optical properties. As part of this effort we have developed new optical constants from attenuated total reflectance measurements of sulfate-nitrate-ammonium aqueous solutions. We also collected a broad range of existing optical constants for aerosol components including numerous mineral optical constants.

The mineral optical constants were used to model and study infrared dust optical signatures as a function of the composition, size, shape and mixing state. This analysis indicated that the non-sphericity of naturally-occurring dust particles must be taken into account when modeling dust optical properties at high spectral resolution in the thermal infrared (IR). Our modeling indicated that the T-matrix method was a good candidate for more accurate modeling. Our new results provide insight into how optical signatures could be used to retrieve dust microphysical properties. We also examined the performance of some of the most common effective medium approximations for internal mixtures by using them to model the optical constants of our newly determined sulfate-nitrate-ammonium mixtures.

The knowledge gained from the optical signature analysis was applied to airborne and satellite high spectral resolution thermal infrared radiance data impacted by Saharan dust events. The spectral signature of these actual dust events confirmed that the non-spherical nature of dust particles must be taken into account and that the use of Mie theory for dust optical modeling is not valid at in the thermal IR. Using T-matrix calculated optical properties we developed a new technique to retrieve dust microphysical properties from the dust spectral signature. We also retrieved dust microphysical properties using a standard dust optical constants dataset based on bulk sample measurements, and noted significant differences in the retrieved dust microphysical properties.

Lastly, we used the microphysics retrieved from our new technique and from the standard approach to investigate the effects of dust on radiative forcing and cooling rates in the thermal IR. We demonstrate substantial differences in the retrieved properties. More critically though, we observed significant differences in radiative forcing and cooling rates when the microphysics from the standard dust model were used in a model based on a mixture of the individual mineral components.

This work demonstrates that the determination of, or correction for, dust radiative effects and the retrieval of dust microphysical properties in the thermal IR must begin with accurate modeling of dust optical properties at high spectral resolution that properly takes into account the composition, shape and size distribution of the dust particles. Doing so will allow for more accurate and consistent quantification of dust climate impacts between measurements and models.

CHAPTER 1

INTRODUCTION

Tropospheric aerosols are well known to play an important role in atmospheric radiation transport and the radiation balance and climate of the Earth [*IPCC*, 2001, 2007; *Charlson et al.*, 1992; *Sokolik and Toon*, 1996; *Buseck and Posfai*, 1999]. Yet they continue to be one of the most uncertain elements in the planetary radiation budget [*IPCC*, 2001, 2007; *Charlson et al.*, 1992; *Schwartz and Andreae*, 1996, *Tegen et al.*, 1996; *Sokolik and Toon*, 1996]. Aerosols affect remote sensing radiance/irradiance measurements, Earth's radiative balance and climate by scattering and absorbing both incoming solar radiation and outgoing terrestrial radiation. By affecting remote sensing radiance/irradiance measurements, the geophysical parameters retrieved from those measurements are adversely impacted. In many cases the retrievals of these geophysical parameters do not adequately account for the effects of aerosols [e.g., *Weaver et al.,* 2003; *Highwood et al.,* 2003]. The quantification of the effects of aerosol on climate, particularly dust, is also still deficient [*IPCC*, 2007; *Sokolik et al.,* 2001; *Textor et al.*, 2007].

Quantification of the radiative impacts of tropospheric aerosol on climate, and also weather, requires that both the solar and TIR components of radiative forcing and radiative heating/cooling be accurately modeled. As noted in *Quijano et al.* [2000] dust radiative heating/cooling particularly must be taken into account in order to accurately predict the overall impact of aerosol because the dust heating/cooling alters atmospheric dynamics and thermodynamics. *Lau et al.* [2009] in their General Circulation Model

study of the response of the atmospheric water cycle of West Africa and the Atlantic to Saharan dust radiative forcing found intricate small and large scale meteorological responses to Saharan dust. These responses depended critically on the total radiative effects, solar and TIR, which in turn depended critically on the aerosol optical properties. In their study though, *Lau et al.* only considered 5 aerosol species, one of which was a generic dust, and they only used aerosol optical properties in 11 broad wavelength bands generated using Mie theory. *Wong et al.* [2009] in their study of the maintenance of the temperature inversion of the Saharan air layer found that the dust impact on the net instantaneous heating rate was an essential component in maintaining the temperature structure against thermal relaxation. In their study though, the TIR component was accounted for only by a parameterization.

All of these studies and others have found that the radiative effects of dust, both solar and TIR, depend greatly on the microphysical and macrophysical properties of dust. For example, *Sokolik and Toon* [1999] highlighted the importance of mineral composition on dust radiative properties. Likewise, *Quijano et al.* [2000] found that dust radiative forcing and heating/cooling rates depended significantly on the mineral composition in addition to the vertical distribution of dust and the presence of clouds and the surface albedo. *Otto et al.* [2007] in their study of atmospheric radiative effects of Saharan dust found that the radiative effects of dust at both solar and TIR wavelengths are highly dependent on the dust microphysical properties including optical constants and particle size distribution. In particular they found that coarse mode particles are especially important at both solar and TIR wavelengths in determining aerosol radiative effects.

All of these studies indicate that the accurate assessment of TIR radiative impacts of aerosol depend on accurately modeling the optical properties of the aerosol and macrophysical properties like the vertical distribution. At high spectral resolution in the TIR it has not been demonstrated that use of bulk optical constants for modeling dust composition and the use of Mie theory with its spherical particle assumption is sufficient, and subsequently needs to be investigated

Therefore, one of the keys to improving our understanding of the radiative impact and climate impact of aerosol is to better understand and to better model aerosol optical properties, which are determined by the concentration, composition-dependent optical constants, size distribution, shape, and physicochemical properties (e.g., hygroscopic properties) of aerosols. To date, most of the aerosol optical research has been focused on the solar part of the electromagnetic spectrum. In the thermal infrared (TIR) the impact of tropospheric aerosol has largely been ignored, in part due to the fact that the availability of their infrared (IR) optical constants with which to do so is very limited. Additional research into IR optical properties of aerosols is needed to address these shortcomings. Addressing this issue is one of the goals of this thesis.

Not only is there a deficiency of research into aerosol IR optical properties, but in particular there has been a lack of research into the IR optical properties of aerosols at high spectral resolution. High spectral resolution optical properties are of concern because aerosol components have spectral features that are resolved at high spectral resolution (the basis of IR spectroscopy), and these resolved spectral features give the composite aerosol unique spectral signatures. Therefore, in order to accurately determine the impact and effects of aerosol the spectral optical properties have to be correct.

Additionally, the radiative and climate impact of aerosol can depend critically on the positioning of aerosol spectral features in relation to those of other atmospheric constituents like water vapor, ozone, carbon dioxide, trace gases, etc. For example if the major TIR optical extinction feature of a tropospheric aerosol overlaps spectrally the 9.6 μm ozone absorption, then the radiative balance effect will be much different than if it occurred in a highly transmissive region of the TIR window. For geophysical property retrievals from high spectral resolution measurements the spectral behavior must similarly be modeled correctly in order to account for the impact of aerosol on retrievals.

Properly accounting for the effect of aerosol on retrievals from high spectral resolution TIR sensors is also important because these sensors are very valuable tools for measuring and monitoring the state of the atmosphere and climate. As atmospheric sounders they provide vertical profiles of temperature, water vapor, carbon dioxide, ozone and other trace gases. They also provide information on cloud properties and on surface properties like sea surface temperature (SST) and surface spectral emissivity. For climate studies they provide detailed spectral information on upwelling and downwelling radiance needed for energy balance calculations. Satellite high spectral resolution TIR sensors are especially valuable because they can provide global day/night information.

Currently there are a number of high spectral resolution TIR satellite sensors in operation. Of particular note are the Atmospheric Infrared Sounder (AIRS) and the Infrared Atmospheric Sounding Interferometer (IASI). An example of a high spectral resolution ground-based IR sensor is the Atmospheric Emitted Radiance Interferometer (AERI) sensor deployed at a number of the Department of Energy Atmospheric Radiation Measurement (ARM) program sites and other locations for atmospheric sounding. A

high spectral resolution airborne IR sensor example is the Airborne Research Interferometer Evaluation System (ARIES), which is used extensively for scientific research of the atmosphere and surface. Table 1.1 shows the spectral range and resolution for these sensors.

Table 1.1 Spectral range and resolution of example atmospheric and climate TIR sensors

Sensor	Spectral Range	Spectral Resolution
AIRS [*Aumann et al.*, 2003]	3.7 – 15.4 μm (2700 – 650 cm^{-1})	2378 spectral bands $\lambda/\Delta\lambda \sim 1200$
IASI [*Chalon et al.*, 2001]	645 – 2760 cm^{-1}	0.25 cm^{-1}
AERI [*Dedecker et al.*, 2005]	520 – 3300 cm^{-1}	1 cm^{-1}
ARIES [*Wilson et al.*, 1999]	550 – 3000 cm^{-1}	0.5 cm^{-1}

Although these systems are being used to retrieve valuable atmospheric and surface geophysical data, as noted earlier they currently do not have the ability to account for the effects of aerosol. Not only do they not have the ability to account for the impact of aerosol, they also are not taking advantage of that impact to retrieve information on aerosol. In particular they do not account for or retrieve information on dust aerosol, which is known to significantly affect the IR radiance measured by these sensors, and has the most uncertainty with respect to climate impact of the major aerosol classes [*IPCC*, 2007]. One reason for this greater uncertainty is due to the broad size spectra of dust aerosol that include fine and coarse particle sizes. Dust particles can interact efficiently with outgoing terrestrial radiation as well as with incoming solar radiation. Therefore dust has a significant impact over a larger portion of the electromagnetic spectrum than other aerosol types, while at the same time the microphysical and macrophysical properties of dust vary greatly spatially due to source mineralogical differences [*Claquin et al.*, 1999] and vary greatly both temporally and spatially due to the stochastic nature of

dust events. Dust is also the most abundant aerosol type by mass [*Zender*, 2004] and therefore any uncertainty is magnified compared to other aerosol types. The ability to use high spectral resolution TIR sensors to detect, monitor, and retrieve information on dust globally is therefore important to improving the quality of the geophysical data retrieved in the presence of dust and to constraining the role of dust in climate.

In the IR it is not only dust that we need to be concerned with. Even though it is the larger aerosol particles like dust that are of primary concern in the TIR, and the focus of this thesis, we must also be concerned and able to model the optical properties of an evolving aerosol mixture because the larger particles can become internally mixed with other components. Generally speaking the optical properties of aerosols can and do change dynamically during the time the particles of the aerosol are resident in the atmosphere; due to processes like heterogeneous chemical reactions, heterogeneous nucleation, coalescence, coagulation, cloud processing, deliquescence or efflorescence due to relative humidity changes, and gravitation settling.

As an example, numerous studies including laboratory experiments, modeling simulations, and observational studies have shown that sea-salt and certain mineral components of dust aerosol can react with sulfur and nitrogen oxides (SO_x and NO_y atmospheric gases), e.g. H_2SO_4, SO_2 and NO, NO_2, HNO_3, HONO, NO_3, N_2O_5, HNO_4, PAN species respectively, particularly as they are transported through polluted regions [*Gard et al.*, 1998; *Zhuang et al.*, 1999; *Krueger et al.*, 2004; *Jordan et al.*, 2003; *Song and Carmichael*, 1999]. These reactions change the composition and physicochemical properties of the particles, which in turn can alter their optical properties and potentially the size distribution. For example, sea-salt particles are often seen to be depleted in

chlorine because of reactions with SO_2, sulfuric acid vapor, or nitric acid vapor resulting in the formation of sodium sulfate Na_2SO_4 and sodium nitrate $NaNO_3$ particles [*Krueger et al.*, 2003; *Laskin et al.*, 2003; *Zhuang et al.*, 1999; *Andreae et al.*, 1986]. As another example, dust aerosol that includes calcium carbonate has been shown to react with SO_x and NO_y to form $CaSO_4$ and $Ca(NO_3)_2$, respectively [*Kline et al.,* 2004; *Dentener et al.*, 1996; *Mamane and Gottlieb*, 1989; *Maxwell-Meier et al.*, 2004]. In addition to heterogeneous chemical reactions, fine mode sulfate and nitrate particles can become internally mixed with mineral dust particles, which alter their thermodynamic properties causing a hydrophobic particle to become hydrophilic. Therefore, it is important to have available high spectral resolution optical constants for all major aerosol components so that potential changes in optical properties can be accurately modeled. This thesis addresses this issue by developing a new set of high spectral refractive indices sulfate-nitrate-ammonium aqueous solutions at concentrations and temperatures relative to tropospheric aerosols.

Accurate optical properties' modeling also requires an understanding of component mixing effects on the composite aerosol and how spectral signatures change during transport due to size distribution changes and compositional changes. Lastly, accurate optical properties' modeling requires properly accounting for any particle shape effects. Particle shape effects are typically ignored in modeling of aerosol optical properties the IR. Given accurate aerosol optical properties, it is also critical to use them in a rigorous radiative transfer code that allows the precise specification of the optical properties on a layer by layer basis so as to maintain the improved accuracy.

To determine the current state of the science of retrieving aerosol properties from high spectral resolution IR radiance measurements, we conducted a literature survey on retrieving dust or other aerosol properties from high spectral resolution IR data. We found that there are very few papers in the literature on the topic, dust or otherwise. The few papers that address this topic fall into one of three categories:

1) retrieval of tropospheric aerosol properties from upwelling or downwelling high spectral resolution IR data,

2) retrieval of stratospheric aerosol properties from occultation or limb viewing high spectral resolution IR, or

3) retrieval of Martian dust aerosol properties from satellite upwelling high spectral resolution IR.

Since the focus of this thesis is tropospheric aerosol and the simplifications used in the retrievals of Martian dust properties are not applicable to the atmosphere of the Earth, the first category is the only one applicable to this research. A total of seven papers were found in the first category (see Table 1.2). For the cases found, none attempt to retrieve the aerosol optical properties directly, particularly as a function of altitude. Instead standard aerosol models are used and various parameters of the aerosol model are estimated or retrieved. Examples include the estimation of size distribution parameters such as number density, median radius and geometric standard deviation, or the number density of predetermined aerosol model components. Some techniques do attempt to retrieve the aerosol spectral optical depth or extinction coefficient, but assumptions about composition are made along with size distribution parameters.

Table 1.2 Prior research on retrieval of aerosol properties from high spectral resolution IR radiance data

Reference	Retrieved Quantities	Assumptions
Kruglanski et al. [2006] Boundary layer aerosol retrieval from thermal infrared nadir sounding – Preliminary results	▪ Ocean surface temperature ▪ Aerosol number density for 2 modes, coarse and accumulation	▪ A single homogeneous isothermal aerosol layer in the boundary layer, 0 – 2 km ▪ Retrieved temperature and atmospheric gas profiles are not affected by the aerosol layer ▪ Aerosol is modeled by bimodal sea-salt aerosol from the Optical Properties of Aerosols and Clouds (OPAC) software package, *Hess et al.* [1998] - aerosol optical depth parameterized by the mode number densities
Shimota and Kobayashi [2001] Error analysis for retrieval of urban atmospheric aerosol properties from downwelling infrared radiation spectra *Shimota. et al.* [2002] Retrieval for physical parameters aerosols in an urban area by ground-based FTIR measurement	▪ Extinction coefficient, β, and particle number density for each component of the FASCODE urban aerosol model	▪ Temperature and gas species profiles are known from radiosondes or other sources ▪ Radiative transfer code, FASCODE, treats particle scattering as equal to particle absorption ▪ FASCODE urban aerosol model is used with three aerosol regimes, 0-2 km, 2-10 km, and >10 km ▪ Size distribution is lognormal with mean radius and standard deviation known - only number density is variable ▪ Extinction cross-section is computed using Mie theory
Moy et al. [2005] Retrieving Aerosols from the Atmospheric Emitted Radiance Interferometer: Can it be Done	▪ Ratio of coarse mode number density to accumulation mode number density using independent measurement of aerosol optical depth @ 500 nm	▪ Three standard aerosol components, ammonium sulfate, ammonium nitrate, and dust used in a bimodal lognormal size distribution of fixed median radius and geometric standard deviation ▪ Independent measurement of AOD @ 500 nm is available

Table 1.2 (continued)

Reference	Retrieved Quantities	Assumptions
Rathke et al. [2002] Properties of coastal Antarctic aerosol from combined FTIR spectrometer and sun photometer measurements	▪ Size distribution parameters determined from VIS/NIR data ▪ Effective optical depth spectrum ▪ Chemical composition from spectral features in the effective optical depth spectrum	▪ *King et al.* [1978] algorithm uses bimodal nuclei and accumulation mode lognormal distribution ▪ King algorithm uses standard ice, water, ammonium sulfate, and sulfuric acid optical constants in the VIS/NIR ▪ No coarse mode is used
DeSouza-Machado et al. [2006] Infrared dust spectral signatures from AIRS	▪ IR spectral optical depths ▪ Median radius ▪ Aerosol layer height	▪ Sea surface temperatures and temperature and water vapor profiles accurate and not biased by the presence of dust ▪ A single homogeneous aerosol layer composed only of dust ▪ A unimodal size distribution with fixed standard deviation ▪ Volz Sahara dust refractive indices are representative of all dust
Pierangelo et al. [2004] Dust altitude and infrared optical depth from AIRS	▪ Dust optical depth @ 10 μm ▪ Dust altitude for nighttime data	▪ AIRS data is over ocean ▪ Aerosol is confined to a single homogeneous layer as defined by their 40 pressure layers ▪ Refractive indices are well modeled by the OPAC mineral-transported (MITR)
Pierangelo et al. [2005] Retrieving the effective radius of Saharan dust coarse mode from AIRS	▪ Coarse mode effective radius	▪ The accumulation mode adds < 10% to the optical depth @ 10μm, justifying a monomodal size distribution ▪ Standard deviation of size distribution has little effect

In all of the above research the aerosol optical properties are based on standard aerosol models. In these models Mie theory is used; so all particles are treated as spherical. There is therefore no ability to account for non-spherical particles. Recent laboratory measurements indicate that for dust particles Mie theory is most likely not an appropriate approximation in the TIR [*Hudson et al.,* 2008a, b]. By using standard aerosol models there is also no ability to account for size-resolved regional compositional differences that would be expected to be found in spatially and temporally varying aerosol. For dust the standard aerosol models use refractive index data for the particles that is based on measurements from a few samples of collected aerosol particles, often measured at low spectral resolution. Here, we will use the term bulk material optical properties to refer to optical properties determined from aerosol samples containing many particles. In contrast we will refer to individual aerosol component optical properties as those that are derived from homogeneous samples of pure component material. Given the mineralogical diversity of dust source regions and the distinctiveness of mineral dust components, it is unlikely that low spectral resolution bulk sample derived refractive index data would be sufficient to model dust globally at high spectral resolution, or even as it is transported and evolves and ages.

Our research goes beyond these studies by investigating size-resolved aerosol modeling based on high spectral resolution optical constants of the aerosol components, many of which have been recently measured. This includes collecting optical constants of aerosol components and determining optical constants for some missing components in order to create a library of atmospheric aerosol refractive indices to support advanced modeling. Our research also investigates the use of techniques to generate optical

properties that don't assume spherical particles. This is an important aspect to investigate since dust particles are well known to be irregularly-shaped and little research has been done on whether treating naturally-occurring dust particles as spheres is appropriate in TIR optical models. We also investigate the effects of aerosol mixing assumptions and changes in the parameters of size distributions on the resulting aerosol optical properties. In our subsequent high spectral resolution radiance modeling using the airborne and satellite data, we use and develop a much more versatile yet very rigorous radiative transfer code than has been used in these previous efforts.

Our work also goes beyond these previous studies by developing a new technique to retrieve dust microphysics that takes advantage of the compositional and size distribution information contained in the high spectral resolution dust signature. A new technique is proposed based on a mineralogy-resolved mixture model that allows the dust signature to be accurately modeled and supports regional and temporal changes in the signature. Subsequently we examine the radiative impacts of tropospheric dust aerosol in the TIR, and compare and contrast the impacts as determined by our new retrieval method to those obtained using a standard aerosol model. Lastly we investigate the sensitivity of tropospheric dust radiative impacts to variations in dust macrophysical parameters and develop recommendations for more accurate assessments of dust radiative forcing in the TIR.

The fundamental goal of our work is to improve the radiative transfer modeling of tropospheric aerosol at high spectral resolution in the TIR so that the radiative and climate effects of tropospheric aerosol, particularly dust, can be better constrained and

that geophysical properties, including dust microphysics, can be better retrieved from remote sensing data.

To that end, Chapter 2 documents our development of a library of high spectral resolution aerosol refractive index data called the Library of Atmospheric Aerosol Refractive Indices (LAARI) to support size-resolved multi-component aerosol optical modeling. The development of the library includes the determination of new IR optical constants of aqueous sulfate-nitrate-ammonium multi-component tropospheric aerosols from attenuated total reflectance (ATR) measurements. The IR optical constants for these ubiquitous aerosol components have not existed until now. The development of LAARI also involves the compilation of an extensive collection of existing refractive index data for the main individual components of aerosols.

Chapter 3 investigates how the high spectral resolution TIR optical signatures of tropospheric aerosol components and mixtures vary depending on how they are computed. The use and limitations of Mie theory with its spherical particle assumption are analyzed. We investigate the use of T-matrix and the Continuous Distribution of Ellipsoids (CDE) techniques for modeling non-spherical particles. We also investigate the dependence of the spectral signature of the optical properties on variations of the size distribution parameters. The spectral signature of a size-resolved regional aerosol model is then analyzed in terms of its fine to coarse particle ratio, modeling it as a mineralogy-based external mixture versus an internal mixture, and modeling it as a mineralogy-based external mixture versus using bulk optical constants data. Finally, a detailed analysis of effective medium approximation (EMA) techniques for aqueous aerosol components is

conducted using the IR optical constants of aqueous sulfate-nitrate-ammonium multi-component tropospheric aerosols determined in Chapter 2.

Chapter 4 uses aircraft and satellite measured high spectral resolution TIR radiance data impacted by large dust events to investigate modeling tropospheric dust aerosol using size-resolved aerosol optical models as compared to the technique of modeling aerosol optical properties using refractive index data from bulk dust samples, i.e. a standard aerosol model approach. The aircraft high spectral resolution radiance data are also used to determine whether Mie theory and the spherical particle assumption is sufficiently accurate for modeling naturally-occurring dust particles, or whether a non-spherical technique is more appropriate for dust particle modeling. The radiative transfer modeling is done using an alpha version of MODTRAN5 that includes the ability to specify the optical properties of an aerosol on a layer by layer basis instead of being constrained to work with predefined aerosol models or limited to simplifications of the optical properties and vertical distribution of the aerosol. This new capability is referred to as the spectral aerosol profile (SAP) capability. Using the approach that best models the high spectral resolution measured radiance data, we develop a new retrieval technique to retrieve dust composition and size distribution information from the high spectral resolution remote sensing data. We then analyze the effects of tropospheric dust on TIR radiative forcing and cooling rate and compare these results to those where the dust properties are retrieved and modeled using a standard dust aerosol model. Lastly, we examine the sensitivity of the radiative forcing and cooling rates to variations in the dust layer vertical position and to its thickness and aerosol particle loading.

Chapter 5 provides a summary of the dissertation and makes recommendations to the science community for further research in this area. Our future efforts are also discussed and detailed. Figure 1.1 lays out the flow of the analysis in this work.

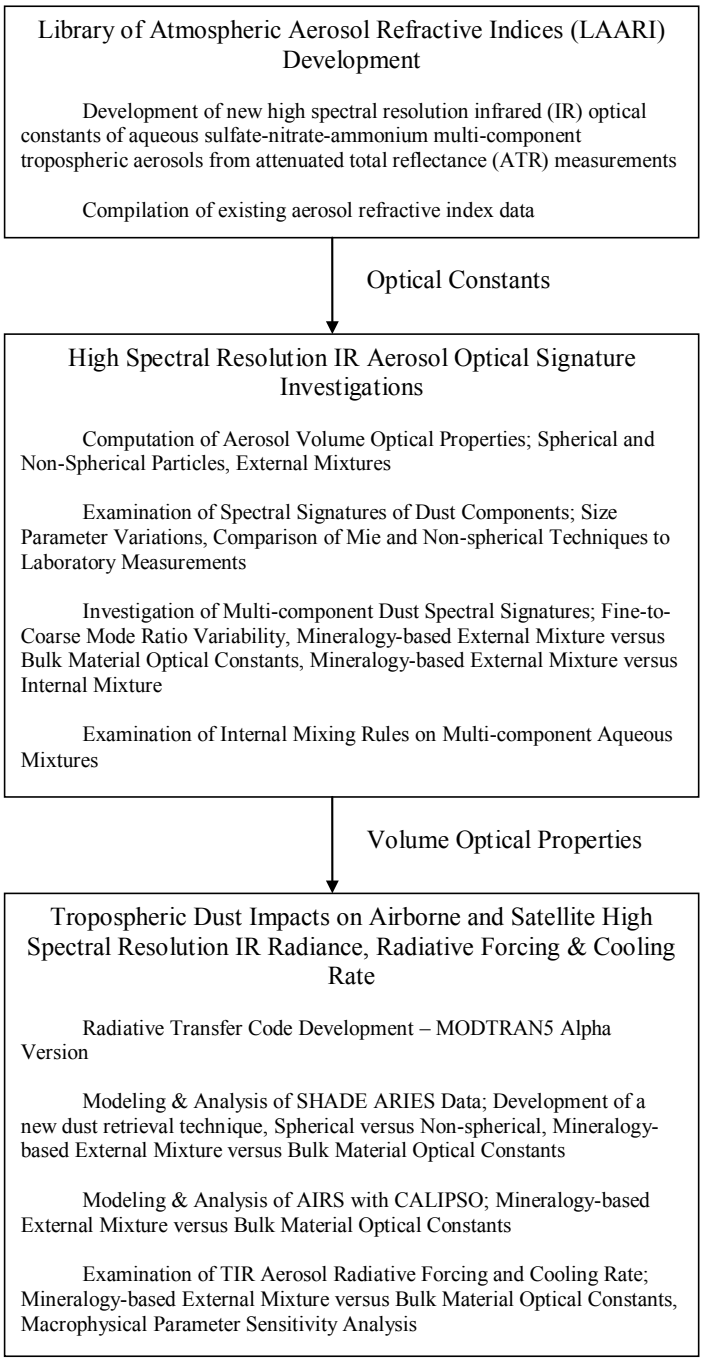

Figure 1.1 Analysis diagram

CHAPTER 2

DEVELOPMENT OF A HIGH SPECTRAL RESOLUTION AEROSOL REFRACTIVE INDEX DATABASE

2.1 Introduction

To support the investigations presented here into the signatures and effects of tropospheric aerosol on high spectral resolution thermal IR radiance, and to support future investigations by ourselves and others, we have undertaken the development of a high spectral resolution aerosol refractive index database of main individual aerosol species (e.g., various minerals, black carbon, sulfates, nitrates, and sea-salt). This effort includes both the compilation of existing refractive index data and the determination of new IR optical constants to begin to fill some of the gaps that exist. In developing the high spectral resolution aerosol refractive index database every attempt has been made to cover the spectral region from 0.2 μm to 40 μm in order to support remote sensing research and modeling efforts from the UV to the far IR.

In considering the development of an aerosol refractive index database, we need to take into account both the spectral properties of aerosols and the capabilities of high spectral resolution sensors. High spectral resolution IR sensors require that the optical properties of tropospheric aerosols be measured or modeled at a spectral resolution high enough to adequately sample all of the spectral features of the aerosol optical properties that will be resolved by the sensors and algorithms that will use them. For example if an algorithm will use individual channels or narrow spectral band regions the spectral resolution of the optical constants needs to be sufficient to accurately capture the variability in those channels or regions. Now even though the spectral absorption features of particulate matter are typically much broader than gas absorption lines at

tropospheric pressures and temperatures, to adequately sample the finest absorption features and the spectral detail in the regions of overlap of absorption features would require optical constants data at a resolution of ~1-10 cm^{-1} in the IR. We have therefore sought out existing refractive index datasets of this resolution or the best available resolution, and we have determined new refractive index data to begin to fill in some of the gaps in available high spectral resolution datasets, specifically aqueous sulfate-nitrate-ammonium aerosol refractive index data.

This chapter is organized as follows; Section 2.2 presents the newly determined IR optical constants of multi-component aqueous sulfate-nitrate-ammonium aerosols and analyses of their spectral features, in particular the spectra of the imaginary part, k, of the refractive index, in the context of high spectral resolution IR remote sensing. Section 2.3 documents the compilation of an extensive collection of refractive index data from the UV to the infrared of the most common tropospheric aerosols components. Section 2.4 provides a summary and discussion of applications of the database.

2.2 New Infrared Optical Constants of Aqueous Sulfate–Nitrate–Ammonium Multi-component Tropospheric Aerosols from Attenuated Total Reflectance Measurements

To date, little attention has been paid to the effects on IR radiative transfer due to aqueous sulfate-nitrate-ammonium tropospheric aerosols, or to the modification of physicochemical and optical properties of other tropospheric aerosols due to mixing with sulfates and nitrates. IR optical constants of sulfuric acid and nitric acid and ternary mixtures of sulfuric and nitric acid are available at tropospheric and stratospheric temperatures over a range of concentrations, but unavailable in the literature are IR optical constants for mixtures of aqueous ammonium sulfate, ammonium nitrate, and their acids. Therefore as part of the development of this library of optical constants we

have undertaken an effort to determine IR optical constants of aqueous sulfate-nitrate-ammonium mixtures at temperatures and concentrations typical of the troposphere, and at a spectral resolution sufficient to support the needs of high spectral resolution remote sensing applications. To accomplish this, attenuated total reflectance infrared spectra of aqueous mixtures of such solutions over a range of temperatures and concentrations that would likely be found in the troposphere were obtained from a research group at Harvard. Using these data we derived the optical constants presented here.

2.2.1 Attenuated Total Reflectance Measurement Data

ATR measurements were made of binary ammonium sulfate, binary ammonium nitrate, ternary ammonium sulfate-ammonium nitrate, ternary sulfuric acid-ammonium sulfate, ternary nitric acid-ammonium nitrate, and quaternary sulfuric acid-ammonium sulfate-ammonium nitrate solutions over a range of temperatures and concentrations that would likely be found in the troposphere. In total about 500 individual temperature and concentration variations were measured (see Table 2.1). The computation of optical constants from the ATR data is based on the Kramers-Kronig (K-K) transformation for which the phase change on reflection is first determined from the ATR measurement via the K-K transformation, and then the optical constants are calculated from the magnitude and phase using the Fresnel equation and Snell's law. To accomplish this we chose to use a code developed by *Bertie and Lan* [1996a], available at:
http://www.ualberta.ca/~jbertie/JBDownload.HTM (8/2003).
The code was modified to reflect the specifics of these measurements and equipment.

Table 2.1 Temperature and solute concentration of aqueous aerosols for which optical constants have been determined (AS – Ammonium Sulfate, AN – Ammonium Nitrate, SA – Sulfuric Acid, NA – Nitric Acid)

T (K) / Solute Mass Fractions				258	263	268	273	278	283	288	293	298
AS	AN	SA	NA									
Group A – Mole Ratios Sulfate/Nitrate = 1/0 and Ammonium/Hydrogen = 1/0												
0.05							X	X	X	X	X	X
0.06							X	X	X	X	X	X
0.07							X	X	X	X	X	X
0.08							X	X	X	X	X	X
0.1						X	X	X	X	X	X	
0.12						X	X	X	X	X	X	X
0.15						X	X	X	X	X	X	X
0.17								X	X	X	X	X
0.2						X	X	X	X	X	X	X
0.25						X	X	X	X	X	X	X
0.3						X	X	X	X	X	X	X
0.35						X	X		X	X	X	X
0.4								X	X	X	X	X
Group B – Mole Ratios Sulfate/Nitrate = 0/1 and Ammonium/Hydrogen = 1/0												
	0.083						X	X	X	X	X	X
	0.156						X	X	X	X	X	X
	0.221					X	X	X	X	X	X	X
	0.279				X	X	X	X	X	X	X	X
	0.331				X	X	X	X	X	X	X	X
	0.377				X	X	X	X	X	X	X	X
	0.42				X	X	X	X		X	X	X
	0.458			X	X	X	X	X	X	X	X	X
	0.494				X	X	X	X	X	X	X	X
	0.526					X	X	X	X	X	X	X
Solution C –Sulfate/Nitrate = 0/1 and Ammonium/Hydrogen = 35/65												
	0.035		0.051				X	X	X	X	X	X
Group D – Mole Ratios Sulfate/Nitrate = 1/0 and Ammonium/Hydrogen = 35/65												
0.055		0.076				X	X	X	X	X	X	X
0.099		0.136		X	X	X	X	X	X	X	X	X
0.135		0.186		X	X	X	X	X	X	X	X	X
0.165		0.228		X	X	X	X	X	X	X		X
0.191		0.263		X	X	X	X	X	X	X	X	X
0.213		0.294		X	X	X	X	X	X	X	X	X
0.232		0.32		X	X	X	X	X	X	X		X
0.249		0.343		X	X	X	X	X	X	X	X	X
0.264		0.364		X	X	X	X	X	X	X	X	X
0.277		0.382					X	X	X	X		X

Continued on next page

Table 2.1 (continued)

T (K) / Solute Mass Fractions				258	263	268	273	278	283	288	293	298
AS	AN	SA	NA									
Group E – Mole Ratios Sulfate/Nitrate = 1/1 and Ammonium/Hydrogen = 7/3												
0.048	0.053	0.029				X	X	X	X	X	X	X
0.087	0.096	0.053			X	X	X	X	X	X	X	X
0.119	0.131	0.072		X		X	X	X	X	X	X	X
0.146	0.161	0.089		X	X	X	X	X	X	X	X	X
0.169	0.186	0.103		X	X	X	X	X	X	X	X	X
0.189	0.208	0.115		X	X		X	X	X	X	X	X
0.206	0.227	0.125			X	X	X	X	X	X	X	X
0.221	0.243	0.134			X	X	X	X	X	X	X	X
0.234	0.258	0.142				X	X	X	X	X	X	X
0.246	0.271	0.149					X	X	X	X	X	
Solution F – Mole Ratios Sulfate/Nitrate = 1/0 and Ammonium/Hydrogen = 7/3												
0.062		0.02					X	X	X	X	X	X
0.116		0.037				X	X	X	X	X	X	X
0.163		0.052				X	X	X	X	X	X	X
0.205		0.065		X	X	X		X	X	X	X	X
0.243		0.077		X	X	X	X	X	X	X	X	X
0.276		0.088								X	X	X
0.306		0.097		X	X	X		X	X	X	X	X
0.334		0.106		X	X	X	X	X	X	X	X	X
0.359		0.114			X	X	X	X	X	X	X	X
0.381		0.121					X	X	X	X	X	X
Group G – Mole Ratios Sulfate/Nitrate = 1/1 and Ammonium/Hydrogen = 1/0												
0.09	0.055					X	X	X	X	X	X	X
0.128	0.077					X	X	X	X	X	X	X
0.191	0.116				X	X	X	X	X	X	X	X
0.218	0.132				X	X	X	X	X	X	X	X
0.243	0.147			X	X	X	X	X	X	X	X	X
0.265	0.161			X	X	X	X	X	X	X	X	
0.286	0.173					X	X	X	X	X	X	X
Solution H – Mole Ratios Sulfate/Nitrate = 0/1 and Ammonium/Hydrogen = 7/3												
	0.047		0.016				X	X	X	X	X	X
	0.09		0.031			X	X	X	X	X	X	X
	0.13		0.044			X	X	X	X	X	X	X
	0.166		0.056			X	X	X	X	X	X	X
	0.2		0.067		X	X	X	X	X	X	X	X

A Nicolet Nexus 670 Fourier transform infrared spectrometer equipped with a Pike Technologies horizontal attenuated total reflectance accessory was employed to collect the infrared spectra from 700 to 4500 cm^{-1} [*Chelf and Martin*, 2001; *Urban*, 1996; *Bertie et al.,* 1993]. The instrument resolution was set to 1 cm^{-1}, an MCT-A detector was employed, and a Ge ATR element was used. A reflection angle of 45° was employed, and there were approximately 10 reflections at the interface of the sample and the ATR element. The sample chamber was fitted with a polarizer to allow only s-polarized IR radiation to pass because a specific polarization was necessary to obtain accurate optical constants from the ATR geometry. The ATR accessory consisted of a metal rectangular cell made of aluminum with Teflon-encapsulated nickel plating. The cell had an internal chamber, through which coolant was flowed to control the temperature of the liquid samples. A thermistor was attached to the top of the ATR cell to measure the temperature of the liquid. For each temperature, consecutive spectra were collected to ensure that thermal equilibrium had been reached and that the spectrum was not changing. For the various mixtures, spectra were measured in intervals of 5 K from 298 K down to a temperature slightly above the freezing point of a given mixture. The minimum temperature for a given mixture was chosen so that neither ice nor solid inorganic crystals were formed. These lower-limited temperatures were established using a thermodynamic model [*Clegg et al.,* 1998].

2.2.2 Numerical Computation of Optical Constants from Attenuated Total Reflectance Data via a Modified Kramers-Kronig Transform

In ATR spectroscopy a single quantity (the reflectance) is measured, whereas two quantities (the magnitude and phase of the complex reflectivity) are needed to determine

the real (n) and imaginary (k) parts of the complex index of refraction (m = n + ik). Because the real and imaginary components of these complex quantities are not independent, the optical constants can be determined from the reflectance measurement alone if a relationship between the reflectance and the phase change on reflection is known. The K-K relations, also known as dispersion relations, describe the interconnection between the real and imaginary parts of the Fourier transform of causal linear system response functions for physical systems [*Arfken and Weber*, 2001]. The complex reflectivity and the complex index of refraction satisfy the normal K-K relations. For ATR, where we measure the square of the magnitude of the complex reflectivity, we require a dispersion relationship between the phase change on reflection and the logarithm of the magnitude of the complex Fresnel reflection coefficient. This requires a modification of the usual K-K derivation because the logarithm of the reflection coefficient does not satisfy all of the requirements for a function to exhibit a dispersion relation. In particular, the logarithm of the reflection coefficient is not square-integrable over the real frequency axis, and for the case of measurements at oblique incidence and/or through a window material, as is the case for ATR measurements, the logarithm of the reflection coefficient cannot be analytically continued into the entire upper-half complex frequency plane. This is because for these cases the logarithm of the reflection coefficient can have singularities and/or square root or logarithmic branch points in the upper-half of the complex frequency plane [*Plaskett and Schatz*, 1963]. There are modified forms of the K-K transformation for the logarithm of the reflection coefficient for normal incidence reflection spectroscopy from vacuum or air, but they do not apply to the case of a window material or non-normal incidence reflection [*Smith*, 1997]. Deriving dispersion relations for these cases is more difficult [*Bertie and Lan*, 1996a; *Plaskett and Schatz*, 1963]. Once the phase is determined the optical constants are then calculated using the Fresnel equation and Snell's law.

The ATR-to-optical constants code and its modified K-K transformation that we used have a number of distinct advantages with respect to accurately computing the optical constants. One advantage involves the phase correction term. The advantage of this modified K-K transformation for these datasets is that it lends itself to more accurately handling the issue of a finite region of integration. If the contour integral used to derive this transform is evaluated with a radius that is fixed at the upper frequency limit of the available data, the modified K-K is still of the same form, i.e.,

$$\theta(\nu) = -\frac{2}{\pi} P \int_0^{\nu_u} \frac{\nu' \ln|r_s(\nu')|}{\nu'^2 - \nu^2} d\nu' + \theta_{\nu_u} \qquad \text{(Eq. 2.1)}$$

The analycity of the complex reflection coefficient in the region of integration guarantees that the correction term θ_{ν_u} is a finite constant. A good estimate of this term can be obtained by employing another feature of the code, i.e., the ability to use a parametric expression for the frequency dependence of the electronic component of n. Using the parametric expression for the electronic component of n provides a good estimate of n at the upper frequency limit of the ATR data, particularly about 8000 cm^{-1}. This n and the fact that k is approximately 0 at the upper frequency limit, true for the aqueous mixtures considered here, in turn allows for an accurate computation of the phase change on reflection from the Fresnel equation. Using this and the computed value of the integral transform at the upper frequency limit results in an accurate determination of the phase correction term:

$$\theta_{\nu_u} = \theta(\nu_u) + \frac{2}{\pi} P \int_0^{\nu_u} \frac{\nu' \ln|r_s(\nu')|}{\nu'^2 - \nu_u^2} d\nu' \qquad \text{(Eq. 2.2)}$$

The other advantage of this code that can improve the resulting optical constants is that it offers a number of ways to handle a lack of data at low frequencies. Based on a

sensitivity analysis described in a following section, we have taken additional steps to improve the accuracy of the resulting optical constants, particularly on the low frequency side.

The ATR-to-optical constants code is set up to process data taken with a CircleCell® ATR attachment and assumes unpolarized light at a 45° incidence angle. The ATR setup for this data uses s-polarized light at a 45° incidence angle. We therefore made the necessary modifications to the code to allow it to work with this setup. A synthetic ATR spectrum of pure water constructed from literature data [*Bertie and Lan*, 1996b] was used in testing the modified code. The output optical constants when compared to the input literature values had a mean normalized error of 0.01% and a maximum normalized error of 0.07% for n, and these errors were 0.02% and 0.1%, respectively for k.

2.2.3 Processing the Attenuated Total Reflectance Data and Implementing the Modified Kramers-Kronig Transform

The modified K-K transformation determines the phase shift on reflection from the magnitude of the attenuated total reflectance. It involves an integral transform and a phase "correction" factor. The ATR-to-optical constants code also uses an iterative scheme involving computing n from k using the normal K-K transformation. The K-K transform for n from k is

$$n(\nu) = n_{\infty} + \frac{2}{\pi} P \int_0^{\infty} \frac{\nu' k(\nu')}{\nu'^2 - \nu^2} d\nu' \qquad \text{(Eq. 2.3)}$$

Bertie and Lan [1995] show that a more accurate determination of n from k in the case of IR limited k data (i.e., the normal K-K transformation is limited to data over IR frequencies only) is obtained not by using a value of n in the visible for n_∞, but instead by using the value of the electronic component of n, n_{el}, at the IR frequency of interest as determined by a power series expansion:

$$n_{el}(\nu) = a_0 + a_2\nu^2 + a_4\nu^4 \qquad \text{(Eq. 2.4)}$$

The accurate determination of the phase correction term in the modified K-K transformation requires that n of the mixture be known at a frequency within the finite range of data used in the transformation for which k is approximately zero. By using the power series parameterization and having the data extended to the highest frequency possible where k is still approximately zero, a more accurate value of n at the upper frequency limit can be determined and from that we can determine an accurate phase shift on reflection and then the phase correction. So in our case the most accurate determination of the optical constants from the ATR data should incorporate the frequency dependence of n_{el}, and the data should extend to the highest frequency possible where k is still approximately zero. In either case, the ATR-to-optical constants code requires that information regarding the value of n at visible frequencies be supplied, either the frequency dependent parameterization of n_{el} (see Eq. (2.4)) or the real index of refraction at a single visible frequency in which case $a_0 = n_\infty$, $a_2 = 0$ and $a_4 = 0$ in Eq. (2.4). We have chosen the former since it is more accurate. Due to the lack of data on the wavelength and temperature dependence of the visible refractive index of considered mixtures as a function of composition, it was not possible to determine the frequency dependence of n_{el} directly. It would not have been possible to even determine n at a single

frequency from measurements because such data for all compositions and temperatures are not available. Therefore, the n_{el} parameterization is based on the Lorentz-Lorenz (L-L) relation and partial molar refraction [*Born and Wolf*, 1999; *Stelson*, 1990].

The L-L formula describes the relationship between n, the molar refraction, R, and the molar volume, V_m, of the medium:

$$R = V_m \frac{n^2 - 1}{n^2 + 2} \qquad \text{(Eq. 2.5)}$$

Then, n of a mixture can be expressed in terms of the ratio of molar refraction to molar volume, R/V_m:

$$n^2 = \left(\frac{1 + 2 R/V_m}{1 - R/V_m} \right) \qquad \text{(Eq. 2.6)}$$

The molar refraction of a mixture is to a good approximation the sum of the partial molar refractions of the components [*Born and Wolf*, 1999]:

$$R = \sum_i x_i R_i \qquad \text{(Eq. 2.7)}$$

Here x_i is the mole fraction of component i of the mixture and R_i is its partial molar refraction. We can rewrite Eq. (2.7) as

$$R/V_m = \rho \sum_i \frac{w_i}{M_i} R_i \qquad \text{(Eq. 2.8)}$$

where ρ is the density of the mixture, w_i is the mass fraction and M_i is the molecular weight of the i*th* component. Given the density of the mixture and the partial molar refraction of the components along with their weight fractions and molecular weights, we can compute n of the mixture. The molar refraction has been shown to be nearly independent of T and concentration [*Born and Wolf*, 1999; *Stelson*, 1990; *Tang*, 1997;

Luo et al., 1996]. The temperature dependence of n is therefore expressed solely through the solution density.

Implementation of this approach requires partial molar refraction data as a function of wavelength for all of the components, i.e. water, sulfuric acid, nitric acid, ammonium nitrate, and ammonium sulfate, and the density of the resulting solution. With respect to the dissociation products, *Stelson* [1990] found that within the accuracy of measurement and prediction, the partial molar refraction of sulfate can be used for the partial molar refraction of sulfuric acid and bisulfate, and that the partial molar refraction of nitrate can be used for the partial molar refraction of nitric acid. For our estimates of visible refractive indices of considered multi-component aqueous mixtures, we assume that we need not determine the partial molar refraction of the various dissociation products. The literature contains partial molar refraction information for all of the components of interest at one wavelength, 0.589 μm, but not for multiple other wavelengths that will be required to determine the frequency dependence.

Luo et al. [1996] have determined apparent partial molar refractions for sulfuric acid and nitric acid as a function of wavelength from the near-UV to near-IR, and have developed a method to calculate the refractive index of aqueous ternary mixtures using the binary partial molar refractions. *Krieger et al.* [2000] provide a code to do so along with the polynomial representations of the binary solution apparent partial molar refractions that are used in the model. All of the mixtures considered here include either ammonium sulfate or ammonium nitrate, and to our knowledge there are not available refractive index data for binary mixtures of aqueous ammonium sulfate and aqueous ammonium nitrate at multiple wavelengths. Because of this we were not able to use the

Luo et al. [1996] model exactly as described, and instead we have adapted their technique.

First, we extended their technique by setting the apparent partial molar refraction of each of the components, sulfuric acid, nitric acid, ammonium sulfate and ammonium nitrate in the multi-component mixture with weight fractions $w_1,\ldots, w_j$ equal to that of a binary solution with weight fraction $w_1 + \ldots + w_j$, where j is the number of solutes. For the partial molar refraction of H_2O and the apparent partial molar refractions of H_2SO_4 and HNO_3 we use their polynomial representations. The apparent partial molar refractions of H_2SO_4 and HNO_3 are functions of wavelength and weight fraction while the partial molar refraction of H_2O is only a function of wavelength. We then used refractive index data as a function of wavelength for ammonium sulfate and ammonium nitrate solids to derive an estimate of their partial molar refractions. As with water, the partial molar refraction is assumed equal to the molar refraction of the pure substance; and since the molar refraction is at most only weakly dependent on concentration, we assume there is no dependence on weight fraction, i.e., it is only a function of wavelength. *Stelson* [1990] and *Tang* [1997] found that the solid ionic partial molar refraction was (within experimental uncertainty) equal to that of the electrolyte partial molar refraction that they determined from experiments at 298 K and 0.589 μm. Therefore, we fit a Sellmeier equation to the visible refractive index data found in International Critical Tables [*Merwin*, 1930] and *Toon et al.* [1976] for ammonium sulfate, and in *Merwin*, [1930] for ammonium nitrate. Using the Sellmeier equation, we can compute the index of refraction at arbitrary wavelengths in the visible. From this and

the L-L equation, we then compute the wavelength-dependent partial molar refraction of ammonium sulfate and ammonium nitrate.

For the density required in Eq. (2.8), we used a parameterization developed by *Laliberte and Cooper* [2004]. It supports all of the electrolytes involved in our study and fits well the density of binary and ternary mixtures of *Luo et al.* [1996] and the density formulation of *Wahab and Mahiuddin* [2001] for aqueous ammonium nitrate. For T below 273 K, we linearly extrapolate the density to the lower temperature. Eqs. (2.6) and (2.8) then allow us to compute an estimate of the refractive index for all of the measured compositions and T at visible wavelengths. For each mixture, resulting refractive indices over the range from 0.4 μm to 0.7 μm are then fit to the polynomial in Eq. (2.4) using a curve-fitting algorithm. The determined parameters are then used in the ATR-to-optical constants code.

The refractive index computed for ammonium sulfate and ammonium nitrate mixtures at 0.589 μm using this model, for which there are experimentally determined values [*Merwin*, 1930], differs by less than 0.1% at low concentrations and by less than 0.5% at the highest concentrations. *Tang and Munkelwitz* [1994] report measurements of the refractive index of ammonium bisulfate at numerous weight fractions at 0.589 μm. Since an ammonium bisulfate solution can be made from equimolar amounts of $(NH_4)_2SO_4$ and H_2SO_4, we used their data to determine the accuracy of ternary mixtures involving ammonium sulfate and sulfuric acid. The n at 0.589 μm for an equimolar mixture of ammonium sulfate and sulfuric acid differed from the *Tang and Munkelwitz* [1994] reported values by an average of 0.2% with a maximum normalized error of 0.3%. Based on this and the reported accuracy of the *Luo et al.* [1996] data, we can expect that

the optical frequency refractive indices computed with this model to be accurate to within 0.5%.

In addition to either n at a visible frequency or a n_{el} parameterization, the ATR-to-optical constants code requires that the IR index of refraction of the ATR crystal and the effective number of reflections be specified, and that a method to handle the finite range of the data at the low wavenumber end of the dataset also be specified. The ATR data were collected using a germanium internal reflection element. In running the code we use the germanium refractive index available from the Bertie website. The effective number of reflections was determined by measuring the ATR spectrum of pure water at 298 K and then, using the H_2O optical constants from the literature, to compute a synthetic ATR spectrum for various values of effective number of reflections. The value that gave the minimum root mean square error to the measured ATR spectrum was then used as the effective number of reflections in the code. The method chosen to handle the finite range of data at low frequency was to extrapolate the logarithm of the reflectance linearly to zero at 0 cm^{-1}.

It is known that optical constants determined via a K-K transformation are sensitive to the limited frequency range of the data used in the transformation (e.g. [*Myhre et al.,* 2003; *Max and Chapados*, 1999]). We conducted a sensitivity analysis to better understand how the limited range of the ATR data affects the resulting optical constants, which is described in the following section. Based on this analysis, we affirmed that the resulting optical constants at the low wavenumber end are particularly sensitive to the truncation of data even with the extrapolation to 0 cm^{-1} available in the code. Because of this, in using the K-K transformation it is extremely beneficial to extend

the data on the low frequency end based on information from another source where possible. As mentioned above, the code was run such that the logarithm of the reflectance is extrapolated linearly from the end of the data provided to zero at 0 cm^{-1}. This option and the option to repeat the last value down to 0 cm^{-1} can be considered first- and zero-order approximations. Our sensitivity analysis showed that the accuracy can be significantly improved by providing a better approximation of the ATR spectrum to lower frequency. For the solutions considered here, the ATR spectrum from 860 cm^{-1} to 400 cm^{-1} can be better approximated by the ATR spectrum of pure water, except in the cases involving sulfuric acid which has fairly strong HSO_4^- absorption features at around 900 cm^{-1} and around 600 cm^{-1}. Therefore, instead of just linearly extrapolating from the end of our data at 860 cm^{-1} to 0 cm^{-1}, we appended synthetic ATR data from 860 cm^{-1} to 400 cm^{-1} that was computed from low frequency temperature-dependent refractive index data, which approximate the behavior of the mixtures in this region to the measured ATR spectrum. In order to better constrain the low frequency behavior for the mixtures involving sulfuric acid, we use the *Myhre et al.* [2003] optical constants for binary sulfuric acid to compute an approximation of the ATR spectrum below 860 cm^{-1} down to 400 cm^{-1}.

The preprocessing of the ATR data consisted of limiting the measurement data to the high signal-to-noise ratio region between 860 cm^{-1} and 4000 cm^{-1}. The data from 700 cm^{-1} to 860 cm^{-1} are not noisy, but for the low temperature datasets it does include temperature-dependent spectral anomalies that correspond to weak germanium absorption features [*Hawkins and Hunneman*, 2004]. Therefore, that part of the ATR spectrum is also removed. In the 3750 to 4000 cm^{-1} region, the spectra of the considered mixtures and

of water are near zero and relatively flat. Therefore, the baseline of the ATR spectrum was adjusted so that the measured ATR spectrum coincides with the ATR spectrum of pure water at 3750 cm^{-1}. The ATR spectrum was then appended with the ATR spectrum of pure water from 3750 cm^{-1} to 8000 cm^{-1} with the 3750 cm^{-1} to 4000 cm^{-1} region overwritten to give a smooth transition to zero in a region where the absorption for these mixtures is extremely small and to also extend the dataset to a frequency where the n_∞ value or the n_{el} parameterization allows for a more accurate phase correction determination and n computation from k via the K-K transform in the iteration step. The ATR spectrum for the mixtures not containing sulfuric acid is appended with the ATR spectrum of pure water [*Ray*, 1972] from 400 cm^{-1} to 700 cm^{-1}, and the region from 860 cm^{-1} to 700 cm^{-1} is linearly interpolated. For mixtures containing sulfuric acid the optical constants data of *Myhre et al.* [2003] for binary sulfuric acid solutions is used to approximate the ATR spectrum from 860 cm^{-1} to 400 cm^{-1}. The preprocessed data is then input to the code to compute the optical constants. The resulting optical constants from 860 cm^{-1} to 4500 cm^{-1} at a resolution of 1 cm^{-1} are then kept.

2.2.4 Uncertainties in the Calculation of Optical Constants from Attenuated Total Reflectance Spectra

The uncertainty in optical constants will of course depend on the uncertainty associated with the experimental measurement. But in determining optical constants from ATR measurements, an additional source of uncertainty involves the calculation of optical constants from the ATR measurements. The amount of uncertainty depends on the sensitivity of the computed optical constants to the limited range of ATR data and the

accuracy of the various parameters used in the calculation. This sensitivity of the code was evaluated by running test cases using literature values of optical constants of water to generate a synthetic ATR spectrum and then varying the spectral range of the ATR spectrum and the input parameters and comparing the output optical constants to the literature optical constants [*Bertie and Lan*, 1996b]. We tested the sensitivity to the range of data, the sensitivity to the parameterization of n_{el} in Eq. (2.4) and the sensitivity to the effective number of reflections, n_{eff}. A very accurate parameterization of n_{el} for water is provided by Bertie and Lan [1995]. To test the sensitivity of the results to the n_{el} parameter, instead of the above parameterization we provided one of the following; either an accurate value of the real index of refraction at a single visible frequency in which case $a_0 = n_\infty$, $a_2 = 0$ and $a_4 = 0$ in Eq. (2.4) with $n_\infty = n(0.589\ \mu m) = 1.33287$, or a value of the real index of refraction at a single visible frequency with some percentage error in the value, or a parameterization where we introduced some percentage error into the a_0 term of the accurate parameterization of Bertie and Lan [1995]. To test the sensitivity of the results to the n_{eff} parameter we introduced a known error into the effective number of reflections.

To isolate the effects of uncertainty in the parameters we ran cases where all parameters were accurate except for one. We also ran cases where all the parameters had some level of inaccuracy. In total 17 test cases were run. In all cases the code was run such that the logarithm of the reflectance is extrapolated linearly from the end of the data provided to zero at 0 cm^{-1}. Table 2.2 provides the details on the data range and parameters used for each test case along with the resulting mean normalized error (mne) and maximum normalized error (maxne) of the computed optical constants from the

literature optical constants between 860 and 3750 cm^{-1} (typical of the range of the measurement data that will be processed here). The mne is defined as

$$mne = \frac{1}{N}\sum_{i=1}^{N}\frac{|x_i - y_i|}{|y_i|} \qquad \text{(Eq. 2.9)}$$

The maxne is defined as

$$maxne = \max_i\left\{\frac{|x_i - y_i|}{|y_i|}\right\} \qquad \text{(Eq. 2.10)}$$

In these equations x_i is the computed n (or k) at wavenumber ν_i and y_i is the literature value of n (or k) at wavenumber ν_i with N being the number of values between 860 and 3750 cm^{-1}.

Table 2.2 Error associated with uncertainty in the calculation of optical constants from ATR spectra

Case	Data Range (cm^{-1})	n_{el} or n_{∞}	# of reflections	mne (%)		maxne (%)	
				n	k	n	k
1	10 - 8000	Accurate n_{el} parameterization	Exact	0.013	0.019	0.073	0.11
2	400 - 8000	Accurate n_{el} parameterization	Exact	0.23	0.34	1.4	1.8
3	860 - 8000	Accurate n_{el} parameterization	Exact	2.2	3.1	19.4	22.5
4	10 - 8000	n_{∞} = 1.33287 (literature 0.589 μm value)	Exact	0.49	0.73	0.77	1.0
5	10 - 8000	Accurate n_{el} parameterization	1% too small	0.053	1.01	0.21	1.3
6	10 - 8000	Accurate n_{el} parameterization	5% too small	0.29	5.3	1.1	6.8
7	10 - 8000	Accurate n_{el} parameterization	10% too small	0.61	11.3	2.3	14.7
8	10 - 8000	Accurate n_{el} parameterization	1% too large	0.061	1.03	0.26	1.35
9	10 - 8000	Accurate n_{el} parameterization	5% too large	0.27	4.9	1.01	6.1
10	10 - 8000	Accurate n_{el} parameterization	10% too large	0.51	9.25	1.9	11.5
11	860 - 4000	n_{∞} = 1.33287 (literature 0.589 μm value)	Exact	2.7	3.75	19.97	23.1
12	10 - 8000	a_0 coefficient of n_{el} 1% too large	Exact	1.05	1.6	1.6	2.1
13	10 - 8000	a_0 coefficient of n_{el} 1% too small	Exact	1.02	1.6	1.5	2.06
14	10 - 8000	n_{∞} 1% larger than literature 0.589 μm value	Exact	1.5	2.3	2.3	3.02
15	10 - 8000	n_{∞} 1% smaller than literature 0.589 μm value	Exact	0.55	0.83	0.84	1.14
16	860 - 4000	n_{∞} 1% larger than literature 0.589 μm value	Exact	3.7	5.2	21.2	24.3
17	10 - 8000 4001-8000 are zero-filled	Accurate n_{el} parameterization	Exact	0.016	0.093	0.11	0.49

The code reproduces the optical constants within the 860 and 3750 cm^{-1} region extremely accurately when the range of data extends well below this measured IR region, the effective number of reflections is known accurately, and the parameterization of electronic component of n is accurately provided. The error due to the limited range of ATR data on the low frequency side is greater for the lower frequency computed optical constants than it is for the higher frequency computed values due to the fact that the integral transform is more sensitive to nearby frequency values.

For these solutions where the absorption from 4000 cm^{-1} to 8000 cm^{-1} is nearly 0, the data can be padded to 8000 cm^{-1}. Doing this allows for an accurate computation of n at that frequency using the power series parameterization (where the electronic component is much larger than the infrared component), which in turn allows for an accurate computation of the phase correction. Zero-padding to extend the data to 8000 cm^{-1} adds very little error to the 860 – 3750 cm^{-1} region over having "true" data in this region.

The largest source of error in determining the optical constants for these solutions is the limited ATR data on the low frequency side. Because of this, in using the Kramers-Kronig transformation it is extremely beneficial to extend the data on the low frequency side based on information from another source where possible. As mentioned earlier the code was run such that the logarithm of the reflectance is extrapolated linearly from the end of the data provided to zero at 0 cm^{-1}. This option and the option to repeat the last value down to 0 cm^{-1} can be considered first and $zero^{th}$ order approximations. For these datasets we seek to improve this approximation of the ATR data on the low frequency side by using either optical constant data for water where that is a good approximation or

optical constant data from auxiliary sources where water is not such a good approximation.

To test this approach we took the infrared optical constants of nitric acid from *Querry and Tyler* [1980] for a 40% solution at room temperature and created a synthetic ATR spectrum. We then computed the optical constants using the ATR data from 860 – 4000 cm^{-1} with the data zero padded to 8000 cm^{-1} and the ATR values of pure water from 400 – 860 cm^{-1} appended. The code was run with the logarithm of the reflectance extrapolated linearly from the end of the data provided at 400 cm^{-1} to zero at 0 cm^{-1}. Next we computed the optical constants using only the ATR values from 860 – 4000 cm^{-1} with the data zero padded to 8000 cm^{-1} and the logarithm of the reflectance is extrapolated linearly from the end of the data provided at 860 cm^{-1} to zero at 0 cm^{-1}. Comparing the resulting optical constants to the original *Querry and Tyler* [1980] optical constants we found in the case of using the ATR data from 860 – 4000 cm^{-1} that we had a mne of 1.3% for n and 2.1% for k with a maxne of 9.7% for n and 14.6% for k with both occurring at the low frequency end of the data. In the case where we appended the ATR values of pure water from 400 – 860 cm^{-1} to the nitric acid ATR spectrum we had a mne of 0.3% for n and 0.5% for k with a maxne of 1.1% for n and 1.8% for k again both occurring at the low frequency end of the data. The error in the optical constants for these solutions due to the limited range of ATR data can be dramatically reduced by providing a better approximation of the ATR spectrum to lower frequency, which for most of these solutions can be done with the ATR spectrum of pure water.

Based on this sensitivity study of the various parameters used in running the code, we affirmed that the resulting optical constants at the low wavenumber end of the dataset

are particularly sensitive to the truncation of data even with the extrapolation to 0 cm^{-1} available in the code. Therefore, instead of just linearly extrapolating from the end of our data at 860 cm^{-1} to 0 cm^{-1}, we appended synthetic ATR data from 860 cm^{-1} to 400 cm^{-1} that was computed from low frequency temperature-dependent refractive index data, which approximates the behavior of the mixtures in this region, to the measured ATR spectrum. This was done as part of the preprocessing of the ATR data. The ATR spectrum from 860 cm^{-1} to 400 cm^{-1} can be reasonably approximated by the ATR spectrum of pure water for the mixtures at these concentrations, except in the cases involving sulfuric acid, which has fairly strong HSO_4^- absorption features at around 900 cm^{-1} and around 600 cm^{-1}. In order to better constrain the low frequency behavior for the mixtures involving sulfuric acid, we have used the *Myhre et al.* [2003] optical constants for binary sulfuric acid at various T to compute an approximation of the ATR spectrum below 860 cm^{-1} down to 400 cm^{-1}.

2.2.5 Computed Optical Constants and Analysis of Spectral Absorption Features

The intensity and position of the spectral features of aqueous aerosols are a result of complex ion-ion and ion-water interactions. The frequencies of IR absorption bands for the inorganic ions ammonium, nitrate, sulfate, and bisulfate as well as for water molecules are well documented [*Miller and Wilkins*, 1952; *Herzberg,* 1991]. The IR spectroscopy of sulfuric acid and nitric acid molecules, hydronium ions, and mixtures containing ammonium, nitrate, sulfate, bisulfate and hydronium ions have also been studied with IR and Raman spectroscopy over many years. Table 2.3 lists the ranges over which the absorption band center frequencies occur for the species of interest within the considered frequency range. Table 2.4 gives some examples of band center values determined for the ions in aqueous mixtures in the temperature range 298 – 303 K. From

this information all of the spectral absorption features in our optical constant datasets are readily identified. To illustrate, Figure 2.1a shows optical constants from a number of the different groups. The spectral absorption features are labeled with the absorption modes listed in Table 2.3. Figure 2.1b is the same optical constants with a MODTRAN^{TM} [*Berk et al.*, 1998] generated top of the atmosphere clear sky mid-latitude summer transmission curve overlaid for reference.

Table 2.3 Range of absorption band center frequencies and assigned spectroscopic absorption modes for the listed inorganic ions and liquid water as reported in the literature

Ion / Molecule	Center Frequency Region (cm^{-1})	Assignment
SO_4^{2-}	1130 – 1080	ν_3, SO_4^{2-} asymmetric stretch
	1065 – 955	ν_1, SO_4^{2-} symmetric stretch Note: Forbidden by symmetry if the environment around the SO_4^{2-} ion is also symmetric, but shows up weakly in the solution phase
	680 – 580	ν_4, SO_4^{2-} bending
HSO_4^-	1190 – 1160	ν_4, asymmetric SO_3^- stretch
	1080 – 1000	ν_1, symmetric SO_3^- stretch
	880 – 840	ν_2, S-OH stretch
NO_3^-	1410 – 1340	ν_3, NO_3^- asymmetric stretch
	860 – 800	ν_2, NO_3^- out of plane bending
	770 – 700	ν_4
	1070 – 1015	ν_1, NO_3^- symmetric stretch Note: IR inactive but appears in many nitrate crystals and solutions
NH_4^+	3335 – 3100	ν_3, NH_4^+ asymmetric stretch
	1490 – 1390	ν_4, NH_4^+ deformation or umbrella bend
	3100 – 3000	$\nu_2 + \nu_4$ combination band
	~ 2800	$2\nu_4$, overtone band
H_3O^+	2650 – 3380	ν_1 and ν_3, very broad bands
	~1742	ν_4
	~1210	ν_2
H_2O	3200 – 3500	O-H stretch region; ν_1 ~3219 cm^{-1}; ν_3 ~3445 cm^{-1}; $2\nu_2$ ~ 3300 cm^{-1}
	~1640	ν_2, H-O-H deformation
	~2100	Associational band
	~690	ν_L, librational band

Table 2.4 Range of ion absorption band center frequencies in aqueous solutions at temperatures from 293 to 303 K as determined from IR measurements reported in the literature

Ion	Absorption Mode	Measured Band Center (cm^{-1})
SO_4^{2-}	ν_3	1100 - 1105
	ν_1	~981
HSO_4^-	ν_4	1185 – 1190
	ν_1	1047 – 1050
	ν_2	880 – 897
NO_3^-	ν_3	1337 – 1385
	ν_1	1042 – 1049
NH_4^+	ν_4	1400 – 1450

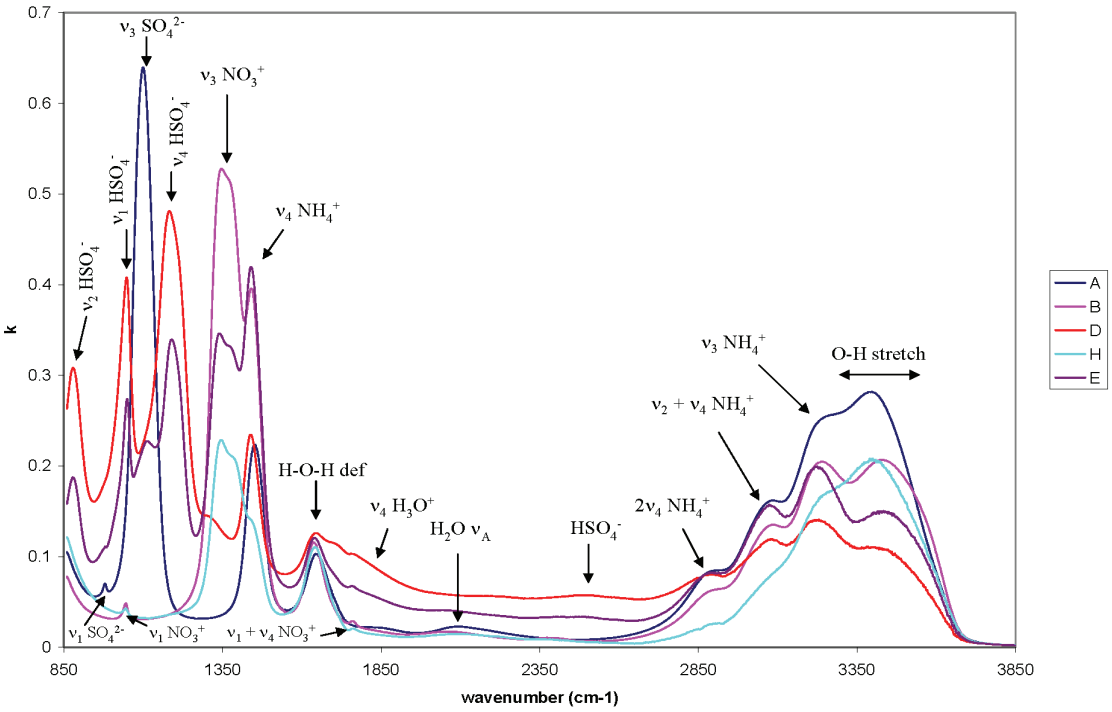

Figure 2.1a A sample of the k spectra that were determined in this study. One k spectrum at T = 298 K from each of the groups A, B, D, H, and E is shown with the absorption features identified.

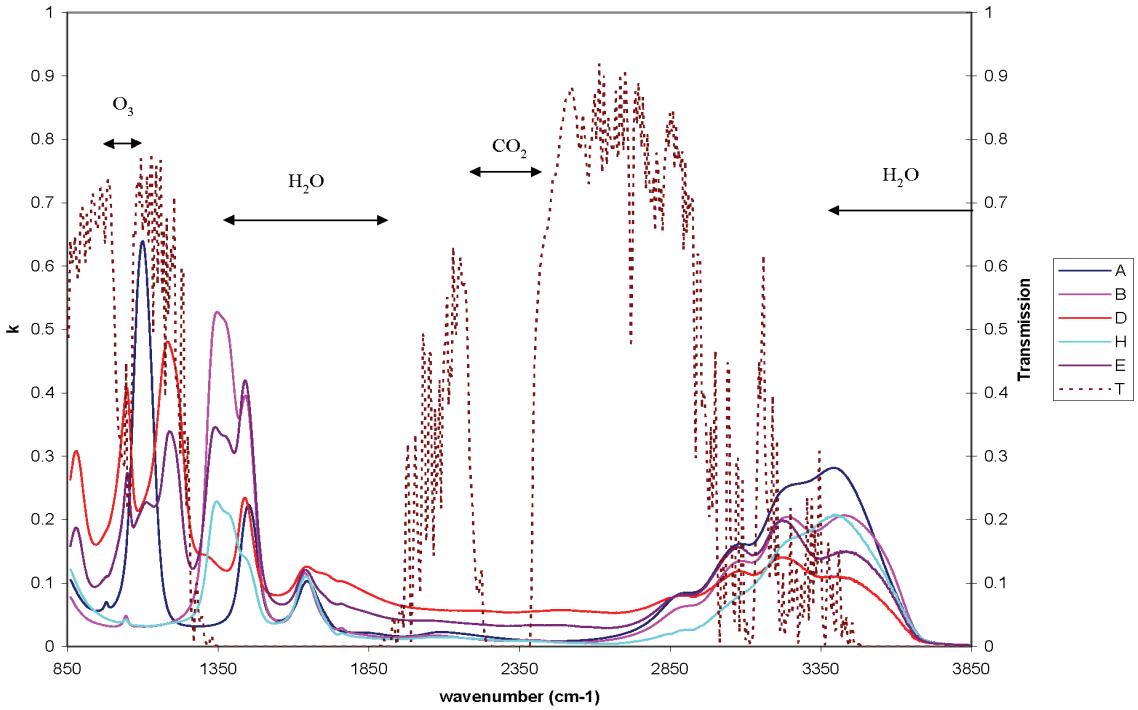

Figure 2.1b The same k spectra as in Figure 2.1a., but with a MODTRAN™ generated clear sky mid-latitude summer TOA transmission spectrum, T, shown for reference with the main atmosphere absorbing gaseous species identified.

The spectral absorption features of water in these aqueous optical constants are in good agreement with what would be expected, e.g., as the concentration goes to 0% the optical constants agree well with those of pure water. The dominant water absorption feature is the O-H stretch feature. The position of the peak is around 3400 cm^{-1}. For a given concentration, the peak intensity increases with decreasing T and the peak position shifts to lower frequencies in agreement with other ion-water measurements [*Zundel and Fritsch*, 1986]. For a given T, the peak intensity decreases as the solute mass fraction increases. Another water feature is the broad, low intensity associational water feature

around 2100 cm^{-1}. Next, there is the H-O-H deformation feature around 1640 cm^{-1}, the position of which is nearly insensitive to the range of T considered here, although the peak intensity decreases slightly with decreasing T. The final water absorption feature that is observed in the optical constants is the increase in k values on the low frequency end of the data, which is due to the broad librational band of water centered around ~690 cm^{-1} outside the range of our data.

In addition to the water absorption features, all of these multi-component mixtures contain ammonium and their optical constants all exhibit the ν_4 NH_4^+ deformation band, with a peak around 1445 cm^{-1}, together with the ν_3 NH_4^+ asymmetric stretch, the $\nu_2 + \nu_4$ combination and the $2\nu_4$ overtone of NH_4^+ in the 3335 to 2800 cm^{-1} region. At low concentrations the ν_3 asymmetric stretch, the $\nu_2 + \nu_4$ combination and the $2\nu_4$ overtone are apparent as an increased asymmetry of the O-H stretch region on the low frequency side. As the concentration increases, they become very pronounced and become distinct from each other and the O-H stretch bands. The $2\nu_4$ overtone of NH_4^+ in the 2800 cm^{-1} region is often noticeable even at the lowest solute concentrations. In some of the optical constants datasets, the triple degeneracy of the $2\nu_4$ overtone of NH_4^+ appears to be lifted and it appears as a triplet.

Group A: Binary Aqueous Ammonium Sulfate Optical Constants

For conciseness the figures illustrating the resulting optical constants are presented in Appendix A. The n and k spectra for all measured ammonium sulfate concentrations at 298 K are shown in Figure A.1. For purposes of clarity the remaining figures of the optical constants will focus on the k spectra and will not show the corresponding n spectra. Figure A.2 shows the k spectra of the 30% weight fraction

ammonium sulfate concentration at all measured T. All k spectra of aqueous ammonium sulfate exhibit the ν_3 SO_4^{2-} absorption band centered at about 1102 cm^{-1}. Its position and peak value at a given concentration are nearly insensitive to T. The k value at the peak of the band varies from about 0.1 at the lowest concentration to over 0.6 at the highest one. At the higher ammonium sulfate concentrations, two additional sulfate absorption features become evident in the spectra. The first feature is the ν_1 SO_4^{2-} band at 980 cm^{-1}. Its position and peak value are also nearly insensitive to T. The ν_1 SO_4^{2-} band at 980 cm^{-1} becomes noticeable in the k spectra at about 20% mass fraction, but even at lower concentrations a weak feature is evident on the shoulder of the water librational band. The second is a weak feature around 1850 cm^{-1} on the high frequency shoulder of the H-O-H deformation band. It only appears when the ν_1 SO_4^{2-} absorption band at 980 cm^{-1} is apparent. It is likely a $2\nu_2 + \nu_1$ SO_4^{2-} combination band.

Group B: Binary Aqueous Ammonium Nitrate Optical Constants

The k spectra for all measured ammonium nitrate concentrations at 298 K are shown in Figure A.3. The major nitrate ion absorption band in this case is the ν_3 NO_3^- band around 1350 cm^{-1}. The maximum k value in this band varies from about 0.1 for the lowest concentration to about 0.53 at the highest concentration. Its position and peak value are nearly insensitive to T. Since the k spectra is nearly insensitive to T outside of the O-H stretch region, as was seen in the aqueous ammonium sulfate spectra in Figure 2.3, we do not show the k spectra as a function of T for a given concentration. Although the ν_3 mode is doubly degenerate, it appears in these datasets and other datasets as a doublet. According to *Querry and Tyler* [1980], the degeneracy is likely removed by coordination of NO_3^- with H_2O. There are three minor spectral absorption features in the k spectra of aqueous ammonium nitrate. The first is a sharp weak feature at 1045 cm^{-1} that corresponds to the ν_1 NO_3^- absorption band. The ν_1 NO_3^- band is distinct at all but

the lowest concentrations presented here, but even then it is evident that there is a weak band located there. At the higher concentrations, two additional nitrate absorption features are evident in the k spectra. The first is a weak feature around 2400 cm^{-1} that is likely a $\nu_1 + \nu_3$ NO_3^- combination band [*Greenberg and Hallgren*, 1960]. The second is a sharp weak feature at 1760 cm^{-1} that is likely a $\nu_1 + \nu_4$ NO_3^- combination band [*Greenberg and Hallgren*, 1960].

Groups C and H: Ternary Aqueous Ammonium Nitrate-Nitric Acid Optical Constants

Figure A.4 shows the k spectra for all measured temperatures at the single measured concentration of aqueous ammonium nitrate-nitric acid for group C. The k spectra for all measured aqueous ammonium nitrate-nitric acid concentrations of group H at 298 K are shown in Figure A.5. As with group B, the major nitrate ion absorption band in the k spectra of aqueous ammonium nitrate is the ν_3 NO_3^- band around 1350 cm^{-1}. It is apparent at all concentrations. The maximum k value in this band varies from about 0.08 for the lowest concentration to about 0.23 at the highest concentration. Its position and peak value are nearly insensitive to T. The three minor nitrate ion spectral absorption features, ν_1, $\nu_1 + \nu_3$, and $\nu_1 + \nu_4$, are also observable in the k spectra of these aqueous ammonium nitrate-nitric acid optical constants. The presence of the hydrogen ion from the nitric acid results in a slight continuum absorption that increases with the increasing nitric acid concentration.

Groups D and F: Ternary Aqueous Ammonium Sulfate-Sulfuric Acid Optical Constants

The k spectra for all measured aqueous sulfuric acid-ammonium sulfate concentrations at 298 K for group D are presented in Figure A.6. The k spectra for all measured aqueous sulfuric acid-ammonium sulfate concentrations at 298 K for group F are shown in Figure A.7. At all of the measured concentrations the ν_1 band and the ν_4

band of the bisulfate ion are evident. The position of the ν_1 band of the bisulfate ion at 1052 cm^{-1} is nearly insensitive to T. The position and magnitude of the ν_4 band of the bisulfate ion, around 1185 cm^{-1}, exhibit some temperature- and concentration-dependence, particularly at the lower measured concentrations, but become nearly insensitive to T at the higher concentrations. Another bisulfate absorption band that appears in these k spectra is the ν_2 absorption band of the bisulfate ion around 880 cm^{-1}. At the lowest solute concentrations it is discernable only at higher temperatures, but becomes very pronounced at higher concentrations.

In addition to the bisulfate ion absorption bands, these optical constants exhibit absorption bands due to sulfate. The ν_3 band of the sulfate ion around 1100 cm^{-1} is most noticeable at lower concentrations. At higher concentrations, it is only evident as an asymmetry on the low frequency side of the ν_4 band of the bisulfate ion. The ν_3 band of the sulfate ion remains distinct from the bisulfate bands at the higher concentration and lower T, which can be explained by the temperature-dependent equilibrium constant between bisulfate and sulfate [*Martin et al*., 1997]. There is also the ν_1 band of the sulfate ion at 980 cm^{-1}, which is most discernable at colder temperatures and moderate concentrations. At high concentrations it appears as a weak feature on the shoulder of the ν_1 band of the bisulfate ion. At higher T for all concentrations the ν_1 SO_4^{2-} band is not discernable. As the concentration of ammonium sulfate and sulfuric acid increases, the intensity of the bisulfate bands becomes temperature insensitive and the changes with T occur mainly in the regions of the ν_3 and ν_1 bands of the sulfate ion.

The continuum absorption, which has been attributed to the hydrated proton [*Kim et al.,* 2002], is apparent in these optical constants. This hydrated proton continuum in the k spectra of binary nitric acid and binary sulfuric acid was also reported in other studies. Figure A.8 illustrates many of the temperature dependence effects exhibited in the k spectra of mixtures containing sulfuric acid and ammonium sulfate. These groups show

significant dependence of k values on T outside the O-H stretch region. Specifically, there is a noticeable increase in the continuum exhibited by the k values of these groups with decreasing T. There is also the temperature dependence of the equilibrium concentration of sulfate and bisulfate ions and, therefore, the strength of their absorption bands. The lack of the intense 965 and 1370 cm^{-1} bands of molecular H_2SO_4 in these k spectra indicates that for these concentrations and temperatures there is not an appreciable amount of undissociated H_2SO_4.

Group E: Quaternary Aqueous Ammonium Sulfate-Sulfuric Acid-Ammonium Nitrate Optical Constants

The optical constants of this multi-component aqueous aerosol are the most complex because this group contains all of the ion species. The k spectra exhibit all of the absorption bands of the ammonium, nitrate, sulfate, bisulfate, and hydronium ions and of water molecules. Figure A.9 presents the k spectra for all measured aqueous sulfuric acid-ammonium sulfate-ammonium nitrate concentrations at 298 K. Figure A.10 shows the k spectra of the 10.3%-16.9%-18.6% weight fraction aqueous sulfuric acid-ammonium sulfate-ammonium nitrate concentration at all measured T. At the resolution of these datasets all of the absorption features are distinct. The magnitude of the bisulfate and sulfate absorption features exhibits a complex concentration and temperature dependence. These optical constants also exhibit the continuum absorption as was seen in the optical constants of groups D and F.

Group G: Ternary Aqueous Ammonium Sulfate-Ammonium Nitrate Optical Constants

Figure A.11 shows the k spectra for all measured ammonium sulfate-ammonium nitrate concentrations at 298 K. The optical constants of these aerosols are dominated by the ν_3 SO_4^{2-} absorption band and the ν_3 NO_3^- band. The sharp weak ν_1 SO_4^{2-} absorption band is also apparent in most of the datasets.

2.2.6 Remote Sensing and Climate Implications

The new optical constants presented have implications for atmospheric remote sensing applications and climate studies because tropospheric aerosols containing these aqueous mixtures have the potential to impact IR radiation transport in the atmosphere. The specific implications will of course depend on a particular application and the spectral region and resolution required for the application. Figure 2.1b shows that over a significant portion of the 860 – 3750 cm^{-1} region the atmospheric transmission from the surface to the TOA is effectively zero. This means that for sensors with a spectral resolution of 1 cm^{-1} or larger that tropospheric aerosols would not affect the IR radiance reaching a satellite. On the other hand, a ground-based or airborne IR sensor could receive a spectral radiance signal that has been affected by the absorption and emission of aqueous sulfate-nitrate-ammonium tropospheric aerosols. Applications of particular interest in this region of the IR include radiative forcing for climate studies, trace gas and/or global warming gas retrievals, and aerosol microphysical property retrievals. The spectral region that is covered by these optical constants includes the long-wave and mid-wave IR windows between about 750 – 1250 cm^{-1} and 1950 –3450 cm^{-1}, respectively, and therefore surface remote sensing can also be impacted.

The liquid water absorption features in these optical constants coincide with water vapor absorption regions, and so for many remote sensing applications they would be obscured by intervening water vapor absorption and emission. On the other hand, they could impact water vapor sounding that used the water vapor lines, for example in the H-O-H deformation region ~1630 cm^{-1} in between the atmospheric windows. Airborne or ground-based sensors in close proximity to the aerosol layer could detect the absorption and emission of the liquid water O-H stretch and H-O-H deformation features. The effect of absorption and emission by these water features could be used to infer the phase of the aerosol particles as either dry or aqueous. They could also be used in laboratory or in situ settings to determine composition and size distribution of the aerosol by fitting to model

radiances. The ν_3, $\nu_2 + \nu_4$ and $2\nu_4$ overtone of NH_4^+ in the 3335 to 2800 cm^{-1} region with their significant k values are positioned on the high frequency edge of the midwave IR window. They have the potential to affect the low frequency end of the solar energy that reaches the surface and the high frequency end of the terrestrial radiation that reaches space through this window region. These ammonium bands also absorb in the same spectral region as the ν_1 and ν_3 absorption bands of the greenhouse gas methane centered near 3000 cm^{-1}. The presence of these aqueous aerosols, therefore, has the potential to affect retrievals of methane. The ν_4 NH_4^+ deformation band, with a peak around 1445 cm^{-1}, falls in the opaque region between the mid-wave and the long-wave IR windows. For a sensor in close proximity to the aerosol layer, the effect of absorption and emission by this feature could be used to retrieve information on the composition of the aerosol by fitting to model radiances.

The sulfate ion is of particular interest to IR remote sensing and climate studies. This is because the ν_3 SO_4^{2-} absorption band has large imaginary index of refraction values positioned in the most transparent portion of the longwave IR window. Previous studies have indicated that the positive surface IR forcing due to dry sulfate can partially offset the TOA negative forcing due to sulfate scattering of solar radiation [*Li and Min*, 2002]. These new optical constants can be used to better quantify the surface and TOA IR forcing due to aqueous sulfate aerosols. Because this spectral absorption feature is located in the most transparent portion of the longwave IR window, the absorption and emission by aqueous sulfate tropospheric aerosols may be detectable in TOA radiance data. The ν_1 SO_4^{2-} absorption band has much smaller k values than the ν_3 band, but it is also in the longwave window region on the low frequency side of the atmospheric ozone absorption region. Since the ν_1 absorption band appears in the aqueous phase and not the solid phase, it may be useful in determining the phase of an aerosol if it is detectable in the measured radiance data.

The nitrate ion is also of interest to IR remote sensing. The ν_3 NO_3^- band falls on the low frequency edge of the opaque region between the midwave and longwave IR windows in a region where it overlaps absorption bands of atmospheric water vapor, methane and nitrous oxide, which are important greenhouse gases. The presence of aqueous aerosols containing nitrate ions could interfere with retrievals of methane and nitrous oxide that use radiance data in the 1350 cm^{-1} spectral region. The sharp weak ν_1 NO_3^- band around 1045 cm^{-1} is found in the aqueous phase but not typically in the solid phase and therefore if detected would indicate that the aerosol is in the aqueous phase. It lies in the center of the 9.6 μm ozone band, so a satellite sensor would not be able to detect its presence. The ν_1 NO_3^- band and the $\nu_1 + \nu_4$ NO_3^- combination band are weak features with small k values at all of these concentration levels and would be difficult to detect in radiance measurements outside of a laboratory setting or possibly in situ measurements or on board an aircraft.

Aqueous multi-component aerosols that contain sulfuric acid and ammonium sulfate have three prominent bisulfate ion absorption features in their k spectra that lie within the longwave IR window. The strongest is the ν_4 HSO_4^- band towards the high frequency side of the longwave window. The next strongest is the ν_1 HSO_4^- band. It is positioned in the middle of the ozone 9.6 μm band. The last major bisulfate ion absorption feature is the ν_2 HSO_4^- band at the low frequency end of these datasets and the low frequency edge of the longwave window region. These HSO_4^- absorption bands like the ν_3 SO_4^{2-} absorption band have the potential to produce positive IR forcing at the surface. The ν_4 and ν_2 bands being outside the ozone region have the potential to impact IR retrievals of sea-surface temperatures. The ν_1 HSO_4^- band would be able to interfere

with ground-based measurements of the 9.6 μm ozone band. For multi-component aqueous aerosols that contain high concentrations of sulfuric acid, the hydrated proton continuum results in aerosols that have k values of about 0.1 across both the midwave and longwave IR windows and the region between the windows.

Summarizing the above discussion, we want to stress that the intensity and position of absorption features in k spectra are dependent on T and on the concentration of all of the solutes because of ion-water and ion-ion interactions. Therefore, we believe that measurements of the optical constants of multi-component aqueous electrolyte aerosols need be made as a function of T and concentration in order to have accurate high spectral resolution data. In particular, the strength of the sulfate and bisulfate absorption bands demonstrates a complex dependency on T and concentration of sulfuric acid and ammonium sulfate. Our study demonstrates that the optical constants of binary ammonium sulfate would not be a good surrogate for binary ammonium nitrate or the ternary and quaternary optical constants. We have also seen that these multi-component aqueous aerosols have complex k spectra with ion absorption bands and continuum absorption in regions of the IR that have important implications to atmospheric remote sensing and radiative transfer. The importance will of course depend on the spectral region and resolution utilized by the application, and whether the IR data is acquired by a satellite or airborne or ground-based sensor. The sulfate and bisulfate ions in particular can have a significant impact on IR remote sensing and also on IR radiative forcing, particularly at the surface due to their large k values in the most transparent region of the IR.

2.3 Compilation of Existing Refractive Index Data

Optical constants for many of the main aerosol species or components exist, but not in a single database or collection that would make modeling different mixtures,

particularly multi-component regional or size-resolved mixtures, convenient. To support the modeling in this work and modeling by others in the scientific community we have therefore compiled an extensive collection of existing refractive index data of the most common tropospheric aerosols components. From this collection and our new sulfate-nitrate-ammonium optical constants a database called LAARI (Library of Atmospheric Aerosol Refractive Indices) has been developed.

2.3.1 Collection and Analysis of Existing Aerosol Refractive Index Data

The goal of LAARI is to compile a database of high spectral resolution refractive index data, preferably from 0.2 to 40 μm, for the most common atmospheric aerosol components (e.g. different minerals, black carbon, sulfates, nitrates, and sea-salt) to support high spectral resolution aerosol radiative transfer modeling using appropriate mixing schemes in the study of the radiative effects of heterogeneous mixtures of atmospheric aerosols. Current databases and libraries of aerosol optical properties and refractive indices are based on a few individual species like ammonium sulfate and sulfuric acid, and generic aerosols like 'dust' or 'insoluble' or 'soot', e.g. Optical Properties of Aerosols and Clouds (OPAC) software package [*Hess et al.*,1998] or Air Force Geophysics Laboratory (AFGL) Handbook of Geophysics and the Space Environment [*Fenn et al.*, 1985]. There is not currently a convenient source of high spectral resolution refractive index data for the main individual constituents of aerosols, which would allow more advanced modeling like size-resolved or region specific aerosols. Additionally, much of the data that are readily available are generally of low spectral resolution. To be able to model at high spectral resolution the radiative effects of

an aerosol of arbitrary composition, or to be able to retrieve microphysical or macrophysical properties aerosols from different regions from such radiance measurements, requires the use of the refractive index of the individual components at a spectral resolution appropriate to the spectral resolution of the measurements. Generic datasets like 'dust-like' or 'insoluble' can not represent the variable high spectral resolution signatures of regional dust aerosols that results from their mineralogical differences.

To compile the LAARI database we conducted an extensive review of the scientific literature and aerosol texts to determine what aerosol and aerosol component refractive index data were available. The datasets that were found were either obtained in a digital format or were digitized from tables or plots. All datasets were interpolated to the same resolution using a piecewise cubic Hermite interpolating polynomial (PCHIP). The LAARI database currently contains the refractive indices of many of the components of atmospheric aerosols, but it is by no means exhaustive. It also contains the refractive index data of mixtures and generic bulk measurements of aerosol samples that are part of the most common aerosol modeling data sets, e.g. in the AFGL Handbook of Geophysics and the Space Environment [*Fenn et al.*, 1985]. The database includes both the original measured data as well as data interpolated to 1 cm^{-1} resolution in the IR and 10 cm^{-1} in the UV to NIR region. Currently, the database contains the following refractive index data that covers the entire desired wavelength range from 0.2 to 40 μm: dry ammonium sulfate $(NH_4)_2SO_4$, sodium chloride NaCl, water at 25 C, various bulk dust samples, and one soot dataset. All other datasets in LAARI cover the original spectral range for which they were measured. Table 2.5 summarizes the data currently included in the database.

Table 2.5 Library of Atmoshperic Aerosol Refractive Indices

Library of Atmospheric Aerosol Refractive Indices			
Aerosol	**Wavelengths (μm)**	**Comments**	**References**
Bulk Material			
"Sahara dust-Barbados"	2.5 - 40	Barbados, West Indies	*Volz* [1973]
"Sahara dust-Niger"	4 - 40	Niamey, Niger	Volz cited in the work by *Fouquart et al.* [1987]
"Negev dust" "Clean" & "Dust storm"	7.5 - 12	Negev Desert, Israel	*Fischer* [1975]
"Afghan dust"	2.5 - 25	Afghanistan-Tadzhikistan	*Sokolik et al.* [1993]
"Southwest USA dust"	1 - 16	Whitehill, Texas, USA	*Patterson* [1981]
"Dust-like"	2.5 - 40	Germany	*Volz* [1972]
"Water soluble"	0.2 - 40	Global precipitation samples	Volz cited in *Shettle and Fenn* [1976 & 1979]
"Sea salt"	0.2 - 40		Volz cited in *Shettle and Fenn* [1979]
Mineral			
Quartz, Amorphous form	7.14 – 50.0		*Popova et al.* [1972]
Quartz, Amorphous form	7.14 – 25.0		*Steyer et al.* [1972]
Quartz, Crystalline form	0.736 – 36.0		*Peterson and Weinman* [1969]
Montmorillonite	5 - 100		*Glotch et al.*[2007]
Montmorillonite	0.185 – 2.6		*Egan and Hilgeman* [1979]
Montmorillonite	5.0 – 40.0		*Toon et al.* [1977]
Montmorillonite	2.5 – 200		*Querry* [1987]
Illite-Smectite	5 - 100		*Glotch et al.*[2007]
Illite	5 - 100		*Glotch et al.*[2007]
Illite	0.185 – 2.6		*Egan and Hilgeman* [1979]
Illite	2.5 – 200		*Querry* [1987]
Kaolinite	5 - 100		*Glotch et al.*[2007]
Kaolinite	0.185 – 2.6		*Egan and Hilgeman* [1979]
Kaolinite	5 - 25		*Roush et al.* [1991]

Table 2.5 (continued)

Library of Atmospheric Aerosol Refractive Indices			
Aerosol	**Wavelengths (μm)**	**Comments**	**References**
Mineral cont.			
Calcite, Amorphous form	2 – 32.8		*Querry et al.* [1978]
Calcite, Crystalline form	2 - 200		*Posch et al.*[2007]
Calcite, Crystalline form	2.5 - 300		*Long et al.* [1993]
Gypsum, Crystalline form	2.5 - 25		*Roush et al.[2007]*
Gypsum, Crystalline form	2.5 - 300		*Long et al.* [1993]
Dolomite	2.5 - 25		*Posch et al.*[2007]
Mica	0.185 – 2.6		*Egan and Hilgeman* [1979]
Feldspar Orthoclase-a	2.5 - 200		*Glotch et al.*[2007]
Feldspar Orthoclase-b	2.5 - 125		*Glotch et al.*[2007]
Feldspar	0.185 – 2.6		*Egan and Hilgeman* [1979]
Chlorite	2.5 - 50		*Mooney and Knacke* [1985]
Serpentine	2.5 - 50		*Mooney and Knacke* [1985]
Serpentine	5 - 25		*Roush et al.* [1991]
Hematite o-ray	5 - 15		*Glotch et al.*[2007]
Hematite e-ray	5 - 15		*Glotch et al.*[2007]
Hematite	0.2 - 50		*Querry* [1987]
Hematite	8.3 – 50.0		*Popova et al.* [1973]
Water			
H_2O	0.2 – 0.32	Absorption values	*Quickenden and Irvin* [1980]
H_2O	0.38 – 0.7	Absorption values	*Pope and Fry* [1997]
H_2O @ 25 C	0.67 - 10000	From various recommended sources	*Bertie and Lan* [1996b]
H_2O @ 25 C	0.2 – 2.5	IAPWS formula for n	*Harvey et al* [1998]

Table 2.5 (continued)

Library of Atmospheric Aerosol Refractive Indices			
Aerosol	**Wavelengths (μm)**	**Comments**	**References**
Black Carbon			
Soot	0.2 - 40		*Twitty and Weinman* [1971]
Soot	0.48 - 10		*Nilsson* [1979]
Soot - Flame	0.3 - 20		*Tien and Lee* [1982]
Soot - Flame	0.2 - 30		*Chang and Charalampopoulos* [1990]
Soot - Flame	0.35 – 0.8		*Wu et al.* [1997]
Soot - Acetylene	0.44 - 10		*Dalzell and Sarofim* [1969]
Soot - Propane	0.44 - 10		*Dalzell and Sarofim* [1969]
Black Carbon	0.3 - 3		*Bergstrom* [1972]
Sulfates			
$(NH_4)_2SO_4$	0.2 – 40	Dry	*Toon et al.* [1976]
$(NH_4)_2SO_4$	1.667 – 16.95	Dry T = 298, 243, 223, and 213 K	*Earle et al.* [2006]
$(NH_4)_2SO_4$	0.7 – 2.6	Aqueous 10, 25, 40%	*Gosse et al.* [1997]
$(NH_4)_2SO_4$	7.7 – 10.3 4.44 – 13.33 (39%)	Aqueous 21, 30, 39, 41%	*Remsberg* [1971]
H_2SO_4			*Mhyre et al.*[2003]
H_2SO_4	0.7 – 2.6	Aqueous 10, 24, 48, 72%	*Gosse et al.* [1997]
H_2SO_4	0.2 - 40	Aqueous 75%	*Shettle and Fenn* [1979]
H_2SO_4	0.4 – 25	Aqueous, various weight %'s	*Palmer and Williams* [1975]
H_2SO_4	2.12 – 12.12	Aqueous, various weight %'s	*Niedziela et al.* [1998]
Nitrates			
HNO_3			*Mhyre et al.[2005]*
HNO_3	0.7 – 2.6	Aqueous 10, 35, 50%	*Gosse et al.* [1997]
HNO_3	2.13 – 13.3	Aqueous, various weight %'s	*Norman et al.* [1999]
HNO_3	1 - 5000	Aqueous, various weight %'s	*Biermann et al.* [2000]
HNO_3	2 - 40	Aqueous, various weight %'s	*Querry and Tyler* [1980]
NH_4NO_3	0.7 – 2.6	Aqueous 10, 25, 40%	*Gosse et al.* [1997]
$NaNO_3$	0.17 - 1000		*Palik and Khanna* [1985]
Salt			
NaCl	0.2 - 30000		*Eldridge and Palik* [1985]

Water, H_20

For water, many different measurements of the refractive index were found. Some of the most often cited references include *Hale and Querry* [1973], *Palmer and Williams* [1974], *Downing and Williams* [1975], *Irvine and Pollack* [1968], *Tam and Patel* [1979], *Kou et al.* [1993], and *Nilsson* [1979]. Unfortunately, no single source completely covered the desired spectral region. When the various datasets were joined, the fits in the overlap regions were not very satisfying. In particular for the real index, n, of refraction, the *Hale and Querry* data and the *Palmer and Williams* data (the most often used shortwave datasets) did not join the *Downing and Williams* data (the most used longwave dataset) very well around 2 μm. In addition to this, there were significant differences in the 2 μm to 3 μm region and in the positioning and depth of the spectral feature near 2.8 μm. Some of these differences may have been due to temperature differences, but more likely they were due to measurement differences. For example, the *Palmer and Williams* data is for water at 27 C and yet agrees well with the *Hale and Querry* data at 25 C from 0.45 μm to 2.4 μm. But neither agrees sufficiently with the *Downing and Williams* data for water at 27 C.

Upon further review of the literature, the paper by *Bertie and Lan* [1996b] was found in which they compiled the best current values of the refractive index of liquid water at 25 C between 15000 and 1 cm^{-1}. This compilation is what was finally included in the database for the 0.67 μm to 40 μm region. In order to cover the region from 0.2 μm to 0.67 μm the measurements of *Pope and Fry* [1997], and *Quickenden and Irvin* [1980] were included for the imaginary part of the index of refraction. For the real part of the index of refraction the empirical function adopted by the International Association

for the Properties of Water and Steam (IAPWS) and described by *Harvey et al.* [1998] was used. Both of these datasets join together smoothly with the recommended dataset of *Bertie and Lan* [1996b]. To create the complete dataset, first the tabulated data from the *Bertie and Lan* were digitized. Then the empirical formula from the IAPWS was implemented and the *Pope and Fry*, and *Quickenden and Irvin* data were converted from absorption coefficient values to imaginary refractive index values using the Lambert absorption coefficient formula.

Sodium Chloride, NaCl

The NaCl refractive index data has been taken from the Handbook of Optical Constants (*Eldridge and Palik*, [1985]). The data for the real index, n, of refraction comes from the empirical formula for the 0.2 μm to 20 μm spectral range. The imaginary index, k, of refraction is interpolated from the data in Table XIII over the entire spectral range 0.2 μm to 40 μm. In the IR NaCl is extremely transparent, which is why it is sometimes used as window material for IR sensors and as prism material for mid-wave and long-wave dispersive sensors. It is important to have it in the database because NaCl as part of seasalt aerosols can form very large particles which can scatter at IR wavelengths more readily than other aerosols and thereby impact IR radiances.

Dry Ammonium Sulfate, $(NH_4)_2SO_4$

Two sets of optical constants for dry ammonium sulfate are contained in the LAARI database. The first set is taken from the paper by *Toon et al.* [1976]. The values given in that paper are a combination of values in the literature and from measurements

made by the authors. These optical constants for ammonium sulfate have been very widely used in the atmospheric and planetary science communities for decades. The second set is based on more recent measurements and described in the paper by *Earle et al.* [2006]. These newer optical constants span the range from the near infrared (NIR) (5990 cm^{-1}) to the far infrared (FIR) (590 cm^{-1}). They are also measured at multiple temperatures, including stratospheric temperatures. Ammonium sulfate has four strong absorption features in the IR, one of which is in the long-wave IR atmospheric window and another one which lies in the mid-wave IR atmospheric window. The other absorption features lie just outside the atmospheric windows and therefore can impact algorithms that sound the atmosphere using the absorption of gases at the window edges.

Aqueous Sulfates

Numerous measurements of sulfuric acid are reported in the literature for many different concentrations and temperatures. The most often cited are those reported by *Shettle and Fenn* [1979] and *Palmer and Williams* [1975]. The *Shettle and Fenn* dataset covers the desired spectral region from 0.2 μm to 40 μm but is only measured for one concentration and temperature. More recent datasets have been measured at many different temperatures and concentration, e.g. *Mhyre et al.* [2003]. There are two aqueous ammonium sulfate datasets, *Gosse et al.* [1997] for the NIR to shortwave infrared (SWIR) and *Remsberg* [1971] for the IR.

Nitrates

As with sulfuric acid, numerous measurements of nitric acid are also reported in the literature for many different concentrations and temperatures. The most often cited are those reported by *Querry and Tyler* [1980]. More recent datasets have been measured at a large number of different temperatures and concentration, e.g. *Mhyre et al.* [2005]. In addition to the nitric acid datasets there is one aqueous ammonium nitrate dataset from *Gosse et al.* [1997] and a solid sodium nitrate dataset from *Palik and Khanna* [1985].

Bulk Aerosol Material

The refractive index data for the bulk aerosol material in LAARI are not based on individual particle optical properties or from uniform single material measurements, instead they are determined from measurements of bulk samples of aerosol particles. In general they are made from samples that are collected in a specific geographical region. The measurements have been done on dry samples of the particles and so any hygroscopic effects or effects due to coating with water have to be extrapolated from these data. Most of the datasets here are for dust aerosol. There is also one generic water soluble dataset and one sea salt dataset.

Black Carbon (BC)

The optical constants for black carbon (soot) that cover the entire range from 0.2 to 40 μm are taken from the aerosol model of *Shettle and Fenn* [1979] and are based on measurements by *Twitty and Weinman* [1971]. The LAARI database also contains the often cited BC measurements of *Tien and Lee* [1982], *Chang and Charalampopoulos*

[1990], *Wu et al.* [1997], *Dalzell and Sarofim* [1969], and *Bergstrom* [1972]. The k spectra of these various soot measurements lacks any sharp spectral features in the IR, but because of the large k values soot particles can have significant effects in the IR particularly when they mix internally with other aerosol species or form the core of an aqueous aerosol particle. The magnitude of k spectra can change significantly based on the combustion materials and temperature that produced the soot. Because of this no one set of BC optical constants will suffice for all instances. The LAARI database will be updated to include additional BC optical constants as they become available. Ideally the LAARI database would include regional data sets of new and aged soot that reflect local sources and processes which produce BC.

Minerals

The optical constants of the minerals in LAARI are a combination of datasets collected by Dr. Sokolik from a variety of sources, and a number of more recent datasets we collected that were measured by astronomical researchers [i.e. *Glotch et al*. 2007, *Posch et al*. 2007, and *Roush et al*. 2007]. Currently, there are several mineral datasets that cover the spectral region from 0.2 to 40 μm (quartz, calcite, gypsum, hematite, illite, and montmorillonite). Hematite is of particular interest currently because of its large absorption in the red portion of the visible and the impact of that to climate [*Lafon et al*., 2006]. IR spectroscopy of minerals for identification is a long established science. This ability to distinguish minerals from each other by their spectral absorption differences is both the reason that we need to be concerned about mineral specific effects on high spectral resolution radiance measurements, and the key to being able to detect the

presence of specific minerals and account for it. Figure 2.2 below shows the imaginary index of refraction in the TIR of many of the minerals included in LAARI. These optical constants are critical to the investigation of high spectral resolution signatures and radiative forcing by tropospheric dust aerosol in the TIR.

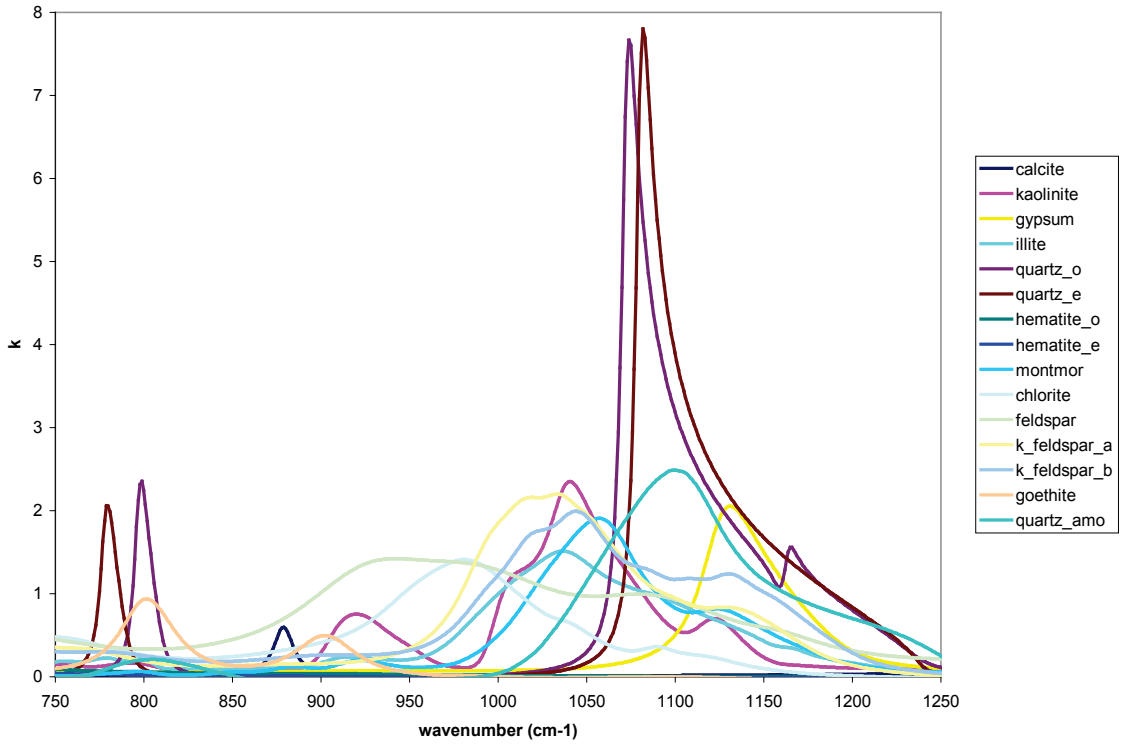

Figure 2.2 Sample of k spectra for minerals contained in the LAARI database

2.4 Summary

We have compiled a new library of refractive indices of aerosols and aerosol components, most at high spectral resolution, in the UV to IR spectral region called LAARI. This library will provide new capabilities for aerosol optical modeling and for the development of aerosol retrieval algorithms and the improvement of atmospheric and

surface geophysical properties retrievals affected by aerosols. Most importantly the LAARI database provides the fundamental refractive index data that can then be used with the appropriate method of calculating optical properties (e.g. Mie code, discrete dipole approximation (DDA), T-Matrix, or others) to allow researchers to model multi-component aerosols from pure species components using an appropriate mixing rule.

LAARI includes new IR optical constants determined in this work that cover the spectral range from 860 to 3750 cm^{-1} at 1 cm^{-1} resolution for multi-component aqueous mixtures composed of ammonium sulfate, ammonium nitrate, sulfuric acid and nitric acid over a range of compositions and temperatures representative of aerosols of these compositions in tropospheric conditions. The optical constants were determined from ATR measurement data using the Kramers-Kronig transformation. In implementing the K-K transformation, efforts were made to reduce errors that stem from the use of ATR data of limited frequency range. This included extending the data on the low frequency side and modeling the frequency dependence of the real part, n, of the refractive index in the visible.

The n of these mixtures at visible wavelengths was modeled using the Lorentz-Lorenz mixing rule and partial molar refraction data, which has been shown to provide good results in the case of the real index of refraction of liquids in the visible. The n of the multi-component aqueous aerosols was modeled at multiple frequencies in the visible in order to determine the frequency dependence for use in the ATR-to-optical constants code. The ATR data on the low frequency side were extended with either a synthetic ATR spectrum of pure water using literature optical constants, where that was a good

approximation, or a synthetic ATR spectrum of binary sulfuric acid calculated from literature optical constants.

Regarding the new refractive index data our major findings are the following:

- The considered multi-component aqueous mixtures have IR optical constants that are spectrally unique from each other, and the spectral absorption features reflect the particular composition of the mixture and the mixture's specific temperature dependence. This uniqueness means that the IR optical constants are not interchangeable. The IR optical constants of a binary mixture are not a good surrogate for those of a ternary mixture or a quaternary mixture, and likewise the IR optical constants of a ternary mixture are not a good surrogate for those of a quaternary mixture.
- The composition of the mixture is the main factor in determining the spectral features of the optical constants. The ammonium sulfate-containing aqueous mixtures have a significant absorption band in the most transparent portion of the atmospheric longwave IR window with the potential that tropospheric aerosols could impact remote sensing applications like sea-surface temperature retrievals, and to contribute to a positive surface radiative forcing. In contrast, the main absorbing feature of nitrate in aqueous ammonium nitrate, and/or nitric acid, is located in a region dominated by water vapor absorption. On the other hand, it overlaps absorption bands of methane and nitrous oxide that are important greenhouse gases. The presence of acids, sulfuric or nitric, results in continuum absorption from 1000 – 3400 cm^{-1}. The sulfuric acid in a combination with ammonium sulfate produces concentration- and temperature-dependent bisulfate

and sulfate absorption bands that nearly cover the entire longwave IR window region with implications for IR remote sensing and surface radiative forcing. The ammonium ion has a significant absorbing band near 1430 cm^{-1}, but it is located in a region dominated by water vapor absorption. More importantly, the ammonium ion has absorbing bands in the midwave IR window that overlap absorbing bands of methane and nitrous oxide.

- The IR optical constants of sulfuric acid or ammonium sulfate should not be used as generic sulfate IR optical constants, and sulfate and nitrate optical constants are not interchangeable in the IR.
- All of these IR optical constants have some temperature dependence. For binary aqueous ammonium sulfate and binary aqueous ammonium nitrate, the dependence on T is mostly found in the O-H stretch region. For the nitric acid containing mixtures, there is some temperature dependence in the continuum absorption. The most significant temperature dependence outside the O-H stretch region is found in the mixtures that contain sulfuric acid and ammonium sulfate. In addition to the continuum absorption temperature dependence, there is significant dependence on T in the bisulfate and sulfate absorption bands resulting from the temperature dependence of the equilibrium concentrations of bisulfate and sulfate ions for a given concentration of sulfuric acid and ammonium sulfate.

CHAPTER 3

INVESTIGATING THE HIGH SPECTRAL RESOLUTION IR OPTICAL SIGNATURES OF TROPOSPHERIC AEROSOL COMPONENTS AND MIXTURES – DUST AND AQUEOUS AEROSOLS

3.1 Introduction

This chapter sets the stage for radiative transfer modeling by investigating how the high spectral resolution optical properties of aerosols change depending on the choices that are made in their modeling. Since the focus of the radiative transfer modeling in Chapter 4 is dust aerosol, which is composed of irregularly shaped particles, it is important to try to ascertain the most appropriate morphology simplification to use in the calculations of its high spectral resolution volume optical properties. To do this, a comparison is made between volume optical properties computed here with optical constants from LAARI and recently published laboratory extinction measurements [*Hudson et al.,* 2008a, b]. We also investigate the difference in volume optical properties' signatures between an external mixture and an internal mixture of dust aerosol components. Additionally other factors that might affect the high spectral resolution volume optical properties of a multi-component aerosol were examined. For example, what is the compositional fidelity required to accurately capture the high spectral resolution features of a multi-component aerosol (i.e. main components only or minor also) and how do the size distribution parameters and the limits of integration of the size distribution of the aerosol affect the spectral optical properties. Finally, the effects of the choice of mixing rule on resulting effective optical constants for internal mixtures is

investigated using the newly determined multi-component aqueous optical constants of Chapter 2. The information garnered here is used in the radiative transfer modeling of the next chapter to guide the choices made in the calculations of optical properties and the retrieval of aerosol microphysical properties from high spectral resolution TIR radiance measurements.

This chapter is organized as follows: Section 3.2 introduces and discusses the computation of the aerosol IR optical signatures in terms of their spectral volume optical properties using Lorentz-Mie theory, T-matrix theory, and CDE. It also details the computation of the volume optical properties of an externally mixed aerosol from the volume optical properties of the components. Section 3.3 examines the volume optical properties for pure components of dust aerosols computed using Lorentz-Mie theory, T-matrix and CDE. The differences between the techniques are examined as is the dependence on size distribution parameters and limits of integration for the size parameter. The results for the various techniques are compared to recently published high spectral resolution TIR extinction measurements to determine which, if any, of the techniques best match the measurements. Section 3.4 investigates the spectral volume optical properties of a size-resolved regional dust model as a function of level of compositional fidelity to determine to what level the composition needs to be modeled to accurately reproduce its spectral signature. The differences in the spectral signature of different regional models is also investigated along with the differences between the volume optical properties of a regional size-resolved model and volume optical properties computed using bulk material refractive index data. Lastly, the differences in spectral volume optical properties for the regional size-resolved dust model are compared for an internal mixture and an external mixture. Section 3.5 investigates the impact of EMA choice on the resulting optical constants of multi-component aqueous aerosols using the aqueous optical constants data determined in Chapter 2. Finally, Section 3.6 provides a summary.

3.2 Computation of Aerosol Volume Optical Properties

The volume optical properties of an aerosol that are required for radiative transfer modeling include the extinction, scattering and absorption coefficients, and the volume scattering function. From these the other required volume optical properties of single scattering albedo, the scattering phase function, and the asymmetry parameter can be computed. In order to compute the volume optical properties an analytic or numerical technique is required that can solve or approximate the solution to Maxwell's equations for the individual particles. This is then integrated over the size distribution of the particles that form the aerosol. For non-spherical particles integration over orientations of particles and over shape distributions would also need to be done. Exact analytical solutions to Maxwell's equations for particles are limited to a few simple shapes. The most common shapes used for aerosol particles are spheres and spheroids, which can be solved by Lorentz-Mie theory and T-matrix theory respectively. Because we are interested in modeling irregularly-shaped particles, we have chosen to investigate both spherical and non-spherical techniques to compute volume optical properties. The Lorentz-Mie theory is used for the approximation of spherical particles, and T-matrix and CDE are investigated as a way to model the particles as non-spherical. The implementation of the Lorentz-Mie theory, T-matrix, and CDE techniques to compute the volume optical properties of aerosol particles is described next followed by a discussion on the computation of volume optical properties for external mixtures.

3.2.1 Computation of Aerosol Volume Optical Properties for Spherical and Randomly Oriented Ellipsoidal Particles

Lorentz-Mie theory provides for the solution of Maxwell's equations for spherical and stratified spherical particles. The spherical particle assumption is by far the most common assumption or simplification in both aerosol remote sensing [*Kaufmann et al*., 2001] and climate modeling studies [*Jacobson*, 2001]. In this work the Mie code developed by Dr. Wiscombe [*Wiscombe*, 1980] is used. The code is available via anonymous ftp from the following website:

ftp://climate.gsfc.nasa.gov/pub/wiscombe/Single_Scatt/Homogen_Sphere/Exact_Mie/

(7/2002). This code computes the single particle optical properties of extinction efficiency, scattering efficiency, forward and backscattering amplitudes, amplitude scattering matrix, and Legendre polynomial expansions of the unpolarized phase function. We developed additional code to perform a numerical integration of the single particle optical properties over a prescribed analytic size distribution function using a Gaussian-Legendre quadrature technique to give the volume optical properties. The Gaussian-Legendre quadrature subroutine is based on the algorithm gauleg found in Numerical Recipes in C [*Press et al.,* 1992]. The documentation distributed with the Mie code provides guidance for size distribution integration. The controlling program that we developed computes size integrated volume optical properties for every wavelength for which complex refractive index data is supplied. The code was tested by comparing the output to other codes that computed volume optical properties of a collection of particles with a given size distribution using Mie theory.

To go beyond the spherical particle assumption, a T-matrix code is used to compute the volume optical properties of randomly oriented and mirror symmetric ellipsoidal particles. The code to do this was developed by Drs. Mishchenko and Travis [*Mishchenko and Travis*, 1998] and was obtained from the NASA website of Dr. Mishchenko: http://www.giss.nasa.gov/~crmim (12/2007). The code was slightly modified to loop over all the wavelengths for which refractive index data was provided as was done for the Mie code. In using the T-matrix code the user selects whether the size of the non-spherical particles is specified in terms of the equal-volume sphere radius or the surface-equivalent-sphere radius. For small particles where absorption dominates it is most appropriate to select volume equivalency since the absorption is proportional to the volume. For larger particles scattering becomes important and it is more appropriate to select surface area equivalence. In the case of tropospheric dust particles and TIR radiation, scattering is not negligible and so the surface area equivalency has been chosen.

Another analytical technique for computing the volume optical properties of small particles is the CDE technique [*Bohren and Huffman*, 1983]. CDE has been widely used in the astrophysics community for modeling interplanetary dust particles [*Vandenbussche et al.*, 2004; *Fabian et al.*, 2001; *Henning and Mutschke*, 1997]. This technique is derived in the Rayleigh limit (the size parameter of the particles is very much less than 1) for a collection of ellipsoidal particles whose shape distribution is described by a uniform probability density function over all possible ellipsoidal shapes, i.e. all possible ellipsoidal shapes occur with equal probability. Under these conditions, closed form analytical formulas are obtained for the absorption cross-section (i.e., $<C_{abs}>$), the

scattering cross-section (i.e., $<C_{sca}>$), and the differential scattering function (i.e., $\gamma(\theta) = \langle S_{11}(\theta) \rangle / \tilde{k}^2$) [*Nevitt and Bohren*, 1984; *Huffman and Bohren*, 1980]. Appendix B contains a corrected derivation of the scattering coefficient and the scattering function.

$$\langle C_{abs} \rangle = \tilde{k} v \, \mathrm{Im}\left\{ \frac{2\varepsilon}{\varepsilon - 1} \ln(\varepsilon) \right\} \tag{Eq. 3.1}$$

$$\langle C_{sca} \rangle = \frac{\tilde{k}^4 v^2}{6\pi} \left[\frac{(2 + 2\beta')}{|\beta''|} \left[\tan^{-1}\left(\frac{1+\beta'}{|\beta''|} \right) - \tan^{-1}\left(\frac{\beta'}{|\beta''|} \right) \right] - \ln\left[(1+\beta')^2 + \beta''^2 \right] + \ln\left(|\beta|^2 \right) \right] \tag{Eq. 3.2}$$

$$\frac{\langle S_{11}(\theta) \rangle}{k^2} = \frac{(3\cos^2\theta - 1)\tilde{k}^4 v^2}{80\pi^2} \left[\frac{(2+2\beta')}{|\beta''|} \left[\tan^{-1}\left(\frac{1+\beta'}{|\beta''|} \right) - \tan^{-1}\left(\frac{\beta'}{|\beta''|} \right) \right] - \ln\left[(1+\beta')^2 + \beta''^2 \right] + \ln\left(|\beta|^2 \right) \right] + \frac{(3\cos^2\theta - 1)\tilde{k}^4 v^2}{80\pi^2} \int_0^1 \mathrm{Re}\left\{ \frac{\ln\left[(\beta + 1 - L_1)/\beta \right]}{\beta^* + L_1} \right\} dL_1 \tag{Eq. 3.3}$$

In the above equations v is the volume of the particles, ε is the complex dielectric function and $\tilde{k}$ is the wavenumber.

$$\beta = \beta' + i\beta'' = (\varepsilon - 1)^{-1} \tag{Eq. 3.4}$$

$$\tilde{k} = \frac{2\pi}{\lambda} \tag{Eq. 3.5}$$

$$\varepsilon = m^2 = (n + ik) \cdot (n + ik) = n^2 - k^2 + i2nk \tag{Eq. 3.6}$$

The scattering phase function is defined in terms of the volume scattering function as

$$P(\theta) = \frac{4\pi}{\langle C_{sca} \rangle} \frac{\langle S_{11}(\theta) \rangle}{\tilde{k}^2} = \frac{4\pi}{\langle C_{sca} \rangle} \gamma(\theta) \tag{Eq. 3.7}$$

From these, the extinction coefficient, single scattering albedo, scattering phase function and asymmetry parameter can be computed. As is seen later, the fact that the

CDE formulas are derived in the Rayleigh limit restricts the use of these formulae to particles that are very much smaller than the wavelength of the interacting radiation. For terrestrial aerosol particles interacting with TIR radiation, the condition that the particles are very much smaller than the wavelength of the radiation is not generally satisfied and CDE does not provide an acceptable model.

In these algorithms it is assumed that the particles have a single complex refractive index. For an external mixture, each individual particle is considered to have a single complex refractive index, but different particles may have different compositions and therefore different refractive indices. The next section discusses the computation of the volume optical properties for an external mixture using the volume optical properties of particles with common refractive indices.

3.2.2 Computation of Volume Optical Properties for Aerosol External Mixtures

An externally mixed aerosol is an aerosol that contains only non-interacting (physically and chemically) individual particles. In the case of an external mixture the volume optical properties of the mixture are just the sum of the volume optical properties of the individual components. For each component of the external mixture, the volume optical properties of the component depend on the composition, shape, and size distribution of the particles within the particular component. Once the coefficients have been determined, e.g. using Mie theory, the total extinction, scattering or absorption coefficient is the sum of the component coefficients.

Letting $\beta_{e,i}$, $\beta_{s,i}$ and $\beta_{a,i}$ be the volume extinction, scattering and absorption coefficients, respectively, for component i, then the total volume extinction, scattering and absorption coefficients are just

$$\beta_{(e,s,a)} = \sum_i \beta_{(e,s,a),i} \qquad \text{(Eq. 3.8)}$$

The single scattering albedo is

$$\varpi = \frac{\beta_s}{\beta_e} \qquad \text{(Eq. 3.9)}$$

which can be written in terms of the component single scattering albedos as

$$\varpi = \frac{\beta_s}{\beta_e} = \frac{\sum_i \beta_{s,i}}{\sum_i \beta_{e,i}} = \frac{\sum_i \left[\beta_{e,i} \frac{\beta_{s,i}}{\beta_{e,i}} \right]}{\sum_i \beta_{e,i}} = \frac{\sum_i \beta_{e,i} \varpi_i}{\sum_i \beta_{e,i}} \qquad \text{(Eq. 3.10)}$$

The scattering phase function and the asymmetry parameter are computed using the volume scattering function, which is the quantity that is additive in an external mixture. The volume scattering function, $\gamma(\theta)$, is defined by the relation

$$I = \frac{d\Phi}{d\omega} = E\gamma(\theta)dv \qquad \text{(Eq. 3.11)}$$

where I is the radiant intensity, E is the irradiance, and Φ is the radiant flux. The volume scattering phase function is defined as

$$P(\theta) = 4\pi \frac{\gamma(\theta)}{\beta_s} \qquad \text{(Eq. 3.12)}$$

The asymmetry parameter is defined as

$$g = \frac{\int_0^\pi \gamma(\theta)\cos\theta \sin\theta d\theta}{\int_0^\pi \gamma(\theta)\sin\theta d\theta} = \langle \cos\theta \rangle \qquad \text{(Eq. 3.13)}$$

The scattering coefficient can be written in terms of the volume scattering function as

$$\beta_s = \int_{4\pi} \gamma(\theta)\, d\omega \qquad \text{(Eq. 3.14)}$$

For spherical particles or random orientations of particles where the scattering has rotational symmetry, this becomes

$$\beta_s = 2\pi \int_0^{\pi} \gamma(\theta) \sin\theta\, d\theta \qquad \text{(Eq. 3.15)}$$

For multiple component systems we can write the above optical properties in terms of the individual components as

$$\gamma(\theta) = \sum_i \gamma_i(\theta) \qquad \text{(Eq. 3.16)}$$

$$P(\phi) = 4\pi \frac{\gamma(\phi)}{\beta_s} = 4\pi \frac{\sum_i \gamma_i(\phi)}{\sum_i \beta_{s,i}} \qquad \text{(Eq. 3.17)}$$

$$g = \frac{\int_0^{\pi} \left[\sum_i \gamma_i(\theta)\right] \cos\theta \sin\theta\, d\theta}{\int_0^{\pi} \left[\sum_i \gamma_i(\theta)\right] \sin\theta\, d\theta} = \frac{\sum_i \left[\int_0^{\pi} \gamma_i(\theta) \cos\theta \sin\theta\, d\theta\right]}{\sum_i \int_0^{\pi} \gamma_i(\theta) \sin\theta\, d\theta} = \frac{\sum_i g_i \beta_{s,i}}{\sum_i \beta_{s,i}} \qquad \text{(Eq. 3.18)}$$

In cases where the individual particles are not homogeneous, i.e. they are internally mixed, the individual particles need to be approximated as homogeneous particles with an "effective" refractive index in order to use one of the above-mentioned techniques to compute the volume optical properties. The computation of effective optical constants is introduced in section 3.5 where their performance in modeling multi-component aqueous aerosols is evaluated. We now investigate the high spectral resolution volume optical properties of individual dust aerosol components and examine the uniqueness of their spectral signatures and the dependence of the spectral signatures

on size distribution parameters, limits of integration for the size distribution, and on the particle morphology used to model the particles.

3.3 IR Spectral Volume Optical Properties of Individual Dust Aerosol Components

Studies have shown that atmospheric dust aerosol is composed largely of silicate minerals, in particular quartz and feldspar from the tectosilicates subclass, and chlorite and clay minerals (predominately illite, kaolinite, and smectite (montmorillonite)) from the phyllosilicates subclass [*Flanigan and DeLong*, 1971; *Pye*, 1987; *Claquin et al.*, 1999; *Goudie and Middleton*, 2001]. A dust aerosol can also contain significant non-silicate minerals such as carbonate minerals like calcite and dolomite or sulfate minerals like anhydrite, and gypsum [*Blanco et al.*, 2003; *Avila et al.*, 1997; *Formeneti et al.*, 2008]. It may also contain iron oxide minerals like hematite and goethite with significant radiative implications in the solar part of the spectrum [*Lafon et al.*, 2006; *Claquin et al.*, 1999; *Goudie and Middleton*, 2001]. In this section we examine the TIR volume optical properties of these individual dust aerosol components with the exception of dolomite and anhydrite, which have very similar absorption spectra to calcite and gypsum respectively in the TIR window region. This is done for a number of reasons. First, a dust aerosol that is modeled as an external mixture requires us to compute the individual mineral volume optical properties. Second, the distinctiveness or lack thereof of the main mineral species can be demonstrated. Third, the variation of the optical properties with changes in the size distribution can be investigated without the complication of multiple components. Finally, by working with individual minerals of a dust aerosol we can examine the spectral differences between spherical and non-spherical approaches to

modeling dust volume optical properties. This also allows us to compare the results to reported laboratory measurements of TIR spectral extinction for pure mineral species. The analysis of the distinctiveness of spectral volume optical properties and the variation of the spectral optical properties with changes in the size distribution parameters can be accomplished using Mie theory results and are not repeated for non-spherical particles.

3.3.1 Spectral Signature Analysis of Mie Generated Volume Optical Properties of the Major Dust Aerosol Components

Dust aerosol, particularly close to the source region, is generally observed to be bimodal, i.e. the particles can be assigned to either a fine mode (submicron) or a coarse mode (supermicron). Giant particles (10s of microns or larger) can also be lifted into the atmosphere and travel hundreds if not thousands of meters, but these are not considered here because their concentration away from the immediate source area is too low to have a significant radiative impact. The mathematical representation of the size distribution of aerosol particles is usually chosen from a small number of probability density functions. One of the most common, and what is used here, is the lognormal function, which describes the lognormal size distribution. The lognormal size distribution is defined as

$$n(r) = \frac{dN}{dr} = \frac{N_0}{\sqrt{2\pi} r \ln \sigma_g} \exp\left(-\frac{1}{2} \left(\frac{\ln r - \ln r_g}{\ln \sigma_g} \right)^2 \right) \qquad \text{(Eq. 3.19)}$$

In the formula above N_0 is the number of particles per cubic centimeter, r_g is the median radius, and σ_g is the geometric standard deviation. For this analysis the fine mode is represented by a mode with $r_g = 0.65$ μm and $\sigma_g = 2$. The coarse mode is represented by a mode with $r_g = 1.5$ μm and $\sigma_g = 2$. These values are representative of a fine and coarse

mode as determined by dust lifting experiments [*Lafon and Sokolik*, in publication]. The limits of integration are selected such that any further expansion of the limits does not yield any significant change in the integrated value. The fine mode high spectral resolution extinction coefficients computed using Mie theory for the main dust aerosol components are presented in Figure 3.1.

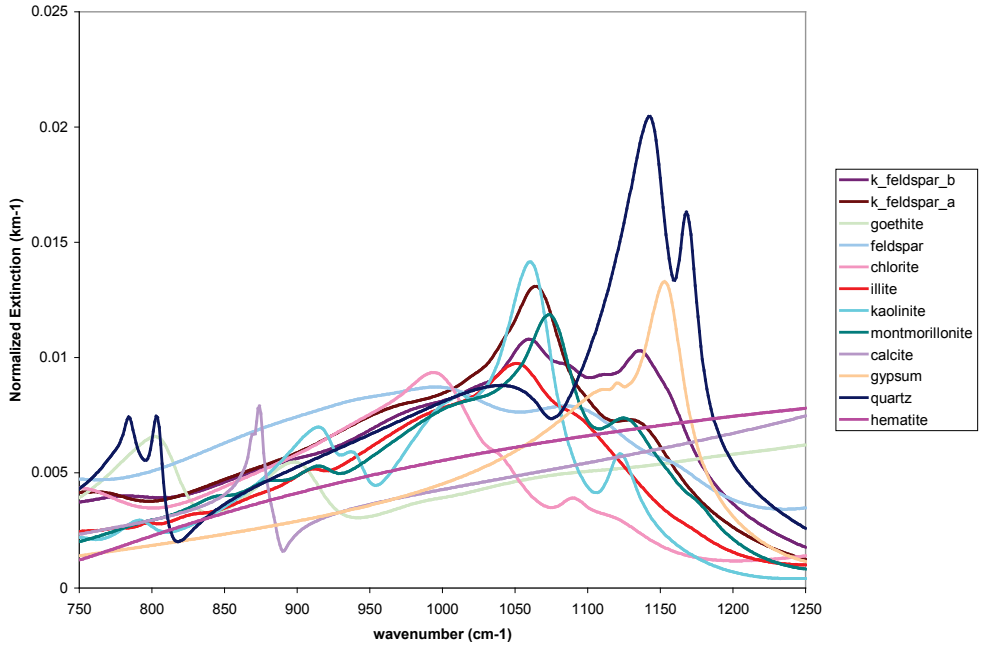

Figure 3.1. Fine mode normalized volume extinction coefficients for the main dust aerosol components computed using Mie theory.

The fine mode extinction spectra of the various minerals in Figure 3.1 exhibit significant differences at high spectral resolution. This indicates that all of them need to be considered when modeling a dust aerosol. A generic mineral-like/insoluble refractive index dataset or the refractive index of a single mineral is not sufficient at high spectral resolution to model regionally and/or temporally varying mineralogy. An examination of Figure 3.1 reveals that there is a general increase in the extinction spectra of the silicate

minerals from about 750 cm^{-1} to about 1000 cm^{-1} – 1050 cm^{-1}, and then a general decrease from about 1070 cm^{-1} to 1250 cm^{-1}, which reflects the dominant Si-O vibration related absorptions. This leads to the aptly named "v-shape" in brightness temperature that is often noted in high spectral resolution TIR measurements impacted by dust. The carbonate, sulfate, and iron oxide have a significantly different spectral behavior that reflects their non-silicate composition. The spectral distinctiveness of the mineral components implies that extinction spectrum of a mixture of them should exhibit evidence of the underlying composition. It is this distinctiveness that holds the promise of allowing for an aerosol's composition to be determined from high spectral resolution radiance measurements. The coarse mode high spectral resolution extinction coefficients computed using Mie theory for the main dust aerosol components are shown in Figure 3.2.

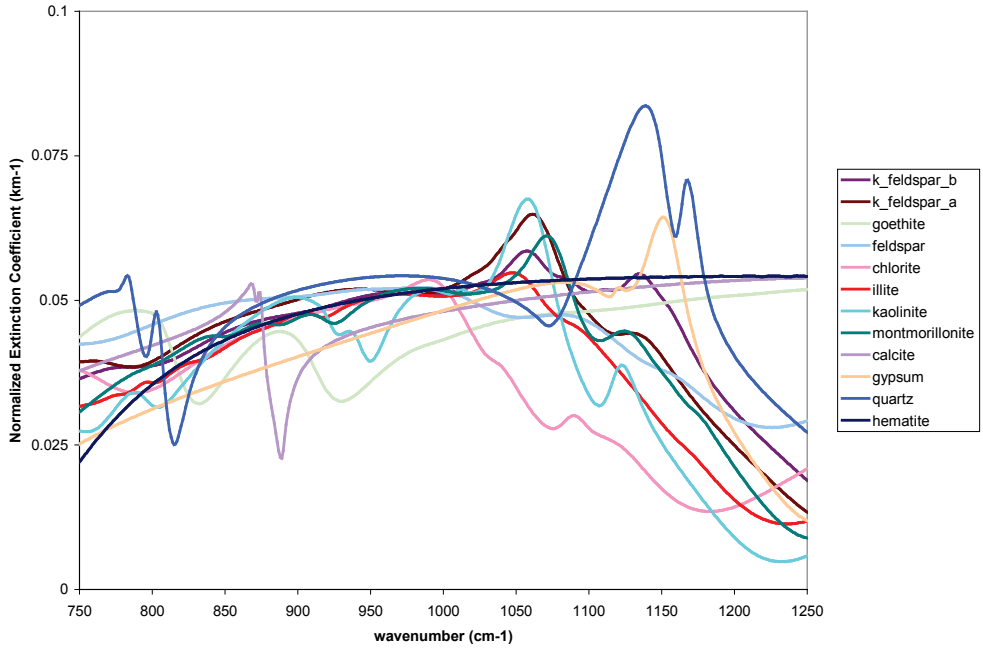

Figure 3.2. Coarse mode normalized volume extinction coefficients for the main dust aerosol components computed using Mie theory.

The coarse mode extinction spectra exhibit a very significant continuum-like extinction. The spectral features are less pronounced and the lower frequency spectral features are seen to be more distorted than the higher frequency features. The increasing continuum-like extinction with the increase in median radius going from fine to coarse mode would result in a more spectrally neutral blackbody-like appearance for any dust plume that had a significant fraction of coarse mode particles compared to a fine mode only dust plume. This reduction in spectral contrast of the extinction features would make it increasingly difficult to discern the composition of a mixed aerosol from high spectral resolution radiance measurements. We can therefore say that the smaller the median radius of a mode, the more spectral contrast there is, and subsequently the more likely it will be to retrieve information on the composition of a dust aerosol.

The calculations above demonstrate that spectral signatures of the extinction spectra of the major mineral components of a dust aerosol exhibit substantial differences between a fine mode and a coarse mode. The next question is how much does the spectral signature of a mineral change as a function of smaller changes in the median radius of a size mode and to changes in the limits of integration for a size mode. To examine the impact of a change in mode median radius of about plus or minus 20% we look at the extinction coefficient for a single mineral component, kaolinite, which has a particularly distinctive spectral signature. The fine mode volume optical properties were calculated for kaolinite with the median radius increased to 0.8 μm and decreased to 0.5 μm. The most apparent difference in the spectral signatures for a given mode as the median radius is changed is the change in magnitude. The spectral shapes remain very

similar. When the largest and smallest median radius spectra are plotted on different axes then the spectral feature differences become more apparent as is shown in Figure 3.3.

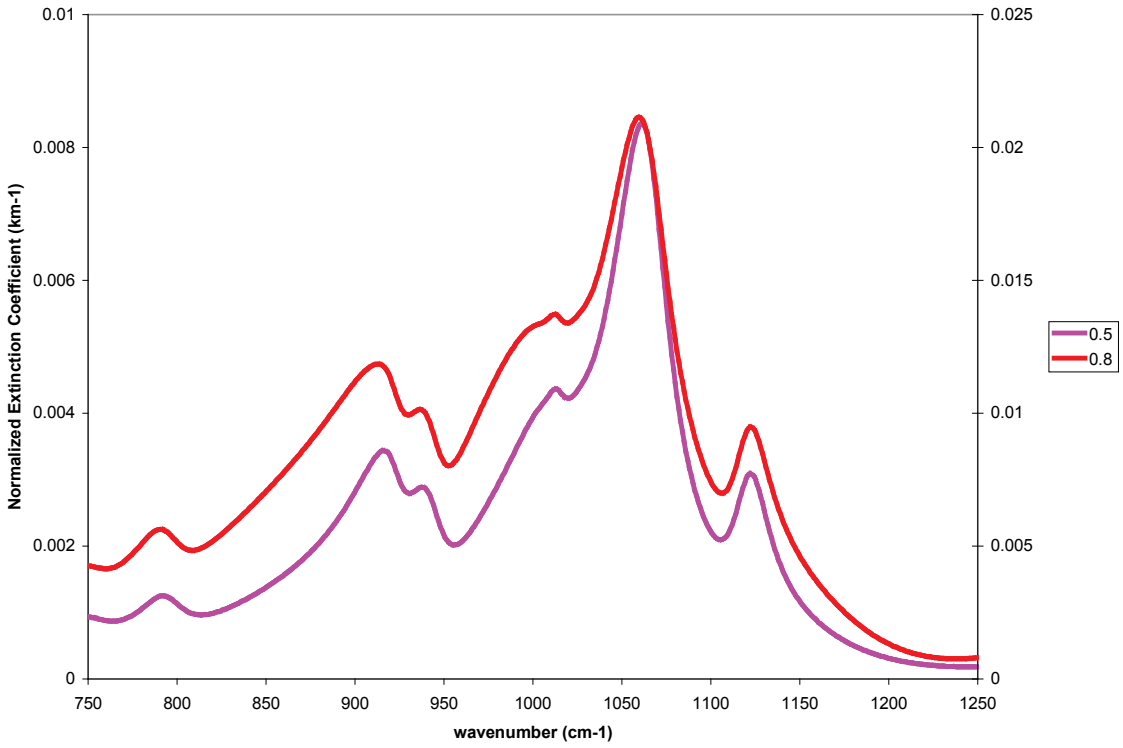

Figure 3.3. Spectral shape differences in the normalized volume extinction coefficients for a kaolinite fine mode with median radii of 0.5 and 0.8 μm.

Here we see that the spectral features become broader with increasing median radius. There are some small shifts in the positions of the spectral features, but not all of the spectral features are affected equally. There is a non-uniform continuum effect just as was seen in the differences between the fine and coarse modes. The increase in the continuum extinction is greater for lower frequencies than higher frequencies. There is also more distortion in the spectral features at mid to low frequencies than at higher frequencies. The same general effects are seen for variations of the median radius in the coarse mode. Figure 3.4 shows that as the largest and smallest median radii are plotted

on separate axes, we again see the same non-uniform behavior in continuum increase and spectral feature distortion that was evident for the fine mode in Figure 3.3. As an aerosol is transported over significant distances we can expect the median radius to change through gravitational settling and other deposition processes and the extinction signature will likely change in a non-uniform way that then needs to be properly modeled in order to accurately model the measured high spectral resolution radiance.

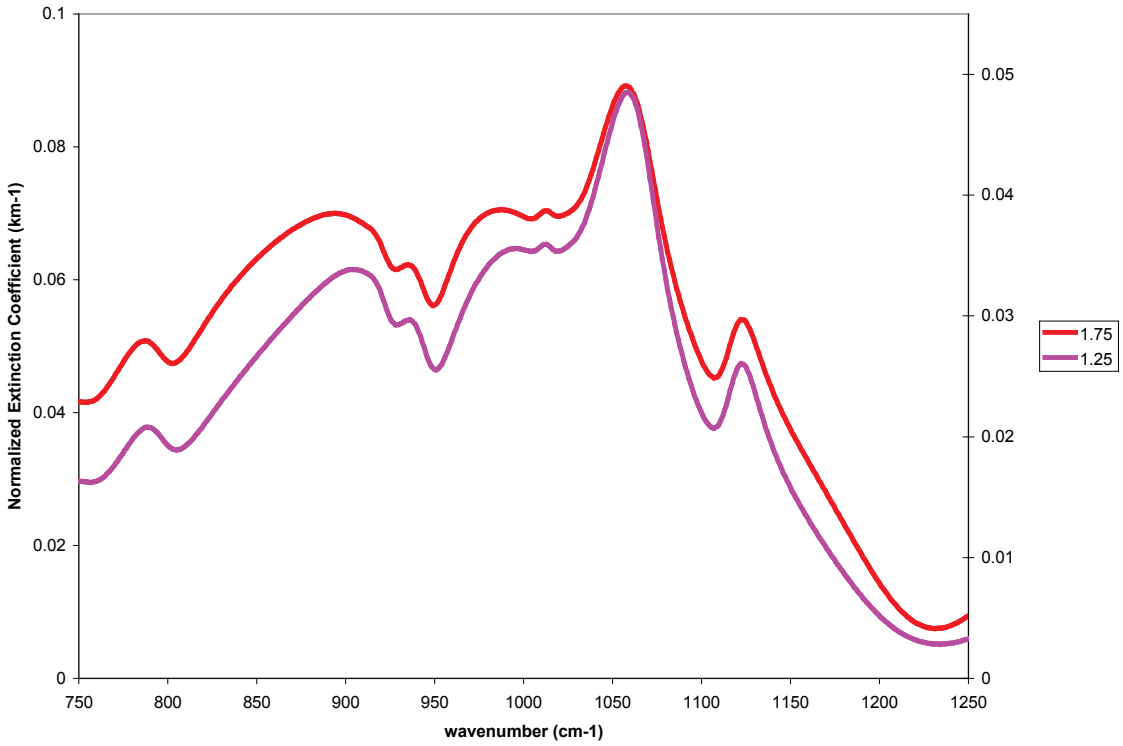

Figure 3.4. Spectral shape differences in the normalized volume extinction coefficients for a kaolinite coarse mode with median radii of 1.25 and 1.75 μm.

As the median radius of a size mode increases or decreases, the magnitude of the volume extinction coefficient will correspondingly increase or decrease as would be expected. The problem is that this variation would be difficult to distinguish from magnitude changes that occur with changes in particle concentration. But because the

spectral features become slightly more or less broad and a frequency dependent continuum change occurs, which would not occur with just a change in particle concentration, there is a possibility to distinguish changes in the median radius of a dust aerosol from particle concentration changes using high spectral resolution measured radiance.

For our modeling and analysis above, the limits of integration of the analytic size distribution were set such that an increase in the limits did not produce changes in the computed optical properties. In order to reach that condition, particles of improbably large and small size become included. Since an analytic representation of a size distribution is just a representation that fits well over some limited range of sizes, it is likely that a truncated integration over the analytical size distribution is more appropriate. To see how the volume optical properties depend on the limits of integration, the volume optical properties of kaolinite for the fine mode with r_g = 0.65 μm and σ_g = 2 were examined. We varied the limits of integration from effectively infinity to 3-sigma limits, i.e. $r_g \pm 3\ln\sigma_g$, to 2-sigma and then 1-sigma. The smallest range of integration that makes physical sense is approximately 2-sigma. If we plot the 2-sigma and the infinite range of integration on different axes, we see that the major difference is in the continuum, which is mostly due to the larger particles, as Figure 3.5 below demonstrates. The change in the continuum is similar to what occurs when the median radius of the size distribution changes, but the changes are not as great. The width of the spectral features does not change appreciably and the deformation of the spectral features is not as large as with changing median radius.

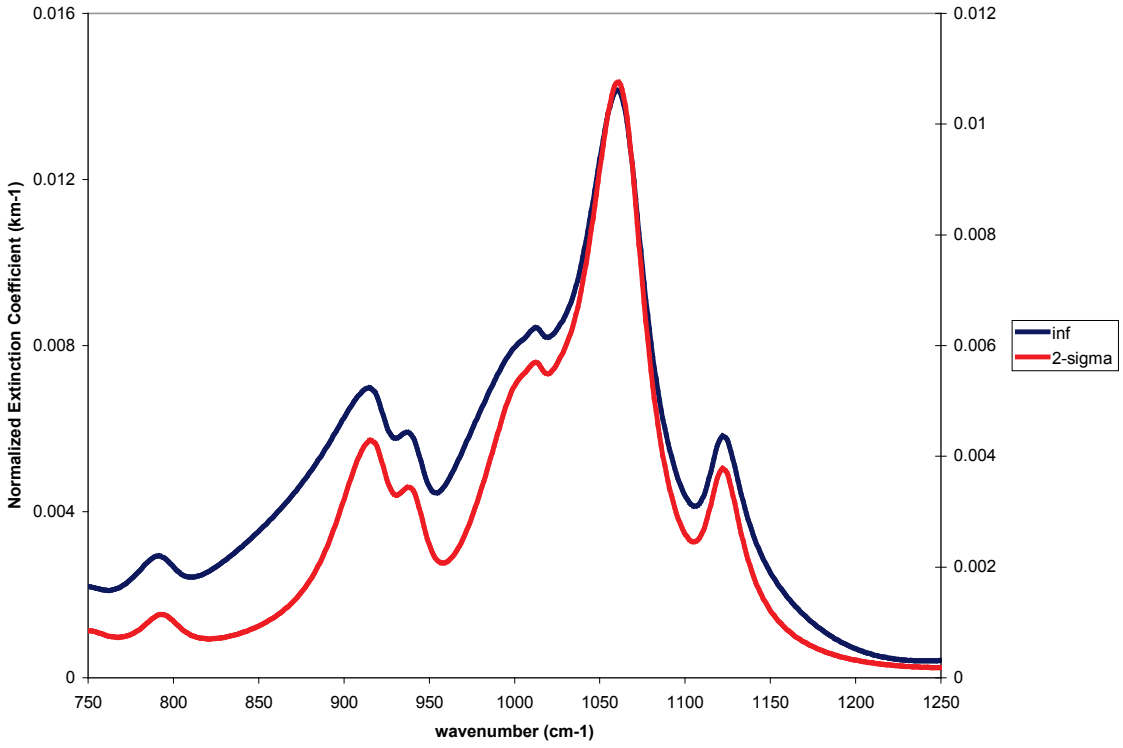

Figure 3.5. Spectral shape changes in the normalized volume extinction coefficients for a kaolinite fine mode (r_g = 0.65 μm and σ_g = 2) for limits of integration at infinity, and 2-sigma.

The above investigation shows that the spectral signatures of the volume optical properties of the mineral components of a dust aerosol are a complex function of many parameters. The possible variations of these parameters will make modeling of the dust aerosol quite a challenge even using a simple external mixture model. On the other hand an internally mixed dust model where some or all of the components are used in an EMA formula has an even greater level of complexity because the volume optical properties are now a nonlinear function of the components instead of just an additive function of the components. Complicating matters further for dust aerosol optical properties' modeling is the unresolved question of whether using Mie generated volume optical properties is a

sufficiently accurate. To investigate the magnitude of the effect of modeling dust particles as non-spherical particles, two of the most common non-spherical techniques have been implemented. These techniques are used to model a number of common dust aerosol components for which simultaneous laboratory measurements of both TIR extinction and size distribution have been recently reported. The results obtained here using these techniques are compared to those laboratory measurements and to each other and Mie results.

3.3.2 Investigating Approaches to Addressing Non-Sphericity: T-matrix and CDE

It has long been known that treating irregularly-shaped strongly absorbing particles as spheres in order to use Mie theory to calculate optical properties can lead to substantial errors in the computed properties [*Bohren and Huffman*, 1983]. This is primarily due to the occurrence of resonance modes in spherical particles, known as surface modes or Fröhlich modes [*Bohren and Huffman*, 1983], which either are not present or are significantly reduced and/or shifted and broadened in irregularly-shaped particles like naturally occurring mineral dust particles. One of the prime examples is crystalline quartz particles. Numerous measurements of crystalline quartz particles in both a potassium bromide medium (KBr) and in-air have shown that Mie theory and the simplification of spherical particles does not reproduce the measurements well [*Bohren and Huffman*, 1983; *Hudson et al.*, 2008b]. These findings have held for both supermicron and submicron particles.

Recently simultaneous laboratory measurements of in-air TIR extinction and size distributions have been made for a number of other mineral dust species with strong

sharp absorbing features (calcite, dolomite, illite, kaolinite, and montmorillonite) [*Hudson et al.*, 2008a, b]. These measurements have shown that the extinction spectra for these minerals are also not well modeled by Mie theory. The extinction peaks are shifted from what is predicted by Mie theory. For extinction coefficients with strong sharp features, a frequency shift for those features on the order of half or more of the spectral width of the feature will result in a complete mismatch between modeled results and measured results. Given the above reported findings it would appear that high spectral resolution volume optical properties, for many if not all of the mineral components, calculated using Mie theory are not likely to be accurate enough for our high spectral resolution radiance modeling. Therefore two techniques that have commonly been used to model non-spherical particles are investigated.

Two of the most common techniques that are used to model the optical properties of non-spherical particles are the T-matrix and CDE techniques. Another very common technique is DDA but it is extremely computationally intensive and requires precise knowledge of the shape of a particle and is applicable only over a certain range of size parameters. The T-matrix method is a powerful technique that provides a numerical solution of Maxwell's equations for a variety of non-spherical shapes. Implementations of the T-matrix technique are readily available that solve Maxwell's equations for polydisperse, randomly oriented, rotationally symmetric particles, e.g. spheroids, finite circular cylinders and even-order Chebyshev particles. The CDE technique is derived in the Rayleigh regime where the characteristic size of the particle is very much less than the wavelength of radiation. In the CDE technique the particles are randomly oriented ellipsoids and all possible ellipsoidal shapes occur with equal probability.

We begin our investigation by applying the T-matrix method to quartz. Because of the very large refractive index values for quartz in the 1060 cm^{-1} to 1170 cm^{-1} region, convergence of the T-matrix code for size modes with median radius greater than about 0.5 μm is an issue. As a first examination of the results of T-matrix modeling and also to compare these results to the recently reported measurement data [*Hudson et al.*, 2008b], we decided to model quartz particles with a lognormal size distribution with r_g = 0.2 μm. This is an approximation to the measured size distribution in the report, but it allows us to make a qualitative comparison. To span the reasonable shape factors and to support a comparison with CDE results, the range of shape factors of the spheroids used in our modeling ranged from 2/1 to 6/1 in steps of 1 for the oblate spheroids and from 1/2 to 1/6 also insteps of 1 for the prolate spheroids. The radius of the particles was chosen to be specified as the surface-equivalent-sphere radius. The results of the T-matrix calculations and the Mie theory results are shown in Figure 3.6.

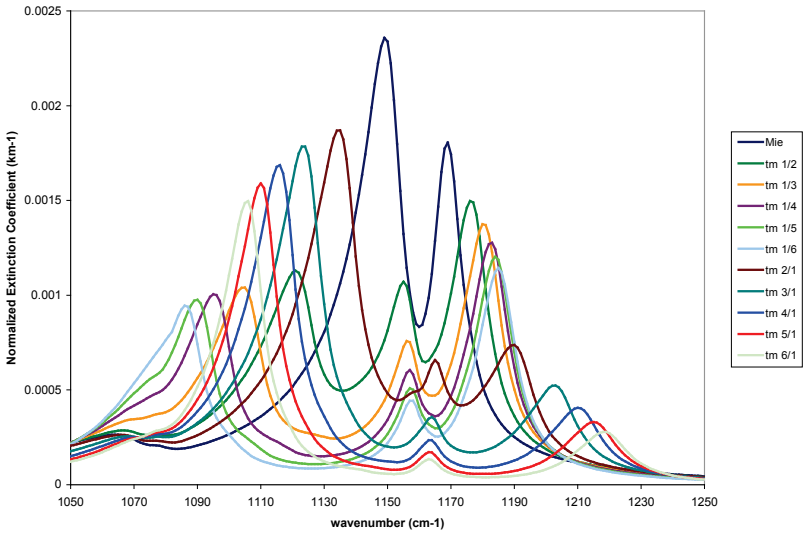

Figure 3.6. Normalized volume extinction coefficients for a Quartz fine mode (r_g = 0.2 μm and σ_g = 2) computed using Mie theory and computed using T-matrix for a variety of shape factors from 6/1 to 2/1 for oblate spheroids and 1/6 to 1/2 for prolate spheroids.

The spectral signature of quartz particles changes dramatically as a function of shape factor. For both oblate and prolate spheroids there are 3 extinction peaks in the 1050 cm^{-1} to 1250 cm^{-1} spectral region, whereas with Mie theory there are only 2 extinction peaks. The main characteristic extinction peaks that are seen in transmission measurements of powdered quartz, usually in a KBr matrix, are at ~1084 cm^{-1} and 1172 cm^{-1} with a small peak at 1150 cm^{-1} that may be observed. *Hudson et al*. [2008b] reported two main extinction peaks in this region, 1109 cm^{-1} and 1164 cm^{-1} in their in-air extinction measurements. It is interesting to note that only the oblate particles with a shape factor of 5/1 have peaks that correspond to what was measured for particles of approximately the same size distribution. The third peak in the 5/1 shape factor spectrum at 1215 cm^{-1} does not correspond to anything in the extinction spectrum measured by *Hudson et al*. or in any of the transmission measurements for powdered quartz.

In the rest of the TIR window region the differences between the Mie and T-matrix extinction spectra are not very large. There are small shifts and small magnitude changes in the spectral features in the 780 – 800 cm^{-1} region, but nothing nearly as dramatic as for the spectral features in the 1050 cm^{-1} to 1250 cm^{-1} region. Although the two major extinction peaks in 1050 cm^{-1} to 1250 cm^{-1} region as measured by *Hudson et al*. are matched well by the 5/1 shape factor, the width of the spectral features is not well reproduced for the 1109 cm^{-1} feature by the 5/1 shape factor for this size distribution. Both Mie and T-matrix produce spectral features that are much narrower than what is reported by *Hudson et al*. and by the transmission measurements of others including

Bohren and Huffman. The T-matrix results are shown in Figure 3.7 in comparison to the spectral extinction reported by *Hudson et al*. [2008b].

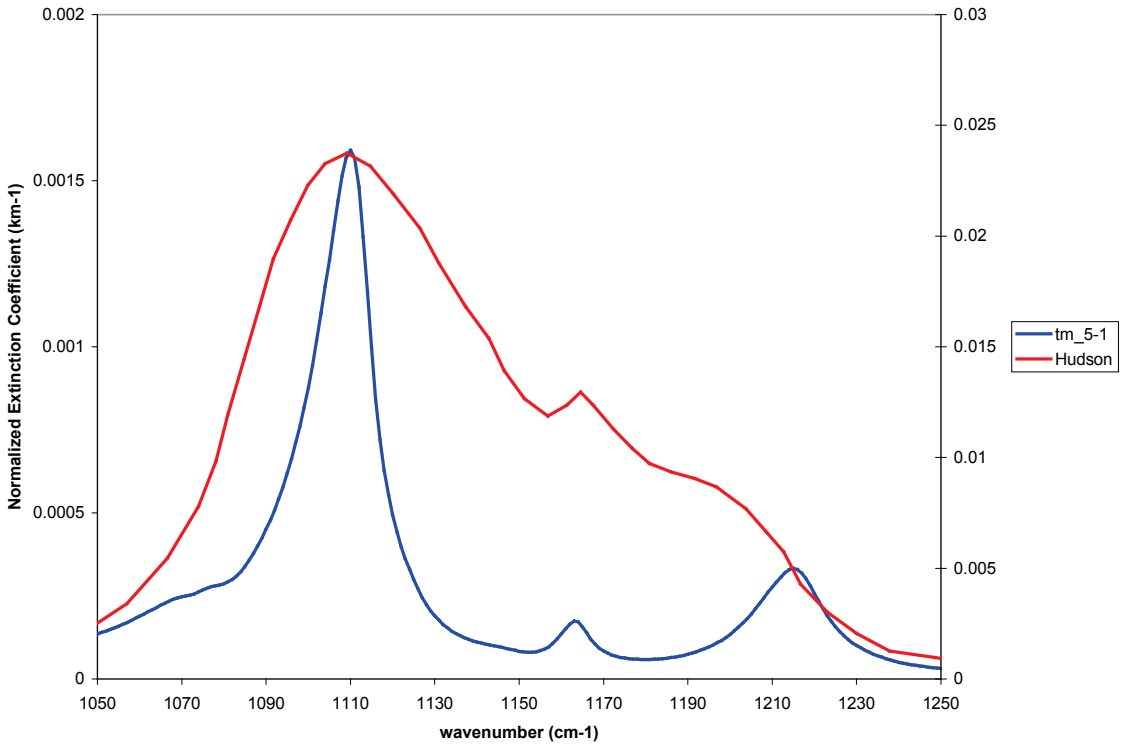

Figure 3.7. Normalized volume extinction coefficients for a Quartz fine mode (r_g = 0.2 μm and σ_g = 2) computed using T-matrix for a shape factor of 5/1 representing an oblate spheroid and the reported extinction measurements of *Hudson et al*. [2008b].

A much better fit is obtained if all of the extinction spectra for the oblate particles, i.e. 2/1 through 6/1, are averaged together with the Mie extinction spectrum. The results of this averaging, a pseudo-CDE, are seen in Figure 3.8. It also appears that the extinction spectrum shape of naturally occurring crystalline quartz particles as seen in numerous transmission measurements are fit better by a distribution of oblate spheroids as is seen here.

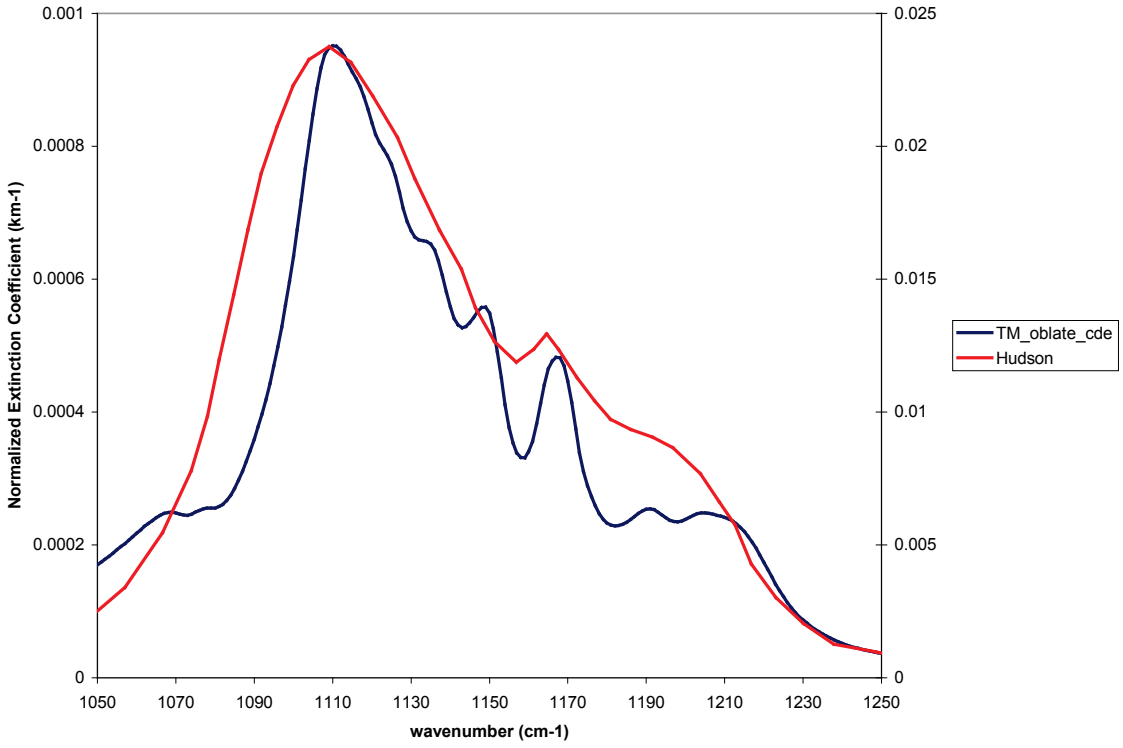

Figure 3.8. Normalized volume extinction coefficients for a Quartz fine mode (r_g = 0.2 μm and σ_g = 2) computed using an average of T-matrix calculations for oblate spheroids of shape factors from 6/1 to 2/1 together with the Mie extinction coefficients, and the reported extinction measurements of *Hudson et al*. [2008b].

To summarize, Mie theory is well known be unable to accurately model crystalline quartz particles because the irregularly-shaped natural particles do not support the specific resonant surface modes that would occur in spherical particles. Based on the laboratory measurements of quartz particles in-air measured by *Hudson et al*., it appears that oblate spheroids with a shape factor of 5/1 have spectral features in the same locations as those measured for an approximately equivalent size distribution, although the widths of the features are too narrow. A better fit is obtained with a distribution of oblate spheroids. To see how non-spherical particle modeling may improve modeling accuracy for other minerals, T-matrix calculations were done for three clay minerals,

illite and kaolinite and montmorillonite, for which *Hudson et al*. [2008a] also made extinction measurements in-air.

In their first paper on coupled IR extinction and size distribution measurements, *Hudson et al*. [2008a] reported that for the most common clay minerals Mie theory did not accurately predict the spectral extinction features. We made T-matrix calculations for the same three minerals studied in that paper to examine whether T-matrix modeling using optical properties for oblate spheroids provides a better result. These common clay minerals are also needed to model the dust event studied in the Chapter 4. For T-matrix calculations, the change in position of spectral extinction features is much less a function of median radius than it is of shape factor and therefore we do not try to exactly match their reported size distribution. The size distributions used for the above minerals have all been approximated with a lognormal size distribution with r_g = 0.2 μm as was done with the quartz modeling. Our objective is to determine whether T-matrix modeling is preferable to Mie by a qualitative comparison to measured data. As before, T-matrix was run with the size of the particles specified in terms of the surface-area-equivalent sphere for shape factors from 2/1 to 5/1 in steps of 1. Surprisingly the best fit was again obtained for a shape factor of 5 for all cases as the following figures illustrate. The Figures 3.9 and 3.10 show the shifting to lower frequency of the main extinction peak for illite, and the fit to the measured data.

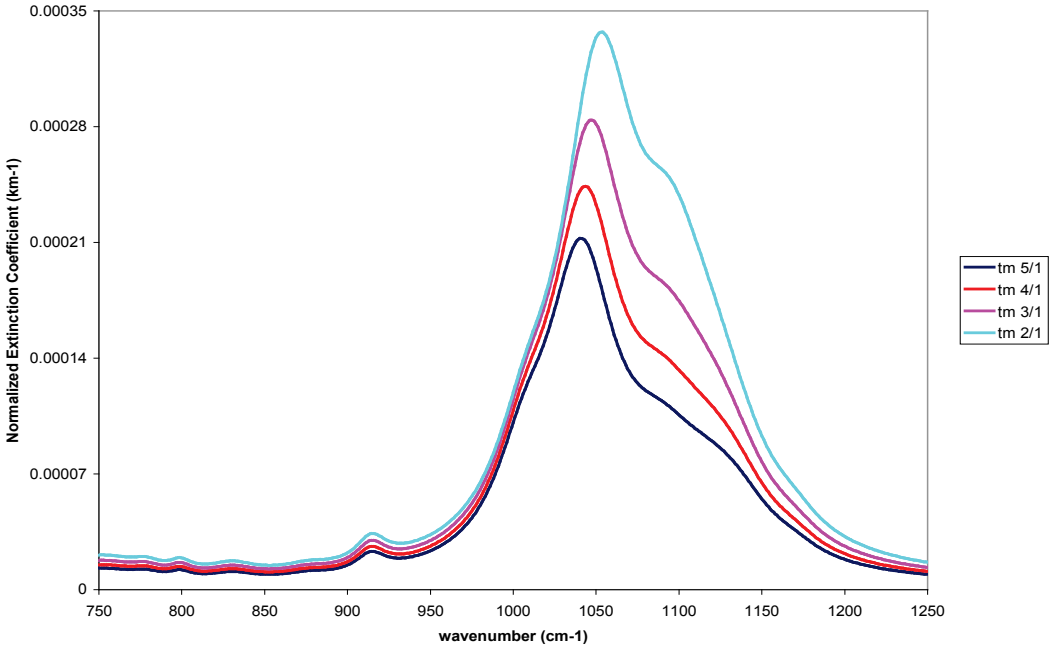

Figure 3.9. Normalized volume extinction coefficients for an illite very fine mode (r_g = 0.2 μm and σ_g = 2) computed using T-matrix calculations for oblate spheroids of shape factors from 5/1 to 2/1.

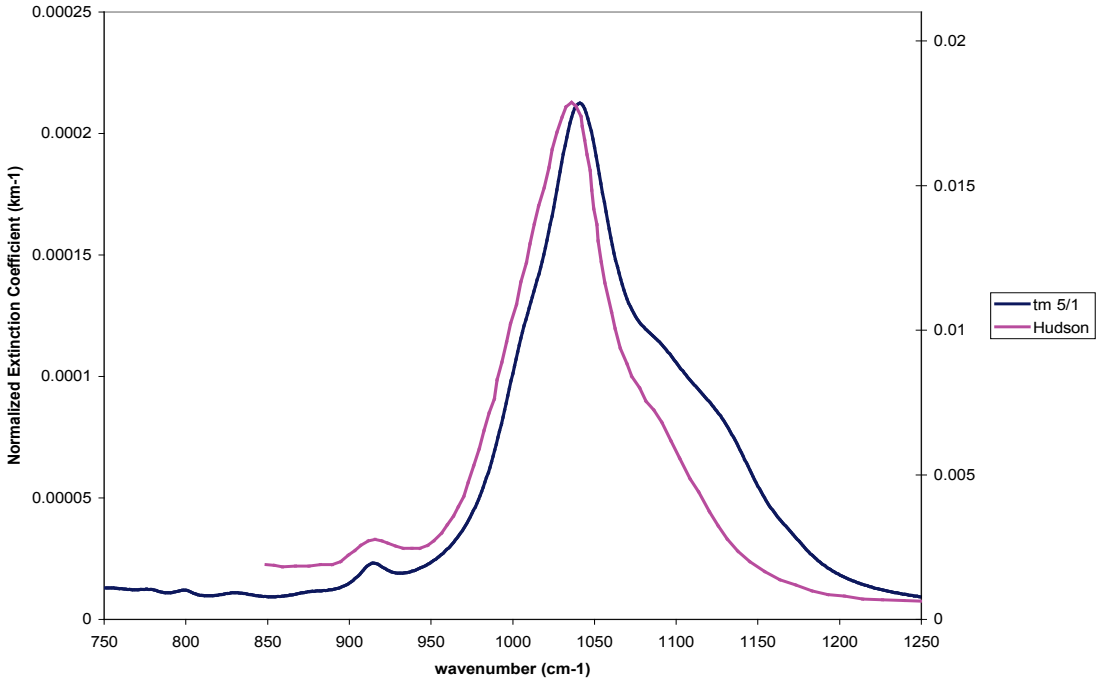

Figure 3.10. Normalized volume extinction coefficients for an illite very fine mode (r_g = 0.2 μm and σ_g = 2) computed using T-matrix calculations for oblate spheroids of shape factor 5/1 together with the extinction spectra measured by *Hudson et al*. [2008a].

Based on these results, it appears that a somewhat smaller size distribution would provide a slightly better fit, but a shape factor of 4 to 5 would still be required to fit the spectral position and shape. It may be, as was the case for quartz, that a continuous distribution of oblate spheroids over a sufficient range of shape factors would provide an even better fit. Compared to the measured observations of *Hudson et al*. [2008a] the above spectral fits for spheroids with shape factor 5 are much better than the Mie or even the disk-shaped particle solutions they reported [*Hudson et al.*, 2008a].

The second and last method to address non-sphericity investigated is the CDE technique. The formula for CDE including scattering, as explained in Appendix B, was implemented for the clay minerals above and for quartz. Figure 3.11 shows the comparison between CDE and the extinction measurements for illite as reported by *Hudson et al*. [2008a]. None of the CDE cases provide a spectral fit that is as good as the T-matrix calculations with a shape factor of 5.

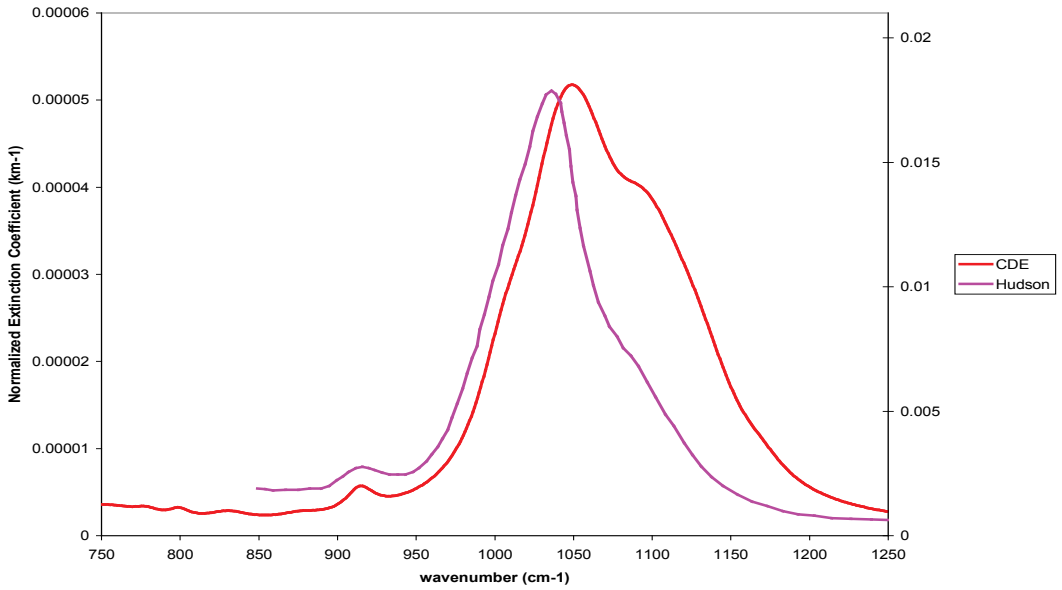

Figure 3.11. Normalized volume extinction coefficients for illite (r_g = 0.2 μm and σ_g = 2) computed using the CDE technique together with the extinction spectra measured by *Hudson et al*. [2008a].

Based on this comparative analysis between reported extinction measurements for pure mineral species in the TIR window region and the spectral volume optical properties for those species modeled using Mie theory and two non-spherical particle techniques, T-matrix and CDE, it appears that T-matrix calculations with a shape factor of 5 give the best fits to the measured extinction spectra for all of these mineral species. In the case of quartz, a shape factor of 5 results in the main extinction peaks being located in the correct position; however, a continuous distribution of oblate spheroids appears to provide the overall best fit. In Chapter 4, we model the spectral signatures of actual dust plumes and re-examine which of these techniques provide the best fit. Our results here confirm that CDE is not likely to be useful for tropospheric dust aerosols. This is a consequence of CDE having been derived in the Rayleigh limit, which results in no continuum extinction outside the main absorbing regions and therefore makes it unable to model particles of the size common in the troposphere.

3.4 Investigating Mixture Approach Effects on Multi-component Dust Aerosol

In this section we examine the TIR spectral signature of tropospheric dust aerosol composed of multiple components under the assumptions of external and internal mixtures. The components and their amounts are based on regional size-resolved mineralogical models developed by *Lafon and Sokolik* [in publication]. The spectral signatures for these models are examined in terms of their dependencies on level of fidelity of the components as well as the amount of fine mode and coarse mode particles, which has a bearing on modeling dust plumes as a function of distance from the source. Finally a comparison is made to two models based on bulk material optical constants

measurements: Volz optical constants data for Saharan dust [*Volz*, 1973] and Sokolik optical constants for Afghan dust [*Sokolik et al.*, 1993]. These are then be compared to an internal mixture of the components using a simple compositionally averaged refractive index.

3.4.1 Optical Signatures of Mineral External Mixtures as Regional Dust Analogs

To see how the extinction coefficient varies as a function of compositional, the size-resolved mineralogical dust aerosol model developed by *Lafon and Sokolik* [in publication] are examined in terms of the spectral difference between a model that has high mineralogical fidelity and one that retains only the major mineralogical components for each size mode. Based on dust lifting experiments and size-resolved mineralogical compositional analysis, *Lafon and Sokolik* came up with different levels of compositional fidelity for modeling the measured dust aerosols for Niger and China. The most detailed model is referred to as Level 1. Levels 2 and 3 are increasingly simplified mineralogical dust models. For this investigation the spectral signatures of the Niger Level 2 and Level 3 models are examined. Using the Mie generated volume optical properties for the size distribution parameters specified in the Niger model implemented as an external mixture, we obtain the following volume extinction coefficients shown in Figure 3.12.

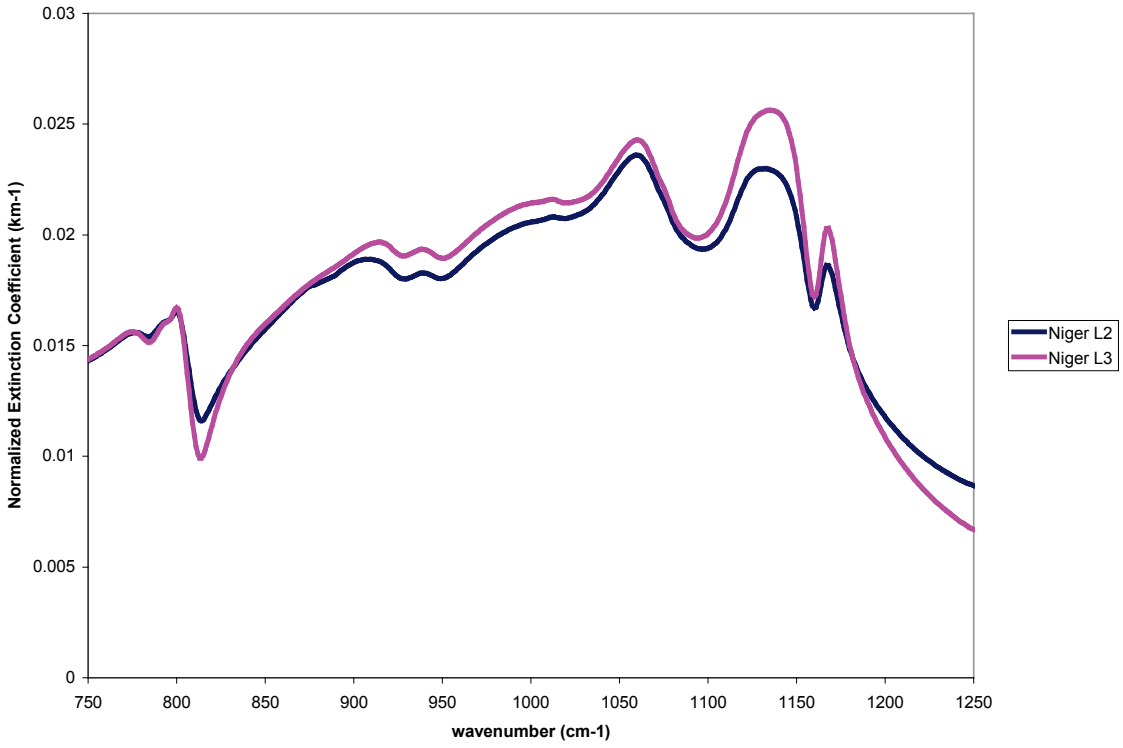

Figure 3.12. Normalized volume extinction coefficients for the Niger size-resolved aerosol model with complexity Levels 2 and 3.

In terms of the position of spectral features in the signature there is no major difference between the Level 2 and Level 3 optical properties. The most significant difference is in the magnitude of the quartz features. The simpler Level 3 model has a larger fractional amount of quartz relative to the other components remaining in the model as it is simplified from the Level 2 composition. This indicates that a more complex model does not translate into significant spectral differences, which would lead to detectable variations in a measured radiance spectrum. This means that only the major components of a dust aerosol need to be retained to achieve accurate modeling results. The above results are dominated by the coarse particles since their optical properties are so much larger in magnitude than those of the fine mode components. As a dust plume is

transported, the ratio of fine mode particles to coarse mode particles changes due to preferential removal of the larger coarse mode particles. Therefore we need to also compare the Level 2 model to the Level 3 model when the fine mode dominates. We did this by computing the extinction coefficient for the case where the coarse mode particle number density is only 1% of the total particle number density. Doing so, we obtain the results shown in Figure 3.13.

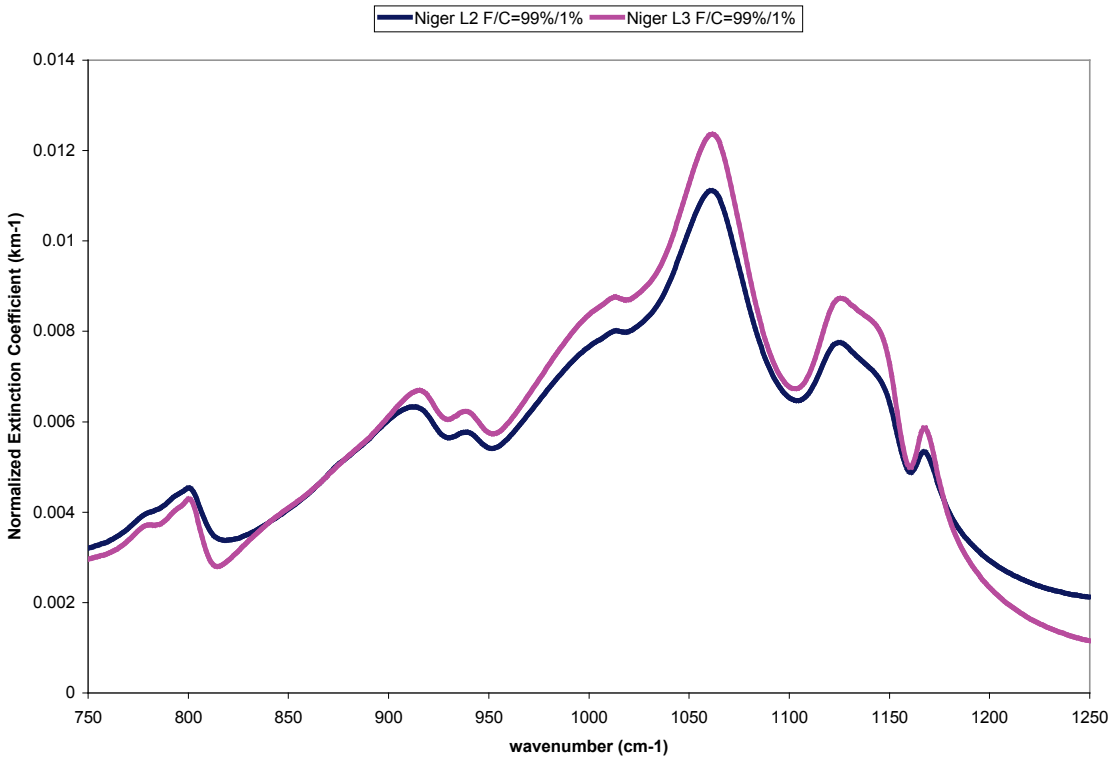

Figure 3.13. Normalized volume extinction coefficients for the Niger size-resolved aerosol model with complexity Levels 2 and 3 for fine to coarse mode concentration ratio of 99% to 1%.

As before, the spectral difference between the models is essentially negligible. Our findings indicate that, regardless of which mode dominates a very high level of

compositional fidelity is not needed to capture the major spectral features of the multi-component dust aerosol in an external mixture. However, as the ratio of fine to coarse mode particles changes during transport important spectral differences appear as seen in Figure 3.14. This figure shows the Niger Level 3 model for a fine to coarse particle number ratio of 70/30 and 99/1 and demonstrates the importance of accurately modeling size-resolved mineralogy when it occurs.

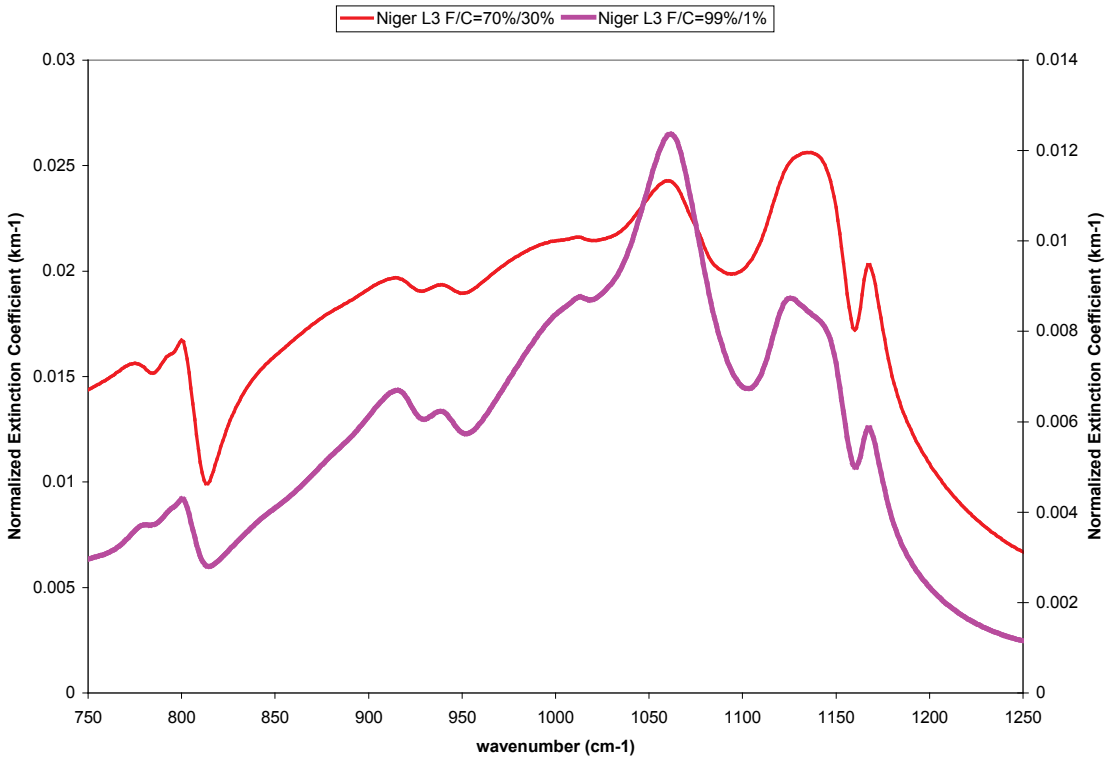

Figure 3.14. Normalized volume extinction coefficients for the complexity Level 3 Niger size-resolved aerosol model for fine to coarse mode concentration ratios of 99% to 1% and 70% to 30%.

We have seen that the spectral signature of a dust aerosol depends significantly on the shape assumption used for the particles. It also depends on the parameters of the size

mode, the limits of integration used, and the size dependent composition. Before investing significant effort in developing size-resolved mineralogical models of aerosols we need to examine the differences between regional models created using bulk dust refractive index data from those regions and regional models using size-resolved mineralogical data. To do so we examine the differences between the Niger model and the China model developed by *Lafon and Sokolik* and dust aerosol volume optical properties generated using bulk material optical constants from Saharan dust and Afghan dust. The results are shown in Figure 3.15.

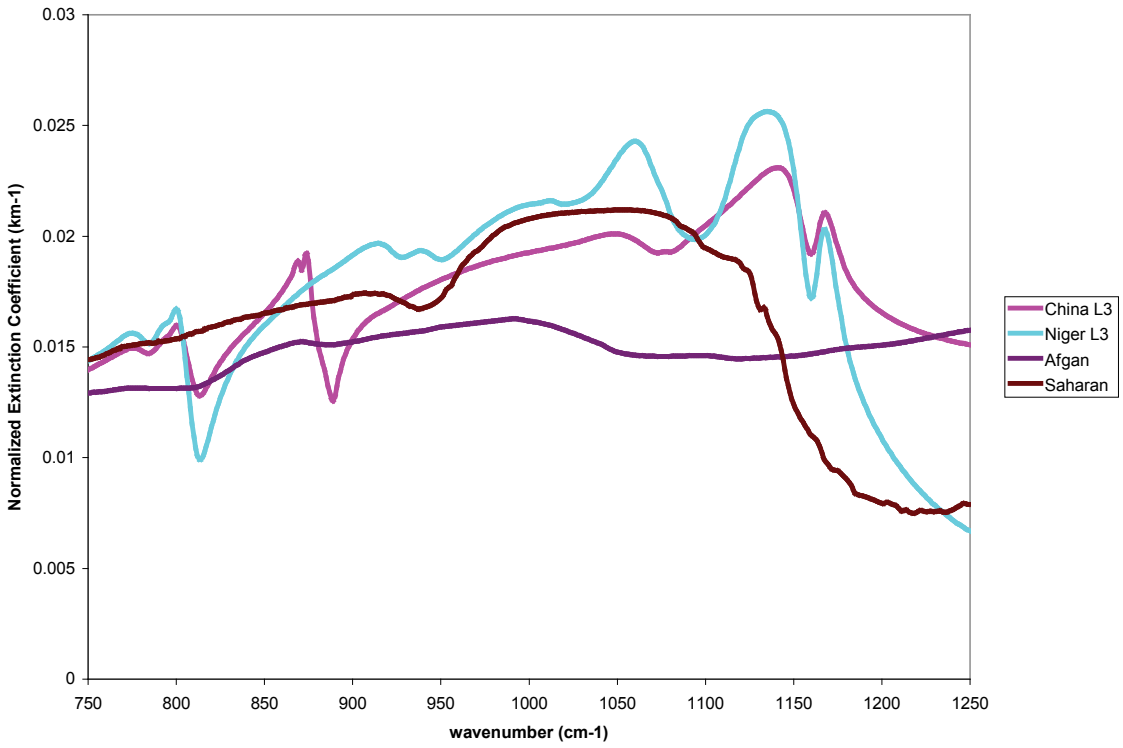

Figure 3.15. Normalized volume extinction coefficients for the complexity Level 3 Niger and China size-resolved aerosol models, and the bulk material derived optical constants models for Saharan and Afghan dust.

These extinction spectra were generated for a dust aerosol composed of a coarse and fine mode with a fine to coarse particle number ratio of 70/30 and the size distribution parameters for these models as given above. There are clearly significant spectral differences in the extinction spectra for these models. The radiance modeled using these optical properties would also show significant and detectable spectral differences. This means that it should be readily evident in high spectral resolution TIR radiance measurements whether size-resolved mineralogy-based regional models are needed to model dust aerosol or whether bulk sample derived optical constants are sufficient to model dust aerosol.

3.4.2 Optical Signatures of Mineral Internal Mixtures as Regional Dust Analogs

It is unclear whether using an EMA to formulate an internal mixture for a dust aerosol is appropriate. Applying an EMA to particles within a given size mode for a dust aerosol requires assuming that all particles within the size mode contain the same fractional amounts of mineral components. It is highly unlikely that dust particles come together in internally mixed particles in proportion to their amount in the dust plume. Also the assumptions used to derive most of the EMA formulae are not strictly valid for discrete particles of differing mineralogy adhering to each other and creating an "internally mixed" particle. To investigate what differences, if any, appear in the spectral signature of a dust aerosol if it is modeled as an internal mixture instead of an external mixture, the Niger Level 3 aerosol model is calculated using an "averaged" refractive index EMA. Each of the two size modes for the Niger Level 3 model is computed with Mie theory using a refractive index for the "internally mixed" particles that is based on a

particle-number-fraction-average of the mineral components in the model. The fine and coarse mode optical properties are then combined as an external mixture of the two "internally mixed" modes using the 70% fine mode particles and 30% coarse mode particles ratio of fine to coarse. Figure 3.16 compares the resulting internal mixture extinction coefficient to the extinction coefficient for the original external mixture model. Figure 3.17 compares the internal to external mixture results for a 99% fine mode particles and 1% coarse mode particles ratio of fine to coarse.

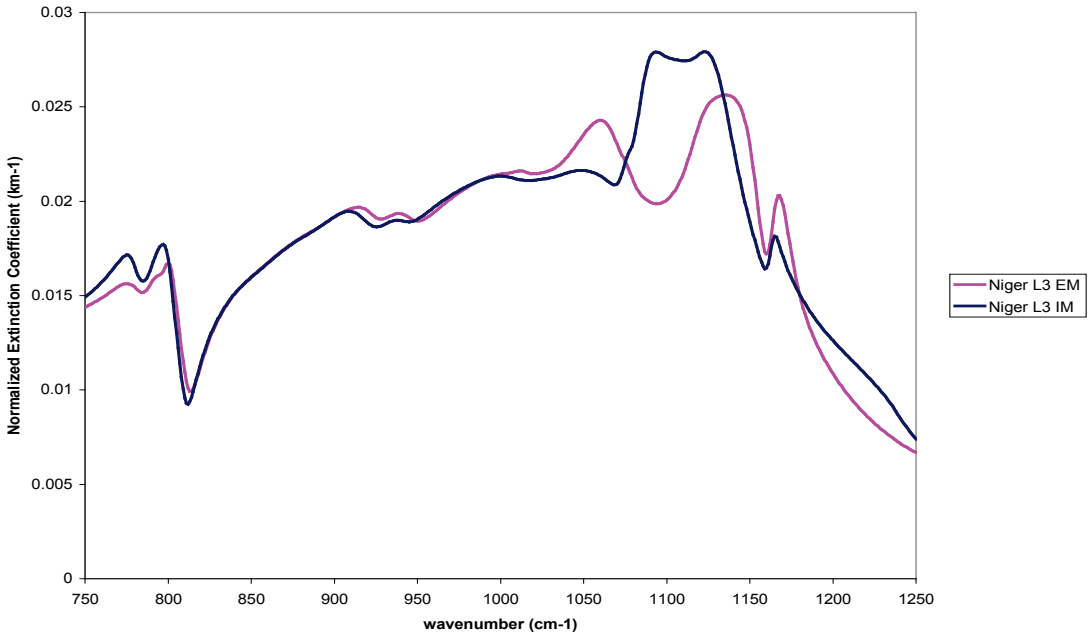

Figure 3.16. Normalized volume extinction coefficients for a Niger Level 3 size-resolved aerosol model as an internal and external mixture.

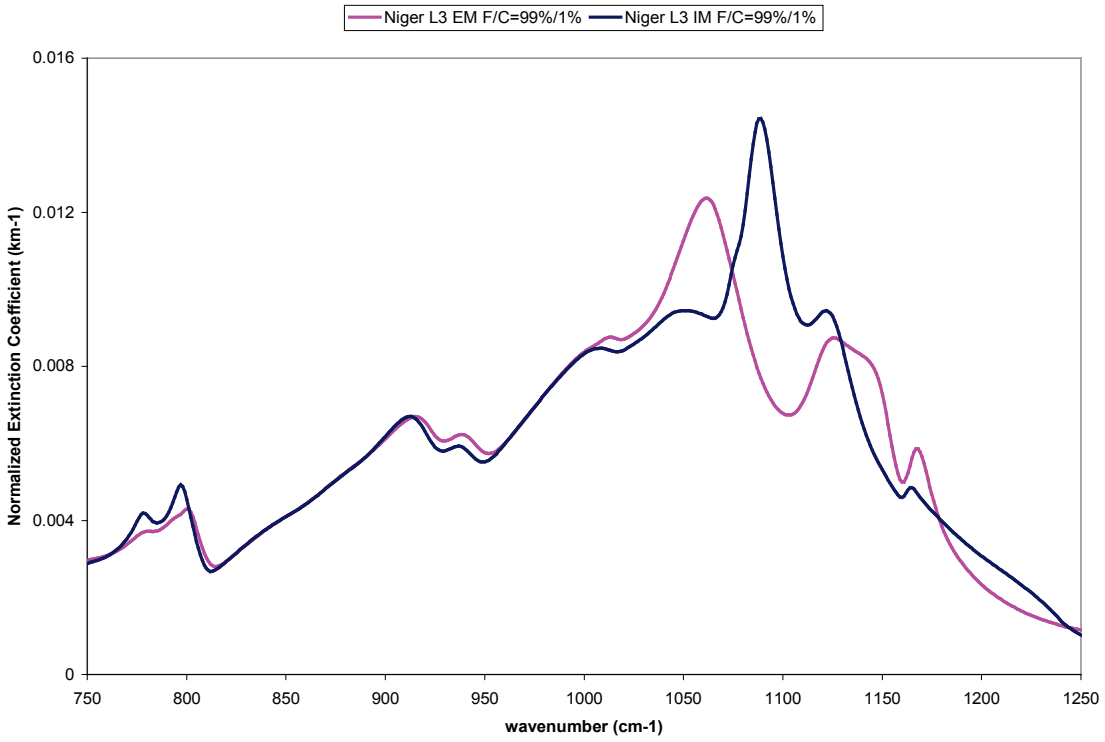

Figure 3.17. Normalized volume extinction coefficients for a Niger Level 3 size-resolved aerosol model as an internal and external mixture with a fine to coarse number density ratio of 99% to 1%.

As these figures illustrate, there are spectrally significant differences between the optical properties calculated using an internal mixture approach and those properties calculated using an external mixture approach. However, the significant spectral differences are isolated to the region where quartz is absorbing very strongly. Outside of this region the differences are rather minor and not likely to be detectable in the measured radiance given the other model variables and their uncertainties. For a dust aerosol having a large quartz fraction, as in the Niger model, a high spectral resolution radiance measurement would confirm immediately whether an internal or an external mixture is the most valid approach. Conversely, a dust aerosol having low concentrations of very

strongly absorbing materials, specifically quartz, would not exhibit much spectral differences and either external or internal mixtures could be used.

This, of course, presupposes that Mie theory is the correct way to compute the optical properties. If other techniques like T-matrix also show the same differentiation between the optical properties of an internal mixture and those of an external mixture, then we can safely say that whichever mixture model best matches measured high spectral resolution radiance is the best model to use. To examine this, we ran the same case using T-matrix to calculate the optical properties from the refractive index data of the internal mixture. Since the extremely large optical constants for quartz pose a convergence problem for the T-matrix method for the coarse size mode, our test of the sensitivity of the optical properties computed by T-matrix to internal or external mixtures is only conducted for the fine mode. The results for the fine mode should hold for the coarse mode as was the case with Mie theory. Since the fine mode is the predominant mode for long-range transport, these results are useful even if there were a difference with the coarse mode. The results of computing the Niger Level 3 fine mode using T-matrix with an internal mixture of the components and with an external mixture of the components are shown in Figure 3.18.

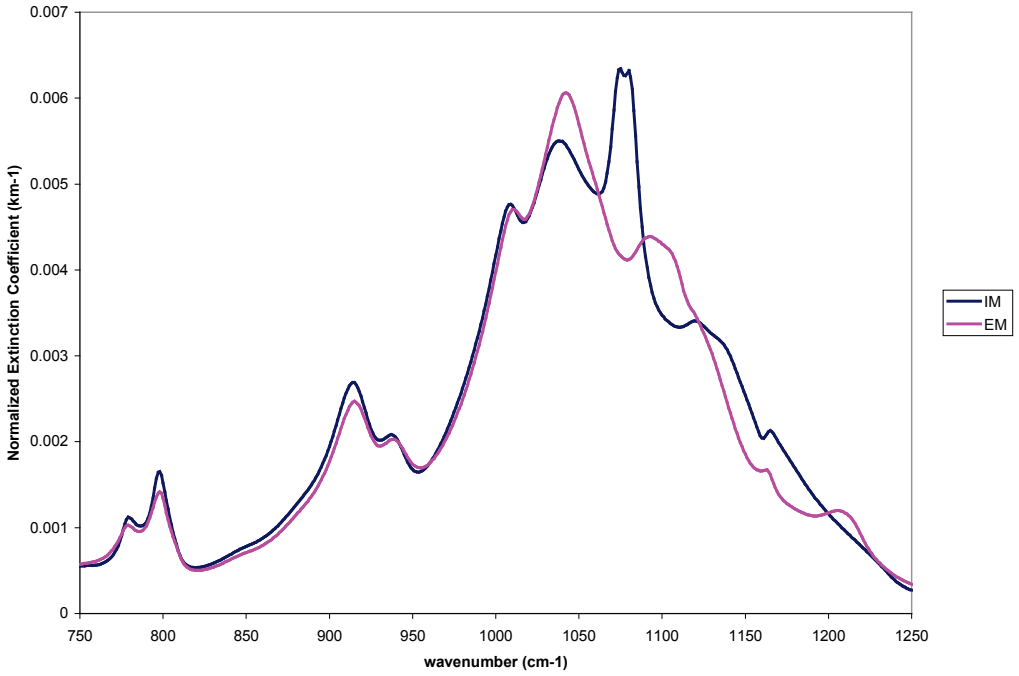

Figure 3.18. Normalized volume extinction coefficients for the fine mode of the Niger Level 3 size-resolved aerosol model as an internal and external mixture.

As with Mie theory the spectral differences are significant in the region of large quartz absorption, but small outside that region. Even for non-spherical techniques, the differences between an internal and external mixture will be minor in the absence of significant amounts of very strongly absorbing material. We now want to examine the behavior of internal mixing rules for truly intimate mixtures, specifically the aqueous solutions using the data derived in Chapter 2.

3.5 Examination of Multi-component Aqueous Mixtures

The extent that the choice of mixing rule and/or mixing components affects the resulting high spectral resolution IR optical constants of an internal mixture has not been fully evaluated. Prior studies of mixing rules for optical constants have typically been

focused on the real part n of the refractive index of colorless liquids in the visible where absorption, and therefore the imaginary part k of the refractive index is approximately zero (e.g., [*Methra*, 2003]). Other studies using mixtures where one of the components has non-negligible absorption focus only on a single wavelength (e.g., [*Lesins et al*., 2002; *Erlick*, 2006]) and only examine the sensitivity of the resulting optical constants to the choice of a mixing rule, but not to measurement data of a known mixture. The lack of measured spectral optical constants for mixtures has hampered the ability to examine the mixing rules in a spectral context. In their study of internally and externally mixed aerosols and the effect on aerosol optical properties, *Lesins et al.* [2002] state that for a homogenous mixture such as a mixture of solutions, a volume-weighted average of the component optical constants should be used. They also state that the Maxwell-Garnett mixing rule should be used for the case of many insoluble particles in a solution and that the Bruggeman mixing rule should be used for a dry mixture of particles where the particles are interspersed. As noted in *Lesins et al.* [2002], it is typical in atmospheric applications to simply use a volume averaging of the component optical constants to determine the optical constants of an internal mixture. This can be seen in aerosol models like that of *d'Almeida et al.* [1991] or that in the *Optical Properties of Aerosols and Clouds (OPAC)* developed by *Hess et al.* [1998]. It can also be seen in many general circulation models that simulate aerosol radiative forcing. In a variation on this theme, *Jacobson* [2002] uses a volume average to compute the optical constants of the shell for a core and shell aerosol model where the core is black carbon and the shell includes a shell solution and non-black carbon insoluble components. The shell solution optical constants are computed using a partial molar refraction approach.

The new optical constants reported in Chapter 2 present a unique opportunity to reexamine this issue for multi-component aqueous mixtures. In particular, for the IR a mixing rule needs to correctly model the spectrum of k, which in large part controls radiative transfer in the IR. We examine several different mixing rules, including L-L, an

alternate form which we will denote L-LA, the Maxwell-Garnett (M-G), the Bruggeman (B), the volume-average refractive index (VARI), the volume-average dielectric constant (VADC), and the weighted-average refractive index (WARI). We also consider a mixing rule for ternary solutions that was proposed recently by *Biermann et al.* [2000]. In examining these rules, we also want to investigate how they perform when the components are not just pure water and pure solutes. In a manner similar to the Biermann rule, we examine how they perform when the components are binary optical constants in the case of the ternary and quaternary mixtures, and ternary and binary optical constants in the quaternary mixture case.

3.5.1 Common Mixing Rules

In this evaluation we consider the Lorentz-Lorenz, the Maxwell-Garnett, the Bruggeman, the volume average refractive index, the volume average dielectric constant, and the weight average mixing rules. More recently *Biermann et al.* [2000] have proposed a mixing rule for the optical constants of ternary solutions based on the binary optical constants of the components, which we also consider. The details of the L-L, M-G, and Bruggeman mixing rules can be found elsewhere, e.g., [*Choy*, 1999, *Shivola*, 1999]. We present the definitions of the mixing rules with the following notation: ρ is the density of the mixture, w_i is the mass fraction of the i*th* component, M_i is the molecular weight of the i*th* component, R_i is the partial molar refraction of the i*th* component, ε is the dielectric constant of the mixture, m is the complex index of refraction of the mixtures, ε_i is the dielectric constant of the i*th* component, f_i is the volume fraction of the i*th* component, ε_{H2O} is the dielectric constant of water, and ρ_{H2O} is the density of water.

The L-L mixing rule, derived from the Lorentz-Lorenz formula, is defined as

$$\frac{\varepsilon - 1}{\varepsilon + 2} = R \Big/ V_m = \rho \sum_i \frac{w_i}{M_i} R_i \qquad \text{(Eq. 3.20)}$$

where R is the molar refraction of the mixture and V_m is the molar volume of the mixture. The summation is over water and all solutes. It is usual to assume (e.g., [*Stelson* (1990); *Luo et al*. (1996)]) that the partial molar refraction of water in the solution is the same as the molar refraction of pure water, that is

$$R_{H2O} = \frac{M_{H2O}}{\rho_{H2O}} \left(\frac{\varepsilon_{H2O} - 1}{\varepsilon_{H2O} + 2} \right) = \frac{M_{H2O}}{\rho_{H2O}} \left(\frac{m_{H2O}^2 - 1}{m_{H2O}^2 + 2} \right) \qquad \text{(Eq. 3.21)}$$

and the apparent partial molar refraction of the solute is computed as

$$R_s^b = \frac{V_m}{x_s} \left(\frac{m^2 - 1}{m^2 + 2} \right) - \frac{x_{H2O} R_{H2O}}{x_s} \qquad \text{(Eq. 3.22)}$$

where R_s^b is the apparent partial molar refraction based on the binary mixture, x_s is the mole fraction of the solute, and x_{H2O} is the mole fraction of water. If measurements of the binary solution are not available, then it would be necessary to estimate the partial molar refractions of both the water and solute by assuming they are the same as the molar refractions of the pure components (i.e., Eq. (3.21) for water), resulting in

$$R_s = \frac{M_s}{\rho_s} \left(\frac{\varepsilon_s - 1}{\varepsilon_s + 2} \right) = \frac{M_s}{\rho_s} \left(\frac{m_s^2 - 1}{m_s^2 + 2} \right) . \qquad \text{(Eq. 3.23)}$$

For ternary mixtures the partial molar refractivity of water in the mixture is assumed to be the same as pure water and the apparent partial molar refraction of each of the solutes is assumed to be the same as in the binary case. A different form of the Lorentz-Lorenz mixing rule, called here L-LA, is

$$\frac{\varepsilon - 1}{\varepsilon + 2} = \sum_i f_i \frac{\varepsilon_i - 1}{\varepsilon_i + 2} \quad . \qquad \text{(Eq. 3.24)}$$

The sum is over all components of the system. This form can be derived from the L-L rule by either assuming that the molar refraction of pure component i is the same as the partial molar refraction of component i in the mixture for all components, or by considering a simple model of molecules as spheres of dielectric constant ε_i (all with the same radii) and assuming the Lorentz local field is the same for all molecules.

The M-G mixing rule is also derived from the Lorentz-Lorenz formula by considering spherical inclusions of dielectric constant ε_i in a host medium with dielectric constant ε_m. If the host material is considered to be water, then the M-G mixing rule is defined as

$$\frac{\varepsilon - \varepsilon_{H2O}}{\varepsilon + 2\varepsilon_{H2O}} = \sum_i f_i \frac{\varepsilon_i - \varepsilon_{H2O}}{\varepsilon_i + 2\varepsilon_{H2O}} \qquad \text{(Eq. 3.25)}$$

where the summation is over all solutes.

Unlike the M-G mixing rule, the Bruggeman mixing rule treats all components symmetrically, i.e., one of the components does not need to be considered as the host. It is defined as

$$\sum_i f_i \frac{\varepsilon_i - \varepsilon}{\varepsilon_i + 2\varepsilon} = 0 \qquad \text{(Eq. 3.26)}$$

The volume average refractive index is defined by

$$m = \sum_i f_i m_i \qquad \text{(Eq. 3.27)}$$

and the volume average dielectric constant is given by

$$\varepsilon = \sum_i f_i \varepsilon_i \qquad \text{(Eq. 3.28)}$$

The weight average refractive index is defined by

$$m = \sum_i w_i m_i \qquad \text{(Eq. 3.29)}$$

The summation in Eqs. (3.26-3.29) is performed over the solvent and all solutes.

Biermann et al. [2000] have proposed a mixing rule for ternary solutions based on binary solution data. Letting Y represent either n or k or m, with w_1 and w_2 the solute 1 and solute 2 weight fractions, the ternary solution optical constant based on the corresponding binary solution binary optical constant with weight fraction ${}^{b}w_1$ and ${}^{b}w_2$ is given by the following formula

$$Y(\lambda, T, w_1, w_2) = \frac{w_1}{w_1 + w_2} Y(\lambda, T, {}^{b}w_1) + \frac{w_2}{w_1 + w_2} Y(\lambda, T, {}^{b}w_2) \qquad \text{(Eq. 3.30)}$$

with ${}^{b}w_1 = {}^{b}w_2 = w_1 + w_2$.

3.5.2 Performance of Mixing Rules in the Modeling of Binary Mixtures

To evaluate the ability of the above rules to accurately model the optical constants of binary mixtures, we selected several cases from our new dataset. The pure components in a binary aqueous mixture are water and the solute. For our datasets the binary solution optical constants are aqueous ammonium sulfate or aqueous ammonium nitrate. The optical constants of water at 298 K are readily available from the literature [*Bertie and Lan*, 1996b] . The optical constants of pure water over the frequencies covered by these datasets are not temperature dependent as long as T is above freezing. As shown in Chapter 2, the spectral absorption features of nitrate and sulfate are insensitive to temperature changes over the range considered here. There is some temperature dependence for the O-H stretch absorption feature of water in electrolyte solutions, but outside of that region we can consider the binary aqueous solution optical constants to be insensitive to T over the considered range. That allows us to examine the case of a single temperature of 298 K, which will then be representative of the results at other T in our

range. If we were trying to model the optical constants of a binary sulfuric acid solution, we would have to consider the $H_2SO_4^-/SO_4^{2-}$ dissociation temperature dependence, but there are additional reasons not to try to model binary sulfuric acid optical constants that we will address shortly. The literature contains the measured optical constants over the IR frequencies that match our data only for ammonium sulfate. Therefore, we restrict ourselves to the case of modeling binary aqueous ammonium sulfate optical constants using the mixing rules and the optical constants of water and ammonium sulfate. Later we will qualitatively examine ammonium nitrate and discuss sulfuric and nitric acid. We have chosen to model the optical constants of 5% and 40% binary ammonium sulfate mixtures and compare the results to the optical constants that we determined from the ATR data. Since the 5% and 40% mixtures represent the largest and smallest concentrations for which we have determined binary optical constants, they will allow us to bound the problem.

For the L-L mixing rule, we applied Eqs. (3.21) and (3.23) to estimate the partial molar refractions that are then used in Eq. (3.20). The density of the resulting solution that is used in Eq. (3.20) is from the density formula of *Laliberte and Cooper* [2004]. The other mixing rules require volume fractions instead of mass fractions. The volume fractions are determined using the partial molar volume information that is used in the density calculation. The volume fraction is computed as

$$f_i = \rho \frac{w_i V_{m,i}}{M_i} \quad . \qquad \text{(Eq. 3.31)}$$

Here f_i is the volume fraction of component i, ρ is the density of the binary mixture, w_i is the weight fraction of component i, M_i is the molar mass, and $V_{m,i}$ is the partial molar volume of component i.

The k spectrum of the 40% and 5% aqueous ammonium sulfate mixtures along with the differences between the modeled and measured k spectra for each of the mixing rules are shown in Figures 3.19 and 3.20, respectively.

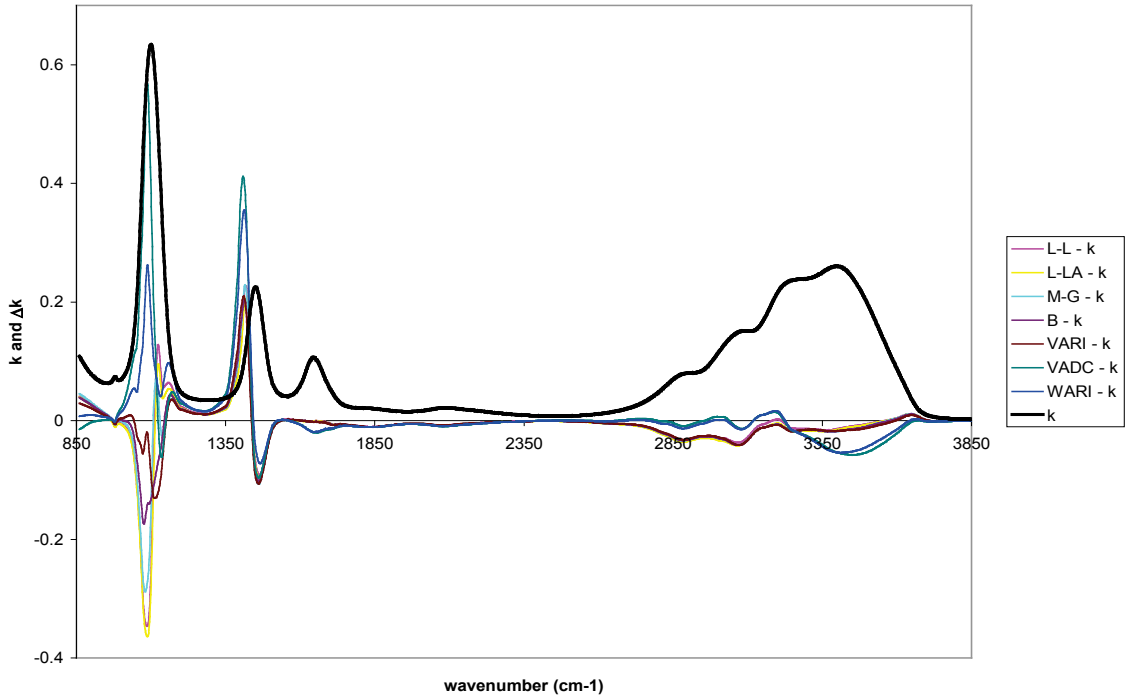

Figure 3.19. The measured k spectrum of 40% aqueous ammonium sulfate and differences between the modeled and measured values for each of the mixing rules.

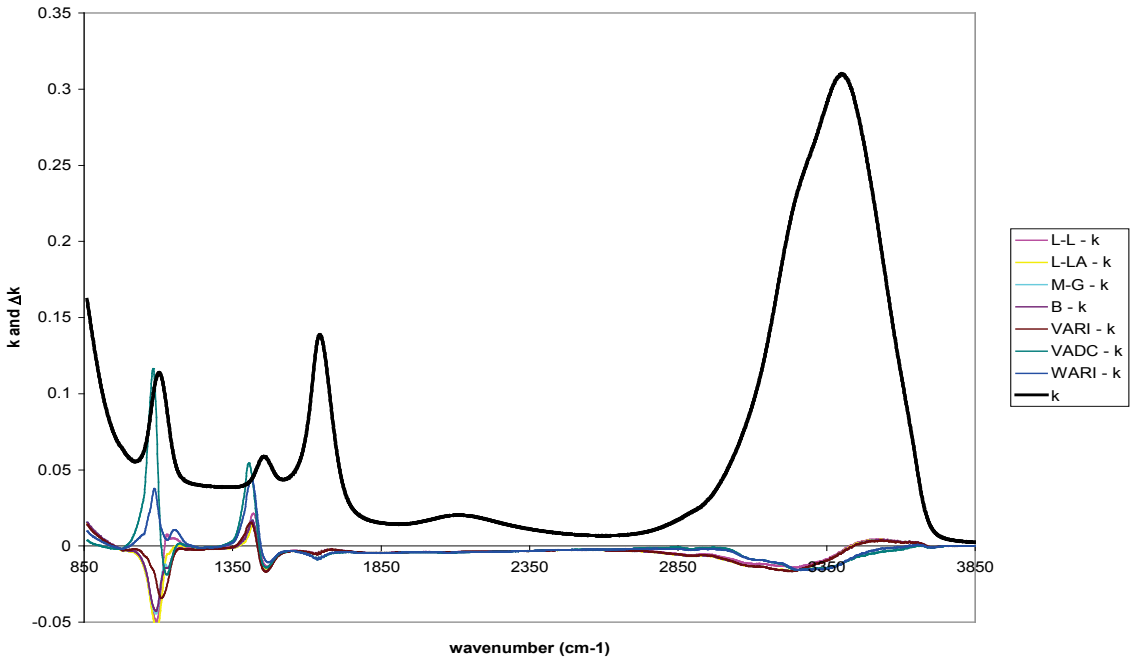

Figure 3.20. The measured k spectrum of 5% aqueous ammonium sulfate and differences between the modeled and measured values for each of the mixing rules.

In both cases significant differences between the modeled and measured k spectra exist in the regions of the ν_4 NH_4^+ absorption band, around 1445 cm^{-1}, and the ν_3 SO_4^{2-} absorption band, around 1100 cm^{-1}. In particular, the differences for the ν_4 NH_4^+ band are between 200% and 500% for the 40% aqueous ammonium sulfate and between 40% and 120% for the 5% aqueous ammonium sulfate. For the ν_3 SO_4^{2-} absorption band the differences are on the order of 50% for the 40% aqueous ammonium sulfate and 40% for the 5% aqueous ammonium sulfate. These differences arise because the positions and magnitudes of these absorption features are not accurately modeled by mixing dry solute optical constants with the optical constants of water. In the 40% solution, the strength of the ν_3 SO_4^{2-} absorption band is modeled fairly accurately by the L-L and M-G mixing rules, and to a lesser extent the L-LA, but not the position. None of the mixing rules accurately models the magnitude of the ν_4 NH_4^+ absorption band for this case. In the 5% mixture none of the mixing rules models the magnitude of the ν_3 SO_4^{2-} absorption band accurately. All except the VADC and WARI model the magnitude of the ν_4 NH_4^+ absorption band acceptably, but again not the position. Because the position of these spectral absorption features is not well modeled by any of the rules, we see significant errors in the k values in these regions for all mixing rules - on the order of 100% for the 40% aqueous ammonium sulfate and on the order of 50% for the 5% aqueous ammonium sulfate. None of the mixing rules models the magnitude of the multiple and overlapping absorption bands of water and NH_4^+ in the 3200 cm^{-1} to 3400 cm^{-1} region. Overall, VADC performed the least well followed by WARI. The VARI performed the best overall. The ν_1 SO_4^{2-} absorption band at 980 cm^{-1} is not present in the dry solute optical constant data because it is IR inactive, and so is not present in the modeled aqueous optical constants even though it becomes IR active in solution.

Although we did not compare mixing rules for aqueous ammonium nitrate, similar results can be expected. Examination of the estimated dry ammonium nitrate optical constants of [*Jarzembski et al*., 2003] shows that the ν_4 NH_4^+ absorption band is not distinct from the ν_3 NO_3^- absorption band around 1350 cm^{-1} as it is in binary aqueous ammonium nitrate optical constants. Also, the ν_3 NO_3^- absorption band is not as recognizable as a doublet as it is in the aqueous data. As with the ammonium sulfate, there is an IR inactive band, the ν_1 NO_3^- absorption band at 1045 cm^{-1}, which is clearly discernable in the solution optical constants but not in the dry ammonium nitrate optical constants. As with ammonium sulfate, the positions of the ammonium nitrate absorption bands in the dry state are different than in the aqueous phase. In the case of sulfuric acid or nitric acid, the absorption bands of molecular H_2SO_4 and HNO_3 are different from those of the sulfate, bisulfate and nitrate ions that are present at these temperatures and concentrations. Trying to form binary solution optical constants from highly concentrated sulfuric acid or nitric acid and water would provide inaccurate high spectral resolution results.

An intermediate possibility between measuring the optical constants of aqueous binary mixtures and modeling them using pure water and dry solute data is to model the optical constants using high concentration binary optical constants and pure water optical constants. To examine this approach, we modified the mixing rules to use high concentration data and pure water. The L-L mixing rule for this case is

$$\frac{\varepsilon-1}{\varepsilon+2}=\rho\left[\frac{w}{w_{\max}}\frac{1}{\rho_{\max}}\frac{\varepsilon_{\max}-1}{\varepsilon_{\max}+2}+\frac{\left(w_{\max}-w\right)}{w_{\max}}\frac{1}{\rho_{H2O}}\frac{\varepsilon_{H2O}-1}{\varepsilon_{H2O}+2}\right]. \qquad \text{(Eq. 3.32)}$$

Here ε is the dielectric constant of the mixture, ρ is the density of the mixture, w is the weight fraction of the solute at the concentration to be modeled, ε_{max} is the dielectric constant of the high concentration data, w_{max} is the weight fraction of the high concentration data, ρ_{max} is the density of the high concentration data, and ε_{H2O} and ρ_{H2O}

are the dielectric constant and the density of water, respectively. The alternate L-L mixing rule for this case is

$$\frac{\varepsilon-1}{\varepsilon+2}=\frac{f}{f_{\max}}\frac{\varepsilon_{\max}-1}{\varepsilon_{\max}+2}+\frac{\left(f_{\max}-f\right)}{f_{\max}}\frac{\varepsilon_{H2O}-1}{\varepsilon_{H2O}+2} \qquad \text{(Eq. 3.33)}$$

where f is the volume fraction of the solute at the concentration to be modeled, and f_{max} is the volume fraction of the solute of the high concentration. The M-G mixing rule for this case is

$$\frac{\varepsilon-\varepsilon_{H2O}}{\varepsilon+2\varepsilon_{H2O}}=\frac{f}{f_{\max}}\frac{\varepsilon_{\max}-\varepsilon_{H2O}}{\varepsilon_{\max}+2\varepsilon_{H2O}} \qquad \text{(Eq. 3.34)}$$

The Bruggeman mixing rule for this case is

$$0=f\frac{y\varepsilon_{\max}-\varepsilon}{y\varepsilon_{\max}+2\varepsilon}+\left(1-f\right)\frac{\varepsilon_{H2O}-\varepsilon}{\varepsilon_{H2O}+2\varepsilon} \qquad \text{(Eq. 3.35)}$$

where

$$y=\frac{1+2x}{1-x} \qquad \text{(Eq. 3.36)}$$

and

$$x=-\frac{\left(1-f_{\max}\right)}{f_{\max}}\frac{\varepsilon_{H2O}-\varepsilon_{\max}}{\varepsilon_{H2O}+2\varepsilon_{\max}} \qquad \text{(Eq. 3.37)}$$

The volume averaged mixing rule for this case is

$$m=\frac{f}{f_{\max}}m_{\max}+\frac{f_{\max}-f}{f_{\max}}m_{H2O} \qquad \text{(Eq. 3.38)}$$

Here m is the complex index of refraction of the mixture to be modeled, m_{max} is the complex index of refraction of the high concentration, and m_{H2O} is the complex index of refraction of water. A weight averaged mixing rule for this case is

$$m=\frac{w}{w_{\max}}m_{\max}+\frac{w_{\max}-w}{w_{\max}}m_{H2O} \qquad \text{(Eq. 3.39)}$$

Figure 3.21 shows the k spectrum of the 5% aqueous ammonium sulfate mixtures along with the differences between the modeled and measured k spectra for each of the mixing rules.

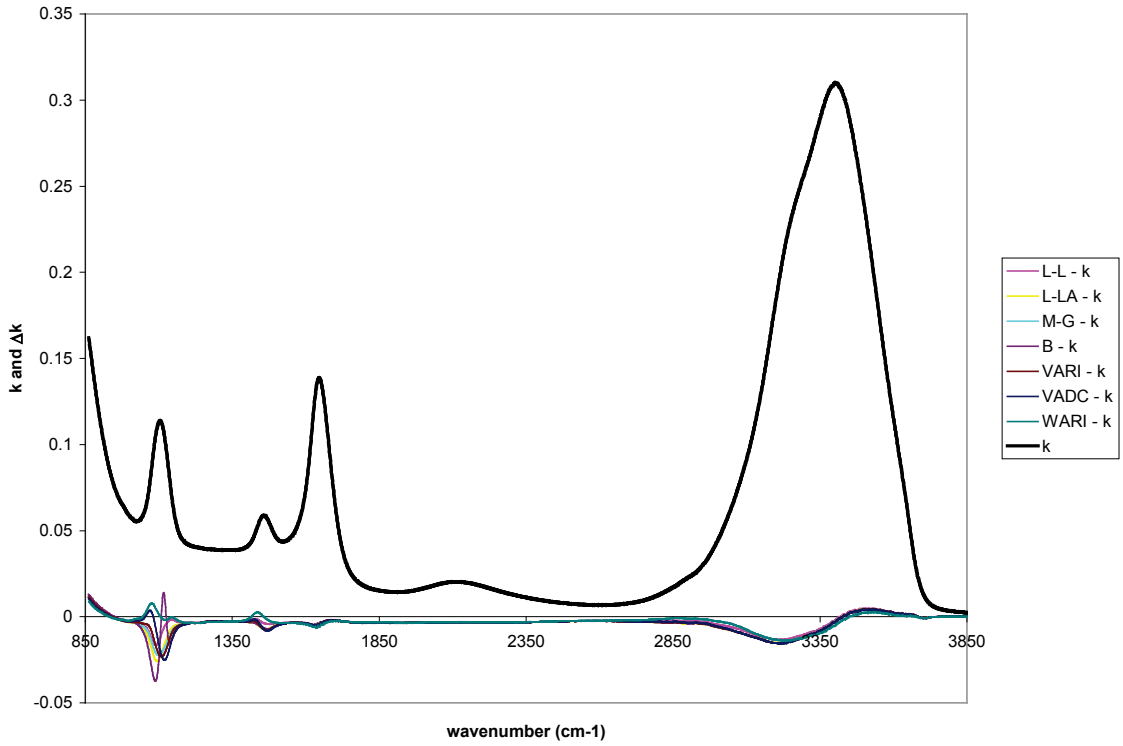

Figure 3.21. The measured k spectrum of 5% aqueous ammonium sulfate and differences between the modeled and measured values for each of the mixing rules when the mixing rules use 40% aqueous ammonium sulfate optical constants data mixed with pure water optical constants data.

In comparison with the results of modeling the mixture with pure water and pure solute, there is a significant improvement particularly with respect to the positions of the absorption bands. Now the best results are obtained using the WARI rule, whereas in the pure component case it gave nearly the worst results, while the Bruggeman performs the least well. Figure 3.22 shows the optical constants calculated for a 20% aqueous

ammonium sulfate mixture using the 40% data. The best overall results are again obtained using the weight fraction average.

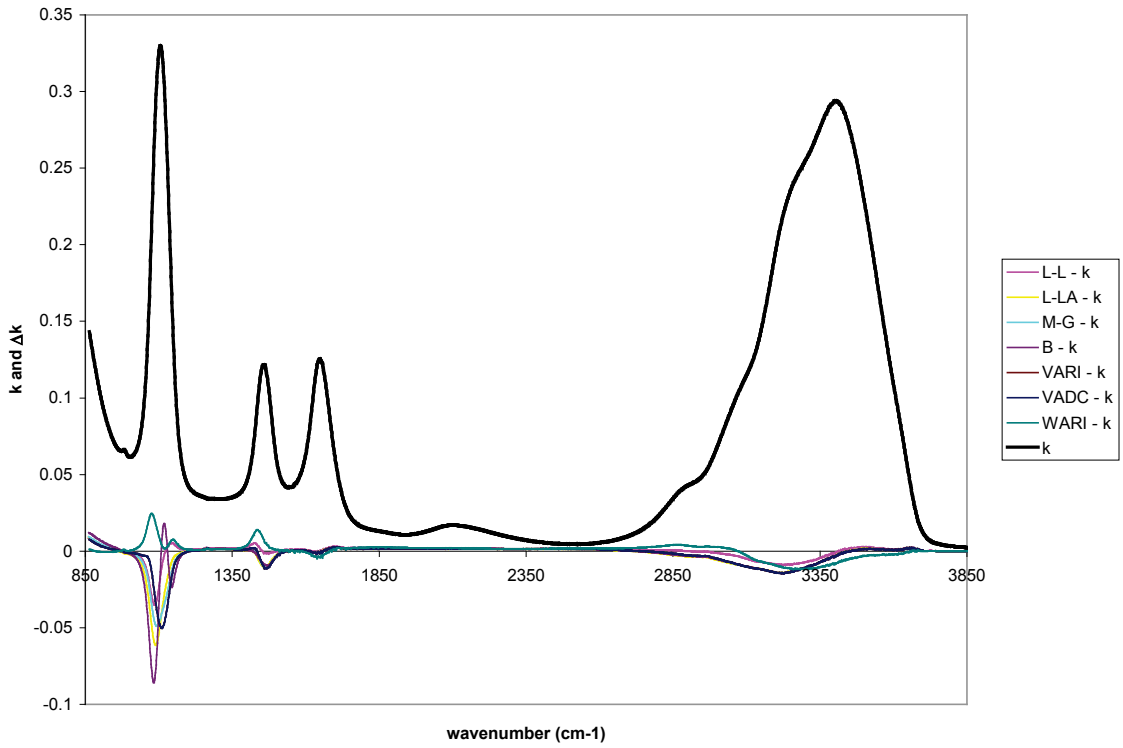

Figure 3.22. The measured k spectrum of 20% aqueous ammonium sulfate and differences between the modeled and measured values for each of the mixing rules when the mixing rules use 40% aqueous ammonium sulfate optical constants data mixed with pure water optical constants data.

For high spectral resolution applications it is clear that the IR optical constants of binary aqueous ammonium sulfate and ammonium nitrate cannot be accurately modeled by a mixing rule that uses the optical constants of water and the dry solute. Similarly, IR optical constants of binary sulfuric acid and binary nitric acid, of which numerous measurements have been made, would not be well modeled by a mixing rule that used water and pure sulfuric or nitric acid optical constants. The mixing rules are not able to capture the ion-ion and ion-water interactions. The same would be true of any aerosol

composed of electrolytes. For example, an aqueous sea-salt aerosol would not be well modeled in the IR at high spectral resolution by a mixture of water and NaCl optical constants. If only high concentration data are available, then acceptable results can be obtained for lower concentration optical constants with a simple weight fraction average using the high concentration optical constants and the optical constants of pure water.

3.5.3 Performance of Mixing Rules in the Modeling of Ternary Mixtures

Since the use of pure solute optical constants did not produce accurate results, we only examine the modeling of ternary mixture optical constants using binary optical constant data. To do this, we model ternary ammonium sulfate-ammonium nitrate optical constants using binary ammonium sulfate optical constants and binary ammonium nitrate solution optical constants. We also model ternary sulfuric acid-ammonium sulfate optical constants using binary ammonium sulfate optical constants and binary sulfuric acid solution optical constants. The binary mixture data was chosen at the same T as the ternary mixture, and was linearly interpolated between measured datasets to get the mass fraction or volume fraction required by the mixing rules. Since our datasets do not include any binary sulfuric acid optical constants, we have used the *Palmer and Williams* [1975] data at 298 K. In the following definitions for the mixing rules using binary data, w_1 and w_2 are the weight fractions of solutes 1 and 2, respectively, in the ternary mixture, ε is the dielectric constant of the ternary mixture, ρ is the density of the ternary mixture, ρ_1 is the density of the binary solution containing solute 1, ρ_2 is the density of the binary solution containing solute 2, ${}^1\varepsilon^b$ and ${}^2\varepsilon^b$ are the dielectric constants of the binary solutions containing solutes 1 and 2, respectively. We set the weight fraction of the binary solutions equal to the total weight fraction of solutes in the ternary mixture, i.e. $w_1^b = w_2^b = w_1 + w_2$. Additionally, f_1 and f_2 are the volume fractions of solutes 1 and 2, respectively, in the ternary solution, and ε_{H2O} is the dielectric constant of pure water. We

set the volume fraction of the binary solutions equal to the total volume fraction of solutes in the ternary mixture, i.e., $f_1^b = f_2^b = f_1 + f_2$.

The L-L mixing rule using binary mixture data is

$$\frac{\varepsilon - 1}{\varepsilon + 2} = \rho \left[\frac{w_1}{w_1 + w_2} \frac{1}{\rho_1^b} \frac{{}^1\varepsilon^b - 1}{{}^1\varepsilon^b + 2} + \frac{w_2}{w_1 + w_2} \frac{1}{\rho_2^b} \frac{{}^2\varepsilon^b - 1}{{}^2\varepsilon^b + 2} \right] \quad \text{(Eq. 3.40)}$$

The M-G ternary mixing using binary mixture data is

$$\frac{\varepsilon - \varepsilon_{H2O}}{\varepsilon + 2\varepsilon_{H2O}} = \frac{f_1}{f_1 + f_2} \frac{{}^1\varepsilon^b - \varepsilon_{H2O}}{{}^1\varepsilon^b + 2\varepsilon_{H2O}} + \frac{f_2}{f_1 + f_2} \frac{{}^2\varepsilon^b - \varepsilon_{H2O}}{{}^2\varepsilon^b + 2\varepsilon_{H2O}} \quad \text{(Eq. 3.41)}$$

The L-LA ternary mixing rule using binary solution data is

$$\frac{\varepsilon - 1}{\varepsilon + 2} = \frac{f_1}{f_1 + f_2} \frac{{}^1\varepsilon^b - 1}{{}^1\varepsilon^b + 2} + \frac{f_2}{f_1 + f_2} \frac{{}^2\varepsilon^b - 1}{{}^2\varepsilon^b + 2} \quad \text{(Eq. 3.42)}$$

For the Bruggeman ternary mixing rule we have

$$f_1 \frac{\varepsilon_1 - \varepsilon}{\varepsilon_1 + 2\varepsilon} + f_2 \frac{\varepsilon_2 - \varepsilon}{\varepsilon_2 + 2\varepsilon} + f_w \frac{\varepsilon_{H2O} - \varepsilon}{\varepsilon_{H2O} + 2\varepsilon} = 0 \quad \text{(Eq. 3.43)}$$

where f_w is the volume fraction of water in the ternary solution, and ε_1 and ε_2 are the dielectric constants of solutes 1 and 2, respectively, as determined from binary mixtures. We set the solute volume fraction of the binary mixtures equal to the total volume fraction of solutes in the ternary solution, i.e., $f_1^b = f_2^b = f_1 + f_2$. The volume fraction of water is the same in the binary and ternary mixtures. The binary Bruggeman mixing rule is given by

$$f_1^b \frac{\varepsilon_1 - \varepsilon^b}{\varepsilon_1 + 2\varepsilon^b} + f_w \frac{\varepsilon_{H2O} - \varepsilon^b}{\varepsilon_{H2O} + 2\varepsilon^b} = 0 \quad \text{(Eq. 3.44)}$$

Since the volume fractions and ε^b are known, we can use Eq. (3.25) to determine ε_1. Similarly, we determine ε_2. We then use ε_1 and ε_2 in Eq. (3.24) and solve for ε using a root finding algorithm. This ε is used to determine the ternary optical constants.

The volume average refractive index ternary mixing rule using binary refractive index data is

$$m = \frac{f_1}{f_1 + f_2}{}^{1}m^{b} + \frac{f_2}{f_1 + f_2}{}^{2}m^{b} \qquad \text{(Eq. 3.45)}$$

The volume average dielectric constant ternary mixing rule using binary dielectric constant data is

$$\varepsilon = \frac{f_1}{f_1 + f_2}{}^{1}\varepsilon^{b} + \frac{f_2}{f_1 + f_2}{}^{2}\varepsilon^{b} \qquad \text{(Eq. 3.46)}$$

The Biermann rule for ternary solutions was described in Eq. 3.30.

The agreement between model and measurement for the optical constants of a ternary ammonium sulfate-ammonium nitrate mixture using as the components the binary optical constants is remarkably good. Figure 3.23 shows the k spectrum of the 24% ammonium sulfate and 15% ammonium nitrate mixture (by weight) along with the differences between the modeled and measured k spectra for each of the mixing rules.

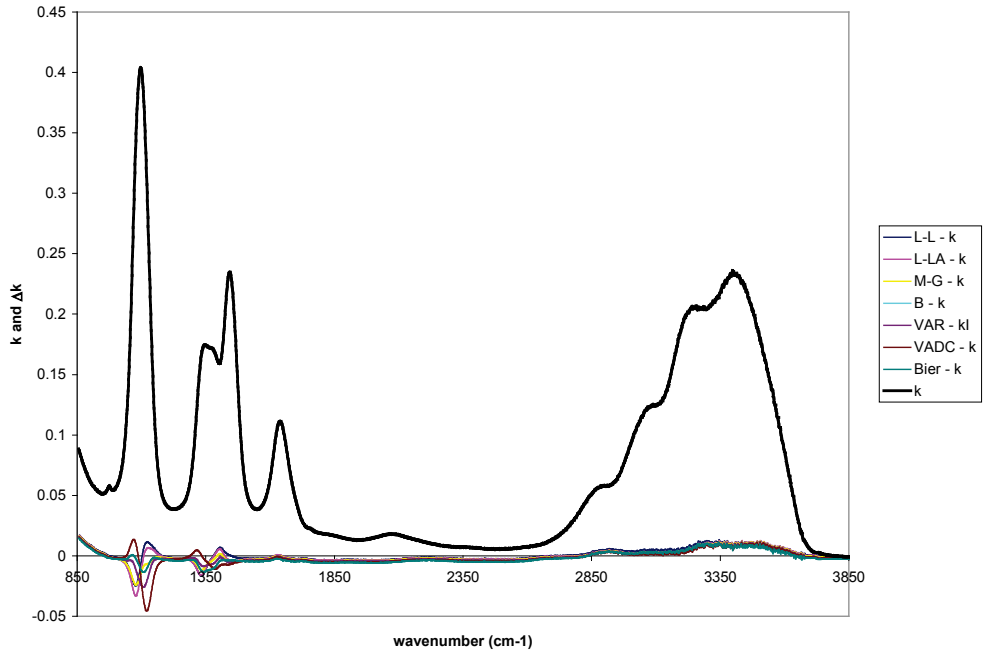

Figure 3.23. The measured k spectrum of a 24% ammonium sulfate and 15% ammonium nitrate ternary mixture and differences between the modeled and measured values for each of the mixing rules using binary optical constants data.

There are slight shifts in the positions of the ν_3 SO_4^{2-} absorption band, but the magnitude is reproduced very well. All rules do a good job of reproducing the overlapping ν_4 NH_4^+ and ν_3 NO_3^- absorption bands, and the ν_1 SO_4^{2-} absorption band at 980 cm^{-1} is captured. The O-H stretch region between 3200 cm^{-1} and 3500 cm^{-1} is also modeled fairly well. The Biermann and VARI rules performed the best with relative error typically less than 5%, while the Bruggeman and VADC rules performed the least well. Figure 3.24 shows the results for the 9% ammonium sulfate and 5% ammonium nitrate ternary solution. Again all of the mixing rules reproduce the measured optical constants very well, typically with relative error less than 5%, with the Bruggeman and VADC rules performing somewhat less well.

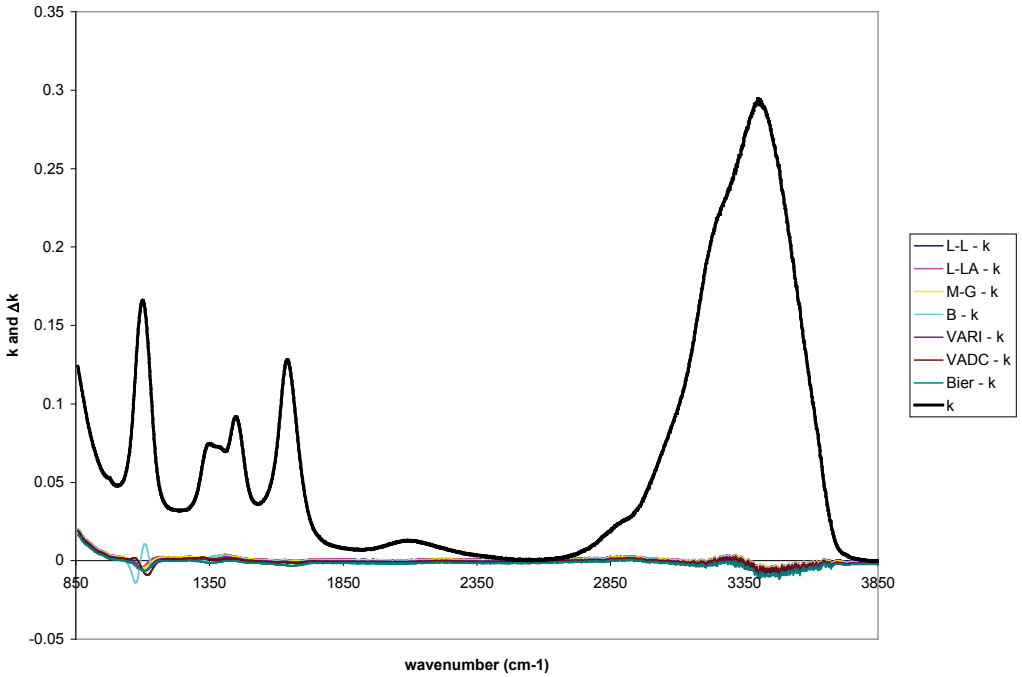

Figure 3.24. The measured k spectrum of a 9% ammonium sulfate and 5% ammonium nitrate ternary mixture and differences between the modeled and measured values for each of the mixing rules using binary optical constants data.

The results of applying these mixing rules to model the optical constants of a ternary sulfuric acid-ammonium sulfate mixture are shown in Figure 3.25. The plot shows the k spectrum of a ternary mixture that is 19% sulfuric acid and 14% ammonium sulfate along with the differences between the modeled and measured k spectra for each of the mixing rules.

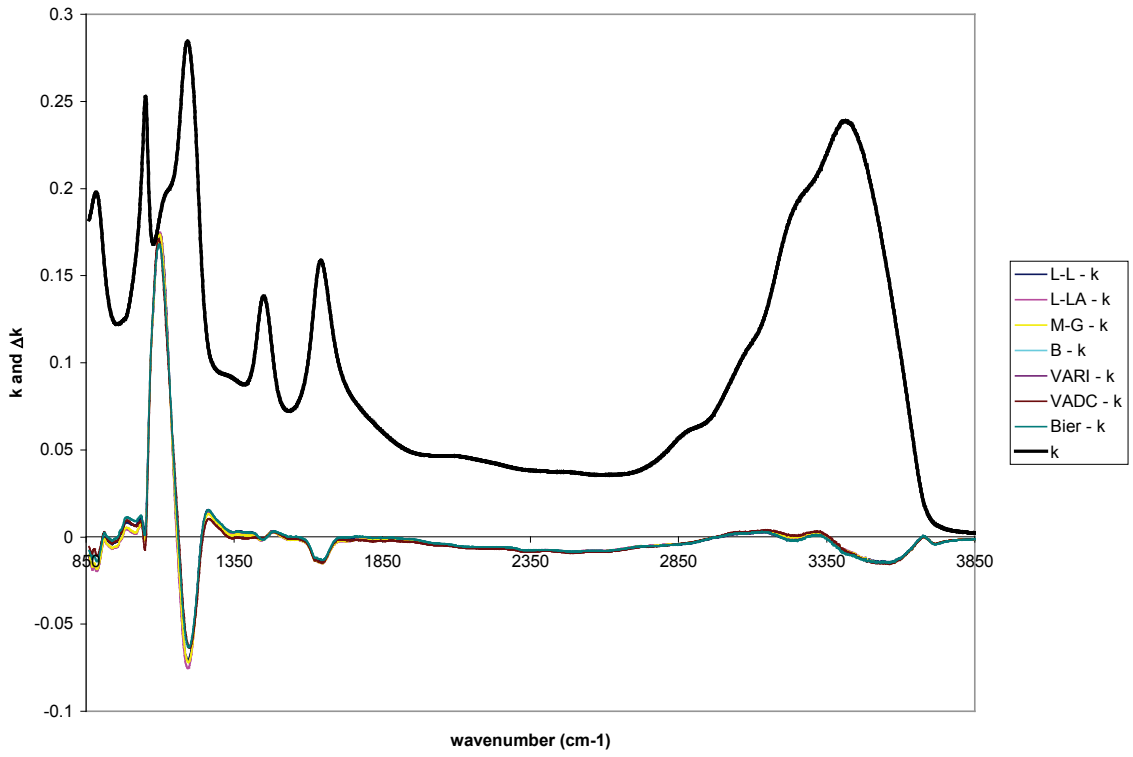

Figure 3.25. The measured k spectrum of a 19% sulfuric acid and 14% ammonium sulfate ternary mixture and differences between the modeled and measured values for each of the mixing rules using binary optical constants data.

None of the mixing rules modeled the ν_4 HSO_4^- absorption band, around 1185 cm^{-1}, the ν_1 HSO_4^- absorption band, around 1052 cm^{-1}, or the ν_3 SO_4^{2-} absorption band well at all. On the other hand, they all modeled the continuum absorption very well along with the ν_4 NH_4^+ absorption band. The magnitude of the H-O-H deformation band,

around 1640 cm^{-1}, is slightly underestimated. Figure 3.26 shows the results for the 8% sulfuric acid and 24% ammonium sulfate ternary mixture.

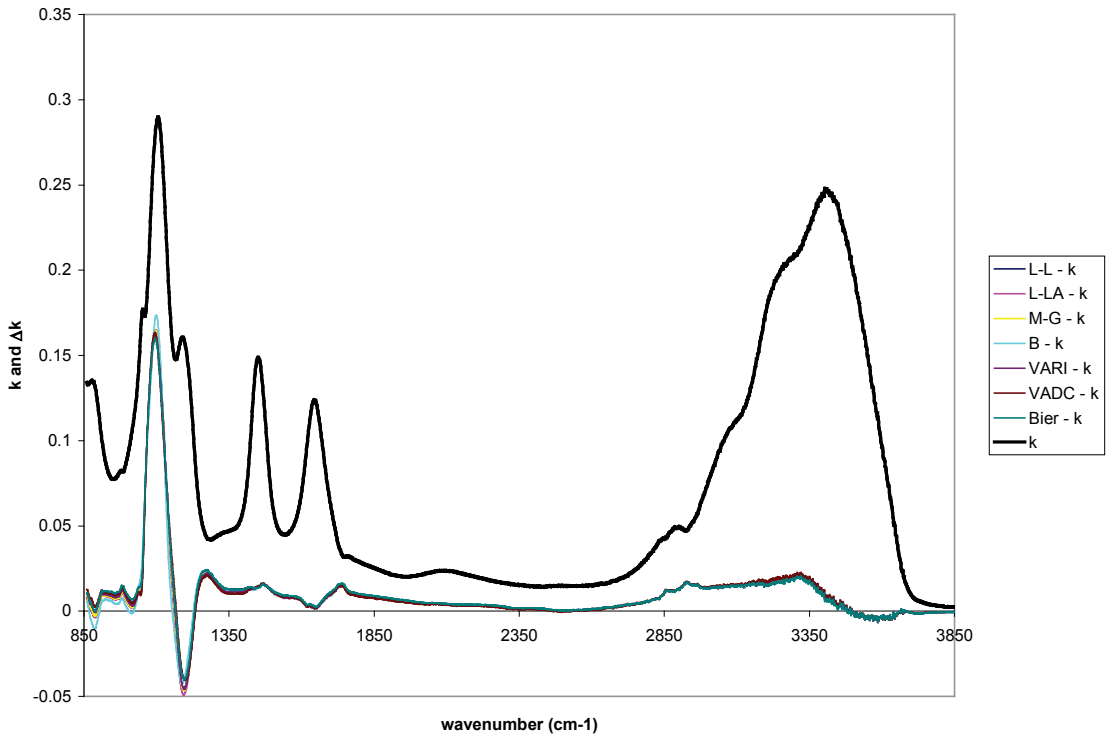

Figure 3.26. The measured k spectrum of an 8% sulfuric acid and 24% ammonium sulfate ternary mixture and differences between the modeled and measured values for each of the mixing rules using binary optical constants data.

All mixing rules model the continuum absorption and the ν_4 NH_4^+ absorption band fairly well. The magnitude of the H-O-H deformation band is very well modeled. The ν_4 HSO_4^- absorption band, the ν_1 HSO_4^- absorption band, and the ν_3 SO_4^{2-} absorption band, however, are again not modeled well. This is because the sulfate ions from the ammonium sulfate form bisulfate ions with hydrogen from the dissociation of sulfuric acid, and therefore the ν_3 SO_4^{2-} absorption band is too large and the HSO_4^- bands are too small. In the previous case the sulfuric acid concentration was larger than the ammonium sulfate concentration, so the ν_3 SO_4^{2-} absorption band is almost nonexistent in the ATR

data whereas the modeled optical constants from binary mixtures have a pronounced ν_3 SO_4^{2-} absorption band. Because of the interaction between the dissociation products of sulfuric acid and ammonium sulfate, none of the mixing rules provides accurate high spectral resolution optical constants.

In general, when the solutes in an aqueous ternary mixture do not interact to an extent greater than what would be expected in a binary mixture with a solute amount equal to the total solute amount in the ternary mixture, then the optical constants can be modeled very well with any of these mixing rules using a binary mixture data. We have seen that, unlike the situation of modeling the optical constants of binary aqueous aerosols, it is possible to accurately model the IR optical constants of ternary aqueous aerosols provided the appropriate component optical constants are used in the mixing rules. We have also seen that all of the common mixing rules can produce accurate results, and that the most straightforward typically provide the best results. For cases where binary optical constants data do not provide accurate ternary optical constants via mixing rules, they need to be obtained from measurements. The sulfuric acid-ammonium sulfate ternary aqueous aerosol optical constants have temperature and composition dependence that is not modeled by the mixing rules even when using binary aqueous sulfuric acid optical constants and binary aqueous ammonium sulfate optical constants in the mixing rules, and so measurement data are required.

3.5.4 Performance of Mixing Rules in the Modeling of Quaternary Mixtures

As before, we do not use pure solute optical constants. Instead, we examine the modeling of quaternary mixture optical constants using binary optical constant data and also using a combination of ternary and binary data. First, we examine the Biermann mixing rule using binary sulfuric acid, binary ammonium sulfate, and binary ammonium nitrate optical constants. We have previously seen that there was no substantial difference between the mixing rules. Since the Biermann rule performed slightly better than the

others and is simple to implement, we have chosen it to model quaternary optical constants using binary optical constants. Next, we modeled the quaternary sulfuric acid-ammonium sulfate-ammonium nitrate mixture optical constants using the ternary mixing rules above but used as inputs ternary sulfuric acid-ammonium sulfate optical constants and binary ammonium nitrate optical constants. The binary and ternary solution data were chosen at the same T as the quaternary, and were linearly interpolated between measured datasets to get the required mass fraction or volume fraction. To implement the Biermann rule for quaternary mixtures using binary mixture data, we extended the rule to the following formula

$$m = \frac{w_1}{w_1 + w_2 + w_3}{}^{1}m^{b} + \frac{w_2}{w_1 + w_2 + w_3}{}^{2}m^{b} + \frac{w_3}{w_1 + w_2 + w_3}{}^{3}m^{b} \qquad \text{(Eq. 3.47)}$$

with ${}^{b}w_1 = {}^{b}w_2 = {}^{b}w_3 = w_1 + w_2 + w_3$.

The results of the optical constants of a quaternary mixture that is 7% sulfuric acid, 12% ammonium sulfate by weight, and 13% ammonium nitrate by weight are shown in Figure 3.27. The plot shows the k spectrum along with the differences between the modeled and measured k spectra. It is immediately obvious that this rule does not model the ν_4 HSO_4^-, the ν_1 HSO_4^-, and the ν_3 SO_4^{2-} absorption bands very well for the same reasons as given previously regarding sulfuric acid-ammonium sulfate mixtures. On the other hand, it does model the continuum absorption very well along with the ν_4 NH_4^+ and ν_3 NO_3^- absorption bands, and the H-O-H deformation band.

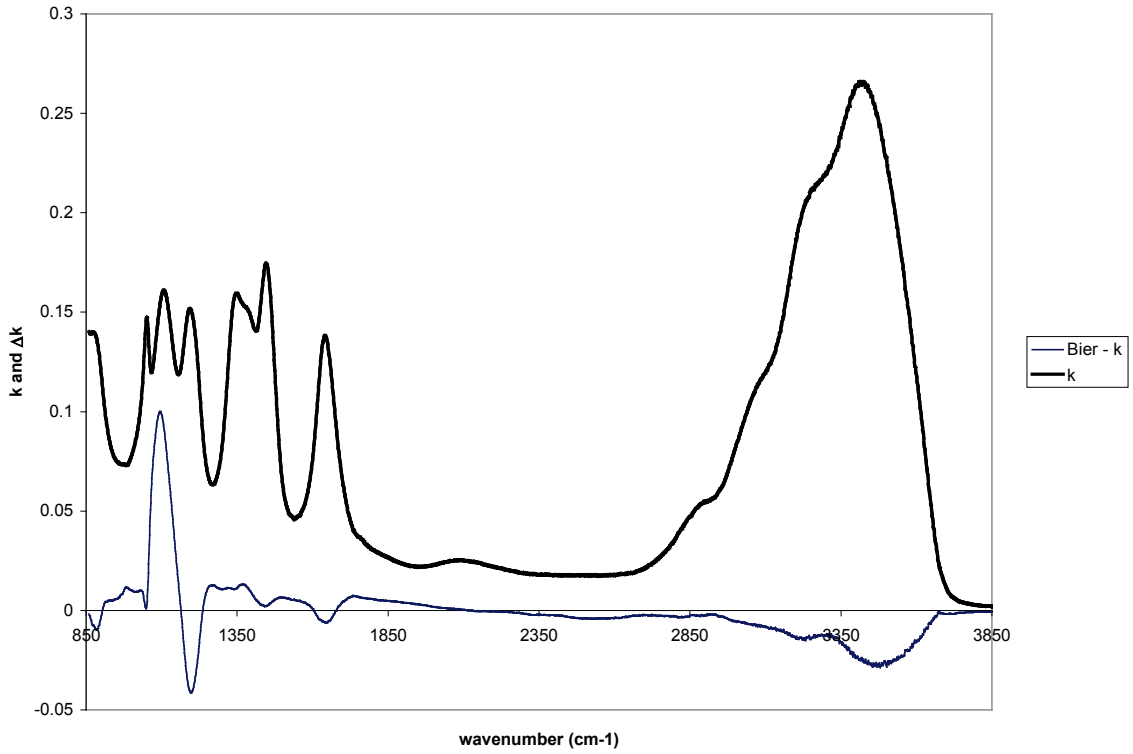

Figure 3.27. The measured k spectrum of a 7% sulfuric acid, 12% ammonium sulfate, and 13% ammonium nitrate quaternary mixture and differences between the modeled and measured values for the Biermann mixing rule using binary optical constants data.

Modeling this quaternary mixture accurately with the considered rules requires different components. We therefore examined using ternary sulfuric acid-ammonium sulfate optical constants and binary ammonium nitrate optical constants. To do this, we use the previous ternary mixing rules, but one of the components is optical constant data from a ternary mixture. To implement the Biermann rule for quaternary mixtures using a combination of ternary and binary mixture data, we use the following formula

$$m = \frac{w_1 + w_2}{w_1 + w_2 + w_3}^{1,2} m^t + \frac{w_3}{w_1 + w_2 + w_3}^{3} m^b \qquad \text{(Eq. 3.48)}$$

where ${}^{1,2}m^t$ is the complex index of refraction of the ternary mixture containing solutes 1 and 2, and ${}^{3}m^b$ is the complex index of refraction of the binary mixture containing solute 3. In the binary mixture the solute weight fraction is equal to the total quaternary weight fraction

$${}^{b}w_3 = w_1 + w_2 + w_3 \qquad \text{(Eq. 3.49)}$$

In the ternary data the total solute weight fraction is equal to the total quaternary weight fraction

$${}^{t}w_1 + {}^{t}w_2 = w_1 + w_2 + w_3 \qquad \text{(Eq. 3.50)}$$

and the individual solute weight fractions in the ternary mixture are

$${}^{t}w_1 = \frac{w_1}{w_1 + w_2}\left(w_1 + w_2 + w_3\right) \qquad \text{(Eq. 3.51)}$$

and

$${}^{t}w_2 = \frac{w_2}{w_1 + w_2}\left(w_1 + w_2 + w_3\right) \qquad \text{(Eq. 3.52)}$$

The volume fractions used in the other ternary mixing rules are modified in a similar fashion. The results are presented in Figure 3.28, and they show a dramatic improvement. All of the "ternary" mixing rules that use a combination of ternary and binary optical constant data model the quaternary optical constants fairly well. The HSO_4^- absorption bands are somewhat underestimated, but this could be due to linearly interpolating the ternary sulfuric acid-ammonium sulfate optical constants. An examination of the ternary sulfuric acid-ammonium sulfate datasets would show that the ν_4 HSO_4^-, ν_1 HSO_4^-, and ν_3 SO_4^{2-} absorption bands are not linear functions of the sulfuric acid and ammonium sulfate weight fractions. These results indicate that the considered

mixing rules can model quaternary mixtures accurately even when the solutes interact if the appropriate components at the correct concentration are used.

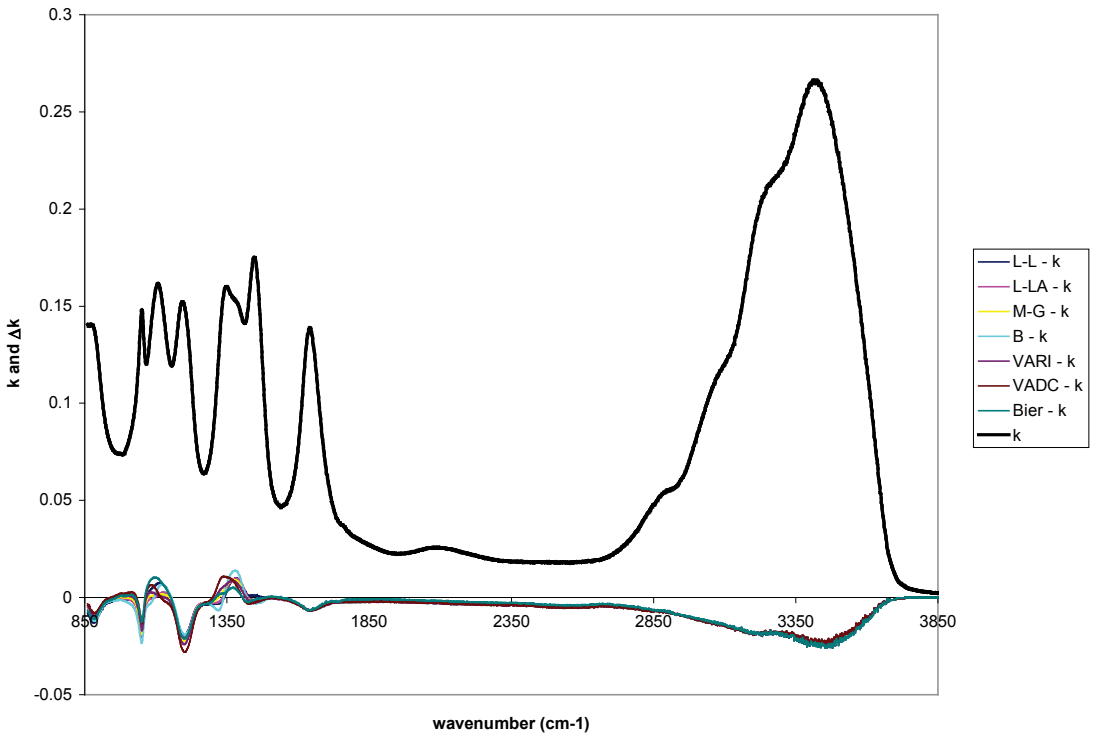

Figure 3.28. The measured k spectrum of a 7% sulfuric acid, 12% ammonium sulfate, and 13% ammonium nitrate quaternary mixture and differences between the modeled and measured values for each of the mixing rules using a combination of ternary and binary optical constant data.

3.5.5 Aqueous Internal Mixture Summary

Overall, our analysis indicates that the choice of mixing rule does not result in a significant or systematic difference. In fact, the simple mass fraction weighting of binary data in the Biermann rule and volume fraction weighting of binary data in the volume average ternary rule give on average slightly better performance than more complicated rules. In cases where one solute interacts with the other solute in the ternary mixture, as

in the case of sulfuric acid and ammonium sulfate, these mixing rules are not able to accurately model the ternary optical constants from the binary optical constants.

We have also shown that for the case of quaternary mixtures, the mixing rules can produce accurate optical constants with the use of appropriate components. For the quaternary mixture considered here, the use of binary data did not produce accurate results. The binary datasets did not represent the resulting interaction between the sulfuric acid and ammonium sulfate components. By using the ternary sulfuric acid-ammonium sulfate data and binary ammonium nitrate data in our modified mixing rules, we were able to achieve reasonably accurate optical constants. The ternary data captured much of the effect on dissociation product equilibrium that the presence of ammonium sulfate had on sulfuric acid. The slight differences between the modeled and measured optical constants in this case may be due to the interpolation required to obtain the needed concentration and/or the non-linear nature of the ternary optical constants as a function of concentration that linear interpolation does not quite capture. The accuracy that was seen for the concentrations used here may not be as good if the concentration of the ternary or quaternary becomes large. If highly concentrated binary or ternary solutions are required as inputs to the mixing rules, the concentration could become large enough that, for example, undissociated sulfuric acid or nitric acid would be present in the mixing component with absorption bands that are not present in the ternary or quaternary solutions to be modeled. Overall, we see that the mixing rules can yield optical constants with accurate results for these aqueous mixtures when the appropriate components are used in the mixing rule. This lessens the requirements for the number of measurements

that need to be made to support accurate optical property calculations for radiative transfer calculations.

3.6 Summary

We have investigated how the high spectral resolution optical properties of tropospheric aerosol components and mixtures, particularly dust and aqueous aerosols, vary depending on how they are computed. The analysis began with dust aerosol components and mixtures. It included examining the uniqueness of the spectral signatures of the individual mineral components and how the spectral signature varies with changes in the size distribution parameters including limits of integration. This was done using Lorentz-Mie theory in order to determine what level of variation made significant spectral changes in the optical signature and would therefore be likely to be discernable in modeled high spectral resolution radiance.

We then investigated techniques that could be used to address the non-spherical nature of dust aerosol particles and examined how the spectral signature is changed. The techniques examined were T-matrix and CDE. For the CDE technique the scattering component, which is typically ignored, was included to see if that made a difference from what other authors had found. The scattering term was based on a corrected derivation of the formula and is detailed in Appendix B. The results were compared to recently reported laboratory measurements for a number of pure mineral species in order to determine if one of these methods is likely to be more appropriate than Mie theory for dust aerosol in general and quartz particles in particular, which long ago were shown to

be poorly modeled by Mie theory in the TIR at high spectral resolution but for which a good method still has not been identified.

Additionally, we investigated the effects of external and internal mixture approaches on multi-component dust aerosol. This included how the spectral signature of an externally mixed dust aerosol depends on the compositional fidelity with which the aerosol is modeled and also how it depends on the fine to coarse particle ratio for an aerosol with size-resolved composition. We also examined the spectral signature differences between externally mixed regional aerosol models and models that use bulk sample derived optical constants. Finally for dust aerosols, we examined the spectral signature differences between a size-resolved aerosol model computed as an external mixture and as an internal mixture using both Mie theory and T-matrix.

We then evaluated the use of mixing rules in modeling the IR optical constants of multi-component aqueous aerosols, including the Lorentz-Lorenz rule, a variant of the Lorentz-Lorenz rule, the Maxwell-Garnett rule, the Bruggeman rule, the volume average refractive index rule, the volume average dielectric constant rule, the weight average refractive index, and the Biermann mixing rule for ternary mixtures.

Our major findings are the following:

- The irregular shapes of dust particles are not adequately approximated by spheres in the calculation of high spectral resolution TIR optical properties.
- A T-matrix computed distribution of oblate spheroids provides a much better fit to the extinction spectrum of quartz particles then any other technique. A T-matrix oblate spheroid with a shape factor of 5 yields a spectral signature with essentially the correct feature positions but the features are too narrow.

- For the phyllosilicate minerals for which measurement data is available, T-matrix calculations with a shape factor of 5 again produce optical properties with correctly positioned spectral features. The overall shapes of the features are also a good match and far exceed the results of Mie theory or CDE or disk-shaped particles.
- CDE is not practical for terrestrial dust particles because their sizes are not in the Rayleigh limit. Also the spectral signature match is not as good as T-matrix with a shape factor of 5 for clay minerals, but it is better than Mie. CDE gets the width of the quartz main feature correct but not the shape, and is not as good a fit as can be obtained with a distribution of oblate spheroids.
- The silicate minerals with their fundamental Si-O vibrational absorption bands, which peak in the 1000 – 1100 cm-1 region, create the noted "v-shaped" depression in brightness temperature spectra in the TIR window for surface radiance transported through atmospheric dust.
- High spectral resolution volume optical properties depend on multiple size distribution parameters that need to be correct in order to accurately model measured radiance.
- Coarse mode signatures have reduced spectral contrast for their spectral features and so retrieving composition would be more difficult. They also have a continuum extinction that becomes blackbody-like at large median radius.
- Smaller size modes have enhanced spectral contrast in their signatures and are therefore easier to retrieve composition from.

- For a fine or coarse size mode small changes in median radius result in a broadening of spectral features and a small increase in continuum extinction. The lower frequency features are more affected by these changes than the higher frequency features. Small shifts in the positions of features also occur with lower frequency features again more affected.
- Changes in median radius can be distinguished from particle number concentration changes because of the broadening/narrowing of the features and the non-uniform continuum changes across the TIR window region.
- Variations in volume optical properties with the limits of integration need to be considered. Infinite limits are not physically reasonable and lead to an increase in continuum extinction for lower frequency features. Comparisons to measurements indicate a more physical limit is required but not too small. A value of about 2.5 sigma appears to work well.
- Based on an examination of spectral signatures of a highly complex size-resolved mineralogical aerosol model and a simpler model that retains only the major components, the spectral differences are found to be minor. Therefore a high level of compositional fidelity is not required in modeling.
- Where size mode mineralogy differs considerably it is important to get the fine to coarse particle ratio correct.
- Internal versus external dust aerosol mixtures show large spectral differences in the region of very strong quartz absorption where the optical constants of the components are dramatically different. Outside of this region the differences are small. External and internal mixtures are likely interchangeable if little or no

components with dramatically different optical constants are present. If there are differences between external and internal mixtures they should be readily apparent at high spectral resolution and only one should work.

- The EMA mixing rules can model aqueous multi-component IR optical constants accurately if the appropriate components are used. As a contra case, the use of pure component IR optical constants (i.e. pure water and pure solute) in these mixing rules does not accurately model multi-component IR optical constants. Binary mixtures therefore, require the use of measured IR optical constants. For ternary mixtures however, in cases where the solute species do not interact strongly, mixing rules accurately predict IR optical constants based on binary optical constant input. For ternary mixtures like aqueous sulfuric acid-ammonium sulfate however, for which the solutes interact, measured IR optical constants must be used. In the quaternary case that was examined here, the use of binary optical constants data in the mixing rules did not accurately model the measured optical constants. A combination of ternary and binary optical constants, however, resulted in good agreement between modeled and measured values.
- The several mixing rules considered in this study performed approximately equally well. On average, the straightforward Biermann and volume average methods performed slightly better than more computationally complex mixing rules for ternary and quaternary mixtures.

We have set the stage for radiative transfer modeling by investigating how the high spectral resolution optical properties of aerosols are affected by the choice of

particle morphology that is used in the computation of the optical properties, the choice of mixing state for multi-component aerosols, and variations in size distribution parameters. We have also examined how the spectral signature of an aerosol depends on the level of compositional fidelity. Finally we examined in detail the performance of a number of EMA mixing rules in modeling the IR optical constants of multi-component aqueous aerosols. The optical constants presented in chapter 2 and contained in the LAARI database together with the investigation of high spectral resolution IR optical signatures of tropospheric aerosol components and mixtures presented here can be used to support the development of aerosol models that accurately model the effects of tropospheric aerosol at high spectral resolution and provide detailed information on the TIR climate impacts of the aerosol.

CHAPTER 4

IMPACT OF DUST AEROSOL ON AIRBORNE AND SATELLITE HIGH SPECTRAL RESOLUTION IR RADIANCE, IR RADIATIVE FORCING AND COOLING RATE

4.1 Introduction

In Chapter 3 it was demonstrated that at high spectral resolution there can be significant spectral differences in the optical properties of dust aerosols depending on whether they are modeled using optical constants derived from bulk samples or modeled using a size-resolved mineralogy-based mixture with optical constants of the individual mineral components. Significant spectral differences in dust optical properties also arise depending on the particle shape assumption, e.g. Mie theory vs. T-matrix results. We also noted the inconsistency between the Mie generated spectral optical properties of some minerals and reported laboratory measurements. This implies that the impact of non-sphericity may be as important as mineralogical composition when modeling the optical properties of a dust aerosol based on its mineral composition. For applications using high spectral resolution radiance measurements these differences can be critical, e.g. geophysical parameter retrievals from high spectral resolution radiance data and/or dust aerosol detection and compensation for those retrievals. Spectral differences between modeling methods would also be critical in any retrieval of dust aerosol

microphysical properties and any forward modeling to predict dust aerosol radiative effects, e.g. radiative forcing or cooling rate.

In addition to spectral differences in optical properties, we need to be concerned with the microphysical properties themselves as they are used and/or retrieved for dust aerosol. Ideally, modeled aerosol optical properties should not only closely reproduce measured radiances when those properties are used in rigorous radiative transfer calculations, they should also be consistent with the actual microphysical properties of the aerosol being modeled. This would ensure closure between modeled and measured quantities and would guarantee that microphysical properties retrieved for an aerosol would be consistent with forward modeling results used for prediction of aerosol radiative effects. If the techniques used to retrieve dust aerosol properties differ from those that are used to predict dust aerosol radiative effects then the retrieved and/or modeled results may be inconsistent with measurements. For example, if a numerical weather prediction (NWP) model or a general circulation model (GCM) uses size-resolved mineralogical composition to predict dust aerosol radiative effects, those results may not be consistent with results based on dust microphysical properties that are retrieved using a generic dust refractive index. The aerosol microphysics of any technique that assumes spherical particles may not be consistent with high spectral resolution measurements if non-sphericity effects are not negligible. To date these differences and their impacts have not been adequately studied or addressed.

To investigate these issues, the radiative effects of tropospheric dust aerosols on observed high spectral resolution TIR radiance measurements are modeled and analyzed in this Chapter. We use a high spectral resolution radiative transfer code to examine both

a size-resolved mineralogy-based aerosol modeling approach employing the external mixtures of individual minerals, which we refer to as MEM (mineralogy-based external mixture), and the bulk optical properties approach to aerosol modeling. We limit the investigation to external mixtures because in Chapter 3 we found that there should not be a significant difference between an external mixture and an internal mixture unless there is a large quartz content. The effect of non-sphericity is investigated by utilizing the T-matrix technique. Here, we develop and present a new technique to retrieve dust aerosol microphysical properties based on its high spectral resolution optical signature. Using the results of this investigation, we analyze the impact of using different modeling techniques for forward and inverse modeling. We also examine the sensitivity of radiative forcing and cooling rate effects to variation of dust particle concentration and to variations of dust layer thickness and position in order to better understand how accurately these quantities need to be determined.

The goals of this Chapter are as follows: 1) Develop tools and techniques that enable the accurate modeling of high spectral resolution TIR radiances impacted by dust aerosol; 2) use these tools and techniques to develop a new technique to retrieve composition and size distribution information for dust aerosol from high spectral resolution TIR radiance data; 3) compare and contrast the results of the new retrieval to standard techniques that use prescribed generic refractive index (bulk) data in order to examine the uniqueness of the retrievals and to examine differences in predicted dust aerosol radiative forcing and cooling rate based on any differences in the retrieved microphysical data; and 4) use these models to examine the sensitivity of spectral and

integrated aerosol TIR radiative forcing and cooling rate to vertical structure, aerosol loading, and size distribution changes during dust transport.

4.2 Methodology and Data

Critical to this investigation is determining whether Mie or non-spherical techniques are more appropriate for modeling naturally-occurring irregularly-shaped dust particles when they are modeled using individual mineral component refractive index data. To determine this issue and achieve of our above stated goals we modeled well characterized high spectral resolution TIR radiance datasets in the presence of a single dust plume over the ocean, which is a relatively homogeneous surface with well known surface properties. Substantial ancillary information on the state of the atmosphere and surface, and the position and thickness of the dust plume were available for these datasets, which limits the number of unknowns in the modeling. Under these circumstances, it should be possible to determine which, if either, of the two morphology assumptions offers the best capability to match the measured radiance, and therefore represents the best method to model the dust optical properties.

Two different datasets have been assembled for this modeling and analysis effort; one involving airborne and the other satellite data. Because ozone absorption obscures a critical part of the TIR atmospheric window, thereby making it difficult to judge how well dust aerosol is being modeled and which of the two morphology assumptions is most appropriate, we begin our investigations with airborne high spectral resolution data collected in close proximity to a dust plume from a major dust event that includes independent information on the state of the atmosphere. Such a unique dataset comes

from the Saharan Dust Experiment (SHADE) campaign [*Tanre et al.*, 2003], and involves two Airborne Research Interferometer Evaluation Instrument (ARIES) datasets [*Highwood et al.*, 2003]. The data were collected during one day of the SHADE campaign when there was a significant dust event. The satellite data come from the AIRS instrument and the Cloud-Aerosol Lidar and Infrared Pathfinder Satellite Observation (CALIPSO) lidar (CALIOP, i.e. Cloud-Aerosol Lidar with Orthogonal Polarization). The latter provide independent information on the dust layer altitude and thickness that allows us to constrain those variables in radiative transfer modeling.

We begin our analysis by modeling clear sky conditions using the best available estimate of the state of the atmosphere and surface properties. This is done to support the creation of an accurate brightness temperature difference (BTD) spectrum between a modeled clear-sky spectrum and measured spectrum, which forms the basis of our new technique for retrieving dust aerosol microphysical properties. The new retrieval technique seeks to determine the composition and size distribution parameters by matching spectral aerosol optical properties to the BTD spectral signatures. First, spectral aerosol optical properties are generated for mineral components that are known to occur in dust samples from the region. Then, optical properties for an external mixture of those components with one or two size modes are created attempting to match the spectral signature of the BTD spectrum. The matching optical properties are then used in a rigorous radiative transfer code and iteratively adjusted based on a mean squared error fit between the modeled and measured radiance to determine what composition and size distribution parameters most accurately match measured radiances. After employing our new technique, we use the common technique of generating optical properties using bulk

material refractive index data. We then use these optical properties to find their best match to the measured radiance. The results of these two techniques are then compared and contrasted in terms of uniqueness of retrieved information and implications of non-uniqueness to forward and inverse modeling of dust aerosol radiative effects. These retrieval results are also used to investigate the sensitivity of aerosol radiative forcing and cooling rates to the position, thickness and loading of the dust aerosol layer. The radiative transfer code used for this effort is discussed in more detail in the following section.

4.3 Development of a Radiative Transfer Code: MODTRAN5 Alpha Version

In order to rigorously analyze tropospheric aerosol effects at high resolution, a radiative transfer code is required that is able to compute at-sensor radiance at a spectral resolution sufficient to model the currently available high spectral resolution sensors. This code also needs to be able to account for the absorption and scattering of aerosol particles in addition to the atmospheric gases. For this research, the radiative transfer code must not only be able to handle aerosol particles, it must allow precise specification of user-defined spectral aerosol optical properties - unlike standard aerosol models with a few adjustable parameters or aerosol optical models based solely on bulk material refractive index data. The code also needs to allow the user to control the vertical profile of aerosol properties in addition to the vertical profiles of the other atmospheric state properties. Lastly, the radiative transfer code must allow the sensor position and orientation to be variable, i.e. not just a nadir/zenith viewing geometry, since many current satellite, airborne and ground-based sensors are more than strictly nadir/zenith

viewing. This also requires the code to accommodate the specification of surface properties not only as a function of wavelength but also as a function of viewing angle.

An alpha version of the radiative transfer code MODTRAN5 [*Berk et al.*, 2005], i.e. MODTRAN5 Version 3 Release 5 (MOD5v3r5), provides all the capabilities required for this modeling and analysis work. Permission was sought and granted from the Air Force Research Laboratory (AFRL) to be an alpha tester of the code and to use it for this research. We rigorously examine the performance of the code, diagnose any discrepancies we discover in our usage, and report our findings and recommendations. In our testing of the Spectral Aerosol Profile (SAP) capability of the code we discovered one software bug, which we reported to AFRL and then fixed and incorporated into our executable by recompiling the source code. As detailed later we also updated the default chlorofluorocarbons (CFC) vertical profiles in the code and then recompiled the code again and provided the updated CFC files to AFRL.

MODTRAN5 also provides the benefit of incorporating the DIScrete Ordinate Radiative Transfer (DISORT) [*Stamnes et al.*, 1988] method to accurately handle multiple scattering calculations. The DISORT method reduces the radiative transfer equation to a set of first-order differential equations at discrete angles, which can be readily solved with current numerical techniques. It is a very efficient and accurate way to compute scattered intensities and fluxes. MODTRAN5 includes a 0.1 cm^{-1} band model built using the high-resolution transmission molecular absorption database HITRAN 2004 [*Rothman et al.*, 2005]. Importantly for the TIR atmospheric window, MODTRAN5 includes the Clough-Kneizys-Davies (CKD) version 2.4 water vapor continuum model [*Clough et al.*, 1989]. The most significant benefit of the alpha version

of MODTRAN5 for this work is that it includes the Spectral Aerosol Profile capability that allows the user complete control over all of the spectral aerosol optical properties and the ability to exactly specify those optical properties on a level by level basis at the vertical resolution of the user's choosing. To use this capability we developed a set of tools that allows us to precisely specify our own high spectral resolution aerosol models developed in this study.

4.4 AIRS Ocean Clear Sky Modeling

In order to isolate the dust spectral signal in the BTD spectrum, we must accurately model the radiance that would be measured in dust-free conditions. This requires demonstrating the ability to accurately model the important gaseous species and surface state under actual clear-sky conditions. To do so, a number of geographically diverse clear-sky open-ocean AIRS Level 1B (L1B) radiance spectra with varying viewing geometries were modeled. The MODTRAN5 user-defined atmosphere was based on the atmospheric state and surface state information retrieved by AIRS and contained in the corresponding AIRS L1 Support Data file. The atmospheric state information used in MODTRAN5 includes the AIRS retrieved temperature, water vapor and ozone vertical profiles at 100 predefined pressure levels as given in the support data. The surface state information used in MODTRAN5 includes the surface skin temperature, surface air pressure and surface air temperature. The viewing geometry, i.e. satellite zenith and azimuth angles, is taken from the L1 radiance dataset.

Initially, we used the spectral surface emissivity built-in to MODTRAN5 (defined as albedo = 1 – emissivity) for ocean water. In reviewing the results, the fit of the

modeled radiance to the measured radiance was not nearly as good as expected. In particular, the overall fit across the 750 – 1250 cm^{-1} TIR window region was not satisfactory. No adjustment of the surface skin temperature was found to provide a good fit across the entire spectral region. The second built-in surface albedo for ocean water, i.e. reference surface #57 in the spec_alb.dat file, gave much improved results, but the lack of any viewing angle dependence for this albedo was cause for concern especially for AIRS data that are often collected at large zenith angles.

There are a number of other emissivity models of water in the literature. For instance, *Wu and Smith* [1997] developed a fairly complex ocean emissivity model that includes factors such as wind speed. Because of the complexity of the *Wu and Smith* model and no guarantee it would solve the problem, it was decided not to try to implement it. Instead we choose to use an approach developed by *Newman et al.* [2005] that provides a temperature and angle dependent model for the optical constants of ocean water based on measurements from their high spectral resolution TIR sensor ARIES. Their model for ocean water optical constants was used to compute the Fresnel reflectance of ocean water as a function of temperature and zenith angle that was then used in MODTRAN5. This Fresnel reflectance model for open-ocean water resulted in excellent agreement between the modeled and measured radiances for nearly all of the selected cases over a wide range of viewing geometries. The surface skin temperature had to be adjusted slightly in a number of the cases, but the adjustment was well within the stated accuracy of the surface skin temperature reported in the AIRS datasets.

Figures 4.1 shows an example of the fit between the AIRS brightness temperature (BT) spectrum and the MODTRAN5 modeled BT spectrum for one of the cases of open-

ocean clear-sky conditions. The maximum difference in BT for any of the modeled cases is only 0.5 K illustrating the accuracy of the fit.

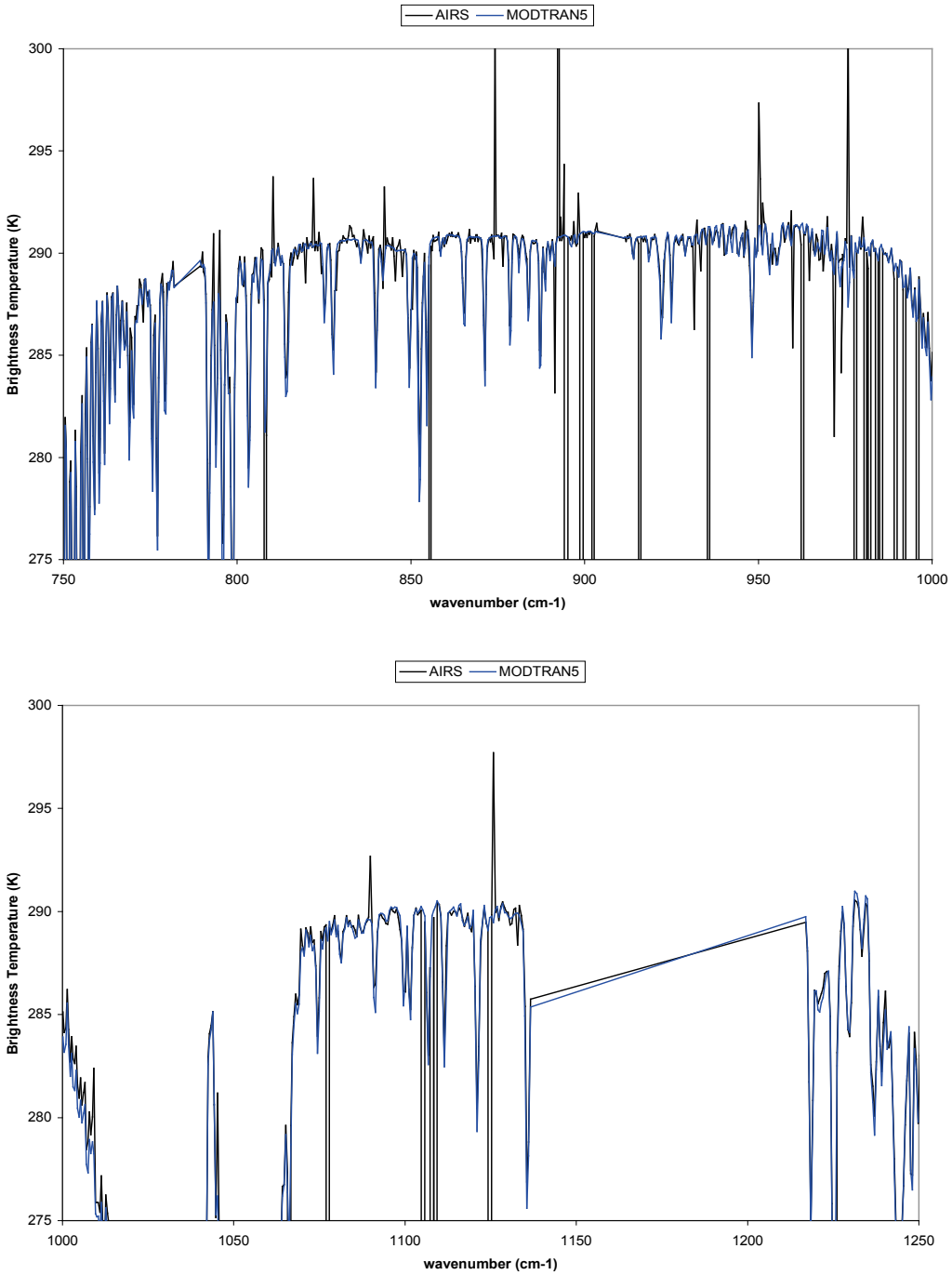

Figure 4.1a and b. AIRS measured and MODTRAN5 modeled brightness temperature spectra for an open-ocean clear-sky scene at a zenith angle of 4°.

We note though that cirrus, particularly thin cirrus, is quite prevalent and presents a potential problem to modeling dust effects. The effect of cirrus on high spectral resolution radiance measurements manifests itself as an increasing attenuation in BT with decreasing wavenumber on the low wavenumber half of the TIR atmospheric window [*Liou*, 2002; *Yang et al.*, 2001]. This is counter to the effect of dust aerosol whose attenuation decreases with decreasing wavenumber in this same spectral region [*Sokolik*, 2002]. The slope of the BT spectrum between 750 cm^{-1} and 950 cm^{-1} should therefore provide an ability to discriminate between dust and cirrus.

We also observed that certain spectral regions in the 750 – 1250 cm^{-1} atmospheric window had consistently larger model radiance values than measured data in the clear-sky cases. The possibilities of stratospheric sulfate aerosol and sea salt aerosol were investigated; however, neither of these possibilities could explain the differences. We then noted that the areas where the modeled radiance consistently exceeded the measured radiance correspond to the regions of spectral absorption by CFCs. The MODTRAN5 default vertical profiles of CFCs are based on a collection of 1990 profiles of CFCs, and are significantly below the current atmospheric CFC conditions. When using the MODTRAN5 default vertical profiles of CFCs, the BT difference between the modeled and the measured radiance was between 0.35 K and 0.5 K in the absorbing regions of CFCs. If no CFCs were included in the model, the BT difference in the absorbing regions of the CFCs can reach over 1.0 K as has been noted in Interferometric Monitor for Greenhouse Gases (IMG) data [*Lubrano et al.*, 2002]. Figure 4.2 shows the spectral differences between a clear-sky open-ocean BT spectrum modeled using the 1990 CFCs data in MODTRAN5 and the same conditions modeled using the Michelson Interferometer for Passive Atmospheric Sounding (MIPAS) determined CFCs data [*Remedios et al.*, 2007]. The figure also shows the difference between a clear-sky open-ocean BT spectrum modeled using no CFCs at all and using the MIPAS CFC data.

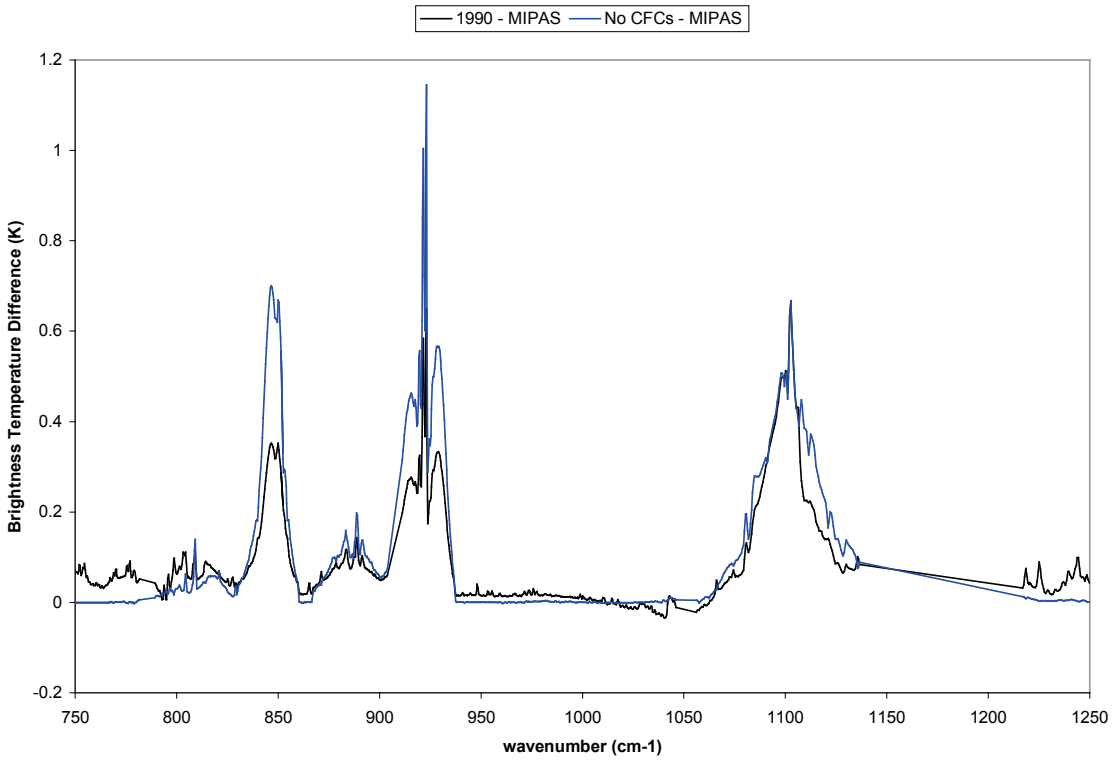

Figure 4.2. The brightness temperature difference between the default 1990 CFC levels and the MIPAS reference atmosphere levels, and the brightness temperature difference between an atmosphere with no CFCs and the MIPAS reference atmosphere.

Because the CFCs' absorbing regions in the TIR window overlap spectral absorbing regions of certain mineral species, our results indicate that it is critical to have a good approximation of the levels of CFCs in the atmosphere. Inaccurate modeling of levels of CFCs could result in confusion with mineral absorption features and the subsequent overestimation of mineral concentration or inaccurate microphysical properties.

4.5 SHADE ARIES Modeling and Analysis

We analyzed two ARIES datasets collected on a pass just above a dust plume over open-ocean off the coast of Africa during the SHADE campaign [*Highwood et al.*, 2003].

Coincident with these collects, dropsondes were released to gather information on the atmosphere below the plane at the time of the collect. The ARIES data have the benefit of providing measurements over a warm uniform surface with well known spectral characteristics and a single dust layer. The two datasets, 1229 and 1301, are from Flight A797 taken during a straight and level run between Dakar and Sal just above the dust plume. Figure 4.3 is a Google Earth image showing the locations of the two ARIES measurements.

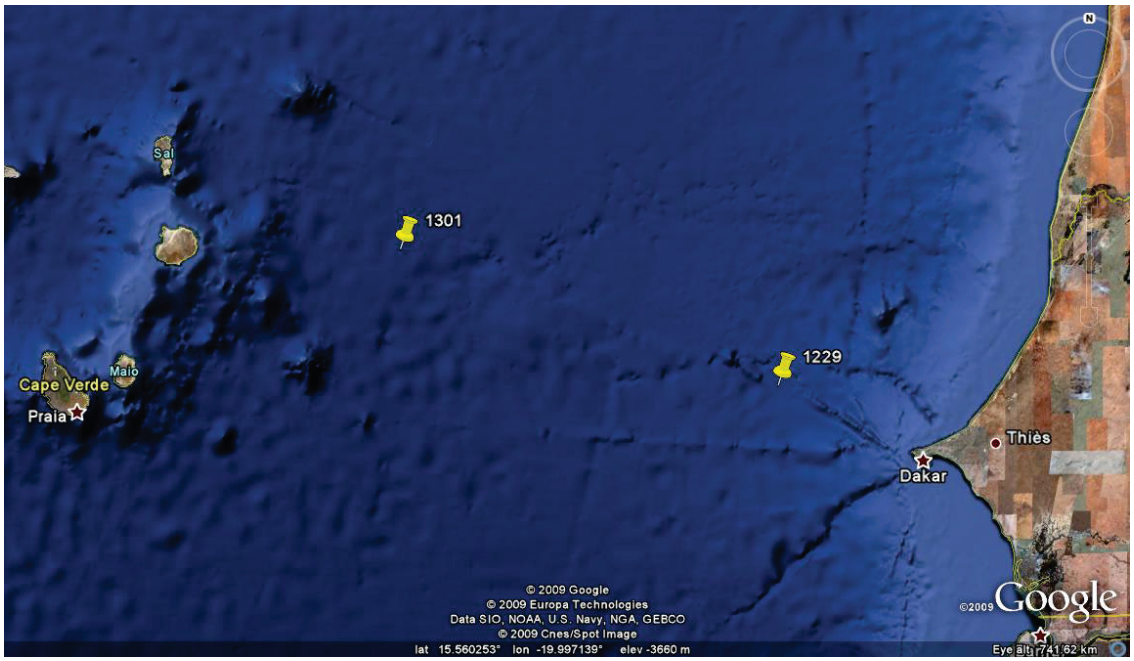

Figure 4.3. Google Earth image of the locations of the ARIES sensor during flight A797 for the two datasets being analyzed.

Figures 4.4 and 4.5 are Moderate Resolution Imaging Spectroradiometer (MODIS) visible composite and aerosol optical depth images that show the dust plume at 1120 GMT and 1300 GMT, respectively. The two ARIES datasets were acquired at 1229

GMT and 1301 GMT. The approximate location of the datasets is marked in the visible composite image by a red dot.

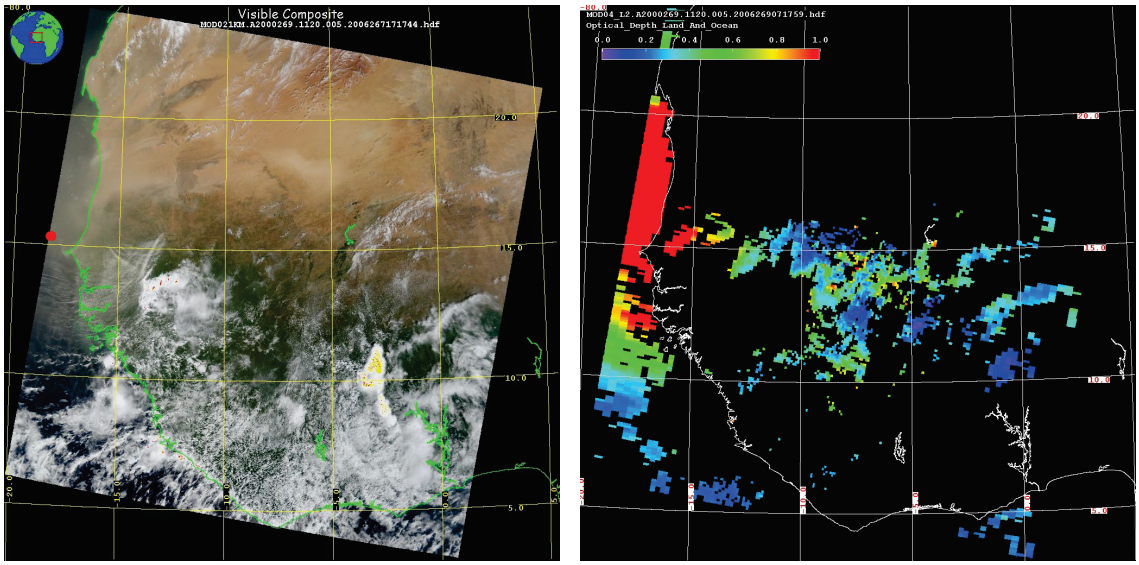

Figure 4.4. MODIS visible composite image, taken at 1120 GMT and covering the start of the flight line, and aerosol optical depth image of the dust plume measured by the ARIES sensor during flight A797

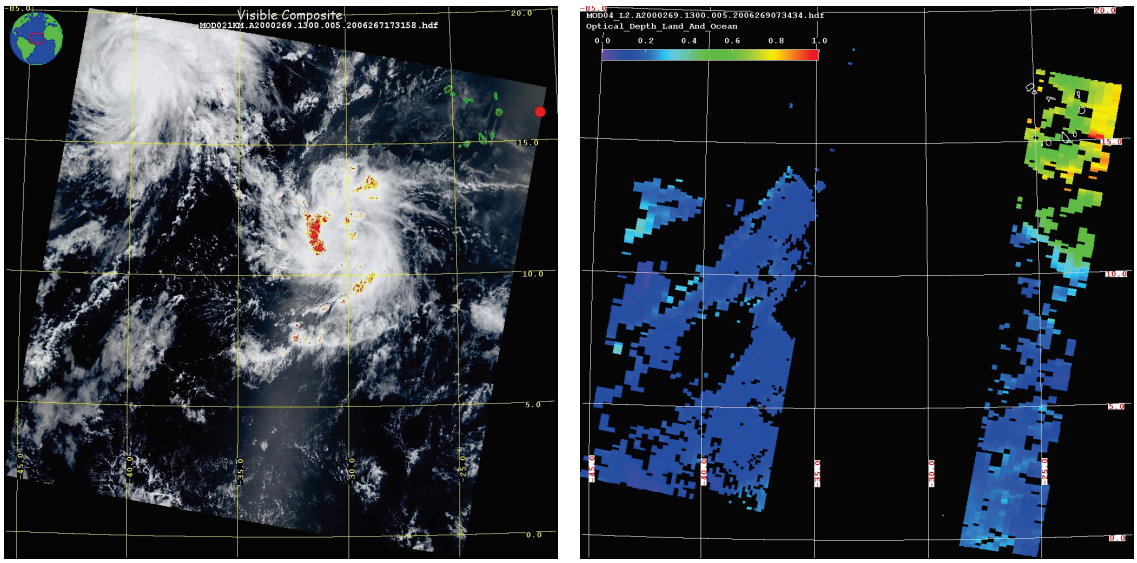

Figure 4.5. MODIS visible composite image, taken at 1300 GMT and covering the start of the flight line, and aerosol optical depth image of the dust plume measured by the ARIES sensor during flight A797

Before converting the dropsonde data into a MODTRAN5 user-defined atmosphere format, the data needed to be resampled to a lower vertical resolution while still maintaining the most significant information. This was accomplished using a software program from the National Center for Atmospheric Research (NCAR) called ASPEN (Atmospheric Sounding Processing ENvironment) available from the NCAR website http://www.eol.ucar.edu/rtf/facilities/software/aspen/aspen.html (6/2004). The temperature and relative humidity profiles from the dropsondes as processed by the ASPEN software are shown in Figures 4.6a-b.

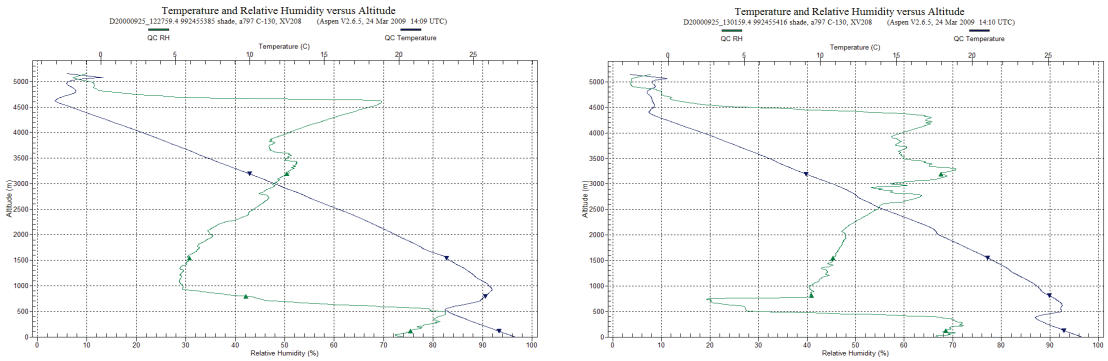

Figure 4.6a and b. Temperature and relative humidity profiles from dropsondes released just prior to collection of the datasets being analyzed.

For the ozone vertical profile we use the data reported by *Highwood et al.* [2003]. The surface temperature was estimated based on the brightness temperature at the high wavenumber edge of the TIR window where the aerosol effect is minimal and was chosen so that the clear-sky radiance just exceeded the measured radiance in this region.

The clear-sky spectrum was modeled as a nadir viewing sensor at the height of the C-130 aircraft using the 0.1 cm^{-1} MODTRAN5 band model. Since no sensor spectral channel response function was available for the ARIES instrument, a standard technique

of modeling the sensor spectral channel response as a triangular function was used. The channel-to-channel spacing of the ARIES instrument is approximately 0.5 cm^{-1}, so 0.5 cm^{-1} full width half maximum triangular response functions centered at each ARIES channel center were used to generate the MODTRAN5 clear-sky spectrum at the ARIES instrument resolution. Figure 4.7 shows the BT spectrum of the ARIES data and the corresponding MODTRAN5 clear-sky BT spectrum. The effect of the dust plume is readily apparent.

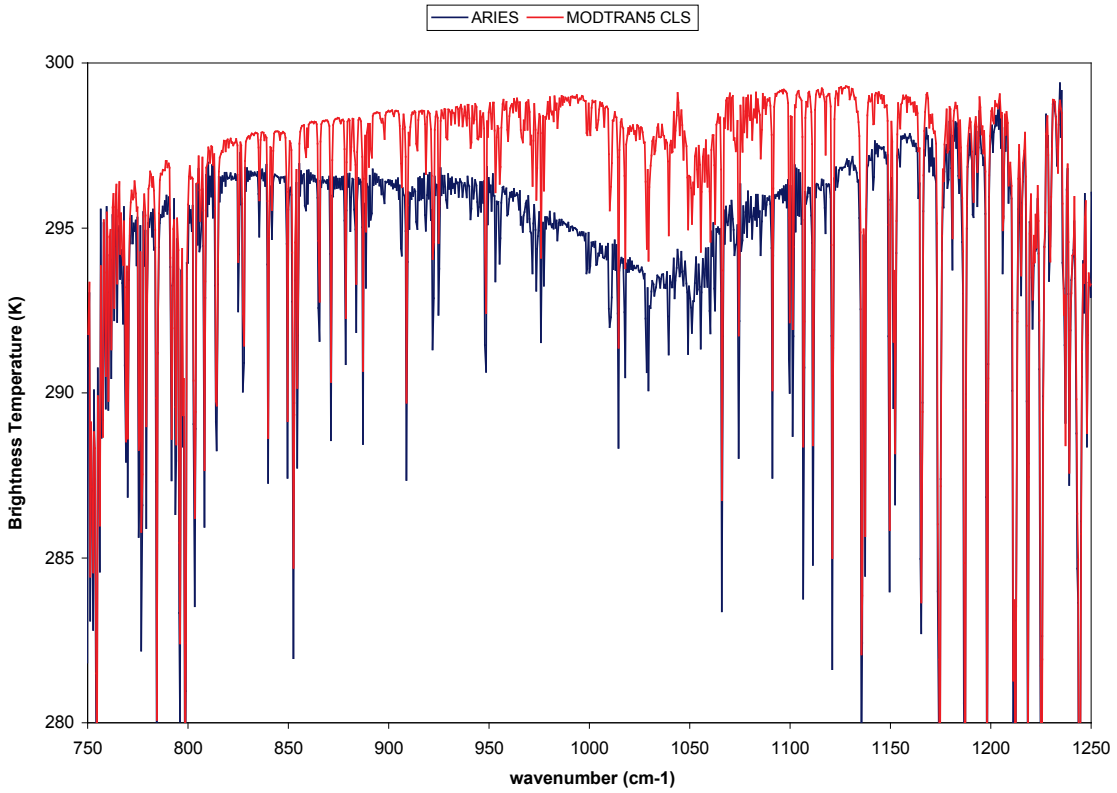

Figure 4.7. Brightness temperature spectrum over a dust plume as measured by the ARIES instrument, A797_1229, and a MODTRAN5 modeled clear-sky brightness temperature at the ARIES resolution for the recorded atmospheric conditions.

Defining a BTD spectrum as simply the difference between the modeled clear-sky radiance and the measured radiance produces a very "noisy" BTD spectrum. The "noise" in such a BTD spectrum results from a combination of sensor noise, inaccuracies in the sensor response function, errors in the modeling of trace gas species, etc. To avoid these problems, the BTD spectrum used in our new approach for characterizing dust aerosol from high spectral resolution radiances is based on the difference between the measured and modeled radiance within what has been termed microwindows. These microwindows are subregions of an atmospheric window where molecular absorption is minimal allowing the effects of the aerosol dominate. The microwindows used for the ARIES analysis (see Table 4.1) were defined by examining a transmission spectrum in the 750 – 1250 cm^{-1} region at the resolution of the ARIES sensor and finding regions that had high transmission and a minimum of 5 spectral samples. Because of noise in the measurements, enough samples must be present within a microwindow to allow for the removal of outliers while providing a sufficient number to form an average BTD within the microwindow.

Table 4.1 ARIES Microwindows within the TIR Atmospheric Window

Lower Limit (cm-1)	Upper Limit (cm-1)
771.4	774.9
777.6	778.8
780.1	783.1
786.3	790.3
800.3	802.4
804.2	807.2
809.0	813.0
815.7	824.1
829.3	834.7
836.5	839.0
840.8	841.4
842.8	848.7
850.5	851.6
855.8	857.8
860.1	864.1
866.4	870.4
872.7	877.6
879.4	880.5
881.8	882.4
884.7	886.3
887.6	888.2
889.0	889.7
892.4	895.4
898.7	904.6
911.7	913.3
915.0	917.6
919.4	920.5
922.8	924.4
925.7	927.7
929.6	939.8
941.6	943.7
949.8	952.3
953.7	954.7
956.6	958.6

Lower Limit (cm-1)	Upper Limit (cm-1)
960.4	965.4
985.0	989.5
990.8	997.2
1001.4	1003.0
1005.3	1006.8
1011.5	1013.6
1015.4	1016.9
1018.8	1026.1
1033.7	1037.7
1041.9	1047.8
1053.0	1054.6
1057.8	1059.4
1060.7	1062.3
1063.1	1065.2
1067.9	1071.4
1076.6	1084.0
1086.3	1089.8
1092.5	1098.4
1102.2	1105.7
1108.0	1110.0
1112.8	1116.8
1118.1	1119.7
1122.9	1129.3
1130.6	1132.7
1139.3	1148.1
1155.2	1163.5
1167.7	1170.8
1177.4	1179.9
1181.2	1183.8
1188.5	1190.1
1191.9	1196.8
1200.5	1209.8
1214.0	1217.1

Figure 4.8 shows the difference in BT between the clear-sky MODTRAN5 radiance and the ARIES radiance. Overlaid on this plot is the BTD when only the microwindow regions are considered.

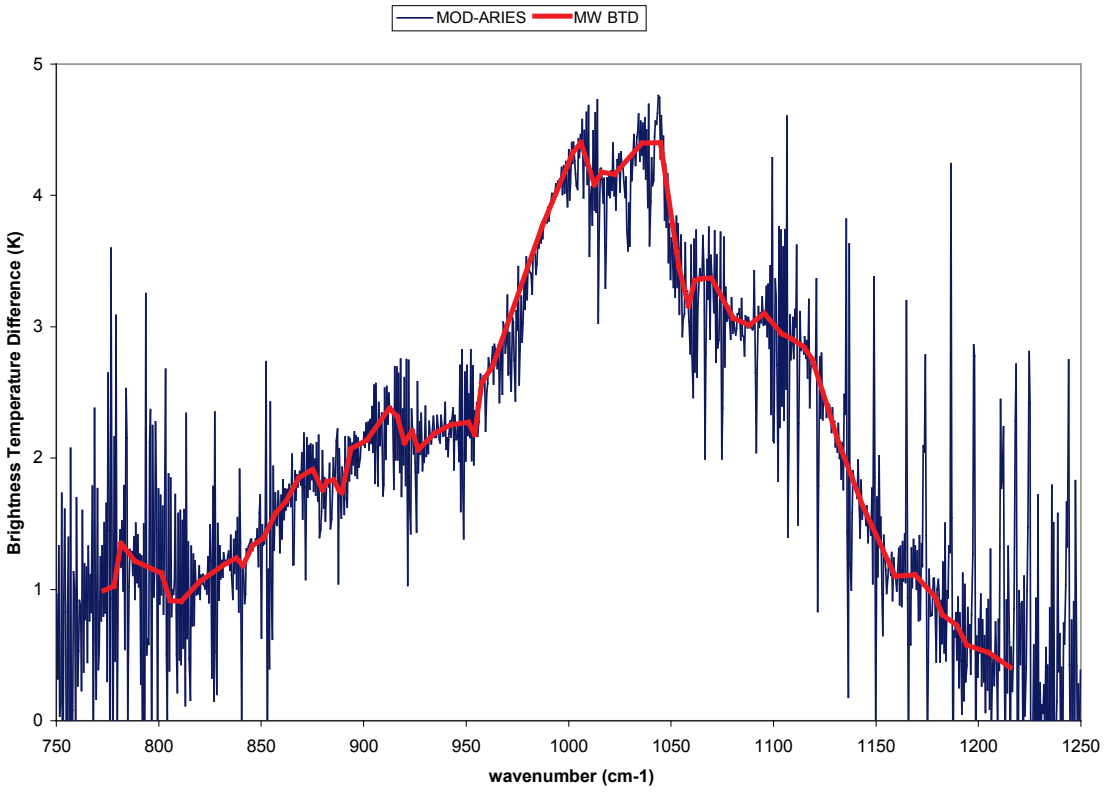

Figure 4.8. BTD spectra between MODTRAN5 clear-sky and ARIES for dataset A797_1229 at full sensor resolution and for the microwindow regions.

Figure 4.9 shows the ARIES BT spectrum for the A797_1301 case with the corresponding clear-sky radiance as modeled by MODTRAN5 using data from the dropsonde. The BTD spectra at full resolution and from the microwindows are shown in Figure 4.10.

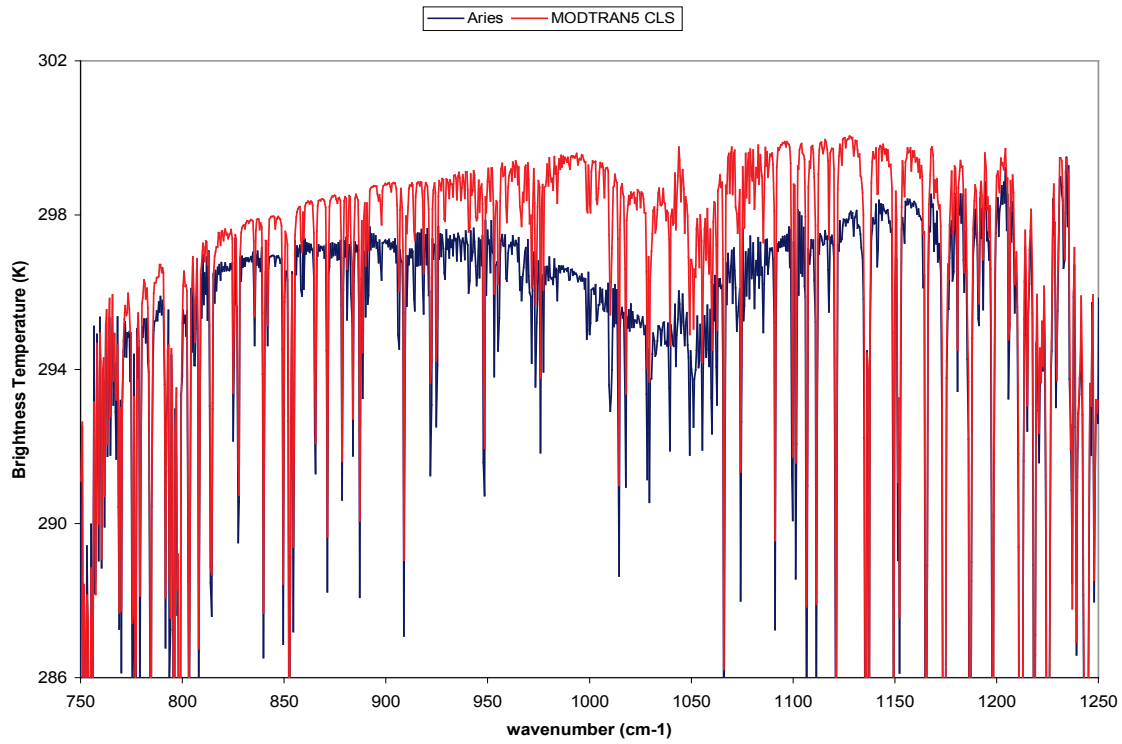

Figure 4.9. Brightness temperature spectrum over a dust plume as measured by the ARIES instrument, A797_1301, and a MODTRAN5 modeled clear-sky brightness temperature at the ARIES resolution for the recorded atmospheric conditions.

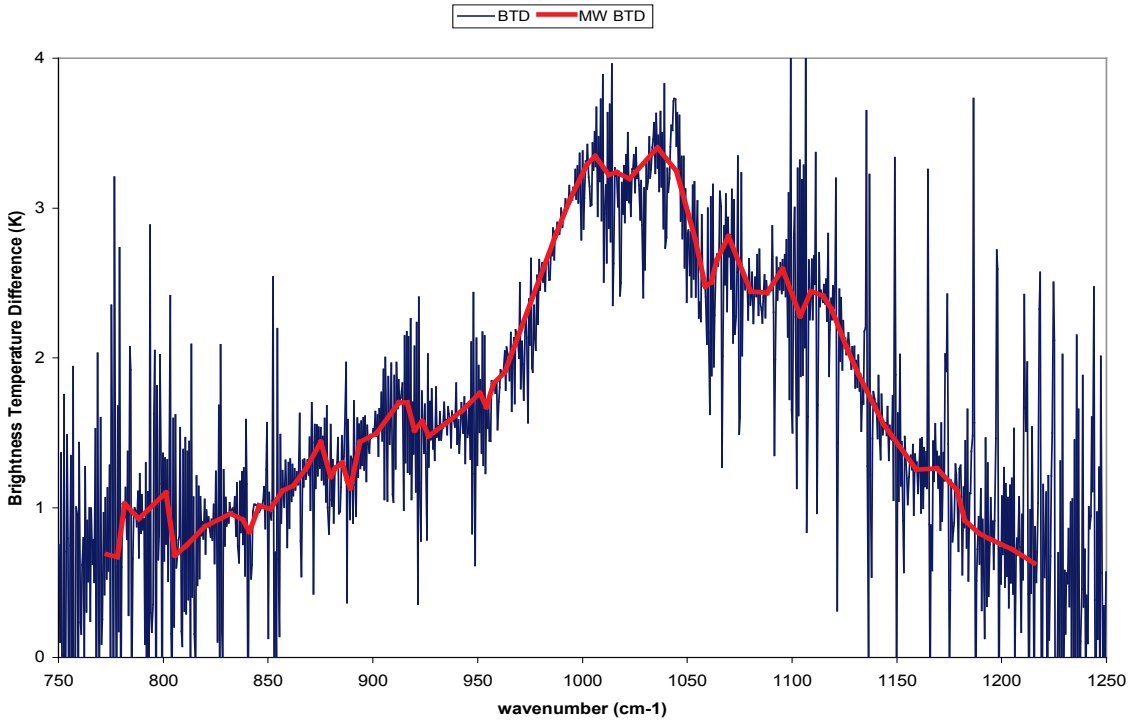

Figure 4.10. BTD spectra between MODTRAN5 clear-sky and ARIES for dataset A797_1301 at full sensor resolution and for the microwindow regions.

As previously noted, in the TIR the spectral BTD between a clear-sky spectrum and the spectrum where a single dust layer is present is highly correlated spectrally to the dust extinction coefficient spectrum. From the modeling in Chapter 3 the width of the aggregate Si-O spectral feature and the continuum of the extinction coefficient spectrum should provide information on the aerosol size distribution. Additionally, the BTD spectrum should provide information on the mineral components that are present in the mixture based on the individual mineral spectral features present or not present in the BTD.

The study of Saharan dust source clay mineralogy by *Goudie and Middleton* [2001] and the Dust Outflow and Deposition to Ocean (DODO) campaign data [*Formeneti et al.*, 2008] indicate that the most likely components of the Western African dust plume measured by ARIES are illite, kaolinite, quartz, feldspar (potassium and/or plagioclase), chlorite, calcite or dolomite and iron oxides. In the TIR, hematite has very low spectrally neutral absorption, while goethite has two small absorbing features around 800 cm^{-1} and 900 cm^{-1}. These features overlap the quartz features at 800 cm^{-1} and the calcite and kaolinite features at 875 and 916 cm^{-1}, respectively. Research has shown that iron oxides are typically aggregated with clay minerals, but that they do not significantly alter the spectral signature of the pure clays [*Lafon et al.*, in preparation]. Therefore iron oxides will not be considered in our TIR dust modeling.

Examining fine size mode optical properties of pure mineral species generated using Mie theory, we see that the correspondence of the peaks in the extinction coefficient and the peaks in the BTD spectrum is not very good as shown in Figure 4.11.

These Mie optical properties were computed for a lognormal size mode with a median radius of $r_g = 0.65$ μm and mode geometric standard deviation of $\sigma_g = 2$.

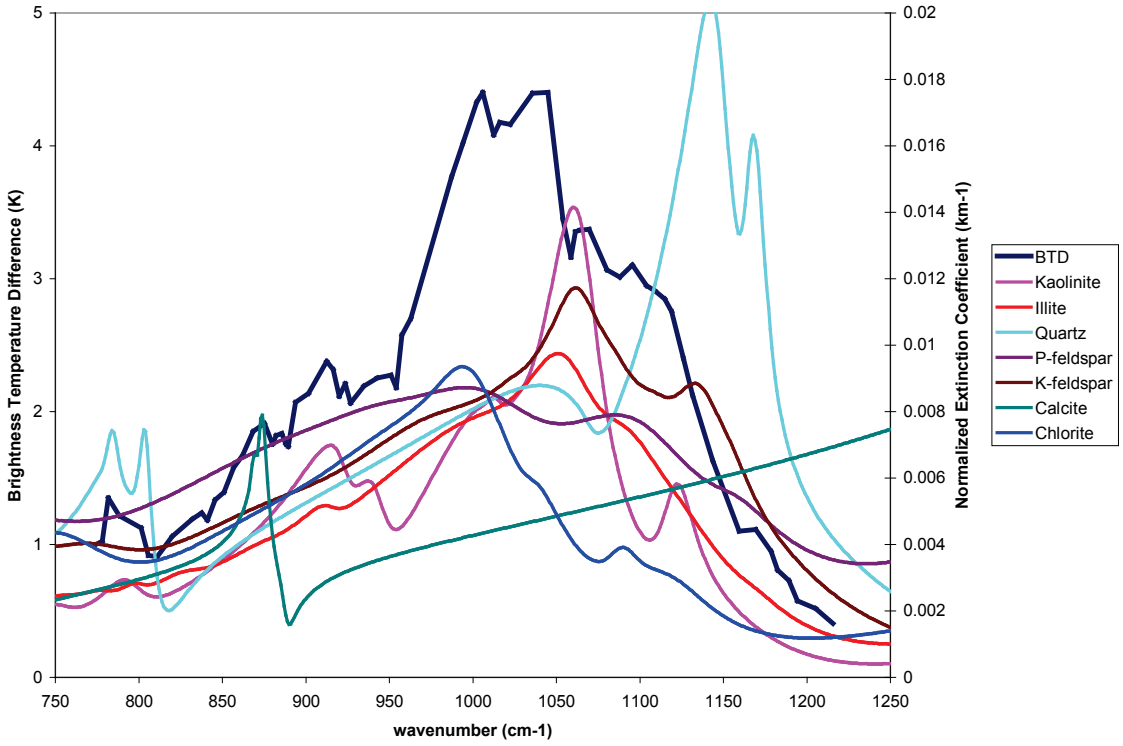

Figure 4.11. A797_1229 BTD spectrum and individual mineral volume extinction coefficient spectra computed using Mie theory for likely mineral components.

The most significant spectral features apparent in and in-common between the BTD spectra for the two datasets, shown in Figures 4.8 and 4.10, occur at about 781, 800, 873, 913, 1006, 1035, 1069, 1095, 1109, and 1169 cm^{-1}. The four lowest wavenumber peaks correspond to the minor peaks in the extinction spectra of quartz, calcite, and kaolinite. However, the major peaks do not correspond to any of the remaining peaks in the BTD spectra. In fact, an extinction spectrum made up of an external mixture of these components would have its major peaks significantly displaced to higher frequencies. As

an example of this, the Level 3 Niger dust aerosol model was implemented using the LAARI optical constants and Mie theory for a lognormal size mode with r_g = 0.65 μm and σ_g = 2. The extinction coefficient, β_e, of this mixture and the A797_1229 data BTD spectrum are plotted in Figure 4.12. This mixture model would obviously be unable to accurately reproduce the at-sensor radiance observed by the ARIES sensor.

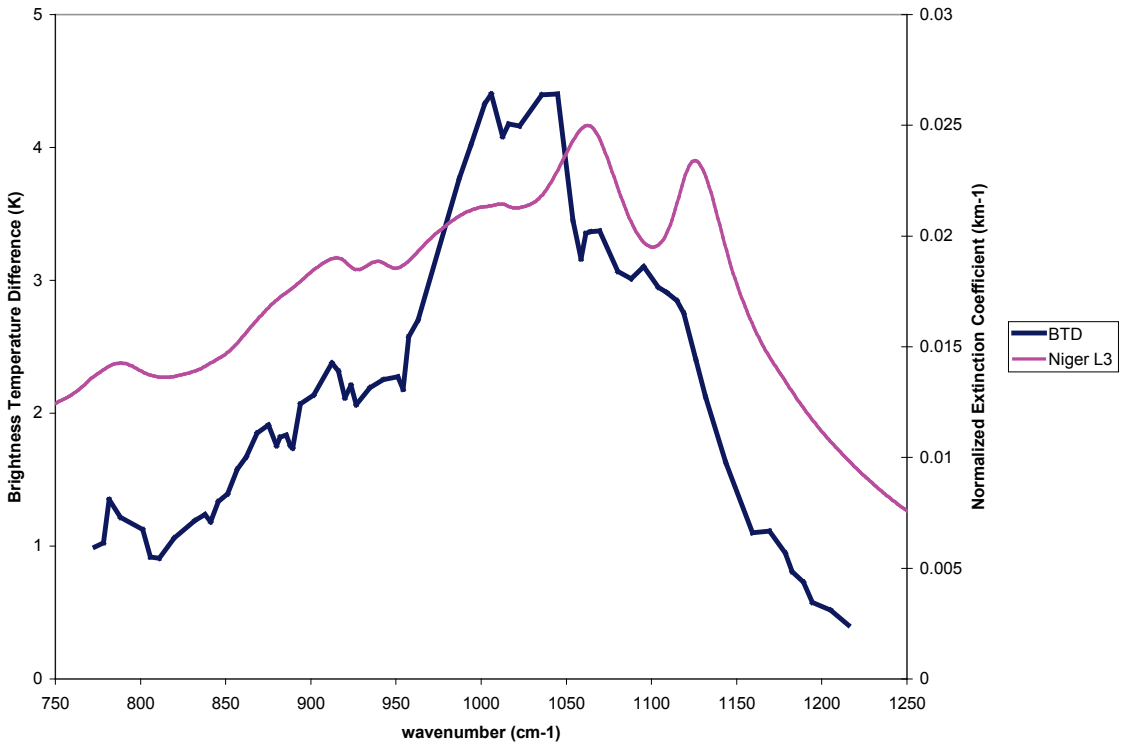

Figure 4.12. A797_1229 BTD spectrum and the Niger Level 3 aerosol model volume extinction coefficient spectrum computed using Mie theory.

The peaks in the BT spectra that have no correspondence to any peaks in the individual mineral Mie-generated extinction coefficient spectra do however correspond to major and minor peaks for quartz, illite, kaolinite, and calcite as measured in the laboratory by *Hudson et al.* [2008a, b]. The double peak at 1006 and 1035 cm^{-1}

corresponds to the major double peak of albite as measured in transmission spectra (e.g., [*Couty and Velde*, 1986; *McKeown*, 2005]). Unfortunately, optical constants for albite are not available in the literature.

Radiances modeled using an external mixture of Mie-generated pure mineral optical properties are therefore incapable of fitting well the spectral region from 1000 – 1250 cm^{-1}, and would only poorly fit the spectral region from 750 – 1000 cm^{-1}. It can be concluded that the non-spherical nature of the dust particles must be taken into account in order to produce optical properties capable of accurately modeling any dust-affected measured spectrum.

Researchers have reported that dust particles, particularly phyllosilicates, often have characteristic dimensions, i.e. length/width/height, which have a ratio of major to minor lengths on the order of 1.6/1 and are approximately oblate in shape (e.g., [*Kandler et al.*, 2007; *Kandler et al.*, 2009; *Chou et al.*, 2008]). When T-matrix calculations were done for shape factors on this order the difference from Mie theory was only minimal, and definitely not enough to align the extinction coefficient peaks with laboratory data or ARIES BTD spectra. The T-matrix results from Chapter 3 indicated that considering a shape factor in the range of 4 to 5 gave results that corresponded extremely well to the peaks measured in the laboratory by *Hudson et al.* [2008a, b]. Since the peaks in the ARIES BTD spectrum can only be due to the mineral components we decided to generate fine mode extinction coefficients for the likely phyllosilicate mineral components using T-matrix with a shape factor of 5. Figure 4.13 presents the modeling results and shows very good correspondence between the pure mineral extinction coefficient peaks and the primary peaks in the A797_1229 BTD spectrum.

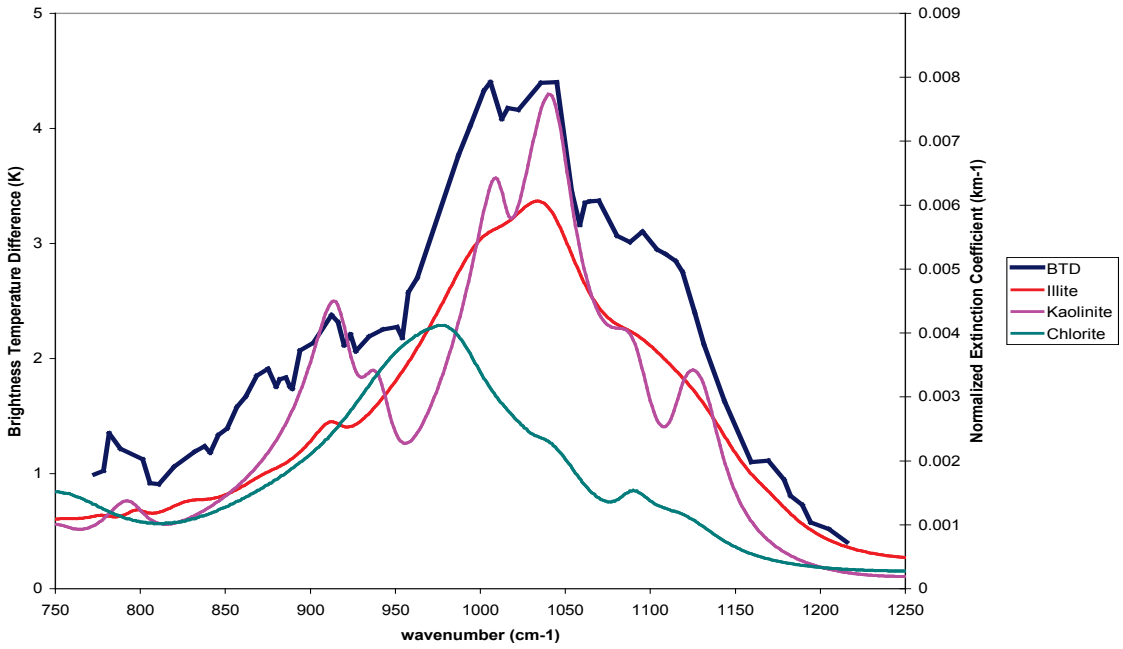

Figure 4.13. A797_1229 BTD spectrum and clay mineral extinction coefficient spectra computed using T-matrix with a shape factor of 5.

For quartz, T-matrix was able to converge for all frequencies within this spectral range when the limits of integration for the size distribution were set to the 2.5-sigma limits, i.e. $r_g \pm 2.5\ln\sigma_g$. With these limits of integration we again observed that a shape factor of 4 to 5 led to the main peak in the β_e spectrum of quartz coinciding with the location of the main peak as measured by *Hudson et al.* [2008b]. The result is also close to that generated by CDE calculations. Unfortunately, the T-matrix calculations produce a secondary peak at 1210 cm^{-1} that does not appear in any measurements of quartz. As discussed in Chapter 3, it is likely that a distribution of oblate spheroids better represents real quartz particles and also would result in a spectrum that does not have this peak. Since the BTD spectra for both of the ARIES cases do not show evidence of a large fraction of quartz, based on the spectral features present and their magnitudes, we decided to form a hybrid quartz dataset using T-matrix data with a shape factor of 5 for

the spectral region 750 – 1163 cm^{-1} and scaled Mie data from 1164 – 1250 cm^{-1}. When this hybrid quartz extinction coefficient spectrum and a Mie generated calcite spectrum are added to the plot as shown in Figure 4.14, the correspondence to all of the major spectral features is immediately obvious. The exception is the sharp peak at 1006 cm^{-1}, which is likely explained by albite.

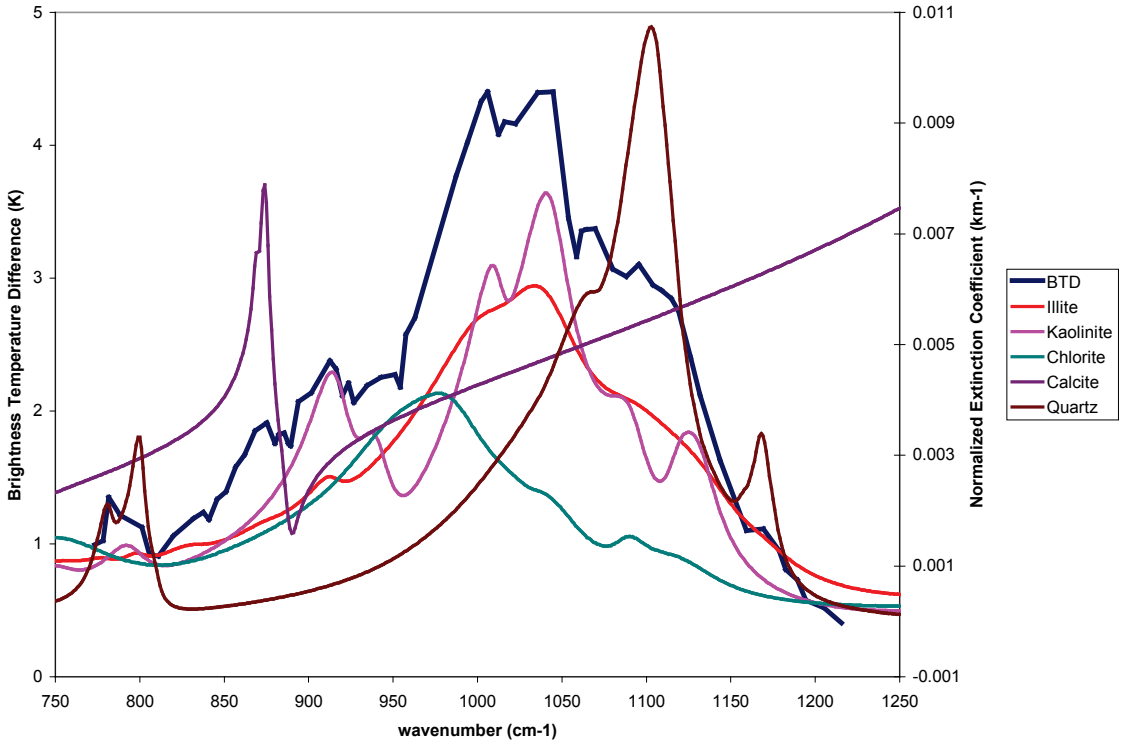

Figure 4.14. A797_1229 BTD spectrum and likely mineral extinction coefficient spectra computed using T-matrix with a shape factor of 5.

Given the findings above, we conclude that the T-matrix technique is a more appropriate method than Mie theory for modeling the optical properties of individual minerals at high spectral resolution in the TIR.

Our new technique for retrieving dust aerosol composition and size distribution information from high spectral resolution TIR data begins with matching the BTD

spectrum to the β_e spectrum of an external mixture of individual minerals whose spectral features are evident in the BTD spectrum. The number of modes and their median radii are chosen so that the mixture β_e spectrum matches the BTD spectrum. An initial guess of the particle concentration is made and the optical properties for that loading are then used together with the ancillary information on the position and thickness of the dust layer to model the radiance using the custom aerosol model in MODTRAN5. The results are compared to the measured radiance and then the composition, size distribution and loading are iteratively changed until a good fit is obtained. Ancillary data collected during one of the runs on flight A797 show that the dust plume extends from 2 km to 4 km.

In the initial attempt to model the ARIES data using T-matrix, only a submicron fine mode was used. Since the shape of a submicron external mixture extinction coefficient correlated fairly well to the BTD spectra, it was anticipated that a coarse mode would not be required to improve the fit. Initial radiance modeling results showed that even the submicron size mode was too broad across the aggregate Si-O feature. The radiance at the edges of the TIR window was fit fairly closely, but the radiance in the center of the window was not. If the aerosol concentration was increased to allow the modeled radiance in the center of the window to have a better fit, the fit on the edges became very poor. Since it has been shown in Chapter 3 that the continuum is reduced and the spectral features become sharper as the limits of integration for a size mode shrink, this modification to the modeling was investigated.

The initial limits to the size distribution were chosen so that they were large enough that increasing the limits would not change the results appreciably. By reducing

the limits of integration, the lognormal size distribution is being truncated, but it is also a more physically realistic situation. A good all around fit was obtained for the case where the size distribution limits of integration were set at $r_g \pm 2.5\ln\sigma_g$.

To obtain a good fit of the β_e spectrum to the BTD spectrum in the 875 to 975 cm^{-1} range also required the inclusion of chlorite. Although it is likely present to some extent in the dust as indicated by *Goudie and Middleton* [2001] and other studies, it is also likely acting as a surrogate to some extent for the missing plagioclase feldspar, which from transmission spectra of small particles in KBr shows a qualitatively similar spectral extinction pattern to chlorite. Plagioclase feldspar is very likely present in the form of albite or a mineral in the albite-anorthite series based on the sharp spectral doublet at 1006 and 1035-1040 cm^{-1}. The feldspars for which optical constants are available and included in the LAARI database are potassium feldspar and one plagioclase feldspar, anorthite. The anorthite optical constants have significantly larger k values on the edges of the TIR window region than the other minerals and the potassium feldspar. The optical properties generated using the anorthite data result in significant elevated baseline extinction across the entire TIR window that causes problems in getting a fit to the radiance data. Therefore, the anorthite data is somewhat suspect and is not being used.

Figure 4.15 shows the normalized β_e spectrum that best matched the ARIES A797_1301 dataset in the MODTRAN5 modeling. It is based on a combination of both fine and coarse modes. The fine mode is an external mixture of 55% illite, 13% kaolinite, 7% quartz, 10% calcite, and 15% chlorite with $r_g = 0.65$ μm and $\sigma_g = 2$. The coarse mode is an external mixture of 50% illite, 25% kaolinite, 10% quartz, 5% calcite,

and 10% chlorite with r_g = 1.5 μm and σ_g = 2. This normalized extinction coefficient is an external mixture of the two modes with a fine to coarse ratio of 97%/3%. The total number density is 27 cm^{-3}.

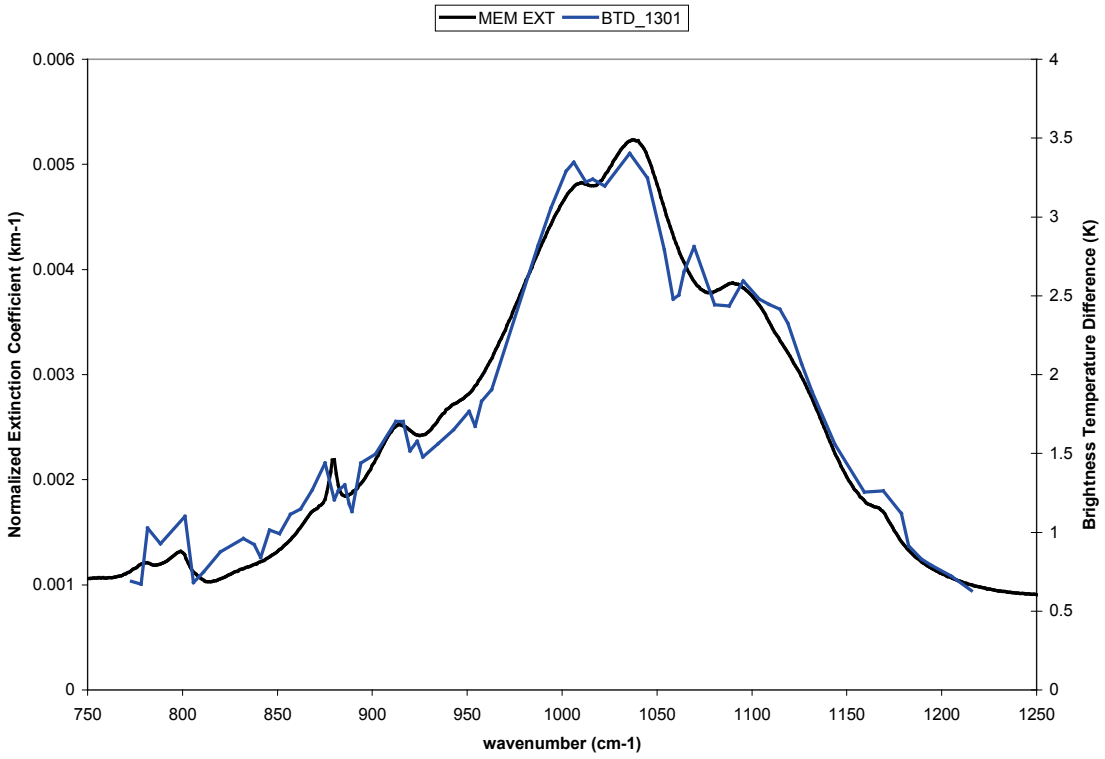

Figure 4.15. A797_1301 BTD spectrum and extinction coefficient spectrum composed of two size modes each of which is a mineralogy-based external mixture.

Using the composition and size distribution described above, a very good fit in terms of root mean square (RMS) error between the modeled and measured BT within the microwindows is obtained as can be seen in Figures 4.18a-b. Only around 1095 cm^{-1} does the modeled radiance not agree with the measured radiance to better than 0.2 K in BT. In the region around 1095 cm^{-1}, where the quartz main peak is located, the maximum absolute error is still only 0.3 K in BT and may be the result of using the hybrid spectrum for quartz.

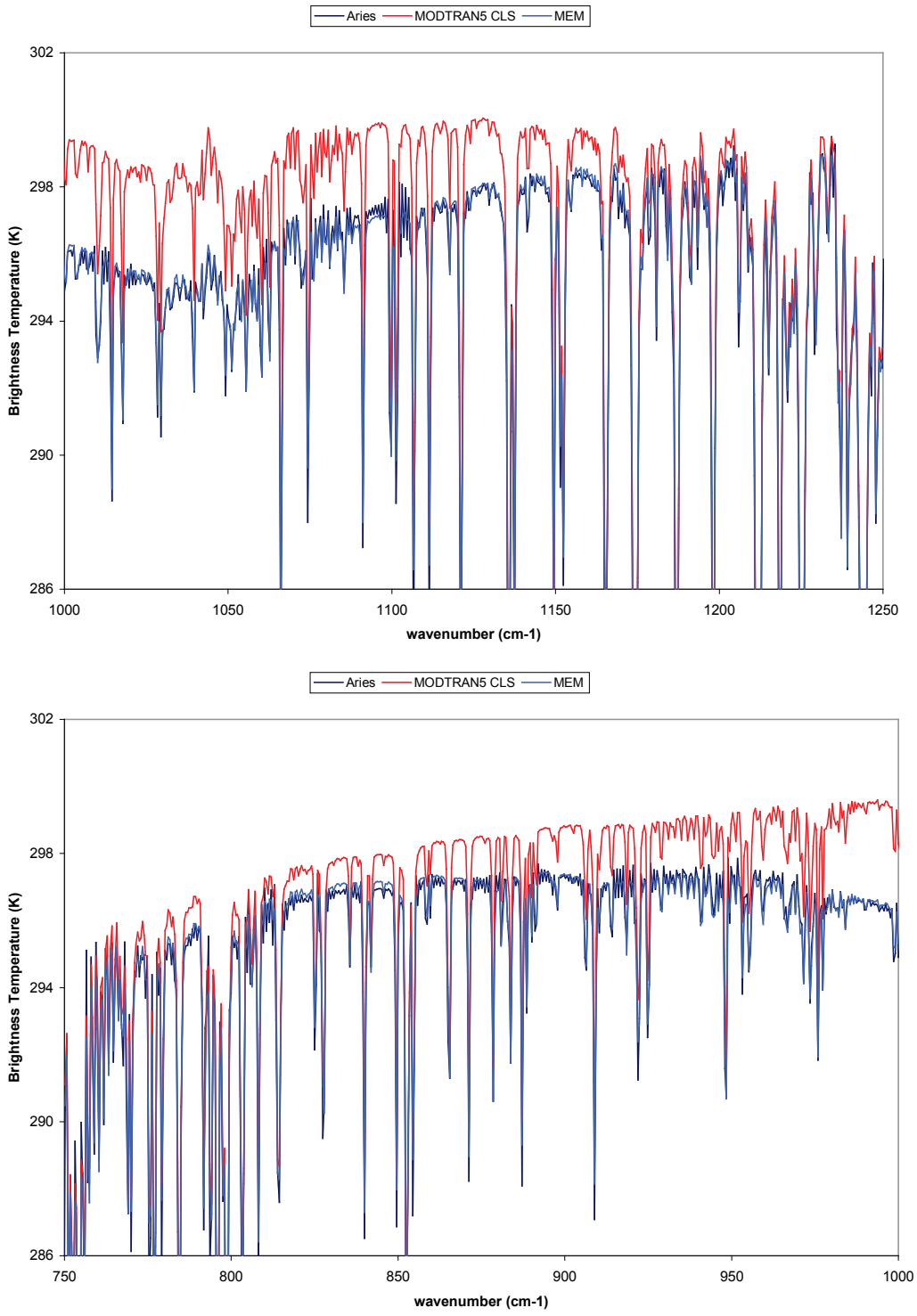

Figure 4.16a and b. BT spectrum of the ARIES A797_1301 dataset (black), the MODTRAN5 clear-sky modeled BT spectrum (red) and the MEM modeled dust plume BT spectrum (blue).

The normalized extinction coefficient that matched the BTD spectrum and provided the best fit to the ARIES A797_1229 dataset in the MODTRAN5 modeling is shown in Figure 4.17. We used an external mixture of 55% illite, 15% kaolinite, 5% quartz, 8% calcite, and 17% chlorite for the fine mode with r_g = 0.65 μm, and an external mixture of 50% illite, 25% kaolinite, 10% quartz, 5% calcite, and 10% chlorite for the coarse mode with r_g = 1.5 μm. The fine to coarse mode ratio used is 92%/8%. Figures 4.18a-b compares A797_1229 BT spectra for ARIES data and MODTRAN5 using the above mentioned external mixture of fine and coarse modes and total number density 30 cm^{-3}. As before, the fit generated is very accurate within the microwindow region with a maximum difference of about 0.4 K.

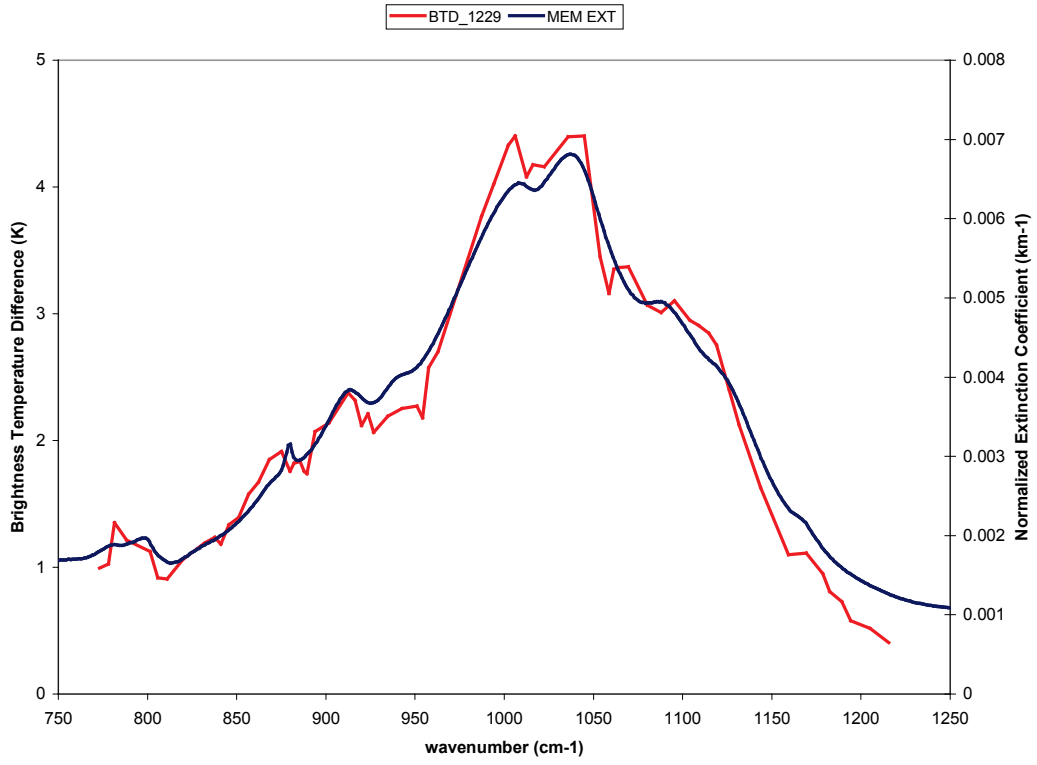

Figure 4.17. A797_1229 BTD spectrum and extinction coefficient spectrum composed of two size modes each of which is a mineralogy-based external mixture.

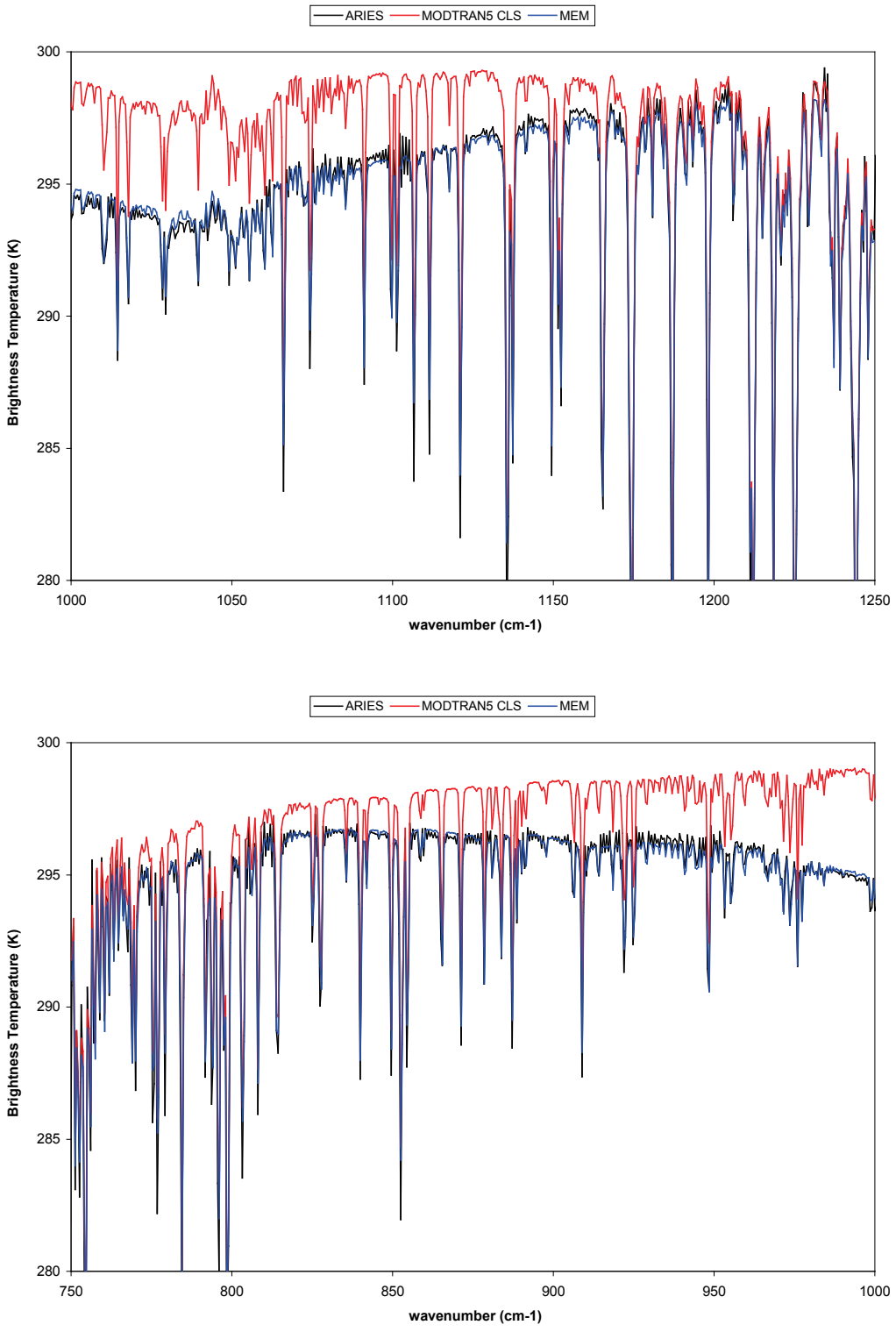

Figure 4.18a and b. BT spectrum of the ARIES A797_1229 dataset, the MODTRAN5 clear-sky modeled BT spectrum and the MEM modeled dust plume BT spectrum.

To summarize, Table 4.2 shows the dust aerosol composition and size distribution determined by our new technique for the two ARIES datasets.

Table 4.2 Size distribution and composition retrieved for dust layer measured by ARIES

Pixel	Mode	Median Radius (μm)	illite	kaolinite	quartz	calcite	chlorite
A797_1301	Fine	0.65	55%	13%	7%	10%	15%
	Coarse	1.5	50%	25%	10%	5%	10%
A797_1229	Fine	0.65	55%	15%	5%	8%	17%
	Coarse	1.5	50%	25%	10%	5%	10%

We now examine the ability of bulk material refractive index data to accurately reproduce observed high spectral resolution radiances. Mie theory is used to calculate optical properties that are based on the Volz Saharan dust refractive index (VRI), which was used by the majority of past studies (see Chapter 2). Because the Volz optical constants are slowly varying functions of frequency, the spectral differences between extinction coefficients computed with Mie theory and with T-matrix are negligible. We begin the analysis using the same size distribution modes as was used in the MEM model analysis to allow for a more direct comparison to the MEM model results.

The first ARIES case considered is the A797_1301 dataset. We use the same atmospheric and surface conditions as used previously for the clear-sky and MEM modeling. In examining the spectral extinction coefficients for the coarse and fine modes and comparing these to the BTD it is obvious that the VRI coarse mode will only degrade the fit to the BTD spectrum. So only a single mode with $r_g = 0.65$ μm and $\sigma_g = 2$ is used. Figure 4.19 shows the spectral extinction coefficient that was generated using the Volz data with an aerosol number concentration of 20 cm^{-3}, as well as the best fit MEM model

extinction coefficient for a total number concentration of 27 cm^{-3}, and the BTD spectrum for the A797_1301 dataset.

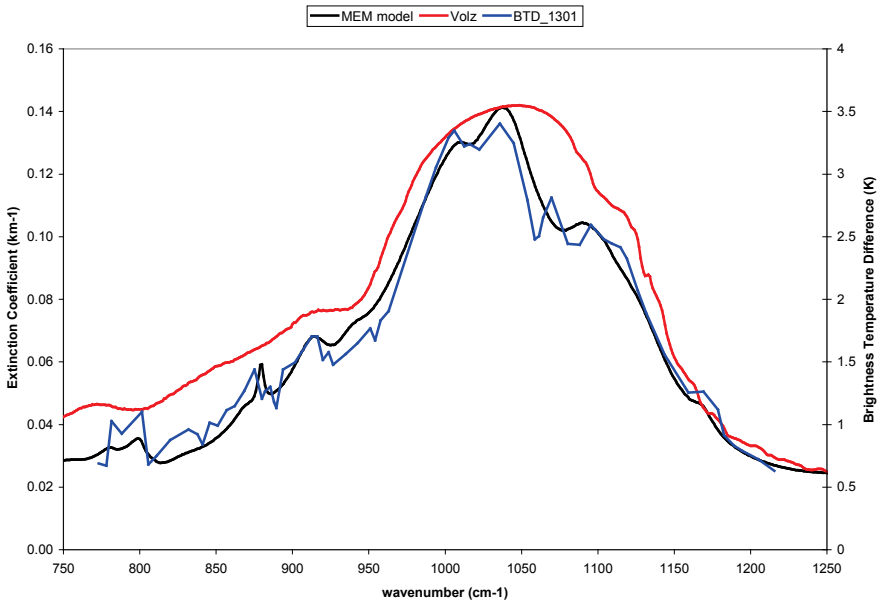

Figure 4.19. A797_1301 dataset BTD spectrum (blue), extinction coefficient spectrum based on the Volz optical constants for Saharan dust computed using Mie theory (red), and best fit MEM model extinction coefficient (black).

The extinction spectrum based on the Volz data generally has the same general shape as the BTD, but not the individual mineral spectral features, suggesting that the fit on "average" could be fairly good but that it would be incapable of matching the individual mineral spectral features. Figures 4.20a-b show the results of the MODTRAN5 calculations for the loading of 20 particles cm^{-3}, which gave a good RMS fit in the microwindows to the measured spectrum.

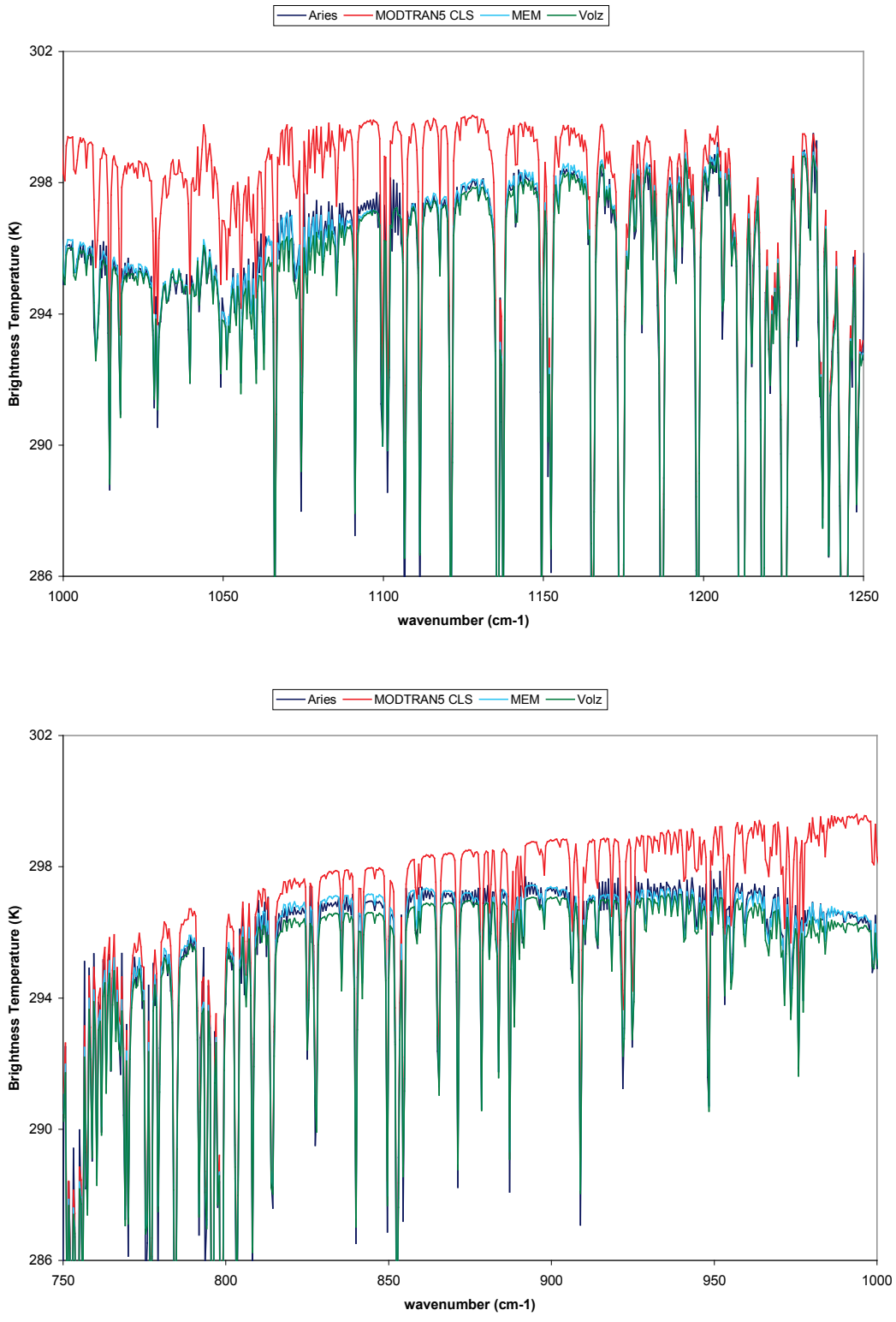

Figure 4.20a and b. BT spectrum of the ARIES A797_1301 dataset, the MODTRAN5 clear-sky modeled BT spectrum, the MEM modeled BT spectrum and the best fit VRI BT spectrum.

There are clear differences in fit between the VRI and MEM models. In the 1000 – 1050 cm^{-1} and 1100 – 1250 cm^{-1} spectral regions, the match with the VRI model is nearly as good as the MEM model of pure mineral species. In the 750 – 1000 cm^{-1} spectral range the MEM model provides a significantly better fit. There is also a notable lack of fit for the VRI model in the regions of individual mineral spectral features. The fit in the 750 – 1000 cm^{-1} spectral region could be improved by decreasing the median radius of the size distribution and correspondingly increasing the particle concentration. This would result in a spectral signature for the VRI extinction coefficient that better matches the BTD spectral signature by "narrowing" the aggregate Si-O spectral feature in the VRI extinction coefficient and reducing the extinction at the edges of the TIR window relative to the center, but it would still not capture the finer mineral spectral features. The bottom line is that the dust aerosol signature at high spectral resolution is more complicated than the VRI signature. The shape of the dust signature has as much or more to do with composition as it does with size distribution parameters.

From the analysis of this dataset we already see that using bulk material refractive index data versus using mineral component refractive index data leads to differences in derived/determined aerosol microphysics, specifically size distribution parameters and particle concentration. From a forward and inverse modeling perspective this could be a critical issue depending on the sensitivity of the aerosol radiative effects to the microphysics. To examine this further we also analyzed the A797_1229 dataset following the same approach. For comparison, the A797_1229 BTD spectrum, the VRI extinction coefficient and the MEM model extinction coefficient are shown in Figure 4.21. The fit to the measured BT is shown in Figures 4.22a-b.

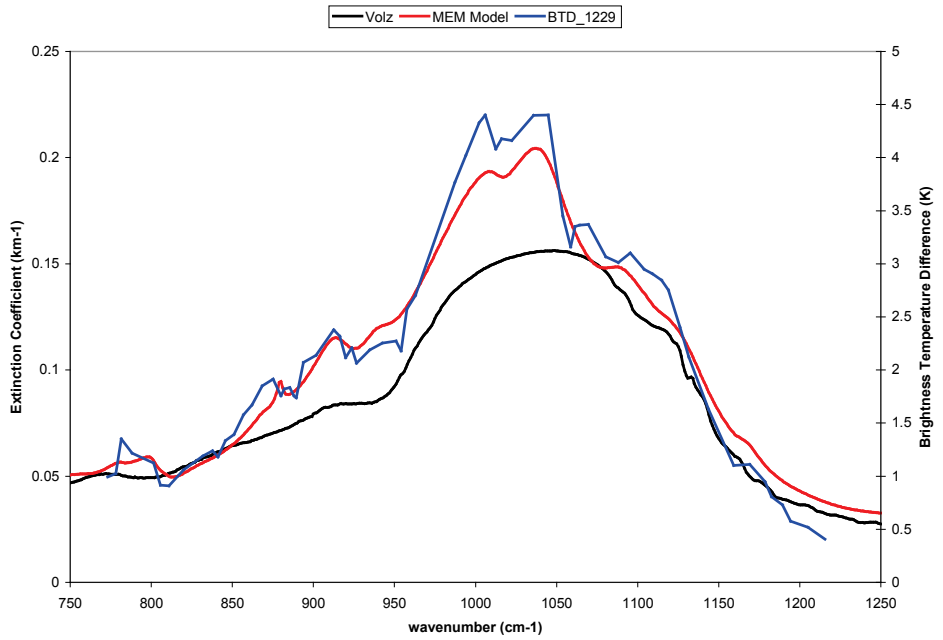

Figure 4.21. A797_1229 dataset BTD spectrum (blue), extinction coefficient spectrum based on the Volz optical constants for Saharan dust computed using Mie theory (black), and best fit MEM model extinction coefficient (red).

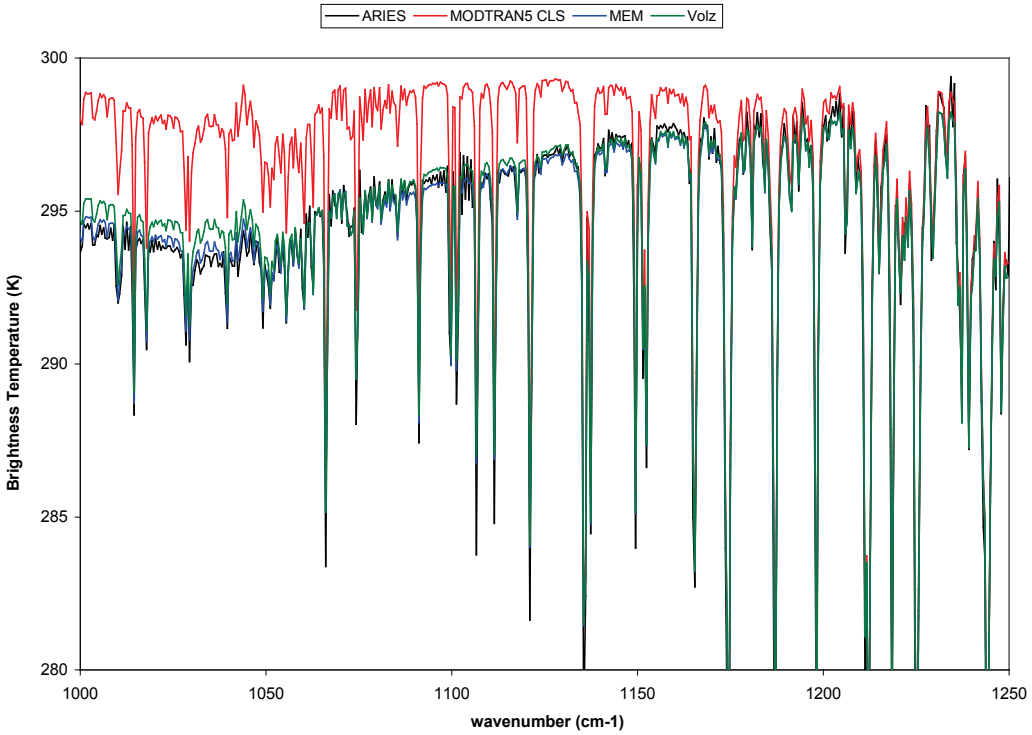

Figure 4.22a. BT spectrum of the ARIES A797_1229 dataset, the MODTRAN5 clear-sky modeled BT spectrum, the MEM modeled BT spectrum and the best fit BT spectrum using the Volz Saharan dust optical constants with Mie theory.

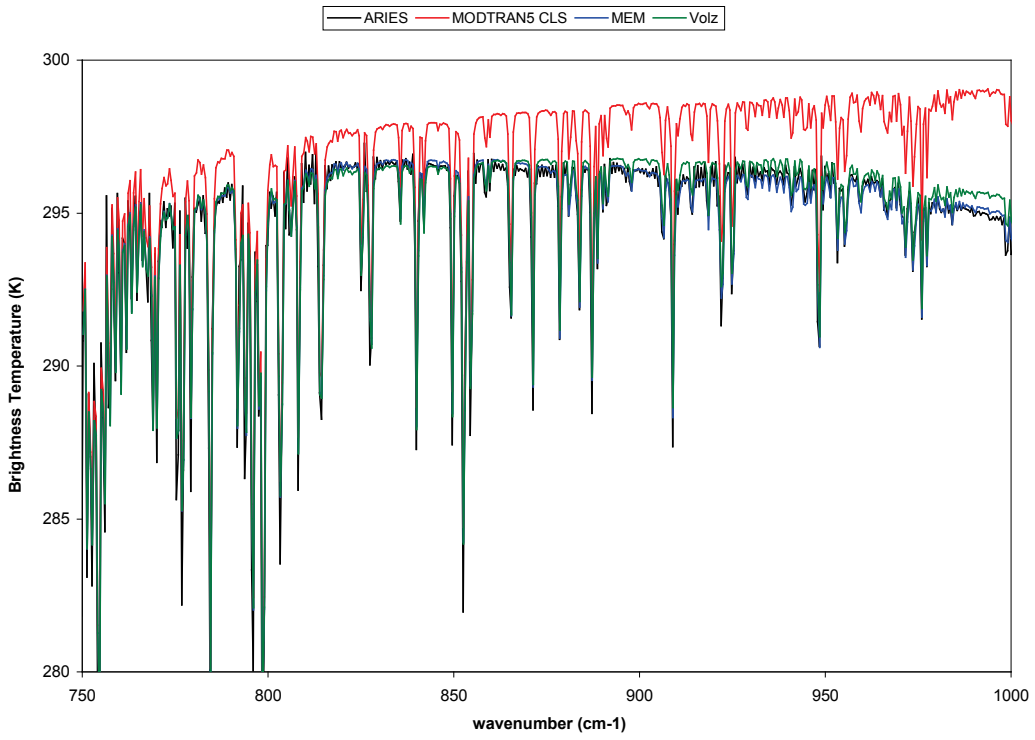

Figure 4.22b. BT spectrum of the ARIES A797_1229 dataset, the MODTRAN5 clear-sky modeled BT spectrum, the MEM modeled BT spectrum and the best fit BT spectrum using the Volz Saharan dust optical constants with Mie theory.

As Figures 4.22a-b illustrate, the fit to the measured BT in the 1050 – 1250 cm^{-1} range is nearly as good for the VRI model as it is for the MEM model. The largest deviation in BT in the microwindows is about 0.3 K for both models. Also, in the 750 – 850 cm^{-1} spectral range, the fit for the VRI model is comparable to that of the MEM model. From 850 – 1050 cm^{-1} the fit for the VRI model is not nearly as good as the MEM model fit. The largest deviation in BT is about 1 K for the VRI model and only about 0.4 K for the MEM model. Table 4.3 summarizes the size distribution parameters used in the MEM and VRI models for the two ARIES datasets analyzed here.

Table 4.3 Retrieved size distribution parameters with MEM and VRI models for ARIES

Dataset	# Size Modes MEM	Median Radius Fine Mode (μm) MEM	Median Radius Coarse Mode (μm) MEM	Fine to Coarse Mode ratio MEM	# cm-3 MEM	# Size Modes VRI	Median Radius Fine Mode (μm) VRI	# cm-3 VRI
A797_1229	2	0.65	1.5	92% / 8%	30	1	0.65	22
A797_1301	2	0.65	1.5	97% / 3%	27	1	0.65	20

The above analysis, using rigorous radiative transfer calculations with a good estimate of the atmospheric state and surface properties, has shown that a MEM model using pure mineral species optical constants is able to model the dust radiative signature for a midrange transported single layer dust plume significantly better than a model that relies on Volz Saharan dust optical constants. The MEM model can capture the individual mineral spectral features and therefore can account for changes in dust particle mineral composition. Modeling with generic refractive index data instead of using individual mineral component refractive index data also results in differences in the derived/determined aerosol microphysics.

One of the contributors to the microphysical differences is the treatment of particle shape. We saw that in order to model the dust signature using individual mineral refractive index data that the non-sphericity of dust particles must be taken into account, which means not using Mie theory. In Chapter 3 we saw that Mie generated extinction coefficients are slightly larger in magnitude than those generated using T-matrix for oblate particles with the same size distribution. As the shape factor moves away from 1 the magnitude of the T-matrix generated extinction coefficient decreases relative to Mie theory. Another contributor to the microphysical differences between the models is fitting disparate spectral signatures, namely the generic dust signature to the real world

dust spectral signature, at high spectral resolution through loading and/or size distribution parameters without the benefit of being able to adjust the spectral signature through compositional changes. In the above cases we saw that for a specified size distribution making the VRI model fit the measured radiance well in the center of the TIR window results in a poorer fit at the edges. Varying the size distribution to achieve a best fit for signatures that are not the same is not as effective as being able to alter both composition and size distribution to get a closer signature match. These different approaches to modeling result in obtaining different microphysics, both of which can not be correct. Mixing these approaches between retrievals of dust microphysics and predictions of dust radiative effects could result in potentially significant inconsistencies.

4.6 Integrated AIRS and CALIPSO Modeling and Analysis

We investigated a Saharan dust event that was observed by both AIRS and the CALIPSO lidar as it was transported across the Atlantic Ocean. This dust event started over the Atlantic off the west coast of Africa around Mauritania on 18 August 2006 and reached the Caribbean on 22 August 2006. *Liu et al.* [2008] provided some analysis of this dust event using CALIPSO data. Here we focused on the first three days of the dust event. By the fourth day the effect of the dust on the TIR radiance is at most 0.5 K, and the MODIS image shows that there is no possibility of finding a non-cloud contaminated AIRS pixel of the plume. Figure 4.23 shows the geographic locations of the analyzed AIRS data, while Table 4.4 gives the dates, geographic coordinates, and satellite zenith angle for each of the datasets along with pixel number that we assigned the dataset.

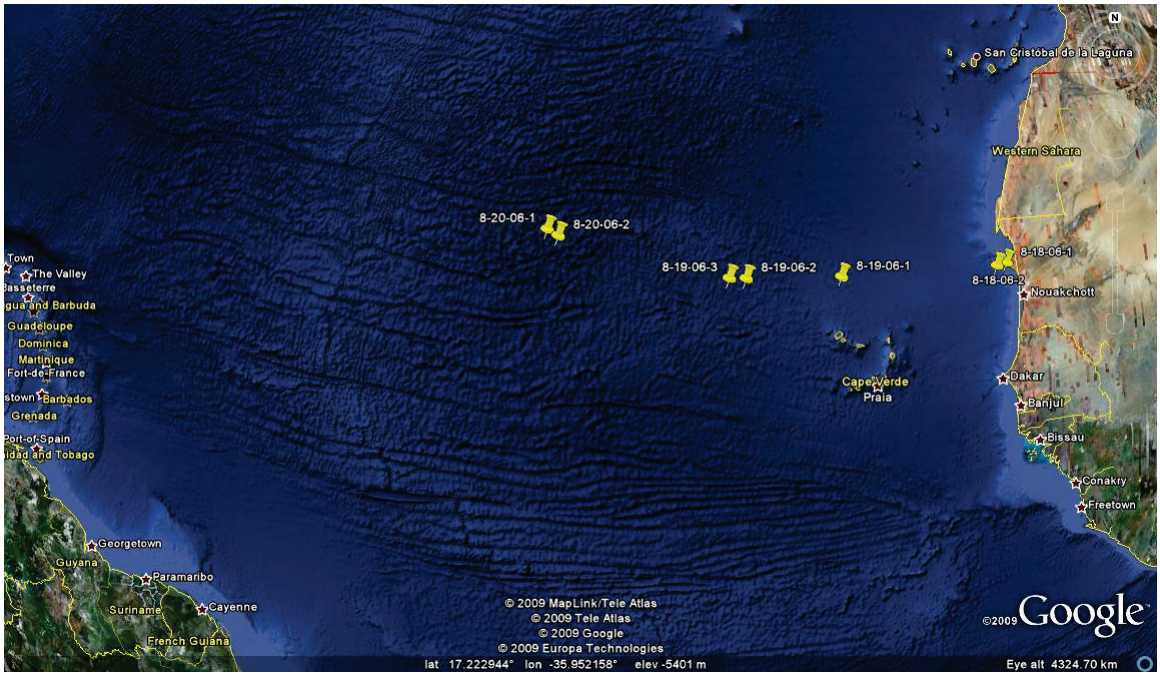

Figure 4.23. Google Earth image showing the locations of the AIRS datasets being analyzed.

Table 4.4 Dates and geographic locations of the AIRS radiance datasets being analyzed

Date	Pixel #	Latitude	Longitude	Satellite Zenith Angle
8/18/2006	1	19.1079	-16.9593	45.7602
	2	19.0114	-17.4757	48.4581
8/19/2006	1	18.9736	-25.0530	28.9893
	2	19.0481	-29.2232	52.6033
	3	19.0757	-29.9396	55.4517
8/20/2006	1	21.0692	-37.5200	36.6035
	2	20.8170	-37.0604	34.0460

Figure 4.24a-c shows MODIS images for the considered cases with the approximate location of the AIRS pixels identified with a red dot.

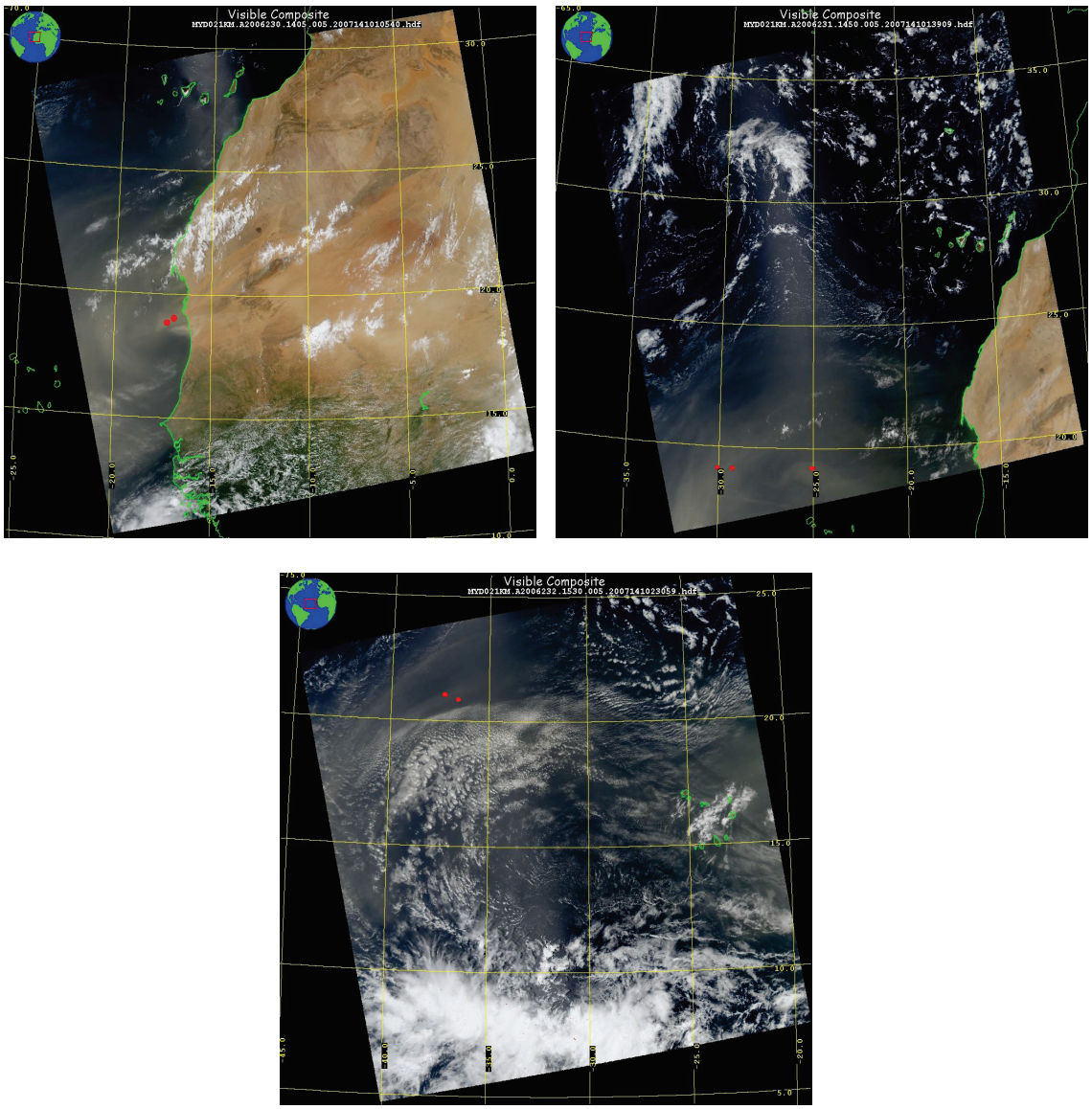

Figure 4.24a-c. MODIS images of the dust plume being analyzed with the AIRS pixels identified by red dots.

As with the ARIES sensor, the microwindows used for the AIRS analysis (Table 4.5) were defined by examining a transmission spectrum in the 750 – 1250 cm^{-1} region at the resolution of the AIRS sensor and finding regions that had high transmission and a minimum of 5 spectral samples.

Table 4.5 AIRS Microwindows within the TIR Atmospheric Window

Lower Limit (cm-1)	Upper Limit (cm-1)
771.39	775.19
779.95	782.08
800.17	802.39
804.55	807.53
809.35	813.48
815.71	824.09
828.71	834.97
836.15	839.32
842.51	848.55
855.61	858.18
859.97	864.46
865.97	870.52
872.06	877.98
879.22	880.61
881.53	882.92
884.51	886.58
891.90	895.70
898.04	901.89
914.95	917.87
918.91	920.75
922.90	924.39
925.45	928.43
929.13	931.01
931.35	932.87
932.84	934.73
935.08	936.61
936.96	938.48
938.84	940.37
941.11	942.27
942.63	943.79
944.53	947.62
949.53	951.09
951.46	952.64
956.14	958.89
960.07	964.43
965.23	970.04
1070.33	1073.67
1075.23	1080.58
1081.67	1085.06
1086.17	1090.60
1092.22	1094.65
1095.27	1098.74
1102.45	1105.96
1108.00	1110.64
1112.34	1116.42
1117.08	1120.13
1122.40	1124.40
1125.07	1128.70
1130.45	1134.11
1219.31	1223.80
1226.99	1228.43
1230.61	1232.57
1233.73	1235.17
1237.39	1241.99
1245.82	1249.42

Two AIRS L1B radiance pixels were analyzed for Day 1: 18 August, 2006. The AIRS and MODTRAN5 generated clear-sky BT spectra are shown in Figure 4.25.

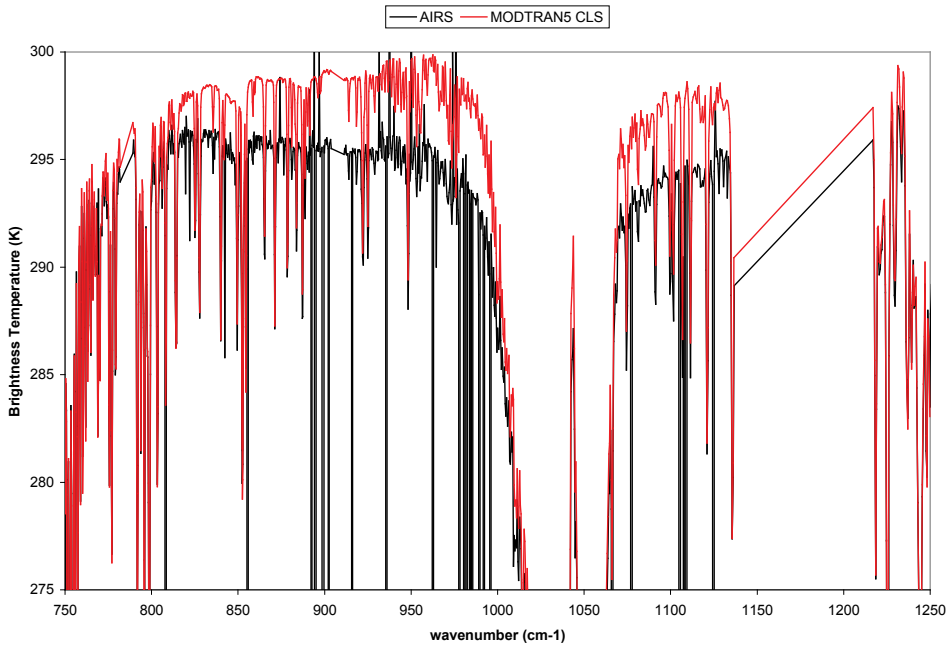

Figure 4.25. BT spectrum measured by the AIRS instrument and the MODTRAN5 modeled clear-sky BT spectrum.

The effect of the dust is dramatically apparent. From the coincident MODIS imagery in Figure 4.24 we know that this was a particularly dense region of the dust plume. In the case of satellite data we are faced with the lose of key diagnostic mineral spectral features in the ozone absorption region from 970 cm^{-1} to 1070 cm^{-1}. The AIRS data analyzed here are in the same geographic region as the ARIES data so the composition of dust aerosol includes illite, kaolinite, quartz, calcite, and chlorite, which were considered in the previous optical modeling.

Using an initial guess size distribution, the composition is preliminarily adjusted so that the mixture extinction coefficient matches the BTD spectrum. If no acceptable match is possible then the size distribution is altered. Once an acceptable fit is achieved, an initial guess of the total particle concentration is made and the optical properties for that loading are then used together with the ancillary information on the position and

thickness of the dust layer to model the radiance using our custom aerosol model in MODTRAN5. The CALIPSO data show that the dust layer extends from about 1 to 6 km. The MODTRAN5 results are compared to the measured radiance and then the composition and loading are iteratively changed until a good fit to the radiance is obtained in the microwindows. As a starting point for the size distribution we used the same size parameters as retrieved from ARIES (see Table 4.3). Figure 4.26 shows the BTD spectrum for this AIRS pixel and an extinction coefficient spectrum using only a fine mode dust mixture.

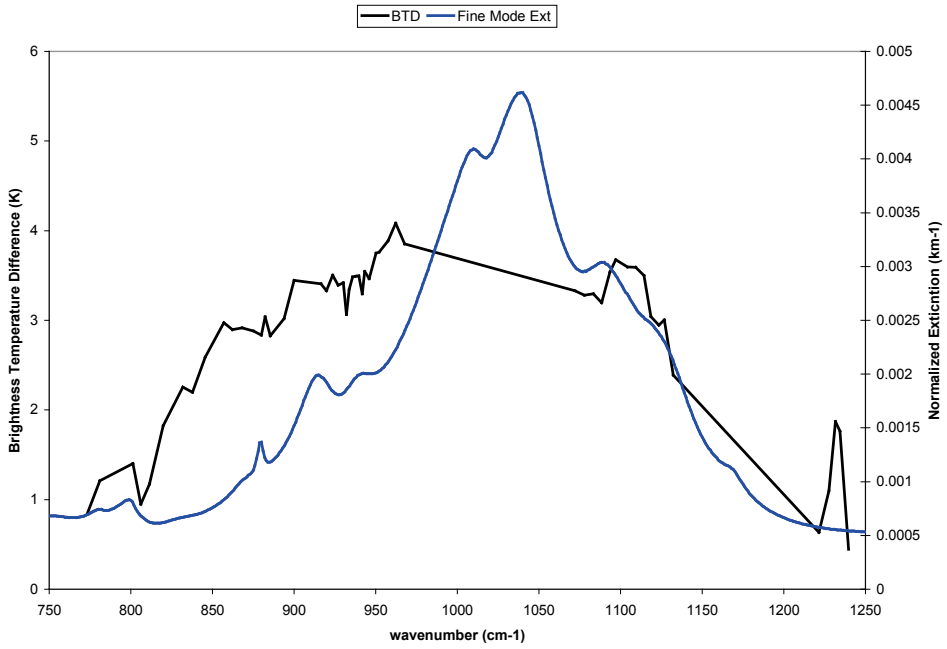

Figure 4.26. AIRS BTD spectrum and extinction coefficient spectrum for a fine mode mixture used in the AIRES analysis.

From Figure 4.26 it is apparent that a single fine mode can not reproduce the AIRS radiances. In Chapter 3 we showed that as the median radius of a mode increases, the spectral absorption features become broader and a continuum extinction builds up,

particularly on the low frequency side of the spectrum, in addition to the extinction coefficient becoming larger overall. The widening of this BTD spectrum indicates that some amount of a coarse dust mode will be required in addition to a fine mode. The normalized extinction coefficient of the external mixture that provided the best match to the BTD spectrum is shown Figure 4.27.

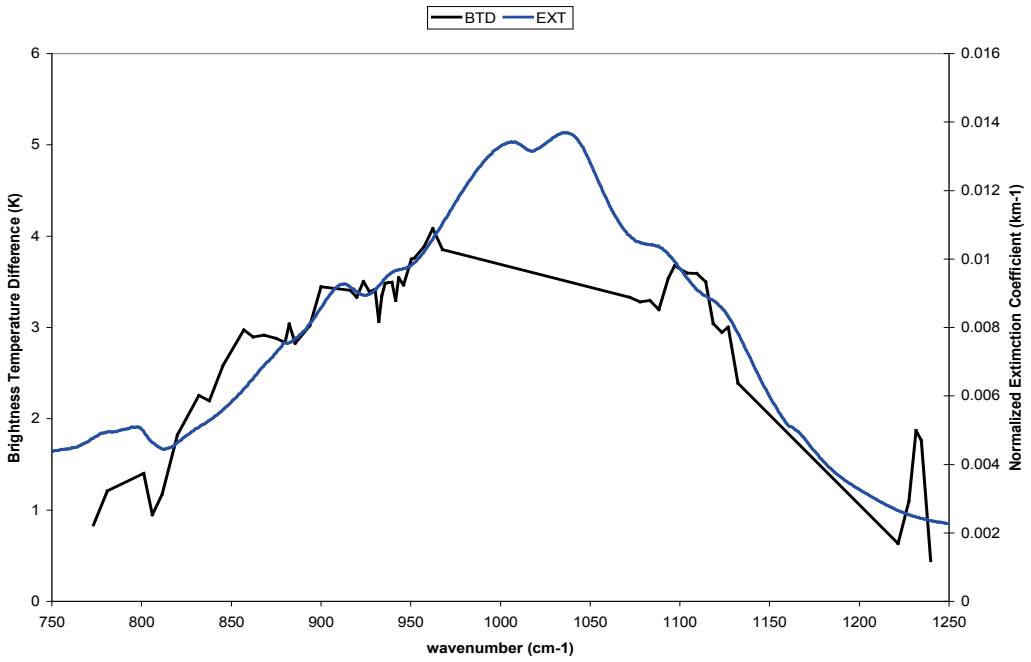

Figure 4.27. AIRS BTD spectrum and the extinction coefficient spectrum that provided the best fit to the BT spectrum.

Figures 4.28a-b show the best fit to the AIRS data that was obtained using a bimodal dust distribution. Table 4.6 provides the details of the size modes and the composition of the MEM model that best matched the data. The MODTRAN5 BT model of the dust plume is in excellent agreement with the AIRS BT spectrum; the maximum difference within the microwindow regions is only about 0.7 K.

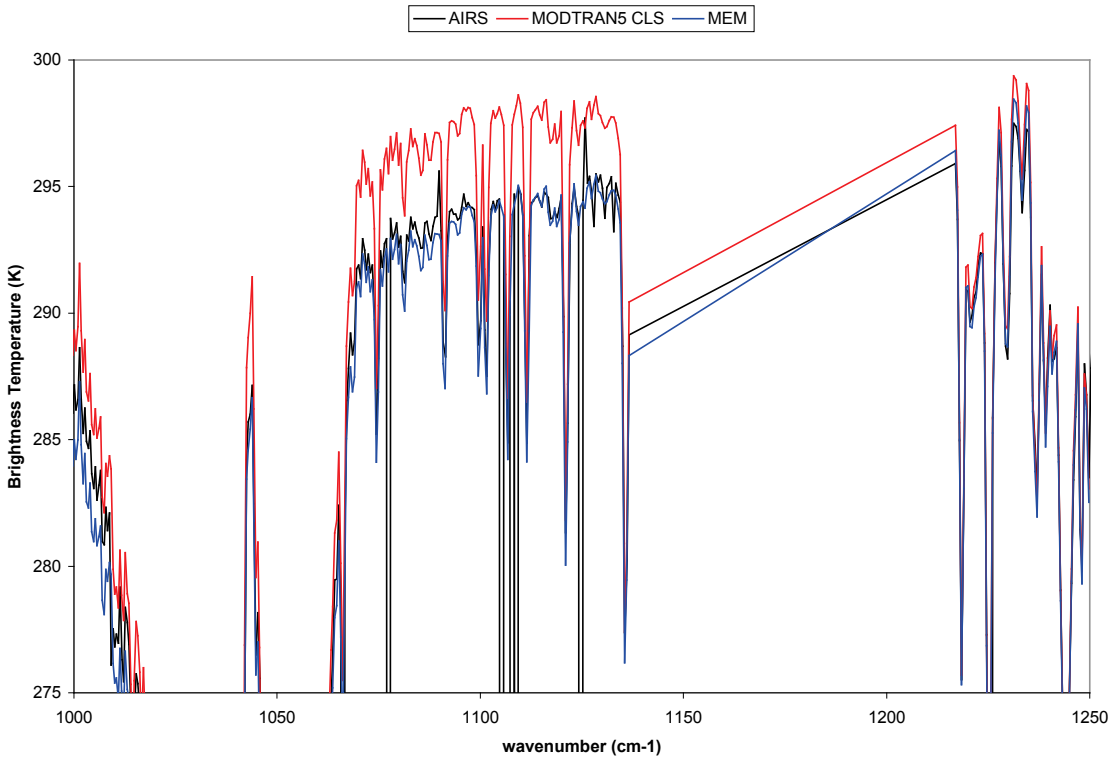

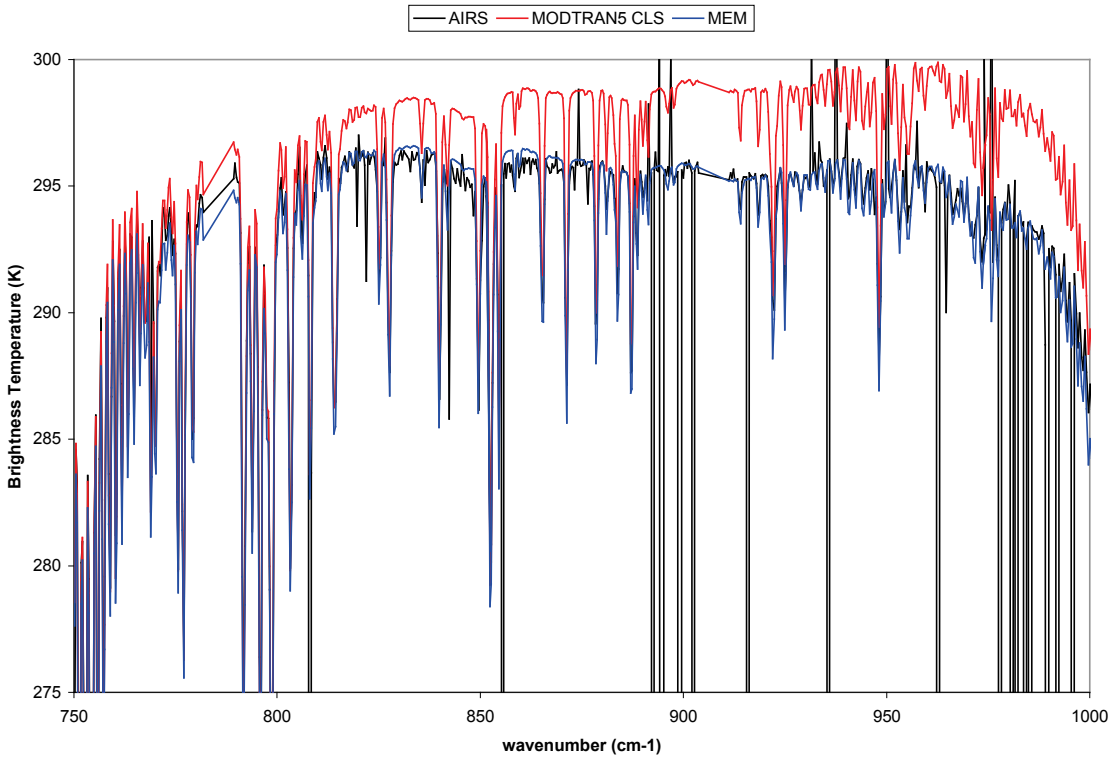

Figure 4.28a and b. AIRS BT spectrum, MODTRAN5 modeled clear-sky BT spectrum and the best fit MEM modeled dust plume BT spectrum.

Table 4.6 Day 1 retrieved size distribution and composition with MEM model

Pixel #	fine/coarse	# cm-3	Median radius (microns)	Mode	illite	kaolinite	quartz	calcite	chlorite
1	70/30	5	1.5	coarse	58%	17%	10%	5%	10%
			0.65	fine	50%	25%	5%	6%	14%
2	70/30	6	1.5	coarse	58%	17%	10%	5%	10%
			0.65	fine	50%	25%	5%	6%	14%

For the second Day 1 pixel, the same mode median radii, composition, and fine to coarse ratio were used as for the first AIRS pixel data for this day. The only difference is that the loading was increased to 6 cm^{-3}. The MODTRAN5 BT model of the dust plume is again in excellent agreement with the AIRS BT spectrum as was the case for the first pixel for this day; the maximum difference within the microwindows is also only about 0.7 K.

In these cases even though the dust radiative effect is larger than in the SHADE data the total particle concentration is lower. One reason for this is that the dust layer in this case is thicker, about 5 km thick, while in the SHADE case it was 2 km thick. More importantly though is that as the fraction of coarse mode particles increases the sensitivity to fine mode particles decreases, i.e. the effect of the coarse mode masks the effect of the fine mode. This implies there are limits to the size distribution information that can be accurately retrieved using high spectral resolution TIR radiance measurements. Table 4.7 lists the composition and size mode retrieved for Days 2 and 3.

Table 4.7 Days 2 & 3 retrieved size distribution and composition with MEM model

Day	Pixel #	# cm-3	Median radius (microns)	illite	kaolinite	quartz	calcite	chlorite
8/19/2006	1	15	0.65	45%	25%	9%	6%	15%
8/19/2006	2	22	0.65	50%	25%	5%	6%	14%
8/19/2006	3	20	0.65	52%	25%	3%	6%	14%
8/20/2006	1	10	0.5	50%	21%	9%	6%	14%
8/20/2006	2	12	0.5	50%	19%	9%	6%	14%

On Day 1 with the dust plume just off the coast of Africa, two size modes (see Table 4.6) are required for the MEM model to match the dust signature in the AIRS spectrum. Given the magnitude of the dust effect and the proximity to the source region an appreciable coarse mode would be expected. With the normalized extinction coefficients for the coarse mode being an order of magnitude greater than those of the fine mode, once the coarse mode particle fraction exceeds 10% the sensitivity to the effect of the fine mode diminishes rapidly. The aerosol radiative effect is dominated by the coarse mode and the fine mode particle concentration can not be determined very well. The total particle concentration is mostly sensitive to the dominant size mode.

On Day 2 the MODTRAN5 BT model of the dust plume, extending from 1.5 km to 5 km based on CALIPSO data, is in excellent agreement with the AIRS BT spectrum; the maximum difference is less than 0.5 K. The two other AIRS radiance spectra for this day were also very well modeled by a MEM model of pure mineral species, both with a single fine mode. The MODTRAN5 BT model of the dust plume for these pixels is also in very good agreement with the AIRS BT spectrum for these cases also; the maximum difference within the microwindows is 0.6 and 0.7 K, respectively.

By Day 3, the dust signal has become fairly weak. The maximum of BTD is only a little greater than 1 K. The width of the aggregate Si-O feature and the individual

mineral features in the BTD spectrum are noticeably narrower than the previous days. The 0.65 μm median radius dust mode was too wide to be able to fit the measured spectrum. A good fit to the BTD spectrum was obtained with a single fine mode with r_g = 0.5 μm. In modeling the radiance, the total particle concentration also had to be reduced from the values of the previous day even with the reduction in the thickness of the layer, now extending from 2 km to 5 km based on CALIPSO data. The MODTRAN5 BT model is again in excellent agreement with the AIRS BT spectrum; the maximum difference is less than 0.5 K. For the second AIRS pixel of this day, the MODTRAN5 BT model is also in very good agreement with the AIRS BT spectrum; the maximum difference within the microwindows is less than 0.6 K.

As with the airborne ARIES data, an external mixture of pure mineral species has been shown to accurately match satellite AIRS radiance spectra for single layer Saharan dust plumes over open-ocean. For large dust events close to the coast, two size modes are required to model the spectral characteristics of the dust layer. For all of these cases it appears that the dust layer can be well modeled as a single homogeneous layer, which is agreement with the findings of *Liu et al.* [2008], *Maring et al.* [2003] and *Reid et al.* [2003] who suggest that the vertical structure of a Saharan dust layer is remarkably uniform.

As the dust plume travels across the Atlantic, our modeling indicates that a change in the microphysical properties occurs. Not only does the number concentration change as a function of distance traveled, but the mode median radius changes and the number of modes required to accurately model the dust TIR radiative effects goes from two near the coast for strong dust events to one dominant size mode whose radius

decreases the further it gets from the source. This is in contrast to the finding of *Liu et al.* [2008], *Maring et al.* [2003] and *Reid et al.* [2003] who suggest that the size distribution changes little during transport across the Atlantic. The composition on the other hand does not exhibit significant changes during the transport from the coast to the mid-Atlantic based on our modeling results.

To examine what if any differences in microphysical properties there are when modeling this dust event using a VRI model as opposed to a MEM model, and to examine whether those properties evolve or remain constant, we modeled one dataset for each of the above three days. For Day 1 pixel number 1 is used, for Day 2 pixel number 2 is used, and for Day 3 pixel number 1 is used. From an examination of the BTD spectrum and the Volz extinction coefficient computed for a bimodal size distribution, it is obvious that the best fit for the Day 1 pixel would be obtained by a single fine mode instead of the two size modes used for the MEM case. For Day 2, since the data in the MEM case were well fit with a single mode with r_g = 0.65 μm, we did not consider a coarse mode. Here also r_g = 0.65 μm provided an overall good spectral match to the BTD spectrum, but the fit could be improved in some spectral regions with a slightly larger or smaller median radius but it would become worse in other spectral regions. For Day 3, a narrower size distribution was required for the VRI model as it was for the MEM model. The BTD spectra in the MEM case were well fit by a single mode with r_g = 0.5 μm, and the BTD spectrum for the case examined here using VRI data is also matched fairly well by a single mode with r_g = 0.5 μm. A smaller median radius would likely have provided a slightly better fit but to keep a more direct comparison between the two models we decided to use a the same single mode with r_g = 0.5 μm as was used in the MEM case.

Table 4.8 summarizes the size distribution parameters for the VRI model for these cases. The same atmospheric and surface state as was used for the MEM modeling.

Table 4.8 Comparison of size distribution parameters between MEM and VRI models

Day	Pixel #	# Size Modes MEM	# Size Modes VRI	Fine to Coarse Mode ratio MEM	Median radius (microns)	Total Particle # cm-3 MEM	Total Particle # cm-3 VRI
8/18/2006	1	2	1	70% / 30%	1.5 0.65	5	10
8/19/2006	2	1	1	100% / 0%	0.65	22	10
8/20/2006	1	1	1	100% / 0%	0.5	10	6

As was the case with the SHADE data, a VRI model can not be adjusted to match the dust spectral signature as well as a MEM model. For Days 1 and 2 the VRI model did not change its median size or its particle concentration. But for the Day 1 dataset the VRI model does not model the AIRS radiance nearly as well in the 1050 – 1150 cm^{-1} region as the bimodal MEM model. In the 900 – 950 cm^{-1} region the fit is nearly identical to the MEM model and in the 850 – 900 cm^{-1} region the Volz data fits better, but the MEM model fits better from 750 – 850 cm^{-1}. The VRI model has to sacrifice the fit to the data in some spectral regions in order to fit the data well in other regions. Changing the median radius and loading to achieve a better fit in the 1050 – 1150 cm^{-1} region would result in a poorer fit elsewhere.

Even with the tradeoffs in model fit to the measured radiance, both the MEM and VRI models show changes in the microphysical properties of the dust plume as it is transported across the Atlantic. By Day 3 both models require a smaller median radius for the dominant size mode, and both models require the total particle concentration to

decrease from Day 2 to Day 3. The MEM model makes very good physical sense, provided that we understand that once the coarse mode reaches a certain fraction of the total particle concentration the sensitivity to the fine mode is dramatically reduced and then lost. The MEM model indicates that near the source region for large dust events both a coarse mode and fine mode are present and measurable. As the dust plume is transported away from the source region it undergoes microphysical changes. The particle number decreases, due to removal processes, and the number of size modes and the median radius of the modes decrease. This is in complete agreement with size preferential removal processes like gravitational settling. These changes that are being exhibited in the TIR high spectral resolution radiative effects of aerosols are much more in line with what would be expected than some of the recent findings that indicate no size distribution changes with long-range transport over the Atlantic.

Matching the BTD signature of the dust for this event indicates that the dust is composed of approximately 75% illite and kaolinite in a 2/1 to 3/1 ratio. The remaining ~25% is composed of quartz, calcite and chlorite/feldspar, with quartz comprising between 5% to 10% and calcite comprising about 5% and chlorite/feldspar comprising between 10% to 15%. In a study from the African Monsoon Multidisciplinary Analysis (AMMA) conducted over Niger in 2006, *Chou et al.* [2008] report the composition of their coarse mode (diameter greater than 1 μm, which corresponds to both our fine and coarse modes) to be 78% aluminosilicates by number, of which 74% were illite and kaolinite and 4% were other clays. The Si-rich group (mostly quartz) accounted for 18%, and the Ca-rich group (mostly calcite) accounted for 3%. *Kandler et al.* [2009] in their study from the Saharan Mineral Dust Experiment (SAMUM) 2006 at Tinfou, Morocco

report the dust composition by volume for particles in our fine and coarse mode range to be approximately 25% feldspars, 25% illite, 5% kaolinite, 5% chlorite, 10% quartz, 10% calcite, with sulfates and other components making up the remaining 20%. In this case the illite to kaolinite ratio is about 5/1. For our fine and coarse particle sizes *Kandler et al.* [2007] report the following mineral composition by volume from their mineralogical model based on dust samples collected at Izana on the island of Tenerife in the Canary Islands; ~45% illite, ~15% albite, ~20% chlorite, ~8% quartz, ~5% calcite and 5-10% other components. Their mineralogical model did not consider kaolinite. *Blanco et al.* [2003] found that for dust samples collected in southern Italy from various dust source regions of northern and western Saharan Africa that all samples contain a significant amount of illite, in agreement with the findings of *Avila et al.* [1997] who found illite to be the most abundant mineral (35% - 41%) in all of their samples collected from northeastern Spain over 11 years. Somewhat to the contrary, *Formenti et al.* [2008] in their report on the composition of mineral dust from western Africa find an illite to kaolinite ratio in Niger to be 0.1 – 0.3, and the illite to kaolinite ratio in Mauritania to be 0.6. They find the kaolinite and illite components to account for 50 – 60% of the mineral dust from their samples with quartz accounting for 30 – 40% and feldspars accounting for ~5% and calcium carbonate accounting for the remaining 10-15%. The composition results determined from our new TIR technique are in good general agreement with most of the reported compositional analyses of dust measured in the same area and/or originating from the same area.

Based on these results we can say that the use of bulk material refractive index data to model regional dust effects in high spectral resolution TIR radiances does not give

results as good those obtained from an MEM model of pure mineral species, although the differences in some cases can be fairly small. In most of our cases, the maximum error in BT between the modeled and measured radiances when using bulk properties was less than 1 K and in no case did the maximum error in BT exceed 1.5 K. Of critical importance though are the differences in the microphysics, particularly the particle concentration, and the implications of those differences to forward and inverse modeling of tropospheric dust at high spectral resolution and the computation of the dust radiative effects. In the above cases we see a difference of almost a factor of 2 in the particle concentrations between the two models. Some of this difference is due to optical properties being computed with Mie theory in the VRI case and T-matrix with a shape factor significantly different from 1 being required for the MEM model, which leads to magnitude differences in the spectral extinction coefficients. If aerosol microphysical properties were retrieved using one model and then aerosol radiative effects were predicted using the other model, significant errors could result.

4.7 Examination of Spectral and Integrated TIR Aerosol Radiative Forcing & Cooling Rate

Given that the spectral radiance is being well modeled we can have confidence that rigorous radiative transfer calculations of radiative forcing and cooling rate using the same microphysical and macrophysical aerosol properties will yield similarly accurate results. Here, we want to 1) examine the spectral characteristics of the aerosol radiative forcing in the TIR window region, 2) examine the differences in forcing and cooling rate between an MEM aerosol model and one based on bulk refractive index data, 3) examine

the consequences of using the microphysics determined from one model on forcing and cooling rate predictions using the other model, and 4) examine the sensitivity of the aerosol radiative forcing and the effect on cooling rates to the aerosol loading and aerosol layer position and thickness.

MODTRAN5 includes the capability to output the profile of spectral and integrated fluxes. Here, we examine the TIR window radiative forcing at the top of the atmosphere (TOA) and at the bottom of the atmosphere (BOA), and cooling rate profile, considering the AIRS data for the August 2006 dust storm event. The IR radiative forcing in the TIR window is by far the most important contribution to the aerosol forcing in the entire thermal IR region. This is because terrestrial radiation peaks in the TIR window and because tropospheric dust aerosol absorption of IR radiation is also a maximum there. Outside of the window-region aerosol IR radiative effects are greatly reduced by molecular absorption of IR radiation.

The radiative forcing at a given level, e.g. TOA or BOA, is defined as the perturbed net flux minus the unperturbed net flux:

$$\textit{Radiative Forcing} \equiv \Delta F = F_{perturb} - F_{unperturbed} \qquad \text{(Eq. 4.1)}$$

The spectral net flux is defined as the downward flux minus the upward flux:

$$F_\nu(z) = F_\nu^{\downarrow}(z) - F_\nu^{\uparrow}(z) \qquad \text{(Eq. 4.2)}$$

In the TIR the net spectral flux, F_ν, at the TOA is equal to the outgoing spectral flux. Given that, the TIR window spectral aerosol radiative forcing, $\Delta F_{a,\nu}$, at the TOA is the clear sky outgoing flux at the TOA in the window region minus the outgoing flux at the TOA in the window-region when the aerosol is present:

$$\Delta F_{a,\nu}(TOA) = F_\nu^{clr\uparrow}(TOA) - F_\nu^{aer\uparrow}(TOA) \qquad \text{(Eq. 4.3)}$$

The TIR window integrated aerosol radiative forcing ΔF_a will be the $\Delta F_{a,\nu}$ integrated over the TIR window.

Assuming that the upwelling flux from the surface is nearly the same for both the perturbed and unperturbed cases, which is a good approximation for highly emissive surfaces like the ocean, the $\Delta F_{a,\nu}$ at the BOA is the downwelling flux at the BOA in the TIR window when the aerosol is present minus the clear sky downwelling flux at the BOA in the TIR window:

$$\Delta F_{a,\nu}(BOA) = F_\nu^{aer\downarrow}(BOA) - F_\nu^{clr\downarrow}(BOA) \qquad \text{(Eq. 4.4)}$$

The spectral IR cooling rate is defined as the rate of change in temperature with time due to spectral radiative flux convergence or divergence for all other quantities held constant:

$$\left(\frac{\partial T}{\partial t}\right)_\nu = \frac{1}{\rho C_p}\frac{dF_\nu(z)}{dz} \qquad \text{(Eq. 4.5)}$$

where F_ν is the spectral net flux at a given level in the atmosphere, ρ is the air density at that level, and C_p is the specific heat at constant pressure for the level.

The total IR cooling rate is the integral over the TIR window:

$$\left(\frac{\partial T}{\partial t}\right)_{IR} = \int_{IR}\left(\frac{\partial T}{\partial t}\right)_\nu d\nu = \frac{1}{\rho C_p}\frac{dF(z)}{dz} \qquad \text{(Eq. 4.6)}$$

where F is the total net flux, i.e. the difference between the total downward and upward fluxes integrated over the TIR.

4.7.1 Cooling Rate Modeling – MEM Model vs. VRI Model and Sensitivity to Variations of Macrophysical Parameters

Two AIRS pixels for each of the 3 days that were analyzed are examined here in terms of the aerosol's effect on the cooling rate. Spectral and integrated cooling rates were calculated both with and without the dust layer present using the MEM model that best fit the high spectral resolution radiance data. Figure 4.29 shows the cooling rate for the AIRS pixel 2 from 19 August, 2006.

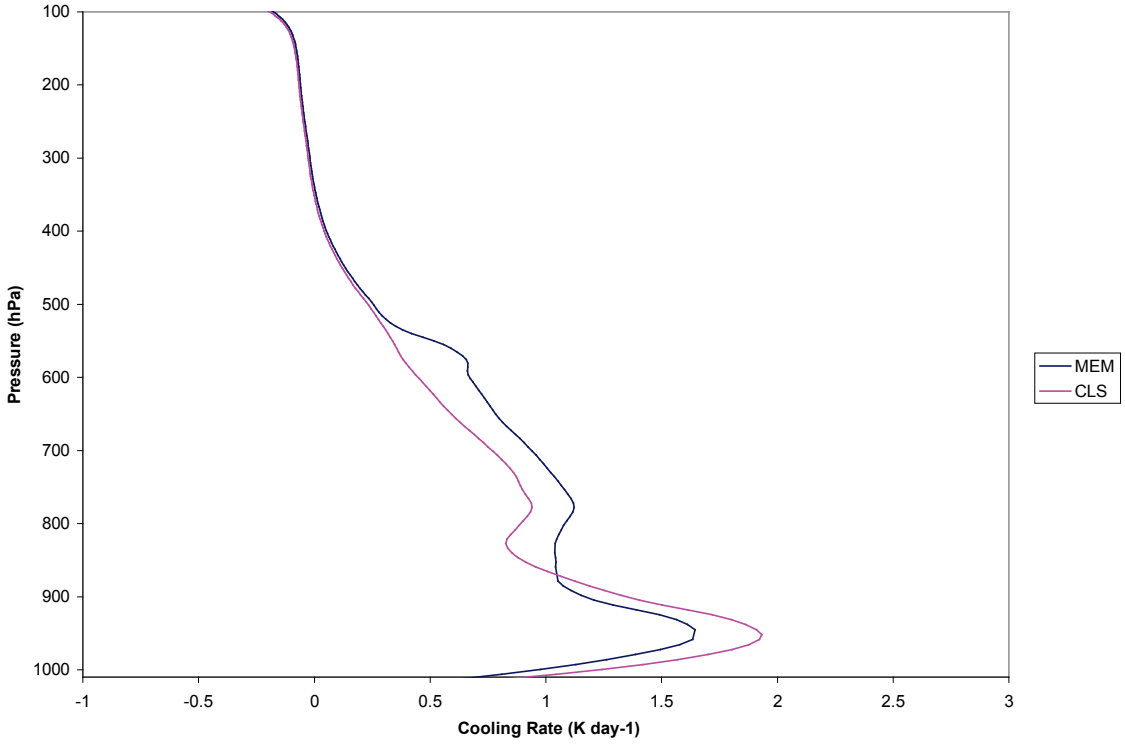

Figure 4.29. AIRS Day 2 pixel 2 integrated TIR cooling rates for clear-sky model and MEM model of dust layer.

The effect of dust is to increase the cooling rate within the dust plume and to reduce the cooling rate below it, with little changes above the plume. The presence of the dust particles means that in the TIR window spectral region the atmosphere at that level

can more effectively absorb infrared radiation, thus increasing the emission from that level and correspondingly increasing the cooling rate at that level. The increased absorption and emission of the dust layer also means that the layers of the atmosphere below can not cool as effectively and so the cooling rate below the dust layer decreases.

We now examine the differences in cooling rates between the dust aerosol modeled using the MEM model and modeled using the VRI model. One pixel from each of the three days that were analyzed in the previous sections was used in this analysis. Figure 4.30 shows the difference in cooling rates between the MEM model using its retrieved aerosol loading and the same MEM model using the aerosol loading that was determined from the VRI model for the selected Day 1 pixel, and similarly for the selected Day 2 pixel.

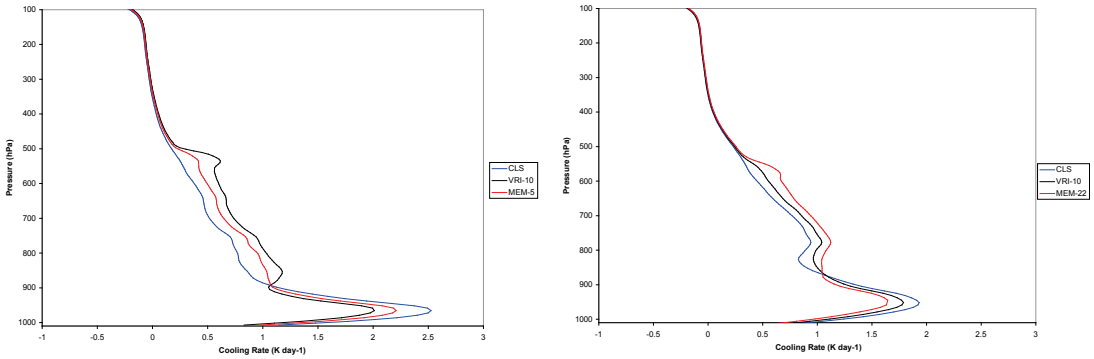

Figure 4.30a and b. a) AIRS Day 1 pixel 1 integrated TIR cooling rates for clear-sky model and MEM model of the dust layer using its retrieved concentration (MEM-5) and using the VRI model retrieved concentration (VRI-10), and b) Day 2 pixel 2 integrated TIR cooling rates for clear-sky model and MEM model of the dust layer using its retrieved concentration (MEM-22) and using the VRI model retrieved concentration (VRI-10).

In the Day 1 case the VRI model loading was twice as large as the MEM loading. The cooling rate is correspondingly increased by nearly a factor of 2 from an average of ~0.13 $Kday^{-1}$ to ~0.27 $Kday^{-1}$ in the dust plume. For the Day 2 case the VRI model loading was about half as large as the MEM loading. The cooling rate is correspondingly decreased by nearly a factor of 2 from an average of ~0.16 $Kday^{-1}$ to ~0.1 $Kday^{-1}$ in the dust plume.

Figure 4.31 shows the inter-comparison of the two models. Here the cooling rates for the Day 2 case for the VRI model using its derived loading are compared to those of the MEM model using its derived loading. The differences are negligible. The results from the other two days also show little differences between the MEM and VRI models.

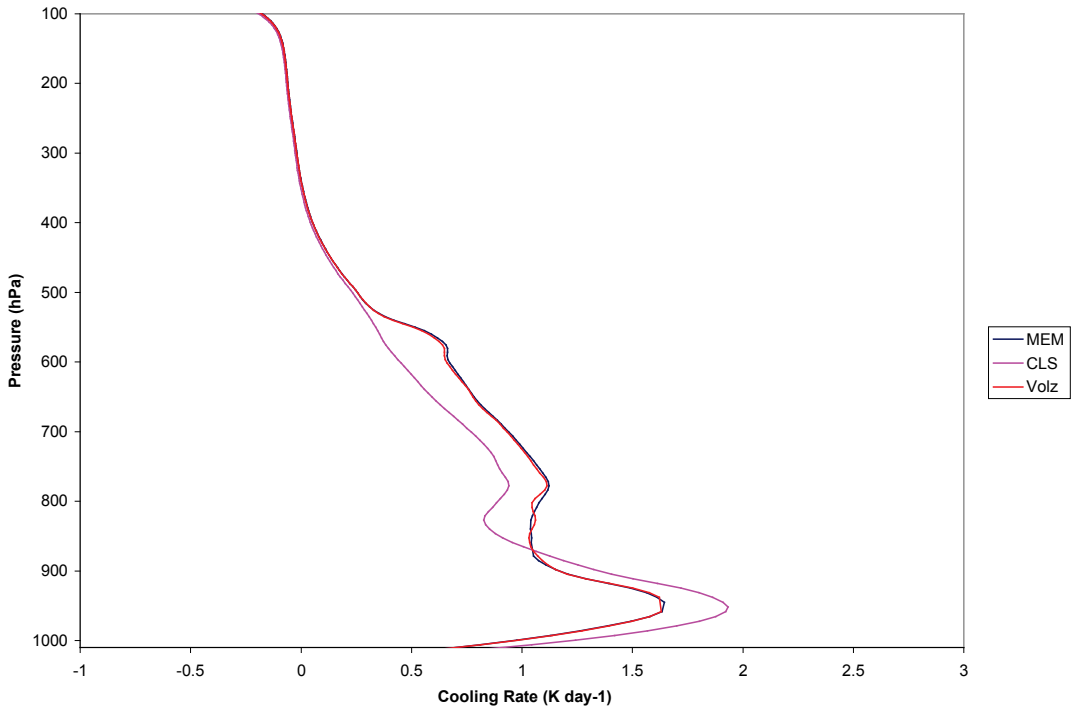

Figure 4.31. AIRS Day 2 pixel 2 integrated TIR cooling rates for clear-sky model and MEM model of the dust layer using its retrieved concentration and the VRI model of the dust layer using its retrieved concentration.

The above results demonstrate that for cooling rate calculations it is critical to use models that are consistent between retrievals/inverse modeling and predictions/forward modeling. This also shows that for spectral-integrated quantities, like cooling rates, it is less important to model the radiance data accurately at high spectral resolution than it is to use models consistently.

To examine the sensitivity of the cooling rates to macrophysical changes we considered three scenarios by varying the concentration of dust particles, the position of the layer, and the thickness of the layer. The first scenario involves shifting the dust layer upwards by 1 kilometer and holding the particle concentration fixed. The second scenario involves contracting the dust layer by 1 kilometer by lowering the top of the layer by 0.5 kilometers and raising the bottom of the layer by 0.5 kilometers while holding the concentration fixed. The third scenario involves increasing the particle concentration by 50% while holding the layer position and thickness fixed. Figure 4.32 compares the resulting cooling rate.

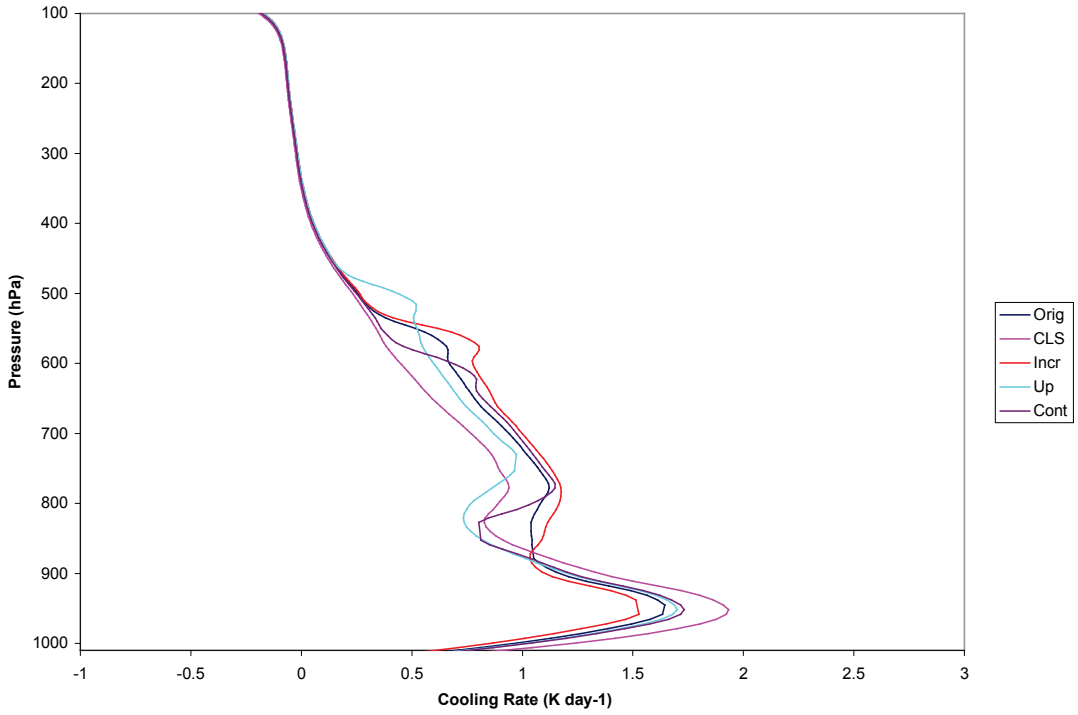

Figure 4.32. AIRS Day 2 pixel 2 integrated TIR cooling rates for clear-sky model, original MEM model of the dust layer (Orig) and 3 variation scenarios; increased concentration (Incr), layer moved up (Up), and layer contracted (Cont).

In this figure Orig is the original cooling rate from the MEM model that best fit the high spectral resolution radiance data. CLS is for the dust-free clear sky case. Incr is the cooling rate when the particle concentration is increased by 50%, Up is when the dust layer is moved up by 1 km, and Cont is when the top and bottom of the dust layer are moved closer together by 0.5 km. The results are in agreement with physical intuition. For the case where the particle concentration is increased, the cooling rate within the dust layer increases beyond that of the original and it decreases below the dust layer. Within the dust layer the increase in the cooling rate is not uniform; instead it is greater at the top and bottom of the layer than in the middle of the layer. For the case where the layer is shifted up by 1 km, the cooling rate is also shifted up by 1 km. The strength of the effect

is also reduced by virtue of the fact that the dust layer is at a higher altitude and colder temperature, and therefore the emitted flux is reduced. For the case where the dust layer is contracted, the cooling rate is also contracted. The magnitude of the dust effect on the cooling rate within the dust layer actually increases slightly because there is less downwelling flux into the contracted layer. This analysis demonstrates that the cooling rate is sensitive to the particle concentration, and the layer thickness and position, but it is particularly sensitive to the height of the aerosol layer.

Our results show that for cooling rate calculations it is very important to get the layer height correct followed by the layer thickness and particle concentration and then lastly the spectral characteristics. At the moment getting the aerosol layer height correct requires the use of ancillary data like the CALIPSO lidar. This demonstrates the importance of having a system of multiple complimentary sensors like the NASA A-Train to monitor the Earth-Ocean-Atmosphere system and monitor climate and climate drivers.

4.7.2 Radiative Forcing Modeling – MEM Model vs. VRI Model and Sensitivity to Variations of Macrophysical Parameters

Figures 4.33 and 4.34 show the TOA and BOA spectral aerosol radiative forcing computed for one of the Day 1 pixels, which are located just off the coast of Mauritania. Overlaid on this plot is the plot of the spectral normalized dust extinction coefficient that gave the best fit to the radiance data. As can be seen in the plot the spectral signature of the aerosol radiative forcing is closely tied to the spectral signature of the extinction coefficient just as the BTD signature was.

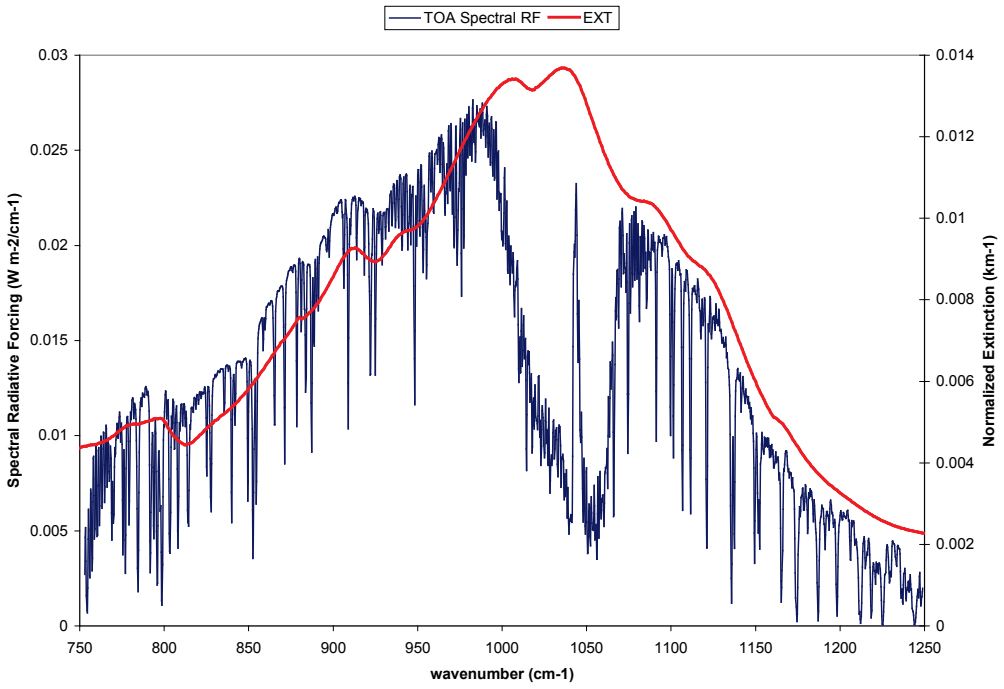

Figure 4.33. AIRS Day 1 pixel 1 TOA spectral radiative forcing and the MEM model normalized extinction coefficient.

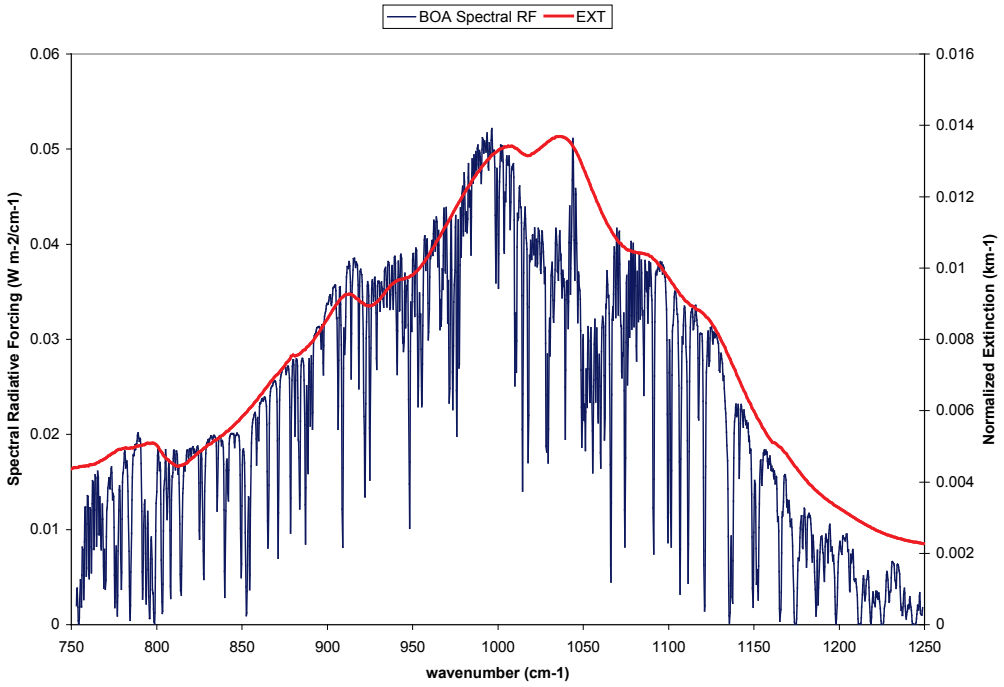

Figure 4.34. AIRS Day 1 pixel 1 BOA spectral radiative forcing and the MEM model normalized extinction coefficient.

Table 4.9 shows the radiative forcing integrated over the TIR spectral region for each of the cases. As the plume advects across the Atlantic the local radiative impacts change as a result of microphysical and macrophysical changes. For example, there are the size distribution changes and concentration changes that were required to accurately model the radiance, and the layer position and thickness changes. In Section 4.5 both the MEM and VRI models results demonstrate evidence of size distribution and particle concentration changes over the three days in which the dust plume traveled more than halfway across the Atlantic. These are the kind of changes we would logically anticipate due to both the spatial dispersion of the plume and size preferential loss of particles due to removal processes and gravitational settling.

Table 4.9 MEM model TOA and BOA TIR integrated radiative forcing (ΔF_a)

Date	Pixel	TOA ΔFa (Wm-2)	BOA ΔFa (Wm-2)
Aug. 18			
	1	6.63	11.4
	2	7.71	13.3
Aug. 19			
	2	5.01	9.91
	3	4.5	9.18
Aug. 20			
	1	1.21	1.83
	2	1.43	2.11

These integrated TIR radiative forcing values are in good agreement with modeled results of other dust events over oceans. For example, *Highwood et al.* [2003] found that the TOA radiative effect of the dust event measured during the SHADE campaign, which is similar in strength to the event modeled here, was 6.5 Wm^{-2}.

Markowicz et al. [2003] reported TOA dust radiative forcing of up to 4.5 Wm^{-2} and BOA dust radiative forcing of 8 - 10 Wm^{-2} using data collected from a dust event during the ACE-Asia cruise.

Of critical importance though is the accuracy of modeling dust radiative effects in the TIR based on retrieved microphysical and macrophysical properties. This would include using properties retrieved based on generic optical properties for dust, e.g. VRI data, and then modeling the dust radiative forcing using a MEM model as might be done in a GCM that has available size-resolved compositional information and is being constrained or adjusted based on retrievals. We first examine what if any differences there are in the integrated radiative forcing when they are computed based on the VRI model and its retrieved microphysical properties. To do so we computed the spectral and integrated radiative forcing at both the TOA and BOA for one AIRS pixel from each of the three analyzed days. Recall that for Days 1 and 2 of the dust event we found significant spectral differences between the VRI model and measured radiances. Compared to the MEM model we would therefore expect the largest differences to occur for those cases. The radiative forcings for the VRI cases are presented in Table 4.10 along with the percentage difference from the MEM model.

Table 4.10 VRI model TOA and BOA TIR ΔF_a and difference from MEM model

Date	Pixel	Volz TOA ΔFa (Wm-2)	% Difference	Volz BOA ΔFa (Wm-2)	% Difference
Aug. 18	1	7.43	12.07	13.3	16.67
Aug. 19	2	4.96	-1.00	9.31	-6.05
Aug. 20	1	1.42	17.36	1.99	8.74

For Day 1 the VRI spectral radiative forcing slightly exceeds that of the MEM throughout most of the TIR window resulting in an overestimation of the integrated TOA and BOA radiative forcing by 12 and 17%, respectively. For the Day 2 case the VRI spectral radiative forcing slightly exceeds that of the MEM in some parts of the TIR window but is slightly less in other parts of the TIR window. This results in the integrated TOA and BOA radiative forcing being very close to that of the MEM model. This indicates that because a generic dust model can not precisely replicate the dust spectral signature, the degree to which a generic dust model and a MEM model (which can precisely match the dust spectral signature) are in agreement with respect to integrated radiative forcing depends on balancing the misfit between the modeled and measured signatures. A MEM model is therefore preferable because it is able to accurately match the spectral radiance, which allows for both the spectral and integrated radiative forcing to be correct. This is especially critical for inter-comparisons of model results with satellite data.

We now examine the differences in radiative forcing when the aerosol microphysics obtained from fitting the VRI model to the radiance data, e.g. from a retrieval based on a VRI model, are subsequently used to predict radiative forcing, e.g. in a GCM. Table 4.11 lists the results.

Table 4.11 TOA and BOA TIR ΔF_a for MEM model using VRI model retrieved loadings along with the difference from the original MEM model

Date	Pixel	MEM with VRI Loading TOA ΔFa (Wm-2)	% Difference	MEM with VRI Loading BOA ΔFa (Wm-2)	% Difference
Aug. 18	1	11.8	77.98	20.4	78.95
Aug. 19	2	2.47	-50.70	4.87	-50.86
Aug. 20	1	0.74	-38.84	1.12	-38.80

As with the cooling rates, there are very significant differences between radiative forcing computed with a model using derived microphysics based on another optical properties model and its own derived microphysics. For the Day 1 case where the fit for the VRI model results in a factor of 2 increase in loading over the MEM fit, the use of the VRI loading with the MEM model results in an 80% overestimation of the radiative forcing. For Days 2 and 3 where the fit for the VRI model results in about a factor of 2 decrease in loading compared to that from the MEM fit, the use of the VRI loading with the MEM model results in an 50% and 40% underestimation of the instantaneous radiative forcing. Consistency between retrievals/inverse modeling and predictions/forward modeling is extremely important to achieving accurate estimates of the radiative impacts of dust aerosol in the TIR.

To examine the sensitivity of the radiative forcing to macrophysical changes we considered the same three scenarios as in Section 4.6.1. Table 4.12 shows the results of these calculations in comparison to the original results.

Table 4.12 TOA and BOA TIR ΔF_a for original MEM model of the dust layer and 3 variation scenarios; increased concentration, layer moved up, and layer contracted; along with the percent change from the original for each scenario.

Date	Pixel	Case	TOA ΔFa (Wm-2)	% Change	BOA ΔFa (Wm-2)	% Change
Aug. 18						
	1	original	6.63		11.40	
		up	9.09	37.10	10.70	-6.14
		contract	5.21	-21.42	8.89	-22.02
		plus 50%	9.33	40.72	16.10	41.23
	2	original	7.71		13.30	
		up	10.60	37.48	12.50	-6.02
		contract	6.11	-20.75	10.50	-21.05
		plus 50%	10.80	40.08	18.70	40.60
Aug. 19						
	2	original	5.01		9.91	
		up	6.45	28.74	8.28	-16.45
		contract	3.68	-26.55	7.32	-26.14
		plus 50%	7.03	40.32	13.90	40.26
	3	original	4.50		9.18	
		up	5.77	28.22	7.72	-15.90
		contract	3.31	-26.44	6.75	-26.47
		plus 50%	6.53	45.11	13.00	41.61
Aug. 20						
	1	original	1.21		1.83	
		up	1.51	24.79	1.51	-17.49
		contract	0.81	-32.73	1.23	-32.79
		plus 50%	1.78	47.11	2.70	47.54
	2	original	1.43		2.11	
		up	1.80	25.87	1.74	-17.54
		contract	0.97	-32.52	1.42	-32.70
		plus 50%	2.10	46.85	3.11	47.39

These results indicate that the radiative forcing can be quite sensitive to variations in the concentration of the dust plume and to the position and thickness of the dust layer. Shifting the layer upwards by 1 km causes the TOA radiative forcing to increase by between 25-40%. The more optically thick the dust layer the larger the resulting variation. Correspondingly, the BOA radiative forcing decreased by between 5-20%. In

this case the more optically thick the layer the lesser the resulting variation. Decreasing the dust layer thickness, by 1 km by moving the bottom of the layer up by 0.5 km and the top of the layer down by 0.5 km, resulted in both the TOA and BOA radiative forcing being decreased by 25-35%. For both TOA and BOA cases, the more optically thick the layer is the lesser the resulting variation is to decreasing the layer thickness. When the concentration of dust particles in the dust plume was increased by 50%, both the TOA and BOA radiative forcing increased by 40-50%. As the optical thickness decreases the change in integrated radiative forcing becomes nearly equivalent to the change in particle concentration.

This analysis demonstrates the need for accuracy in high spectral resolution modeling of dust aerosol optical properties and the consistent use of models between retrievals and prediction of dust radiative effects. It also demonstrates the importance of getting the correct microphysics and macrophysics for the dust aerosol. This includes using the information on dust microphysics contained in the high spectral resolution TIR dust spectral signature, and using ancillary information for dust layer position and thickness.

4.8 Summary

We investigated the impact of dust aerosol on radiance, radiative forcing and cooling rates at high spectral resolution in the TIR, and how that impact depends on how the dust aerosol is modeled. The airborne and satellite data for several Saharan dust events were analyzed and modeled. As part of the modeling investigation, we compared modeling the dust radiative effects using a mineralogy-based external mixture (MEM)

approach to the common approach of using generic dust optical properties derived from bulk aerosol material samples. For the MEM approach we also investigated whether the spherical particle assumption is sufficient at high spectral resolution in the TIR, or whether the non-sphericity of the dust particles must be taken into account in the high spectral resolution modeling.

To accomplish this we developed tools and techniques that allowed us to rigorously and accurately model high spectral resolution TIR radiance impacted by dust aerosol. In particular, we developed a new technique using the MEM approach to retrieve size distribution and compositional information from the high spectral resolution dust signature. We compared the results of this new retrieval technique to a retrieval that used generic dust optical properties. We examined the differences in the retrieved dust microphysical properties and the implications of not applying the different techniques consistently. We also investigated the sensitivity of dust aerosol radiative forcing and cooling rate to variations of the position and thickness of the dust layer, and to variations of the particle concentration of the dust layer.

Our major findings are the following:

- High spectral resolution TIR radiance impacted by dust aerosol contains information on the composition and size distribution of the aerosol in its spectral signature as defined by a microwindow brightness temperature difference (BTD) spectrum between the measured radiance and a clear-sky modeled radiance.
- Accurate clear-sky modeling for BTD determination requires a spectrally accurate surface emissivity as a function of viewing angle and temperature for ocean surfaces. It also requires accurate modeling of CFCs levels, since inaccurate

CFCs modeling could result in confusion with mineral absorption features and the subsequent overestimation of mineral concentration or inaccurate microphysical properties.

- The high spectral resolution optical properties of a dust aerosol can be accurately modeled by a mineralogy-based external mixture of the mineral species of which it is composed. Additional mineral optical constants are likely to be required, e.g. feldspar species.
- Non-sphericity of dust particles must be taken into account when modeling the optical properties of individual minerals at high spectral resolution in the TIR. Mie theory is not sufficient. The T-matrix technique appears to be the most appropriate method. However, selection of the aspect ratio and its size dependence will need to be addressed.
- Because the dust signature at high spectral resolution depends on particle composition, shape and size distribution, we can not accurately model it and the aerosol radiative effects using just a generic refractive index dataset, like the Volz data, with only size distribution adjustments.
- Using bulk material refractive index data versus using mineral component refractive index data to model a dust aerosol leads to differences in derived/determined aerosol microphysics, specifically size distribution parameters and particle concentration.
- As the fraction of coarse mode particles increases the sensitivity to fine mode particles decreases, i.e. the effect of the coarse mode masks the effect of the fine mode and the fine mode particle concentration can not be determined very well.

- As the dust plume traveled across the Atlantic, our modeling, both MEM and VRI, indicated that a change in the microphysical properties occurred.
- Consistency between retrieval/inverse modeling and prediction/forward modeling is extremely important to achieving accurate estimates of the radiative impacts of dust aerosol in the TIR. If aerosol microphysical properties were retrieved using one model and then aerosol radiative effects were predicted using the other model, significant errors could result.

This analysis of the radiative effects of dust aerosol demonstrates the need for accuracy in high spectral resolution modeling of dust aerosol optical properties and the consistent use of models between retrievals and prediction of dust radiative effects. It also demonstrates the importance of getting the correct microphysics and macrophysics for the dust aerosol. This includes using the information on dust microphysics contained in the high spectral resolution TIR dust spectral signature, and using ancillary information for dust layer position and thickness. At the moment getting the aerosol layer height correct requires the use of ancillary data, e.g. the CALIPSO lidar. This demonstrates the importance of having a system of multiple complimentary sensors like the NASA A-Train to monitor the Earth-Ocean-Atmosphere system and monitor climate and climate drivers.

CHAPTER 5

SUMMARY AND CONCLUSIONS

5.1 Conclusions

Tropospheric aerosols are often complex mixtures of multiple materials each with its own distinct spectral characteristics in the TIR, and often consisting of irregularly shaped particles. Both of these conditions are particularly true for tropospheric dust. Such compositional and morphological complexity present significant problems for modeling the optical properties of an aerosol at high spectral resolution in the TIR, and pose a challenge to an accurate understanding of aerosol radiative and climate impacts. Current aerosol TIR optical modeling does not adequately address these issues and therefore is not able to accurately model the high spectral resolution optical properties of aerosols in the TIR. The standard approach of modeling aerosols by assuming spherical particles in order to use Mie theory and using bulk material optical constants, e.g. the ubiquitous "dust-like" or "insoluble" optical constants found in numerous aerosol models that are commonly used within GCMs and in remote sensing applications, fails to capture the true high spectral resolution characteristics of the aerosol. This problem is compounded by the fact that the composition and size distribution of an aerosol often varies spatially and temporally, even within an air mass, and therefore aerosol models must be adjustable to the specific conditions.

This dissertation addresses these issues by 1) compiling an extensive database of high spectral resolution aerosol component optical constants, including the development of new TIR optical constants of aqueous sulfate-nitrate-ammonium mixtures, to support

the advanced optical modeling efforts herein and future modeling efforts by other researchers; 2) investigating the high spectral resolution optical signatures of aerosol components and mixtures to determine how the optical properties vary depending on the techniques used for their modeling, e.g. mixing state and particle shape assumptions where the non-spherical technique results are compared to laboratory measurements; 3) developing tools and techniques to more accurately model aerosol radiative effects, particularly dust; and 4) applying those techniques to actual airborne and satellite high spectral resolution data of Saharan dust events to determine the techniques that most accurately model the measured data, and to develop a new technique to retrieve dust microphysical properties by taking advantage of the high spectral resolution optical signature. Based on our analysis of spectral signatures and the results of modeling the airborne and satellite high spectral resolution data we were able to make specific and unexpected recommendations for the improved modeling of high spectral resolution TIR optical properties of tropospheric dust, and the need for consistent use of dust models when retrieving dust properties and predicting dust radiative effects.

The newly developed LAARI database contains an extensive collection of high spectral resolution refractive indices of atmospheric aerosol components, many from the UV through the IR. By providing optical constants of individual components of aerosols, the database is designed to support advanced modeling of aerosol mixtures using an appropriate mixing rule and the most appropriate method of calculating optical properties. It also permits modeling of spatial and temporal variations of aerosol that provides new capabilities for the development of geophysical data retrieval algorithms and the study of radiative and climate impacts of aerosol. In an effort to fill in some of

the gaps in the existing refractive index data, we determined new IR optical constants for multi-component aqueous mixtures composed of ammonium sulfate, ammonium nitrate, sulfuric acid and nitric acid over a range of compositions and temperatures representative of aerosols of these compositions in tropospheric conditions.

After compiling the LAARI database, we used the optical constants to examine the spectral signatures of the components to see how distinct they are from one another. We found that the individual solid components and the multi-component aqueous mixtures have IR optical constants that are spectrally unique. For the multi-component aqueous mixtures the spectral absorption features reflect the particular composition of the mixture and the mixture's specific temperature dependence. This uniqueness means that the IR optical constants are not interchangeable. Dust, which is a mixture of multiple minerals, can not accurately be represented by a single mineral species or a generic "dust" refractive index dataset for high spectral resolution applications. For the aqueous mixtures, the IR optical constants of a binary aqueous mixture are not a good surrogate for those of a ternary or a quaternary aqueous mixture, and the IR optical constants of a ternary aqueous mixture are not a good surrogate for those of a quaternary aqueous mixture.

In analyzing the optical constants in the LAARI database, we found that nearly all of the aerosol components have IR spectral features that have the potential to impact remote sensing applications and climate. For example the ammonium sulfate-containing aqueous mixtures have a strong absorption band in the most transparent portion of the atmospheric TIR window and therefore could impact remote sensing applications like sea-surface temperature retrievals and contribute to a positive surface radiative forcing.

Also, sulfuric acid in a combination with ammonium sulfate produces concentration- and temperature-dependent bisulfate and sulfate absorption bands that nearly cover the entire TIR window region with potentially significant implications for IR remote sensing and surface radiative forcing. All of the mineral optical constants, with the exception of hematite, have strong absorbing bands in the TIR atmospheric window and therefore have the potential to impact remote sensing applications and climate. The silicate minerals with their fundamental Si-O vibrational absorption bands, that peak in the 1000 – 1100 cm^{-1} region, create the noted "v-shaped" depression in brightness temperature spectra in the TIR window for surface radiance transported through atmospheric dust. Because of the larger sizes of dust particles and their more effective interaction with TIR radiation, the impact of dust on remote sensing and climate is quite large and is clearly demonstrated in the results of this dissertation.

The optical constants of the aerosol components are only the building blocks for an aerosol model. From these, the optical properties of the aerosol need to be computed to be used in radiative transfer modeling. Because accurate radiative transfer modeling of the effects of aerosol on high spectral resolution radiance in the TIR critically depends on the correct spectral behavior of the aerosol optical properties, we have investigated how these properties vary based on the microphysical parameters that are used in their computation and on the mixing state. The analysis included examining the uniqueness of the spectral signatures of the individual mineral components and the variation of the aerosol signature with changes in the size distribution parameters including limits of integration. We then investigated techniques that could be used to address the non-spherical nature of dust particles and examined how the spectral signature changed. The

non-spherical techniques examined were T-matrix and CDE. The results the non-spherical particle techniques were compared to recently reported laboratory measurements for a number of pure mineral species in order to determine if either of these methods is more appropriate than Mie theory for dust particles. Additionally, we investigated the effects of external and internal mixture approaches on multi-component dust. This included characterizing the dependencies of the spectral signature of an externally mixed dust on the compositional fidelity with which the aerosol is modeled and also on the fine to coarse particle ratio for an aerosol with size-resolved composition. We also examined the spectral signature differences between externally mixed regional aerosol models, and models that use bulk sample derived optical constants. Finally for dust, we examined the spectral signature differences between a size-resolved aerosol model computed as an external mixture and as an internal mixture using both Mie theory and T-matrix.

In this investigation we found that the irregular shapes of dust particles are not adequately approximated by spheres in the calculation of optical properties. For quartz particles it appears that the optical properties of a distribution of oblate spheroids computed with T-matrix provides a much better fit to the published examples of measured extinction spectrum than any other technique that has been proposed. The quartz optical properties computed with T-matrix for an oblate spheroid with a shape factor of 5 yields a spectral signature with features in the correct positions, but the features are too narrow. In addition to these results for quartz, we found that for the phyllosilicate minerals, T-matrix calculations with a shape factor of 5 also produce optical properties with correctly positioned spectral features. We determined that the

CDE technique is not practical for terrestrial dust particles due to the lack of continuum extinction, a result of being derived in the Rayleigh regime, and the fact that the spectral signature match using CDE is not as good as T-matrix for clay minerals. Although CDE provided better results than Mie, it lacks the continuum extinction that Mie would be able to model.

We found that the high spectral resolution optical properties of an aerosol depend significantly on the size distribution parameters, and that these parameters need to be correctly adjusted to accurately model measured radiance. We also found that coarse mode signatures have reduced spectral contrast for their features, which means that retrieving composition information would be more difficult. For smaller size modes, the spectral contrasts of features are larger and therefore retrieving compositional information and size distribution parameters is less difficult.

Based on a comparison of the spectral signatures of a highly complex size-resolved mineralogical aerosol model and that of a simpler model retaining only the major components, we found the spectral differences to be minor. Therefore a high level of compositional fidelity is not advised. We also found that internal versus external dust mixtures show large spectral differences in the region of very strong quartz absorption, but outside of this region the differences are small. Therefore external and internal mixtures are interchangeable if quartz composes a small fraction of the aerosol. If there are differences between external and internal mixtures they should be readily apparent at high spectral resolution.

We also evaluated the use of EMA mixing rules in modeling the IR optical constants of multi-component aqueous aerosols using the newly determined IR optical

constants. We found that the mixing rules examined can model aqueous multi-component IR optical constants accurately if the appropriate components are used. For binary mixtures the appropriate components are not the IR optical constants of pure water and pure solute. Binary mixtures require the use of measured IR optical constants. Low concentration binary mixtures can be accurately modeled using high concentration optical constants and pure water optical constants in a mixing rule. For ternary mixtures we found that in cases where the solute species do not interact strongly, the mixing rules can accurately predict IR optical constants based on binary optical constant input. For ternary mixtures like aqueous sulfuric acid-ammonium sulfate however, for which the solutes do interact, measured IR optical constants must be used. In the quaternary mixture case examined, we found that the use of binary optical constants data in the mixing rules did not accurately model the measured optical constants. A combination of ternary and binary optical constants, however, resulted in good agreement between modeled and measured values.

Surprisingly, we found that the several mixing rules considered in this study all performed well. On average, the straightforward Biermann and simple volume average mixing rules performed slightly better than the more computationally complex mixing rules for ternary and quaternary mixtures.

Using optical constants from the LAARI database and insights gained from investigating the optical signatures of aerosol components and mixtures, we have demonstrated here for the first time that a relatively simple dust model, the Mineralogy-based External Mixture (MEM) model based on one or two size modes each composed of only a small number of mineral species in an external mixture, can accurately reproduce

measured radiance attenuated by a dust plume at high spectral resolution. We initially demonstrated this capability with two airborne datasets taken over different locations above a Saharan dust plume being advected across the Atlantic. We then successfully demonstrated the capability for multiple satellite datasets taken over three days as a Saharan dust plume moved from the coast of Africa to more than halfway across the Atlantic. The ability to accurately reproduce high spectral resolution remote sensing measurements with a composition-resolved dust model will be extremely valuable to the development of improved atmospheric correction of the data for geophysical parameter retrievals.

We also used the MEM model and our optical signature analysis results to develop a new technique to retrieve dust microphysical information from the dust signature in the measured radiance that is based on a new microwindows approach. In doing so we developed tools and techniques for dust optical properties modeling and radiative transfer modeling. We found that addressing particle non-sphericity is critical for modeling dust optical properties at high spectral resolution in the TIR. Using our new tools and techniques on the airborne and satellite high spectral resolution measurements of TIR radiance affected by large dust events, we verified the previous finding that Mie theory can not be used for accurate modeling of the optical properties of irregularly-shaped dust particles. Optical properties computed with Mie theory for pure mineral species produce spectral signatures with spectral features that do not correspond to those of actual dust plumes. The non-spherical irregular shapes of dust particles prohibit the use of Mie theory. We then found that the optical properties of phyllosilicates and quartz can successfully be modeled with T-matrix using oblate spheroids of shape factor 5, or a

distribution of oblate spheroids, which results in a good match to the spectral signatures of naturally occurring dust particles. We can also note that the accurate generation of the aerosol optical properties depends on using quality high spectral resolution optical constants.

In accomplishing our aerosol radiative modeling we found that a rigorous high spectral resolution radiative transfer code that allows for the complete specification of the spectral optical properties of an aerosol as a function of height is essential to accurate modeling of radiance affected by aerosol. Accurate radiative transfer modeling for aerosol modeling also requires accurate spectral surface emissivity, collection viewing geometry controls, and good estimates of the state of the atmosphere and surface. For dust modeling in particular, good estimates of profiles for CFCs are critical because a number of CFCs have absorption features that align with or overlap absorption features of minerals. We also note that it is very important to have information about the dust layer position and thickness in order to accurately model its effects. This reinforces the critical need for coincident and complementary sources of geophysical information like CALIPSO.

In our analysis of dust modeling with bulk refractive index data, we found that the high spectral resolution dust signature in TIR aircraft and satellite observations can not be accurately modeled by these generic dust optical properties. We also found that using bulk material refractive index data versus mineral component refractive index data in modeling dust leads to differences in the retrieved properties of the dust. This in turn can lead to significant differences in assessments of the radiative impacts of dust if the models are used inconsistently or interchangeably. For both models in the cases studied,

we found that the dust median radius and the dust particle concentration changes with distance transported. For the MEM model we found in addition to those changes that the number of size modes and the fine to coarse particle ratio changes with distance traveled, which is consistent with physical expectations.

Using our new microwindow dust signature approach, we were able to for the first time assess the spectral IR radiative forcing and cooling rates of dust with a composition-resolved dust model that was constrained by observations. In comparing the radiative effects of radiative forcing and cooling rate for dust as determined by the MEM model and the bulk material aerosol model, we saw that there can be significant differences in these quantities depending on the model that is used. More importantly though, we observed that very large differences in radiative forcing and cooling rate can result from the inconsistent use of the models. For example, if dust microphysics is retrieved using bulk refractive index data and then that information is used for modeling with an external mixture of mineral components, large errors can occur. This result demonstrates the importance of understanding retrieved quantities and the assumptions used in retrieving them, and applying that retrieved information carefully when forward modeling.

Lastly, in our sensitivity analysis of dust radiative forcing and cooling rate to dust loading and dust layer position and thickness, we found significant sensitivity to these quantities. This means that these quantities need to be accurately determined in order to accurately quantify the climate impacts of dust. Our analysis of the AIRS data together with CALIPSO data demonstrates how this can be effectively addressed.

5.2 Recommendations and Future Work

The results of this work indicate that a dramatically different approach is required to accurately model dust properties and effects at high spectral resolution in the TIR. The non-spherical nature of dust particles must be accounted for. Also, even though the use of bulk sample dust refractive index data can provide reasonable answers in limited situations, e.g. for aerosol in the geographic region where the dust was sampled and with similar microphysical properties, bulk sample data can not be used generically for diverse regions and conditions or even for a given dust event from start to finish as it is transported. T-matrix calculations have been shown here to provide results that are in good agreement spectrally with measured data. The shape factor that is required though is not in agreement with physically measured shape factors. On the other hand, naturally occurring dust particles are not smooth surfaced spheroids. A better understanding of how and why these T-matrix calculations provide good agreement with measured data is required. To accomplish that we recommend that the scientific community undertake high spectral resolution TIR extinction measurements in air of 1) individual mineral species for size distributions that are representative of those that occur naturally and 2) actual dust samples from multiple geographic regions and transport distances that have been separated into fine and coarse size modes. We also see a need for extensive DDA modeling using measured 3-dimensional shape and size distribution information for random orientations to determine whether DDA results agree with measurement data and to help explain why large shape factors are able to accurately model measured data. We propose that the findings reported here be used to develop improved algorithms to retrieve dust microphysical properties and to detect and correct for the effect of dust on

high spectral resolution TIR radiance measurements. Lastly, we recommend that aerosol component optical constants continue to be updated as the techniques to derive them and equipment to make these measurements improve.

For future work we suggest the following:

1) Develop a look-up table of optical properties as a function of median radius using T-matrix calculations for individual mineral dust species at high spectral resolution in the TIR to support rapid calculations of regional size-resolved Mineralogy-based External Mixture models,
2) Using the techniques described here, continue the analysis of AIRS and other high spectral resolution TIR data sources for other geographic regions, and
3) Apply the techniques described here to ground-based atmospheric sounding instruments like the AERI instrument.
4) Conduct a closure study to determine if the modeled mineralogical composition of the external mixture that provides the best fit to the radiance data is in good agreement with the composition of the actual dust particles, and whether the size distribution(s) that provide the best fit are in agreement with the actual size distribution(s) of the dust particles. This will require a coordinated effort of radiance measurements, particle sampling, and analysis both in the laboratory and in the field.

APPENDIX A

ADDITIONAL FIGURES

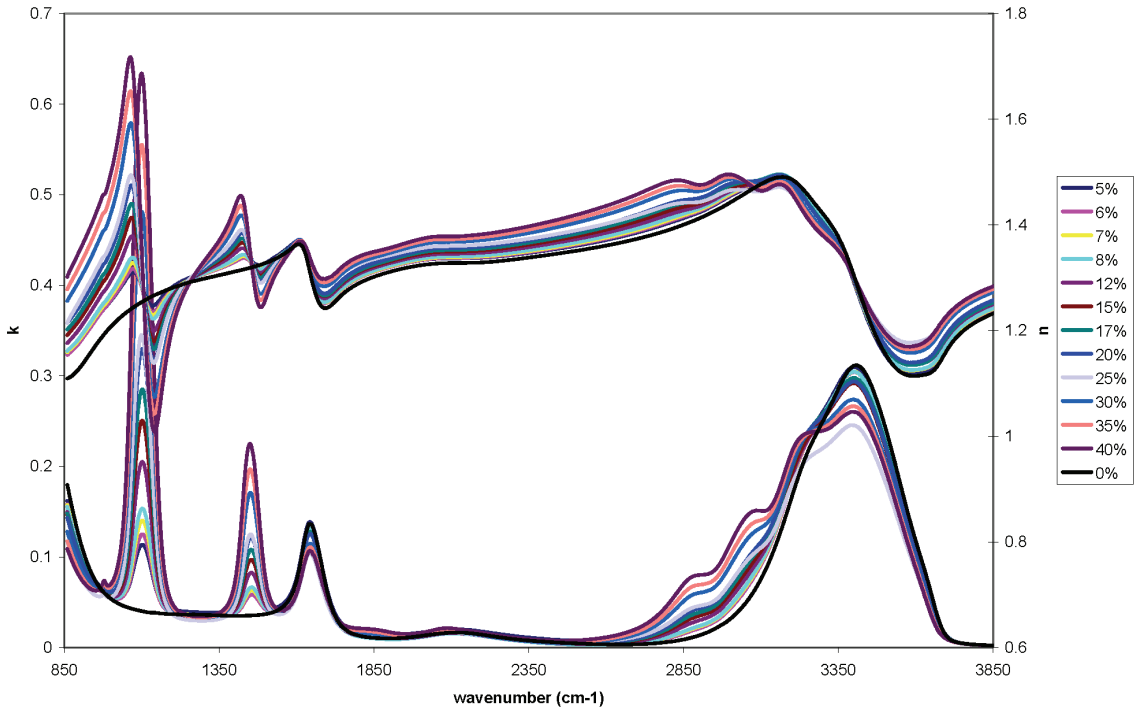

Figure A.1. The n and k spectra of group A aqueous ammonium sulfate binary mixtures at all measured concentrations at 298 K along with the n and k spectrum of pure water from the literature (0%).

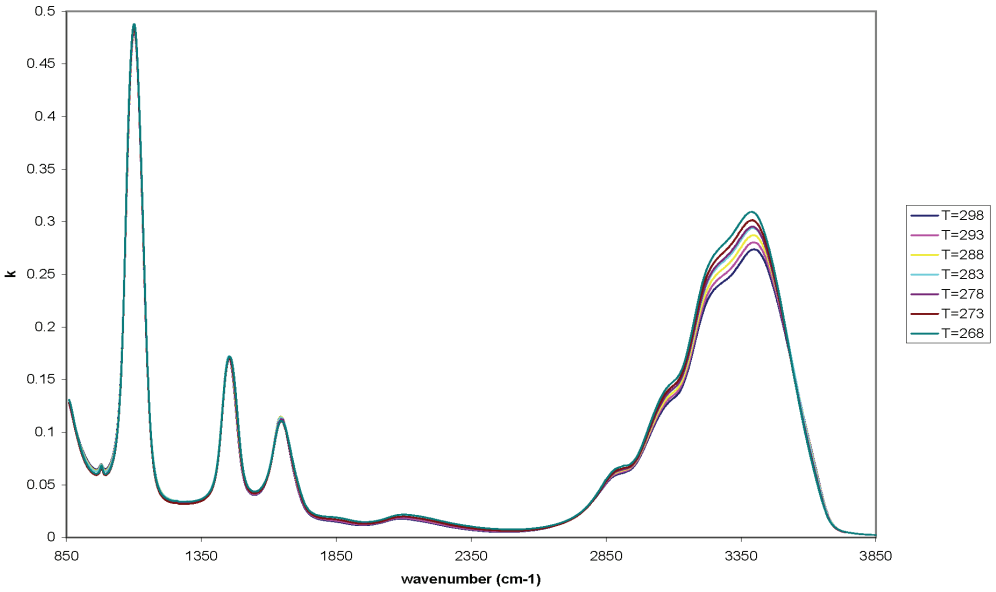

Figure A.2. The k spectra of 30% binary aqueous ammonium sulfate at all measured temperatures.

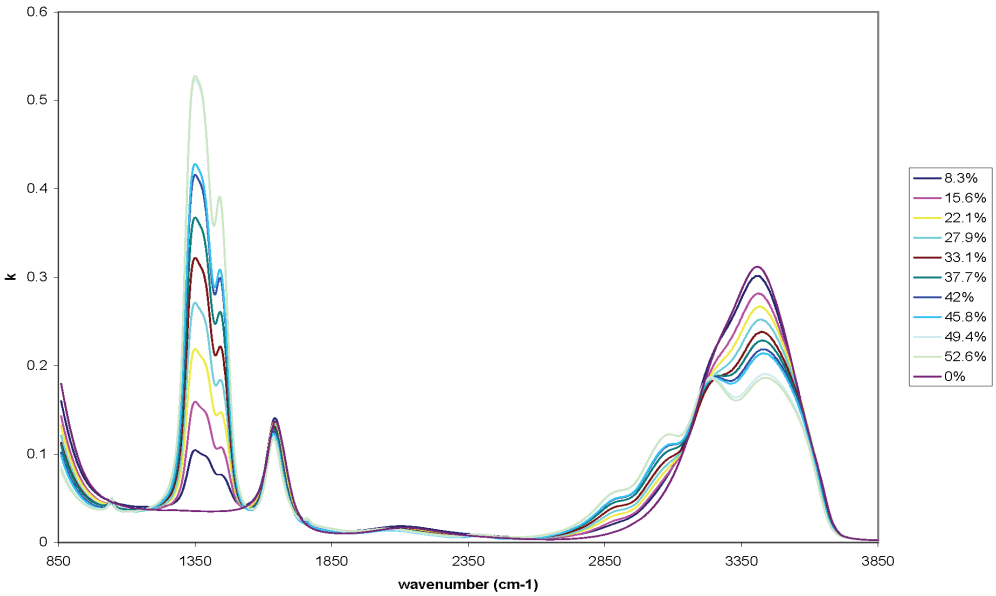

Figure A.3. The k spectra of group B aqueous ammonium nitrate binary mixtures at all measured concentrations at 298 K along with the k spectrum of pure water from the literature (0%).

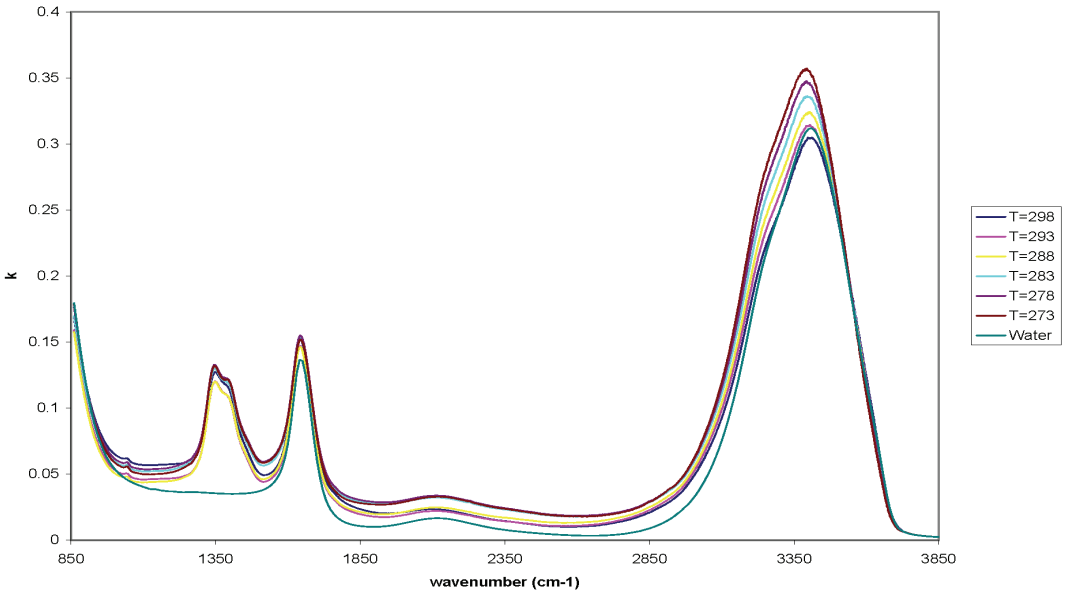

Figure A.4. The k spectra of 5.1% - 3.5% aqueous nitric acid - ammonium nitrate ternary mixtures at all measured temperatures along with the k spectrum of pure water from the literature (0%).

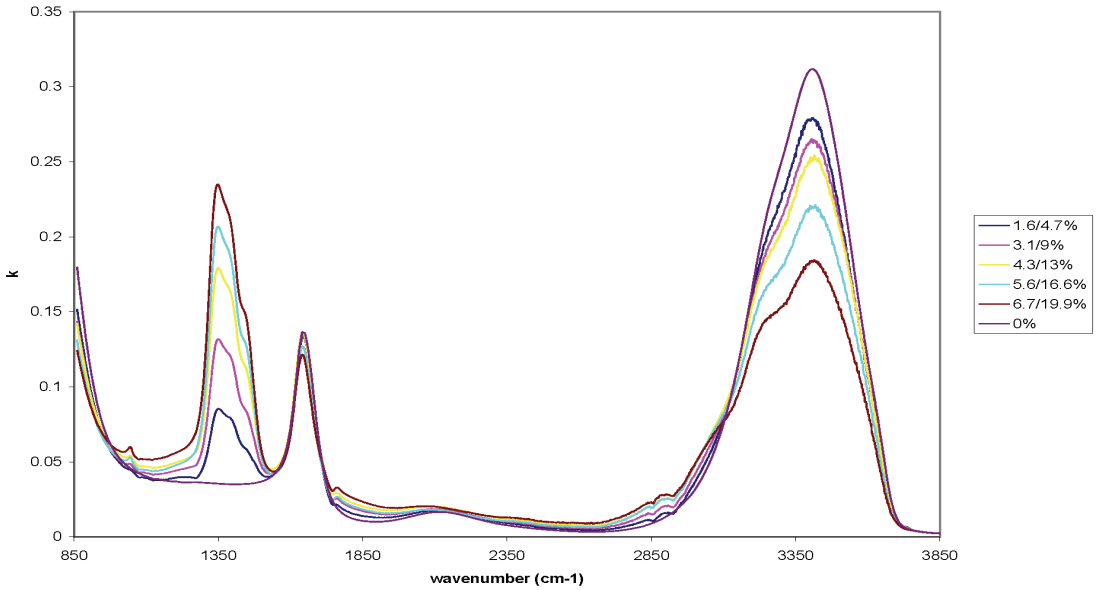

Figure A.5. The k spectra of group H aqueous nitric acid - ammonium nitrate ternary mixtures at all measured concentrations at 298 K along with the k spectrum of pure water from the literature (0%).

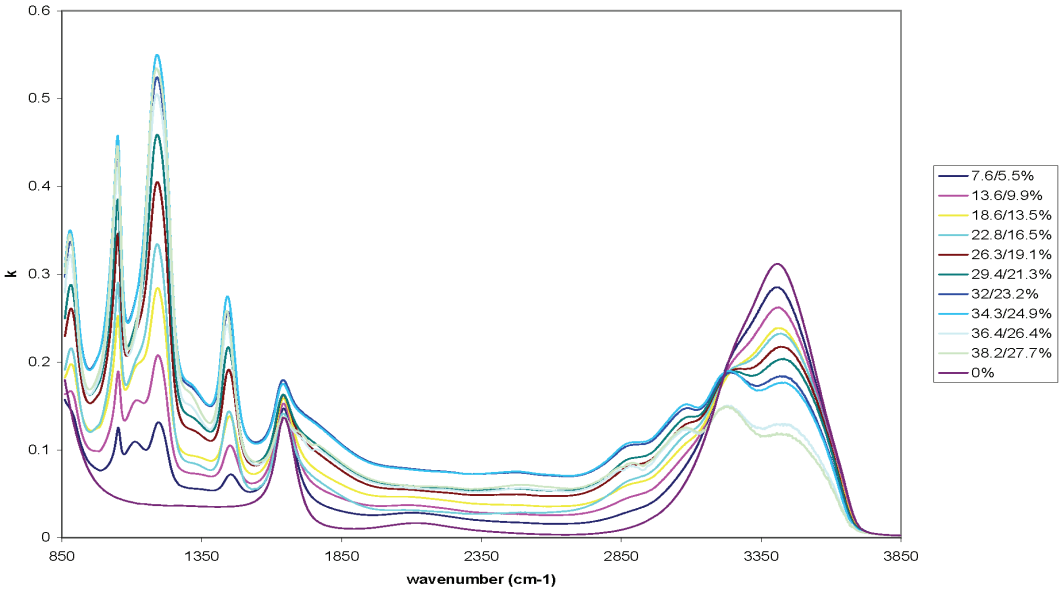

Figure A.6. The k spectra of group D aqueous sulfuric acid - ammonium sulfate ternary mixtures at all measured concentrations at 298 K along with the k spectrum of pure water from the literature (0%).

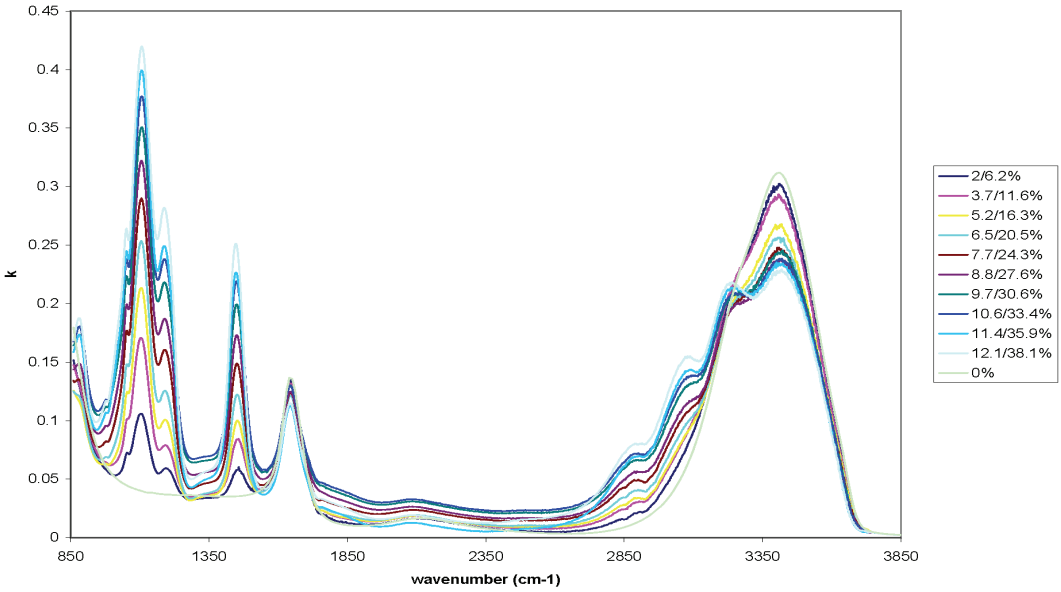

Figure A.7. The k spectra of group F aqueous sulfuric acid - ammonium sulfate ternary mixtures at all measured concentrations at 298 K along with the k spectrum of pure water from the literature (0%).

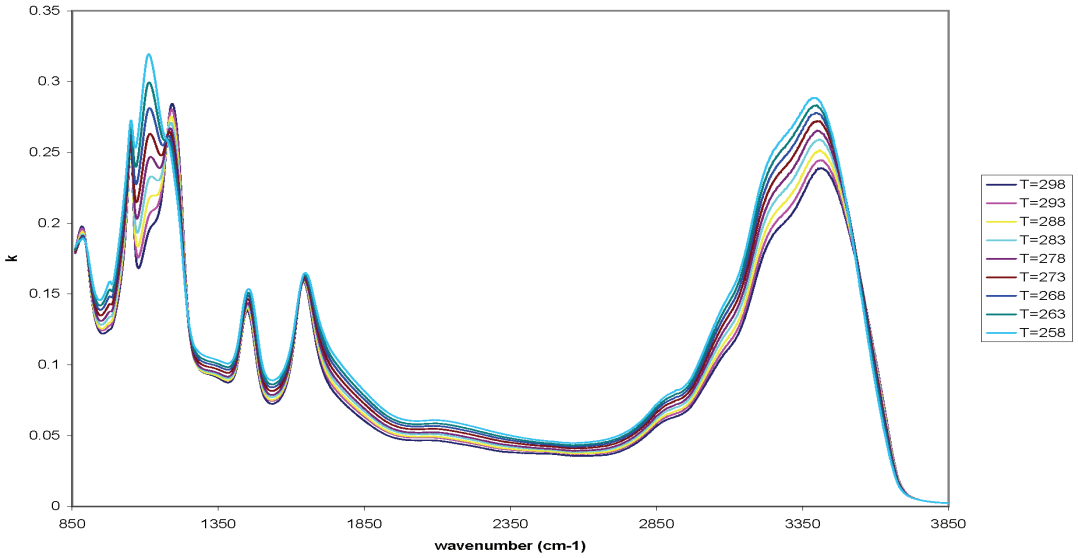

Figure A.8. The k spectra of 18.6% - 13.5% aqueous sulfuric acid - ammonium sulfate ternary mixtures at all measured temperatures showing the temperature dependence of the imaginary index of refraction.

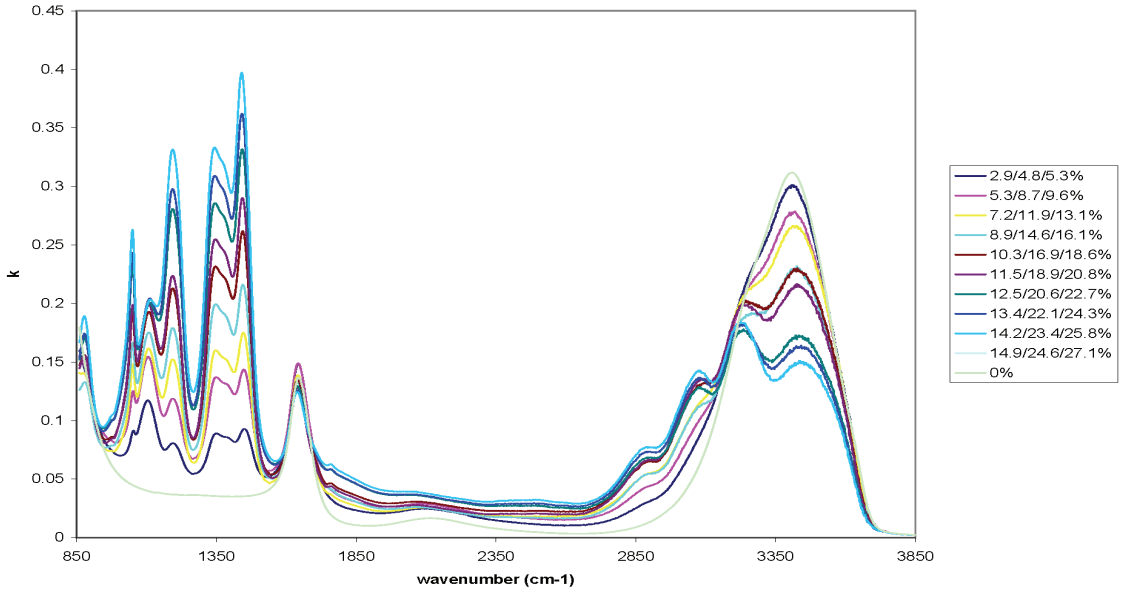

Figure A.9. The k spectra of group E aqueous sulfuric acid - ammonium sulfate - ammonium nitrate quaternary mixtures at all measured concentrations at 298 K along with the k spectrum of pure water from the literature (0%).

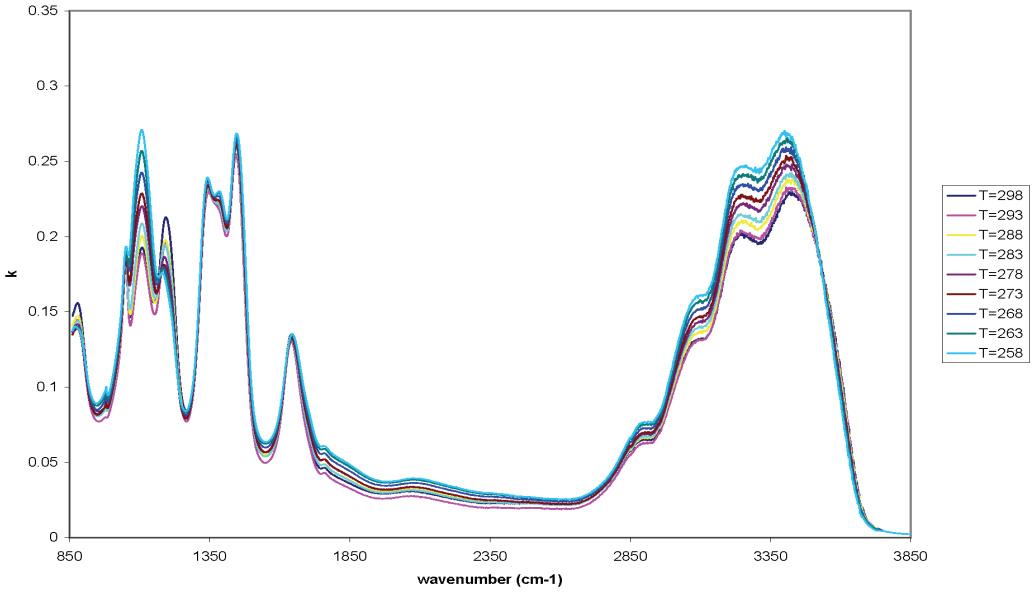

Figure A.10. The k spectra of 10.3% - 16.9% - 18.6% aqueous sulfuric acid - ammonium sulfate - ammonium nitrate quaternary mixtures at all measured temperatures showing the temperature dependence of the imaginary index of refraction.

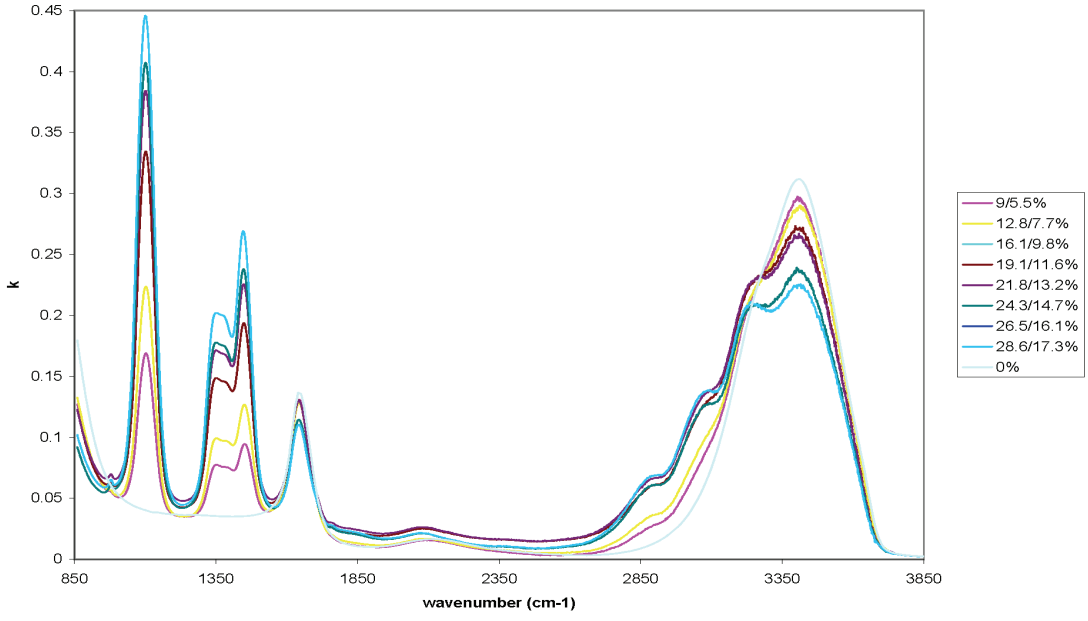

Figure A.11. The k spectra of group G aqueous ammonium sulfate - ammonium nitrate ternary mixtures at all measured concentrations at 298 K along with the k spectrum of pure water from the literature (0%).

APPENDIX B

DERIVATION OF THE CDE SCATTERING COEFFICIENT AND SCATTERING FUNCTION

From *Bohren and Huffman* [1983] and *Nevitt and Bohren* [1984] the average scattering cross section for a collection of randomly-oriented identical ellipsoids of volume V may be written in the form

$$\langle C_{sca} \rangle = \frac{\tilde{k}^4 v^2}{18\pi} \sum_{j=1}^{3} \left| \frac{1}{\beta + L_i} \right|^2 \qquad \text{(Eq. B.1)}$$

where

$$\beta = \beta' + i\beta'' = (\varepsilon - 1)^{-1} \qquad \text{(Eq. B.2)}$$

The L_j are the geometric factors dependent on the ratio of the semiaxes of the ellipsoid, and ε is the complex dielectric function. The Lj satisfy the condition

$$L_1 + L_2 + L_3 = 1 \qquad \text{(Eq. B.3)}$$

For a sphere $L_1 = L_2 = L_3$. Now for an ellipsoid the polarizability is

$$\alpha_i = 4\pi abc \frac{\varepsilon - 1}{3\left(1 + L_i(\varepsilon - 1)\right)} = 4\pi abc \frac{1/\beta}{3\left(1 + L_i/\beta\right)} = \frac{4\pi abc}{3(\beta + L_i)} = \frac{4\pi abc}{3} \frac{1}{\beta + L_i} \qquad \text{(Eq. B.4)}$$

The volume of the ellipsoid is

$$v = \frac{4\pi abc}{3} \qquad \text{(Eq. B.5)}$$

so

$$\alpha_i = \frac{v}{\beta + L_i} \qquad \text{(Eq. B.6)}$$

and

$$|\alpha_i|^2 = v^2 \left| \frac{1}{\beta + L_i} \right|^2 \qquad \text{(Eq. B.7)}$$

therefore the average scattering cross section can be written as

$$\left\langle C_{sca} \right\rangle = \frac{\tilde{k}^4 v^2}{18\pi} \sum_{j=1}^{3} \left| \frac{1}{\beta + L_j} \right|^2 = \frac{\tilde{k}^4}{18\pi} \left[\left|\alpha_1\right|^2 + \left|\alpha_2\right|^2 + \left|\alpha_3\right|^2 \right] \qquad \text{(Eq. B.8)}$$

Following *Bohren and Huffman* [1983] and *Nevitt and Bohren* [1984], the average scattering cross section for a collection of small ellipsoidal particles of the same volume but varying geometric shape factors can be modeled by integrating Eq. B.8 over all possible values of L_1 and L_2 weighted by a shape probability function $P(L_1, L_2)$.

$$\left\langle\left\langle C_{sca} \right\rangle\right\rangle = \frac{\tilde{k}^4 v^2}{18\pi} \int_0^1 \int_0^{1-L_1} \sum_{j=1}^{3} \left| \frac{1}{\beta + L_i} \right|^2 P\left(L_1, L_2\right) dL_2 dL_1 \qquad \text{(Eq. B.9)}$$

Letting

$$A_1 = \int_0^1 \int_0^{1-L_1} \left| \frac{1}{\beta + L_1} \right|^2 P\left(L_1, L_2\right) dL_2 dL_1 \qquad \text{(Eq. B.10)}$$

$$A_2 = \int_0^1 \int_0^{1-L_1} \left| \frac{1}{\beta + L_2} \right|^2 P\left(L_1, L_2\right) dL_2 dL_1 \qquad \text{(Eq. B.11)}$$

$$A_3 = \int_0^1 \int_0^{1-L_1} \left| \frac{1}{\beta + L_3} \right|^2 P\left(L_1, L_2\right) dL_2 dL_1 = \int_0^1 \int_0^{1-L_1} \left| \frac{1}{\beta - L_1 - L_2} \right|^2 P\left(L_1, L_2\right) dL_2 dL_1 \qquad \text{(Eq. B.12)}$$

$$\left\langle\left\langle C_{sca} \right\rangle\right\rangle = \frac{\tilde{k}^4 v^2}{18\pi} \left(A_1 + A_2 + A_3 \right) \qquad \text{(Eq. B.13)}$$

For the case where all ellipsoidal shapes are equally probable, i.e. $P(L_1, L_2) = 2$, the integrals A_1, A_2, and A_3 are evaluated to give

$$A_1 = A_2 = A_3$$
$$= \frac{\left(2 + 2\beta'\right)}{\left|\beta''\right|} \left[\tan^{-1}\left(\frac{1 + \beta'}{\left|\beta''\right|} \right) - \tan^{-1}\left(\frac{\beta'}{\left|\beta''\right|} \right) \right] - \ln\left[\left(1 + \beta'\right)^2 + \beta''^2 \right] + \ln\left(\left|\beta\right|^2 \right) \qquad \text{(Eq. B.14)}$$

Carrying out the derivation for A_1 we have

$$A_1 = \int_0^1 \int_0^{1-L_1} \left| \frac{1}{\beta + L_1} \right|^2 2dL_2 dL_1 = \int_0^1 \int_0^{1-L_1} \frac{2}{\left|\beta + L_1\right|^2} dL_2 dL_1$$

$$= \int_0^1 \int_0^{1-L_1} \frac{2}{\left|\left(\beta' + L_1\right) + i\beta''\right|^2} dL_2 dL_1 = \int_0^1 \int_0^{1-L_1} \frac{2}{\left(\beta' + L_1\right)^2 + \beta''^2} dL_2 dL_1$$

$$= \int_0^1 \frac{2L_2}{\left(\beta' + L_1\right)^2 + \beta''^2} \Bigg|_0^{1-L} dL_1 = \int_0^1 \frac{2 - 2L_1}{\left(\beta' + L_1\right)^2 + \beta''^2} dL_1$$

$$= 2\int_0^1 \frac{1}{\left(\beta' + L_1\right)^2 + \beta''^2} dL_1 - 2\int_0^1 \frac{L_1}{\left(\beta' + L_1\right)^2 + \beta''^2} dL_1 \qquad \text{(Eq. B.15)}$$

Now letting

$$x = \beta' + L_1 \qquad \text{(Eq. B.16)}$$

We have

$$\int_0^1 \frac{L_1}{\left(\beta' + L_1\right)^2 + \beta''^2} dL_1 = \int_{\beta'}^{1+\beta'} \frac{x - \beta'}{x^2 + \beta''^2} dx = \int_{\beta'}^{1+\beta'} \frac{x}{x^2 + \beta''^2} dx - \beta' \int_{\beta'}^{1+\beta'} \frac{1}{x^2 + \beta''^2} dx$$

$$= \frac{1}{2} \ln\left(x^2 + \beta''^2\right) \Big|_{\beta'}^{1+\beta'} - \frac{\beta'}{\left|\beta''\right|} \left[\tan^{-1}\left(\frac{1+\beta'}{\left|\beta''\right|} \right) - \tan^{-1}\left(\frac{\beta'}{\left|\beta''\right|} \right) \right]$$

$$= \frac{1}{2} \left[\ln\left[\left(1+\beta'\right)^2 + \beta''^2 \right] - \ln\left(\left|\beta\right|^2 \right) \right] - \frac{\beta'}{\left|\beta''\right|} \left[\tan^{-1}\left(\frac{1+\beta'}{\left|\beta''\right|} \right) - \tan^{-1}\left(\frac{\beta'}{\left|\beta''\right|} \right) \right] \qquad \text{(Eq. B.17)}$$

and

$$\int_0^1 \frac{1}{\left(\beta' + L_1\right)^2 + \beta''^2} dL_1 = \int_{\beta'}^{1+\beta'} \frac{1}{x^2 + \beta''^2} dx = \frac{1}{\left|\beta''\right|} \tan^{-1}\left(\frac{x}{\left|\beta''\right|} \right) \Bigg|_{\beta'}^{1+\beta'}$$

$$= \frac{1}{\left|\beta''\right|} \left[\tan^{-1}\left(\frac{1+\beta'}{\left|\beta''\right|} \right) - \tan^{-1}\left(\frac{\beta'}{\left|\beta''\right|} \right) \right] \qquad \text{(Eq. B.18)}$$

Substituting Eqs. B.17 and B.18 back into Eq. B.15 gives

$$A_1 = \frac{\left(2 + 2\beta'\right)}{\left|\beta''\right|} \left[\tan^{-1}\left(\frac{1+\beta'}{\left|\beta''\right|} \right) - \tan^{-1}\left(\frac{\beta'}{\left|\beta''\right|} \right) \right] - \ln\left[\left(1+\beta'\right)^2 + \beta''^2 \right] + \ln\left(\left|\beta\right|^2 \right) \qquad \text{(Eq. B.19)}$$

A_2 and A_3 can be derived similarly. Therefore

$$\left\langle\left\langle C_{sca}\right\rangle\right\rangle = \frac{\tilde{k}^4 v^2}{18\pi}\left(A_1 + A_2 + A_3\right)$$
$$= \frac{\tilde{k}^4 v^2}{6\pi}\left[\frac{\left(2+2\beta'\right)}{\left|\beta''\right|}\left[\tan^{-1}\left(\frac{1+\beta'}{\left|\beta''\right|}\right) - \tan^{-1}\left(\frac{\beta'}{\left|\beta''\right|}\right)\right] - \ln\left[\left(1+\beta'\right)^2 + \beta''^2\right] + \ln\left(\left|\beta\right|^2\right)\right]$$

(Eq. B.20)

To this point all particles were considered to have the same volume. If there is no correlation between shape and volume, then the total scattering cross section of the collection of particles is

$$\left\langle\left\langle C_{sca}\right\rangle\right\rangle = \frac{\tilde{k}^4 \left\langle v\right\rangle^2}{6\pi}\left[\frac{\left(2+2\beta'\right)}{\left|\beta''\right|}\left[\tan^{-1}\left(\frac{1+\beta'}{\left|\beta''\right|}\right) - \tan^{-1}\left(\frac{\beta'}{\left|\beta''\right|}\right)\right] - \ln\left[\left(1+\beta'\right)^2 + \beta''^2\right] + \ln\left(\left|\beta\right|^2\right)\right]$$

(Eq. B.21)

where <v> is the average particle volume.

The scattering phase function is defined in terms of the differential scattering cross section and the total scattering cross section as

$$P\left(\theta\right) = \frac{4\pi}{\left\langle C_{sca}\right\rangle}\frac{d\left\langle C_{sca}\right\rangle}{d\omega} \qquad \text{(Eq. B.22)}$$

For unpolarized light the differential scattering cross section for the I Stokes parameters component of the scattered electromagnetic wave is

$$\frac{d\left\langle C_{sca}\right\rangle}{d\omega} = \frac{\left\langle S_{11}\right\rangle}{\tilde{k}^2} \qquad \text{(Eq. B.23)}$$

where $\langle S_{11}\rangle$ is from the scattering matrix for a collection of ellipsoidal particles.

From *Bohren and Huffman* [1983]and *Nevitt and Bohren* [1984]

$$\left\langle S_{11}\right\rangle = \frac{3\tilde{k}^2\left\langle C_{sca}\right\rangle}{8\pi}\frac{1}{2}\left(\frac{6-M}{5} + \frac{2+3M}{5}\cos^2\theta\right) \qquad \text{(Eq. B.24)}$$

where

$$M = \frac{\mathrm{Re}\left\{\alpha_1^*\alpha_2 + \alpha_1^*\alpha_3 + \alpha_2^*\alpha_3\right\}}{\left|\alpha_1\right|^2 + \left|\alpha_2\right|^2 + \left|\alpha_3\right|^2} \qquad \text{(Eq. B.25)}$$

We need to integrate the differential scattering term over the shape distribution in order to obtain the scattering phase function for the distribution of ellipsoids.

$$\frac{\langle S_{11}\rangle}{\tilde{k}^2}=\frac{3\langle C_{sca}\rangle}{16\pi}\left(\frac{6-M}{5}+\frac{2+3M}{5}\cos^2\theta\right)$$
$$=\frac{3\langle C_{sca}\rangle}{80\pi}\left(6+2\cos^2\theta+3M\cos^2\theta-M\right)$$
$$=\frac{3\langle C_{sca}\rangle}{80\pi}\left(2\left(3+\cos^2\theta\right)+M\left(3\cos^2\theta-1\right)\right)$$
$$=\frac{6\left(3+\cos^2\theta\right)\langle C_{sca}\rangle}{80\pi}+\frac{3\left(3\cos^2\theta-1\right)\langle C_{sca}\rangle M}{80\pi}$$
$$=\frac{6\left(3+\cos^2\theta\right)}{80\pi}\frac{\tilde{k}^4}{18\pi}\left[\left|\alpha_1\right|^2+\left|\alpha_2\right|^2+\left|\alpha_3\right|^2\right]$$
$$+\frac{3\left(3\cos^2\theta-1\right)}{80\pi}\frac{\tilde{k}^4}{18\pi}\mathrm{Re}\left\{\alpha_1^*\alpha_2+\alpha_1^*\alpha_3+\alpha_2^*\alpha_3\right\}$$
$$=\frac{\left(3+\cos^2\theta\right)}{80\pi}\frac{\tilde{k}^4v^2}{3\pi}\left[\left|\frac{1}{\beta+L_1}\right|^2+\left|\frac{1}{\beta+L_2}\right|^2+\left|\frac{1}{\beta+L_3}\right|^2\right]$$
$$+\frac{\left(3\cos^2\theta-1\right)}{80\pi}\frac{\tilde{k}^4v^2}{6\pi}\mathrm{Re}\left\{\frac{1}{\left(\beta^*+L_1\right)\left(\beta+L_2\right)}+\frac{1}{\left(\beta^*+L_1\right)\left(\beta+L_3\right)}+\frac{1}{\left(\beta^*+L_2\right)\left(\beta+L_3\right)}\right\}$$

(Eq. B.26)

Integrating the differential scattering over shape distribution we have

$$\frac{\langle\langle S_{11}\rangle\rangle}{\tilde{k}^2}=\frac{\left(3+\cos^2\theta\right)}{80\pi}\frac{\tilde{k}^4v^2}{3\pi}\left[A_1+A_2+A_3\right]+\frac{\left(3\cos^2\theta-1\right)}{80\pi}\frac{\tilde{k}^4v^2}{6\pi}\mathrm{Re}\left\{I_1+I_2+I_3\right\}\quad\text{(Eq. B.27)}$$

where

$$I_1=\int_0^1\int_0^{1-L_1}\frac{1}{\left(\beta^*+L_1\right)\left(\beta+L_2\right)}P\left(L_1,L_2\right)dL_2dL_1$$

(Eq. B.28)

$$I_2=\int_0^1\int_0^{1-L_1}\frac{1}{\left(\beta^*+L_1\right)\left(\beta+L_3\right)}P\left(L_1,L_2\right)dL_2dL_1=\int_0^1\int_0^{1-L_1}\frac{1}{\left(\beta^*+L_1\right)\left(\beta+1-L_1-L_2\right)}P\left(L_1,L_2\right)dL_2dL_1$$

(Eq. B.29)

$$I_3=\int_0^1\int_0^{1-L_1}\frac{1}{\left(\beta^*+L_2\right)\left(\beta+L_3\right)}P\left(L_1,L_2\right)dL_2dL_1=\int_0^1\int_0^{1-L_1}\frac{1}{\left(\beta^*+L_2\right)\left(\beta+1-L_1-L_2\right)}P\left(L_1,L_2\right)dL_2dL_1$$

(Eq. B.30)

For the case where all ellipsoidal shapes are equally probable, i.e. $P(L_1, L_2) = 2$, the integrals I_1, I_2, and I_3 are evaluated to give

$$I_1 = I_2 = I_3 = 2\int_0^1 \frac{\ln\left(\left[\beta + 1 - L_1\right]/\beta\right)}{\left(\beta^* + L_1\right)} dL_1 \tag{Eq. B.31}$$

Carrying out the derivation for I_1 we have

$$\begin{aligned} I_1 &= \int_0^1 \int_0^{1-L_1} \frac{2}{\left(\beta^* + L_1\right)\left(\beta + L_2\right)} dL_2 dL_1 \\ &= 2\int_0^1 \frac{\ln\left(\beta + L_2\right)}{\left(\beta^* + L_1\right)}\Bigg|_0^{1-L_1} dL_1 \\ &= 2\int_0^1 \frac{1}{\left(\beta^* + L_1\right)}\left[\ln\left(\beta + 1 - L_1\right) - \ln\left(\beta\right)\right] dL_1 \\ &= 2\int_0^1 \frac{\left[\ln\left(\left[\beta + 1 - L_1\right]/\beta\right)\right]}{\left(\beta^* + L_1\right)} dL_1 \end{aligned} \tag{Eq. B.32}$$

Utilizing the previous results for the A_js we therefore have

$$\begin{aligned} \frac{\left\langle\left\langle S_{11}\right\rangle\right\rangle}{\tilde{k}^2} = {} & \frac{\left(3 + \cos^2\theta\right)\tilde{k}^4 v^2}{80\pi^2}\left[\frac{\left(2 + 2\beta'\right)}{\left|\beta''\right|}\left[\tan^{-1}\left(\frac{1+\beta'}{\left|\beta''\right|}\right) - \tan^{-1}\left(\frac{\beta'}{\left|\beta''\right|}\right)\right] - \ln\left[\left(1+\beta'\right)^2 + \beta''^2\right] + \ln\left(\left|\beta\right|^2\right)\right] \\ & + \frac{\left(3\cos^2\theta - 1\right)\tilde{k}^4 v^2}{80\pi^2}\int_0^1 \mathrm{Re}\left\{\frac{\left[\ln\left(\left[\beta + 1 - L_1\right]/\beta\right)\right]}{\left(\beta^* + L_1\right)}\right\} dL_1 \end{aligned} \tag{Eq. B.33}$$

Finally the scattering phase function is

$$P(\theta) = \frac{4\pi}{\left\langle\left\langle C_{sca}\right\rangle\right\rangle}\frac{\left\langle\left\langle S_{11}(\theta)\right\rangle\right\rangle}{\tilde{k}^2} \tag{Eq. B.34}$$

REFERENCES

Arfken, G. B., and H. J. Weber (2001), *Mathematical Methods for Physicists 5th Ed.*, Academic Press, San Diego.

Andreae, M. O., R. J. Charlson, F. Bruynseels, H. Storms, R. Van Grieken, and W. Maenhaut (1986), Internal Mixture of Sea Salt, Silicates, and Excess Sulfate in Marine Aerosols, *Science*, *232*(4758), 1620-1623.

Aumann, H. H., M. T. Chahine, C. Gautier, M. D. Goldberg, E. Kalnay, L. M. McMillan, H. Revercomb, P. W. Rosenkranz, W. L. Smith, D. H. Staelin, L. L. Strow, and J. Susskind (2003), AIRS/AMSU/HSB on the AQUA Mission: Design, Science Objectives, Data Products, and Processing Systems, *IEEE Trans. on Geosci. Remote Sens.*, *41*, 253-264.

Avila, A., I. Queralt-Mitjans, and M. Alarcon (1997), Mineralogical composition of African dust delivered by red rains over the northeastern Spain, *J. Geophys. Res., 102*, 21,977-21,996.

Bergstrom, R. W. (1972), Predictions of the Spectral absorption and extinction coefficients of an urban air pollution model, *Atmos. Env., 6***,** 247–258.

Berk, A., L. S. Bernstein, G. P. Anderson, E. P. Shettle, P. K. Archarya, D. C. Robertson, J. H. Chetwynd, and S. M. Alder-Golden (1998), MODTRAN cloud and multiple scattering upgrades with application to AVIRIS, *Remote Sens. Environ., 65*, 367-375.

Berk, A., G. P. Anderson, P. K. Acharya, L. S. Bernstein, L. Muratov, J. Lee, M. Fox, S. M. Adler-Golden, J. H. Chetwynd, M. L. Hoke, R. B. Lockwood, J. A. Gardner, T. W. Cooley, C. C. Borel, and P. E. Lewis (2005), MODTRAN^{TM} 5, A Reformulated Atmospheric Band Model with Auxiliary Species and Practical Multiple Scattering Options: Update, in Algorithms and Technologies for Multispectral, Hyperspectral, and Ultraspectral Imagery XI, *Proc. of SPIE*, *5806*, 662-667.

Bertie, J. E., S. L. Zhang, H. H. Eysel, S. Baluja, and M. K. Ahmed (1993), Infrared intensities of liquids XI: Infrared refractive indices from 8000 to 2 cm^{-1}, absolute integrated intensities, and dipole moment derivatives of methanol at 25°C, *Appl. Spectrosc., 47*, 1100-1114.

Bertie, J. E., and Z. Lan (1995), The refractive index of colorless liquids in the visible and infrared: Contributions from the absorption of infrared and ultraviolet radiation and the electronic molar polarizability below 20500 cm^{-1}, *J. Chem. Phy., 103*(23), 10152-10161.

Bertie, J. E., and Z. Lan (1996a), An accurate modified Kramers-Kronig transformation from reflectance to phase shift on attenuated total reflection, *J. Chem. Phy., 105*(19), 8502-8514.

Bertie, J. E., and Z. Lan (1996b), Infrared intensities of liquids XX: The intensity of the OH stretching band of liquid water revisited, and the best current values of the optical constants of H2O(l) at 25C between 15000 and 1 cm^{-1}, *Appl. Spectrosc., 50*, 1047-1057.

Biermann, U. M., B. P. Luo, and Th. Peter (2000), Absorption spectra and optical constants of binary and ternary solutions of H_2SO_4, HNO_3, and H_2O in the mid infrared at atmospheric temperatures, *J. Phys. Chem. A, 104*, 783-793.

Blanco, A., F. De Tomasi, E. Filippo, D. Manno, M. R. Perrone, A. Serra, A. M. Tafuro, and A. Tepore (2003), Characterization of African dust over southern Italy, *Atmos. Chem. Phys.*, *3*, 2147-2159.

Bohren, C. F., and D. R. Huffman (1983), *Absorption and Scattering of Light by Small Particles*, John Wiley & Sons, Inc., New York.

Born, M., and E. Wolf (1999), *Principles of Optics 6th Ed.*, pp. 87-90, Cambridge University Press, Cambridge, UK, New York.

Buseck P. R., and M. Posfai (1999), Airborne minerals and related aerosol particles: Effects on climate and the environment, *Proc. Natl. Acad. Sci.*, *96*, 3372-3379.

Chalon, G., F. Cayla, and D. Diebel (2001), IASI: An Advanced Atmospheric Sounder for Operational Meteorology, *Proc. of the 52nd Congress of IAF*, Toulouse France, 1-5 Oct. 2001.

Chang, H., and T. T. Charalampopoulos (1990), Determination of the wavelength dependence of refractive indices of flame soot, *Proc. R. Soc. Lond. A, 430***,** 577–591.

Charlson, R. J., S. E. Schwartz, J. M. Hales, R. D. Cess, J. A. Coakley, J. E. Hansen, and D. J. Hofmann (1992), Climate Forcing by Anthropogenic Aerosols, *Science, 255*, 423-430.

Chelf, J. H., and S. T. Martin (2001), Homogeneous ice nucleation in aqueous ammonium sulfate aerosol particles, *J. Geophys. Res., 106*(D1), 1215-1226.

Chou, C., P. Formenti, M. Maille, P. Ausset, G. Helas, M. Hamilton, and S. Osborne (2008), Size distribution, shape, and composition of mineral dust aerosols collected during the African Monsoon Multidisciplinary Analysis Special Observation Period 0: Dust and Biomass-Burning Experiment field campaign in Niger, January 2006, *J. Geophys. Res., 113*(D00C10), doi:10.1029/2008JD009897.

Choy, T. C. (1999), *Effective Medium Theory: Principles and Applications*, Oxford University Press, Oxford.

Claquin T., M. Schultz, and Y. J. Balkanski (1999), Modeling the mineralogy of atmospheric dust sources, *J. Geophys. Res.*, *104*(D18), 22,243-22,256, doi:10.1029/1999JD900416.

Clegg, S. L., P. Brimblecombe, and A. S. Wexler (1998), Thermodynamic model of the system $H^+/NH_4^+/SO_4^{2-}/NO_3^-/H_2O$ at tropospheric temperatures, *J. Phys. Chem. A., 102*, 2137-2154.

Clough, S. A., F. X. Kneizys and R. W. Davies (1989), Line shape and the water vapor continuum, *Atmos. Res.*, *23*, 229-241.

Couty, R., and B. Velde (1986), Pressure-induced band splitting in infrared spectra of sandine and albite, *American Mineralogist, 71*, 99-104.

d'Almeida, G. A., Koepke, P., and Shettle, E. P. (1991), *Atmospheric Aerosols: Global Climatology and Radiative Characteristics*, A Deepak Publishing, Hampton, Virginia.

Dalzell, W. H., and A. F. Sarofim (1969), Optical constants of soot and their application to heat-flux calculations, *Trans. ASME Series C, J. Heat Transfer, 91,* 100–104.

Dedecker, R. G., F. A. Best, W. F. Feltz, R. O. Knuteson, and H. E. Revercomb (2005), The AERI: new developments, upgrades, and measurement applications, *Multispectral and Hyperspectral Remote Sensing Instruments and Applications II. Edited by Larar A.M. et al., Proceedings of the SPIE*, *5655*, 489-499.

Dentener, F.J., G. R. Carmichael, Y. Zhang, J. Lelieveld, and P. J. Crutzen (1996), Role of mineral aerosol as a reactive surface in the global troposphere. *J. Geophys. Res.*, *101*(D17), 22869-22889.

DeSouza-Machado, S. G., L. L. Strow, S. E. Hannon, and H. E. Motteler (2006), Infrared dust spectral signatures from AIRS, *Geophy. Res. Lett., 33*(L03801), 1-5.

Downing, H. D., and D. Williams (1975), Optical constants of water in the infrared, *J. Geophys. Res., 80***,** 1656-1661.

Earle, M. E., R. G. Pancescu, B. Cosic, A.Y. Zasetsky, and J. J. Sloan (2006), Temperature-dependent complex indices of refraction for crystalline $(NH_4)_2SO_4$, *J. Phys. Chem. A, 110*, 13022-13028.

Egan, W. G., and T. W. Hilgeman (1979), *Optical properties of inhomogeneous materials: Applications to Geology, Astronomy, Chemistry, and Engineering*, 235 pp., Academic Press, New York.

Eldridge, J. E., and E. D. Palik (1985), Sodium Chloride (NaCl), in *Handbook of Optical Constants of Solids*, edited by E. D. Palik, pp. 775-793, Academic Press, New York.

Erlick, C. (2006), Effective refractive indices of water and sulfate drops containing absorbing inclusions, *J. Atmos. Sci., 63*, 754-763.

Fabian, D., Th. Henning, C. Jager, H. Mutschke, J. Dorschner, and O. Wehrhan (2001), Steps towards interstellar silicate mineralogy – VI, Dependence of crystalline olivine IR spectra on iron content and particle shape, *Astron. Astrophys.*, *378*, 228-238.

Fenn, R. W., S. A. Clough, W. O. Gallery, R. E. Good, F. X. Kneizys, J. D. Mill, L. S. Rothman, E. P. Shettle, and F. E. Volz (1985), Optical and infrared properties of the atmosphere, in *Handbook of Geophysics and the Space Environmen,* A. S. Jursa, editor, National Technical Information Service, Springfield, Virginia, 18-1-18-80.

Fischer, K. (1975), Mass absorption indices of various types of natural aerosol particles in the infrared, *Appl. Opt.*, *14*(12), 2851-2856.

Flanigan, D. F., and H. P. DeLong (1971), Spectral absorption characteristics of the major components of dust clouds, *Appl. Opt.*, *10*(1), 51-57.

Formetti, P., J. L. Rajot, K. Desboeufs, S. Caquineau, S. Chevaillier, S. Nava, A. Gaudichet, E. Journet, S. Triquet, S. Alfaro, M. Chiari, J. Haywood, H. Coe, and E. Highwood (2008), Regional variabiltiy of the composition of mineral dust from western Africa: Results from the AMMA SOP0/DABEX and DODO field campaigns, *J. Geophys. Res., 113*(D00C13), doi:10.1029/2008JD009903.

Fouquart, Y. B., G. Bonnell, J. C. Brogniez, L. Smith, J. J. Morcrette, and A. Cerf (1987), Observations of Saharan aerosols: Results of ECLATS field experiment. Part II: Broadband radiative characteristics of the aerosols and vertical radiative flux divergence, *J. Clim. Appl. Meteorol.*, *26*, 38-52.

Gard E. E., M. J. Kleeman, D. S. Gross, L. S. Hughes, J. O. Allen, B. D. Morrical, D. P. Fergenson, T. Dienes, M. E. Gälli, R. J. Johnson, G. R. Cass, and K. A. Prather (1998), Direct observation of heterogeneous chemistry in the atmosphere. *Science*, *279*, 1184-1187.

Glotch, T. D., G. R. Rossman, and O. Aharonson (2007), Mid-infrared (5-100mm) reflectance spectra and optical constants of ten phyllosilicate minerals, *Icarus, 192***,** 605-622.

Gosse, S. F., M. Wang, D. Labrie, and P. Chylek (1997), Imaginary part of the refractive index of sulfates and nitrates in the 0.7-2.6 mm spectral region, *Appl. Opt*., *36*(16), 3622–3631.

Goudie, A. S., and N. J. Middleton (2001), Saharan dust storms: nature and consequences, *Earth-Science Reviews*, *56*, 179-204.

Greenberg, J., and L. J. Hallgren (1960), Infrared absorption spectra of alkali metal nitrates and nitrites above and below the melting point, *J. Chem. Phys., 33*(3), 900-902.

Hale, G. M., and M. R. Querry (1973), Optical constants of water in the 200 nm to 200 μm wavelength region, *Appl. Opt*., *12*(3), 555–563.

Harvey, A. H., J. S. Gallagher, and J. M. H. L. Sengers (1998), Revised Formulation of the refractive index of water and steam as a function of wavelength, temperature and density, *J. Phys. Chem. Ref. Data, 27*(4), 761-774.

Hawkins, G., and R. Hunneman (2004), The temperature-dependent spectral properties of filter substrate materials in the far-infrared (6-40 μm), *Infrared Phys. Technol., 45*, 69-79.

Henning, Th., and H. Mutschke (1997), Low-temperature infrared properties of cosmic dust analogues, *Astron. Astrophys.*, *327*, 743-754.

Herzberg, G. (1991), *Molecular Spectra and Molecular Structure, Volume II, Infrared and Raman Spectra of Polyatomic Molecules*, Krieger Publishing Company, Malabar, FL.

Hess, M., P. Koepke, and I. Schult (1998), Optical Properties of Aerosols and Clouds: The software package (OPAC), *BAMS, 79*(5), 831-844.

Highwood, E. J., J. M. Haywood, M. D. Silverstone, S. M. Newman, and J. P. Taylor (2003), Radiative properties and direct effect of Saharan dust measured by the C-130 aircraft during Saharan Dust Experiment (SHADE): 2. Terrestrial spectrum, *J. Geophys. Res., 108* (D18), doi:10.1029/2002JD002552.

Hudson, P. K., E. R. Gibson, M. A. Young, P. D. Kleiber, and V. H. Grassian (2008a), Coupled infrared extinction and size distribution measurements for several clay components of mineral dust aerosol, *J. Geophys. Res., 113*(D01201), 1-11.

Hudson, P. K., M. A. Young, P. D. Kleiber, and V. H. Grassian (2008b), Coupled infrared extinction spectra and size distribution measurements for several non-clay components of mineral dust aerosol (quartz, calcite, and dolomite), *Atmos. Environ., 42*, 5991-5999.

Huffman, D. R., and C. F. Bohren (1980), Infrared absorption spectra of non-spherical particles treated in the Rayleigh-Ellipsoid approximation, in *Light Scattering by Irregularly Shaped Particles*, edited by D. W. Schuerman, chap. 4, pp. 103-111, Plenum Press, New York.

Intergovernmental Panel on Climate Change (IPCC) (2001), *Climate Change 2001: The Scientific Basis: Contributions of Working Group I to the Third Assessment Report of*

the Intergovernmental Panel on Climate Change, edited by J. T. Houghton *et al.*, pp. 881. Cambridge Univ. Press, New York.

IPCC 2007, *Contribution of Working Group I to the Fourth Assessment Report of the Intergovernmental Panel on Climate Change*, edited by Solomon, S., D. Qin, M. Manning, Z. Chen, M. Marquis, K.B. Averyt, M. Tignor and H.L. Miller, pp. 996. Cambridge Univ. Press, New York.

Irvine, W. M., and J. B. Pollack (1968), Infrared optical properties of water and ice spheres, *Icarus, 8*, 324–360.

Jacobson, M. Z. (2001), Strong radiative heating due to the mixing state of black carbon in atmospheric aerosols, *Nature*, *409*, 695-697.

Jacobson, M. Z. (2002), Analysis of aerosol interactions with numerical techniques for solving coagulation, nucleation, condensation, dissolution, and reversible chemistry among multiple size distributions, *J. Geophys. Res., 107*(AAC 2), 1-23.

Jarzembski, M. A., M. L. Norman, K. A. Fuller, V, Srivastava, and D. R. Cutten (2003), Complex refractive index of ammonium nitrate in the 2 – 20 μm spectral range, *Appl. Opt., 42*(6), 922-930.

Jordan, C. E., J. E. Dibb, B. E. Anderson, and H. E. Fuelberg (2003), Uptake of nitrate and sulfate on dust aerosols during TRACE-P. *J. Geophys. Res.*, *108*(D21), doi:10.1029/2002JD003101.

Kandler, K., N. Benker, U. Bundke, E. Cuevas, M. Ebert, P. Knippertz, S. Rodriguez, L. Schutz, and S. Weinbruch (2007), Chemical composition and complex refractive index of Saharan mineral dust at Izana, Tenerife (Spain) derived by electron microscopy, *Atmos. Environ., 41*, 8058-8074.

Kandler, K., L. Schutz, C. Deutscher, M. Ebert, H. Hofmann, S. Jackel, R. Jaenicke, P. Knippertz, K. Lieke, A. Massling, A. Petzold, A. Schladitz, B. Weinzierl, A. Wiedensohler, S. Zorn, and S. Weinbruch (2009), Size distribution, mass concentration, chemical and mineralogical composition and derived optical parameters of the boundary layer aerosol at Tinfou, Morocco, during SAMUM 2006, *Tellus*, 61B, 32-50.

Kaufman, Y. J., D. Tanre´, O. Dubovik, A. Karnieli, and L. A. Remer (2001), Absorption of sunlight by dust as inferred from satellite and groundbased measurements, *Geophys. Res. Lett., 28*, 1479–1482.

Kim, J., U. W. Schmitt, J. A. Gruetzmacher, G. A. Voth, and N. E. Scherer (2002), The vibrational spectrum of the hydrated proton: Comparison of experiment, simulation, and normal mode analysis, *J. Chem. Phys., 116*(2), 737-746.

King, M. D., D. M. Byrne, B. M. Herman, and J. A. Reagan (1978), Aerosol size distributions obtained by inversions of spectral optical depth measurements, *J. Atmos. Sci.*, *35*, 2153-2167.

Kline, J., B. Huebert, S. Howell, B. Blomquist, J. Zhuang, T. Bertram, and J. Carillo (2004), Aerosol composition and size versus altitude from the C-130 during ACE-Asia, *J. Geophys. Res.*, *109*(D19S08), doi:10.1029/2004JD004540.

Kou, L., D. Labrie, and P. Chylek (1993), Refractive indices of water and ice in the 0.65–2.5 μm spectral range, *Appl. Opt*., *32*, 3531–3540.

Krieger, U. K., J. C. Mossinger, B. Luo, U. Weers, and T. Peter (2000), Measurement of the refractive indices of H2SO4-HNO3-H2O solutions to stratospheric temperatures, *Appl. Opt., 39*(21), 3691-3703.

Krueger, B. J., V. H. Grassian, M. J. Iedema, J. P. Cowin, and A. Laskin (2003), Probing heterogeneous chemistry of individual atmospheric particles using scanning electron microscopy and energy-dispersive X-ray analysis, *Anal. Chem.*, *75*, 5170-5179.

Krueger, B. J., V. H. Grassian, J. P. Cowin, and A. Laskin (2004), Heterogeneous chemistry of individual mineral dust particles from different dust source regions: The importance of particle mineralogy, *Atmos. Environ.*, *38*, 6253-6261.

Kruglanski, M., M. De Maziere, A. C. Vandaele, and D. Hurtmans (2006), Boundary layer aerosol retrieval from thermal infrared nadir sounding – Preliminary results, *Advances in Space Research*, *37*, 2160-2165.

Lafon, S., I. N. Sokolik, J. L. Rajot, S. Caquineau, and A. Gaudichet (2006), Characterization of iron oxides in mineral dust aerosols: Implications for light absorption, *J. Geophys. Res., 111*(D21207), doi:10.1029/2005JD007016.

Laliberte, M., and W. E. Cooper (2004), Model for calculating the density of aqueous electrolyte solutions, *J. Chem. Eng. Data, 49*, 1141-1151.

Laskin, A., D. J. Gaspar, W. Wang, S. W. Hunt, J. P. Cowin, S. D. Colson, and B. J. Finlayson-Pitts (2003), Reactions at interfaces as a source of sulfate formation in sea-salt particles, *Science*, *301*, 340-344.

Lau, K. M., K. M. Kim, Y. C. Sud, and G. K. Walker (2009), A GCM study of the response of the atmospheric water cycle of West Africa and the Atlantic to Saharan dust radiative forcing, *Ann. Geophys.*, 27, 4023-4037

Lesins, G., P. Chylek, and U. Lohmann (2002), A study of internal and external mixing scenarios and its effect on aerosol optical properties and direct radiative forcing, *J. Geophys. Res., 107*(AAC 5), 1-12.

Liou, K. N. (2002), *An Introduction to Atmospheric Radiation*, Academic Press, San Diego, California.

Liu, Z., A. Omar, M. Vaughan, J. Hair, C. Kittaka, Y. Hu, K. Powell, C. Trepte, D. Winker, C. Hostetler, R. Ferrare, and R. Pierce (2008), CALIPSO lidar observations of the optical properties of Saharan dust: A case study of long-range transport, *J. Geophys. Res., 113*(D07207), doi:10.1029/2007JD008878.

Long, L. L., M. R. Querry, R. J. Bell, and R. W. Alexander (1993), Optical properties of calcite and gypsum in the crystalline and powdered form in the infrared and far-infrared, *Infrared Phys*., *34*(2), 191-201.

Lubrano, A. M., G. Masiello, C. Serio, M. Matricardi, and R. Rizzi (2002), IMG evidence of chlorofluorocarbon absorption in the atmospheric window region 800-900 cm^{-1}, *J. Quant. Spectrosc. Radiat. Transfer*, *72,* 623-635.

Luo, B., U. K. Krieger, and T. Peter (1996), Densities and refractive indices of H2SO4/HNO3/H2O solutions to stratospheric temperatures, *Geophys. Res. Lett., 23*(25), 3707-3710.

Mamane, Y., and J. Gottlieb (1989), Heterogeneous reactions of minerals with sulfur and nitrogen oxides, *J. Aerosol Sci., 20*, 303-311.

Maring, H., D. L. Savioe, M. A. Izaguirre, L. Custals, and J. S. Reid (2003), Mineral dust aerosol size distribution change during atmospheric transport, *J. Geophys. Res., 108*(D19), 8592, doi:10.1029/2002JD002536.

Markowicz, K. M., P. J. Flatau, A. M. Vogelmann, P. K. Quinn, and E. J. Welton (2003), Clear-sky infrared radiative forcing at the surface and the top of the atmosphere, *Q. J. R. Meteorol. Soc.*, *129*, 2927-2947.

Martin, S. T., D. Salcedo, L. T. Molina, and M. J. Molina (1997), Phase transformations of micron-sized H2SO4/H2O particles studied by infrared spectroscopy, *J. Phys. Chem. B, 101*, 5307-5313.

Max, J-J., and C. Chapados (1999), Influence of anomalous dispersion on the ATR spectra of aqueous solutions, *Appl. Spectrosc., 53*(9), 1045-1053.

Maxwell-Meier, K., R. Weber, C. Song, D. Orsini, Y. Ma, G. R. Carmichael, and D. G. Streets (2004), Inorganic composition of fine particles in mixed dust-pollution plumes observed from airborne measurements during ACE-Asia. *J. Geophys. Res.*, *109*(D19S07), doi:10.1029/2003JD004464.

McKeown, D. A. (2005), Raman spectroscopy and vibrational analyses of albite: From 25° C through the melting temperature, *American Mineralogist, 90*, 1506-1517.

Merwin, H. E. (1930), *International Critical Tables of Numerical Data; Physics, Chemistry and Technology, vol. 7*, pp. 16-33, McGraw-Hill, New York.

Methra, R. (2003), Application of refractive index mixing rules in binary systems of hexadecane and heptadecane with n-alkanols at different temperatures, *Proc. Indian Acad. Sci., 115*(2), 147-154.

Miller, F. A., and C. H. Wilkins (1952), Infrared Spectra and Characteristic Frequencies of Inorganic Ions, *Anal. Chem., 24*(8), 1253-1294.

Mishchenko, M. I., and L. D. Travis (1998), Capabilities and limitations of a current Fortran implementation of the T-Matrix method for randomly oriented, rotationally symmetric scatterers, *J. Quant. Spectrosc. Radiat. Transfer*, *60*(3), 309-324.

Mooney, T., and R. F. Knacke (1985), Optical constants of Chlorite and Serpentine between 2.5 and 50 μm, *Icarus*, *64***,** 493-502.

Moy, L., H. E. Revercomb, and R. O. Knuteson (2005), Retrieving Aerosols from the Atmospheric Emitted Radiance Interferometer: Can it be Done?, *Fifteenth ARM Science Team Meeting Proceedings*, Daytona Beach, Florida, March 14-18.

Myhre, C. E. L., D. H. Christensen, F. M. Nicolaisen, and C. J. Nielsen (2003), Spectroscopic study of aqueous H2SO4 at different temperatures and compositions: Variations in dissociation and optical properties, *J. Phys. Chem. A, 107*, 1979-1991.

Myhre, C. E. L., H, Grothe, A. A. Gola, and C. J. Nielsen (2005), Optical constants of HNO3/H2O and H2SO4/HNO3/H2O at low temperatures in the infrared region, *J. Phys. Chem. A, 109*(32), 7166-7171, doi:10.1021/jp0508406 S1089-5639(05)00840-6.

Nevitt, T. J., and C. F. Bohren (1984), Infrared backscattering by irregularly shaped particles: A statistical approach, *J. Clim. Appl. Meteorol.*, *23*, 1342-1349.

Newman, S. M., J. A. Smith, M. D. Glew, S. M. Rodgers, and J. P. Taylor (2005), Temperature and salinity dependence of sea surface emissivity in the thermal infrared, *Q. J. R. Meteorol. Soc.*, *131*, 2539-2557.

Niedziela, R. F., M. L. Norman, R. E. Miller, and D. R. Worsnop (1998), Temperature- and composition-dependent infrared optical constants for sulfuric acid, *Geophys. Res. Lett., 25*(24), 4477-4480.

Nilsson, B. (1979), Meteorological influence on aerosol extinction in the 0.2-40-μm wavelength range, *Appl. Opt.*, *18*(20)**,** 3457–3473.

Norman, M. L., J. Qian, and R. E. Miller (1999), Infrared complex indices of supercooled liquid HNO_3/H_2O aerosols, *J. Geophys. Res.*, *104*(D23)**,** 30,571–30,584.

Otto, S., M. de Reus, T. Trautmann, A. Thomas, M. Wendisch, and S. Borrmann (2007), Atmospheric radiative effects of an in situ measured Saharan dust plume and the role of large particles, *Atmos. Chem. Phys.*, 7, 4887-4903.

Palik, E. D., and R. Khanna (1985), Sodium Nitrate ($NaNO_3$), in *Handbook of Optical Constants of Solids*, edited by E. D. Palik, pp. 871-881, Academic Press, New York.

Palmer, K. F., and D. Williams (1974), Optical properties of water in the infrared, *J. Opt. Soc. Am.*, *64*, 1107-1110.

Palmer, K. F., and D. Williams (1975), Optical constants of sulfuric acid; Application to the clouds of Venus?, *Appl.Opt.*, *14***,** 208-219.

Patterson, E. M. (1981), Optical properties of the crustal aerosol: Relation to chemical and physical characteristics, *J. Geophys. Res.*, *86***,** 3236–3246.

Peterson, J. T., and J. A. Weinman (1969), Optical properties of quatrz dust particles at infrared wavelengths, *J. Geophys. Res.*, *74***,** 6947–6952.

Pierangelo, C., A. Chedin, S. Heilliette, N. Jacquinet-Husson, and R. Armante (2004), Dust altitude and infrared optical depth from AIRS, *Atmos. Chem. Phys.*, *4*, 1813-1822.

Pierangelo, C., M. Mishchenko, Y. Balkanski, and A. Chedin (2005), Retrieving the effective radius of Saharan dust coarse mode from AIRS, *Geophy. Res. Lett.*, *32*(L20813), 1-4.

Plaskett, J. S., and P. N. Schatz (1963), On the Robinson and Price (Kramers-Kronig) method of interpreting reflection data taken through a transparent window, *J. Chem. Phys., 38*(3), 612-617.

Pope, R. M., and E. S. Fry (1997), Absorption spectrum (380–700 nm) of pure water. II. Integrating cavity measurements, *Appl. Opt*., *36*(33), 8710–8723.

Popova, S. I., T. S. Tolstykh, and V. G. Vorobev (1972), Optical characteristics of amorphous quartz in the 1400-200 cm^{-1} region, *Opt. Spectrosc*., *33*, 444.

Popova, S. I., T. S. Tolstykh, and L. S. Ivlev (1973), Optical constants in Fe2O3 in the infrared range of the spectrum, *Opt. Spectrosc*., *35*(5), 551-552.

Posch, T., H. Mutschke, A. Baier, and T. Henning (2007), IR properties of calcite and dolomite at low temperatures, *Astron. Nachr.*, *328*(7), 648.

Press, W. H., S. A. Teukolsky, W. T. Vetterling, and B. P. Flannery (1992), *Numerical Recipes in C: The Art of Scientific Computing*, Cambridge University Press, Cambridge.

Pye, K. (1987), *Aeolian Dust and Dust Deposits*, 334 pp., Academic Press, San Diego, Calif.

Querry, M. R., G. Osborne, K. Lies, R. Jordan, and R. M. Coveney (1978), Complex refractive index of limestone in the visible and infrared, *Appl. Opt., 17*, 353-356.

Querry, M. R., and I. L. Tyler (1980), Reflectance and complex refractive indices in the infrared for aqueous solutions of nitric acid, *J. Chem. Phys., 72*(4), 2495-2499.

Querry, M. R. (1987), Optical constants of minerals and other materials from the millimeter to the UV, *Report CRDEC-CR-88009*, US Army, Aberdeen, MD.

Quickenden, T. I., and J. A. Irvine (1980), The ultraviolet absorption spectrum of liquid water, *J. Chem. Phys., 72*(8), 4416-4428.

Quijano A. L., I. N. Sokolik, and O. B. Toon (2000), Radiative heating rates and direct radiative forcing by mineral dust in cloudy conditions, *J. Geophys. Res.* , D10, 12,207-12,219.

Rathke, C., J. Notholt, J. Fischer, and A. Herber (2002), Properties of coastal Antarctic aerosol from combined FTIR spectrometer and sun photometer measurements, *Geophy. Res. Lett*., *29* (23), 46-1-46-4.

Ray, P. S. (1972), Broadband complex refractive indices of ice and water, *Appl. Opt., 11*(8), 1836-1844.

Reid, J. S., et al. (2003), Analysis of measurements of Saharan dust by airborne and ground-based remote sensing methods during the Puerto Rico Dust Experiment (PRIDE), *J. Geophys. Res., 108*(D19), 8586, doi:10.1029/2002JD002493.

Remedios, J. J., R. J. Leigh, A. M. Waterfall, D. P. Moore, H. Sembhi, I. Parkes, J. Greenhough, M. P. Chipperfield, and D. Hauglustaine (2007), MIPAS reference atmospheres and comparisons to V4.61/V4.62 MIPAS level 2 geophysical data sets, *Atmos. Chem. Phys. Discuss.*, *7*, 9973-10017.

Remsberg, E. E. (1971), *Radiative Properties of Several Probable Constituents of Atmospheric Aerosols*, Ph.D. Thesis, Department of Meteorology, University of Wisconsin, Madison.

Rothman, L. S., D. Jacquemart, A. Barbe, D. Chris Benner, M. Birk, L. R. Brown, M. R. Carleer, C. Chackerian Jr., K. Chancea, L. H. Couderth, V. Danai, V. M. Devic, J.-M. Flaudh, R. R. Gamache, A. Goldman, J.-M. Hartmann, K. W. Jucks, A. G. Maki, J.-Y. Mandin, S. T. Massie, J. Orphal, A. Perrin, C. P. Rinsland, M. A. H. Smith, J. Tennyson, R. N. Tolchenov, R. A. Toth, J. Vander Auwera, P. Varanasi, and G. Wagner (2005), The HITRAN 2004 molecular spectroscopic database, *J. Quant. Spectrosc. Radiat. Transfer*, *96*, 139-204.

Roush, T., J. Pollack, and J. Orenberg (1991), Derivation of midinfrared (5-25 μm) optical constants of some silicates and palagonite, *Icarus*, *94*, 191-208.

Roush, T. L., F. Esposito, G. R. Rossman, and L. Colangeli (2007), Estimated optical constants of gypsum in the regions of weak absorptions: Applications of scattering theories and comparisons to independent measurements, *J. Geophys. Res.*, *112*, E10003, doi:10.1029/2007JE002920.

Schwartz, S. E., and M. O. Andreae (1996), Uncertainty in climate change caused by aerosols, *Science*, *272*, 1121-1122.

Shettle, E. P., and R. W. Fenn (1976), Models of the atmospheric aerosols and their optical properties, in *AGARD Conference Proceedings No. 183 Optical Propagation in the Atmosphere*, Wave Propagation Panel Symposium, Lyngby, Denmark, 27-31 October 1975, AGARD-CP-183, NTIS, ADA 028615.

Shettle, E. P., and R. W. Fenn (1979), Models for the aerosols of the lower atmosphere and the effects of humidity variations on their optical properties, *AFGL-TR-79-0214, Environmental Research Paper No. 675*, NTIS, ADA 085951, 94pp.

Shimota, A., and H. Kobayashi (2001), Error analysis for retrieval of urban atmospheric aerosol properties from downwelling infrared radiation spectra, *Appl. Optics*, *40* (9), 1493-1499.

Shimota, A., H. Kobayashi, and K. Wada (2002), Retrieval for physical parameters aerosols in an urban area by ground-based FTIR measurement, *J. Geophys. Res., 107*(D14), AAC 6-1-6-10.

Shivola, A. (1999), *Electromagnetic mixing formulas and applications*, The Institute of Electrical Engineers, London.

Smith, D. Y. (1997), Dispersion relations for complex reflectivities, *J. Opt. Soc. Am., 67*(4), 570-571.

Sokolik, I. N., A. Andronove, and T. C. Johnson (1993), Complex refractive index of atmospheric dust aerosols, *Atmos. Environ., 27A***,** 2495–2502.

Sokolik, I.N. and O.B. Toon (1996), Direct radiative forcing by airborne mineral dust. *J. Aerosol Sci.* 27, Supplement 1, S11.

Sokolik, I.N. and O.B. Toon (1999), Incorporation of mineralogical composition into models of the radiative properties of mineral aerosols from ultraviolet to infrared wavelengths, *J. Geophys. Res., 104*, 9423-9444.

Sokolik, I. N., D. M. Winker, G. Bergametti, D. A. Gillette, G. Carmichael, Y. J. Kaufman, L. Gomes, L. Schuetz, and J. E. Penner (2001), Introduction to special section: Outstanding problems in quantifying the radiative impacts of mineral dust, *J. Geophys. Res.*, *106*(D16), 8014 - 8027.

Sokolik, I. N. (2002), The spectral radiative signature of wind-blown mineral dust: Implications for remote sensing in the thermal IR region, *Geophy. Res. Lett*., *29* (24), 2154, doi:10.1029/2002GL015910.

Song, C. H., and G. R. Carmichael (1999), The ageing process of naturally emitted aerosol (sea-salt and mineral aerosol) during long range transport, *Atmos. Environ.*, *33*, 2203-2218.

Stamnes, K., S.-C. Tsay, W. Wiscombe, and K. Jayaweera (1988), Numerically Stable Algorithm for Discrete-Ordinate-Method Radiative Transfer in Multiple Scattering and Emitting Layered Media, *Applied Optics*, *27*, 2502-2509.

Stelson, A. W. (1990), Urban aerosol refractive index prediction by partial molar refraction approach, *Environ. Sci. Technol., 24*(11), 1676-1679.

Steyer, T. R., L. Day, and D. R. Huffman (1974), Infrared absorption by small amorphous quartz spheres, *Appl. Opt., 13***,** 1586–1590.

Tam, A. C., and C. K. N. Patel (1979), Optical absorptions of light and heavy water by laser optoacoustic spectroscopy, *Appl. Opt., 18***,** 3348–3358.

Tang, I. N., and H. R. Munkelwitz (1994), Water activities, densities, and refractive indices of aqueous sulfates and sodium nitrate droplets of atmospheric importance, *J. Geophys. Res., 99*(D9), 18801-18808.

Tang, I. N. (1997), Thermodynamic and optical properties of mixed-salt aerosols of atmospheric importance, *J. Geophys. Res., 102*(D2), 1883-1893.

Tanre et al., (2003), Measurement and modeling of the Saharan dust radiative impact: Overview of the Saharan Dust Experiment (SHADE), *J. Geophys. Res., 108*(D18), doi:10.1029/2002JD003273.

Tegen, I., A. A. Lacis, and I. Fung (1996), The influence on climate forcing of mineral aerosols from disturbed soils, *Nature*, *380*, 419-422.

Textor, C., M. Schulz, S. Guibert, S. Kinne, Y. Balkanski, S. Bauer, T. Berntsen, T. Berglen, O. Boucher, M. Chin, F. Dentener, T. Diehl, J. Feichter, D. Fillmore, P. Ginoux, S. Gong, A. Grini, J. Hendricks, L. Horowitz, P. Huang, I.S.A. Isaksen, T. Iversen, S. Kloster, D. Koch, A. Kirkevåg, J.E. Kristjaansson, M. Krol, A. Lauer, J.F. Lamarque, X. Liu, V. Montanaro, G. Myhre, J.E. Penner, G. Pitari, S. Reddy, Ø.P. Stier, T. Takemura, and X. Tie (2007), The effect of harmonized emissions on aerosol

properties in global models — An AeroCom experiment, *Atmos. Chem. Phys.*, *7*, 4489-4501.

Tien, C. L., and S. C. Lee (1982), Flame radiation, *Prog. Energy Combust. Scit., 8***,** 41–59.

Toon, O. B., J. B. Pollack, and B. N. Khare (1976), The Optical Constants of Several Atmospheric Aerosol Species: Ammonium Sulfate, Aluminum Oxide, and Sodium Chloride, *J. Geophys. Res.*, *81*(5), 733-735,748.

Toon, O. B., J. B. Pollack, and C. Sagan (1977), Physical properties of the particles composing the Martian dust storms of 1971-1972, *Icarus*, *30*, 663-696.

Twitty, J. T., and J. A. Weinman (1971), Radiative Properties of Carbonaceous Aerosols, *J. Appl. Meteorol.*, *10*, 725-731.

Urban, M. W. (1996), *Attenuated Total Reflectance Spectroscopy of Polymers: Theory and Practice*, American Chemical Society, Washington, D.C.

Vandenbussche, B., C. Dominik, M. Min, R. van Boekel, L. B. F. M. Waters, G. Meeus, and A. de Koter (2004), Tentative detection of micron-sized forsterite grains in the proto-planetary disk surrounding HD 100453*, *Astron. Astrophys.*, *427*, 519-523.

Volz, F. E. (1972), Infrared refractive index atmospheric aerosol substances, *Appl. Opt*., *11*(4), 755-759.

Volz, F. E. (1973), Infrared optical constants of Ammonium Sulfate, Sahara dust, volcanic pumice, and flyash, *Appl. Opt*., *12*(3), 564-567.

Wahab, A., and S. Mahiuddin (2001), Electrical conductivity, speeds of sound, and viscosity of aqueous ammonium nitrate solutions, *Can. J. Chem., 79*, 1207-1212.

Weaver, C. J., J. Joiner and P. Ginoux (2003), Mineral Aerosol Contamination of TOVS Temperature and Moisture Retrievals, *J. Geophys. Res.*, 108 doi:10.1029/2002JD002571

Wilson, S. H. S., N. C. Atkinson, and J. A. Smith (1999), The development of an airborne infrared interferometer for meteorological sounding studies, *J. Atmos. Oceanic Tech.*, *16***(**12**),** 1912-1927.

Wiscombe, W. J. (1980), Improved Mie scattering algorithms, *Appl. Opt.*, *19*(9), 1505-1509.

Wong, S., A. E. Dessler, N. M. Mahowald, P. Yang, and Q. Feng (2009), Maintenance of Lower Tropospheric Temperature Inversion in the Saharan Air Layer by Dust and Dry Anomaly, *J. Climate*, 22, 5149-5162.

Wu, J.-S., S. S. Krishnan, and G. M. Faeth (1997), Refractive indices at the visible wavelengths of soot emitted from turbulent diffusion flames, *J. Heat Transfer, 119*, 230–237.

Wu, X., and W. L. Smith (1997), Emissivity of a rough sea surface for 8-13 μm: Modeling and verification, *Appl. Opt.*, *36*, 2609-2619.

Yang, P., B. C. Gao, B. A. Baum, Y. X. Hu, W. J. Wiscombe, S. C. Tsay, D. M. Winkler, and S. L. Nasiri (2001), Radiative properties of cirrus clouds in the infrared (8 – 13 μm) spectral region, *J. Quant. Spectrosc. Radiat. Transfer*, *70*, 473-504.

Zender, C. S., R. L. Miller, and I. Tegen (2004), Quantifying mineral dust mass budgets: terminology, constraints, and current estimates, *EOS, Transactions, American Geophysical Union*, 85 (48), 509-512.

Zhuang, H., C. K. Chan, M. Fing, and A. S. Wexler (1999), Formation of nitrate and non-sea-salt sulfate on coarse particles, *Atmos. Environ.*, *33*, 4223-4233.

Zundel, G., and J. Fritsch (1986), Interactions in and structures of ionic solutions and polyelectrolytes – Infrared results, in *The Chemical Physics of Solvation: Part B, Spectroscopy of Solvation*, R. R. Dogonadze, E. Kalman, A. A. Kornyshev, J. Ulstrup, editors, p. 32, Elsevier, New York.

VITA

GREGORY J. BOER

Gregory Boer was born in Redlands, California. He moved to El Cajon, California, outside of San Diego, at age 10. He attended the University of California, San Diego where he received a B.S. in Mathematics and Physics with a specialization in Earth Sciences in 1987. After graduating from UCSD, Greg took a job with the Defense Mapping Agency in the Washington DC area. In 1996 he moved to Rochester, New York for a year where he attended the Rochester Institute of Technology and received a M.S. in Image Science in 1997 with two specializations: Digital Image Processing and Remote Sensing. Greg returned to the Washington DC area and continued working for the newly formed National Imagery and Mapping Agency. In 2001 he moved to Boulder, Colorado to study Atmospheric Science at the University of Colorado, Boulder where he received a M.S. in Atmospheric Science in 2003. Greg returned to the Washington DC area to continue working for the newly-named National Geospatial-Intelligence Agency, and transferred to Georgia Tech to pursue a doctorate in Atmospheric Science. His research interests include radiative transfer, remote sensing, and dust aerosol. When he is not working on his research, Greg enjoys woodworking and carpentry along with bike riding, hiking and running.